申报	系列：教师系列（科研为主型）
	专业：农业电气化与自动化
	职称：副教授

业绩成果材料

（申报人的业绩成果材料包括论文、科研项目、获奖以及其他成果等）

单　位（二级单位） 工程学院

姓　名 姜 锐

材料核对人:　　　　　　　　　　单位盖章:

核对时间:

华南农业大学制

目　录

一、科研项目

1.1 主持科研项目 …………………… 1
1.2 主参科研项目 …………………… 42

二、科研成果

2.1 代表性学术论文 …………………… 71
2.2 参编专著 …………………… 179
2.3 发明专利 …………………… 189
2.4 第三方检测报告 …………………… 198
2.5 科研平台建设 …………………… 213
2.6 科技奖励与成果评价 …………………… 221
2.7 学术兼职 …………………… 225

三、团队荣誉

3.1 第二十五届“广东青年五四奖章集体” …………………… 228
3.2 广东农技服务“轻骑兵”十大先锋队伍 …………………… 229
3.3 全国文化科技卫生“三下乡”优秀团队 …………………… 232

四、指导学生竞赛和创新训练项目

4.1 指导学生竞赛 …………………… 236
4.2 大学生创新训练项目 …………………… 239

五、生产锻炼与社会服务

5.1 生产锻炼证明 …………………… 248
5.2 社会服务证明 …………………… 249

子课题编号：2022YFD200150102 **密　　级：公开**

国家重点研发计划
子课题任务书

子课题名称（编号）：	农机无人作业环境信息感知 （2022YFD200150102）
子课题承担单位：	华南农业大学
子课题负责人：	姜锐
课题名称（编号）：	小麦无人农场信息感知与生产决策 （2022YFD2001501）
课题承担单位：	华南农业大学
项目名称（编号）：	小麦生产全程无人化作业技术装备创制与应用 （2022YFD2001500）
项目牵头单位：	北京市农林科学院智能装备技术研究中心
执行期限：	2022 年 11 月至 2027 年 5 月

11010210018680

中华人民共和国科学技术部制

一、目标及考核指标、评测方式/方法

子课题目标、成果与考核指标表

课题目标[1]	预期成果		考核指标[2]				考核方式（方法）及评价手段[4]
	预期成果名称	预期成果类型	指标名称	立项时已有指标值/状态	中期指标值/状态[3]	完成时指标值/状态	
通过空地协同感知方法精准识别和语义分割农田地头、边界、障碍物等农田典型元素，解决无人农机在不同农田作业环境下的自主认知难题。	农机无人作业环境信息感知系统	□新理论 □新原理 ■新产品 ■新技术 □新方法 □关键部件 □数据库 □软件 □应用解决方案 ■实验装置/系统 □临床指南/规范 □工程工艺 □标准 ■论文 ■发明专利 □其他	指标 1.1 技术指标	/	初步研制农机无人作业环境信息感知装置样机	障碍物探测距离≥30m；障碍物方位、尺寸检测精度≥90%；农田地头、边界识别，准确率≥95%；研发障碍物感知系统 10 套，农田地头及边界识别系统 10 套；TRL7	第三方检测机构出具检测报告
			指标 1.2 高水平论文	0	1	2	发表或录用
			指标 1.3 发明专利	0	1	2	申请或授权

科技报告考核指标	序号	报告类型[5]	数量	提交时间	公开类别及时限[6]
	1	子课题年度进展报告和科技报告	1	2022 年 12 月	延期 3 年公开
	2	子课题年度进展报告和科技报告	1	2023 年 12 月	延期 3 年公开
	3	子课题年度进展报告和科技报告	1	2024 年 12 月	延期 3 年公开
	4	子课题中期进展报告和科技报告	1	2025 年 6 月	延期 3 年公开
	5	子课题年度进展报告和科技报告	1	2025 年 12 月	延期 3 年公开
	6	子课题年度进展报告和科技报告	1	2026 年 12 月	延期 3 年公开
	7	子课题综合绩效评价报告和科技报告	1	2027 年 5 月	延期 3 年公开

其他目标与考核指标：培养技术骨干 1 名，研究生 2 名。

九、子课题参加人员基本情况表

填表说明： 1.职称分类：A、正高级　B、副高级　C、中级　D、初级　E、其他；

2.投入本课题的全时工作时间（人月）是指在课题实施期间该人总共为课题工作的满月度工作量；累计是指课题组所有人员投入人月之和；

3.课题固定研究人员需填写人员明细；

4.是否有工资性收入：Y、是　N、否；

5.人员分类代码：A、课题负责人　B、课题骨干　C、其他研究人员；

6.工作单位：填写单位全称，其中高校要具体填写到所在院系。

序号	姓名	性别	出生日期	身份证号码（军官证、护照）	技术职称	职务	学位	专业	投入本课题的全时工作时间（人月）	人员分类	是否有工资性收入	工作单位
	（1）	（2）	（3）	（4）	（5）	（6）	（7）	（8）	（9）	（10）	（11）	（12）
1	姜锐	男	1993-04-29	142427199304296310	C	无	博士	农业电气化与自动化	40	A	Y	华南农业大学工程学院
2	周志艳	男	1972-11-23	432923197211230314	A	无	博士	农业电气化与自动化	30	B	Y	华南农业大学工程学院
3	万欢	男	1986-01-01	429004198601015370	C	无	硕士	农业工程	40	B	Y	华南农业大学工程学院
4	陈羽立	男	1995-11-11	422202199511110012	E	无	硕士	农业电气化	40	B	N	华南农业大学工程学院
5	黄俊浩	男	1997-06-04	445221199706047258	E	无	学士	农业电气化	40	B	N	华南农业大学工程学院
6	林键沁	男	1997-06-10	44522199970610657X	E	无	学士	农业工程	40	B	N	华南农业大学工程学院
7	欧媛珍	女	1994-05-28	445381199405285748	E	无	学士	农业工程	40	B	N	华南农业大学工程学院

8	刘梓博	男	1998-05-29	440106199805291000	E	无	学士	机器人工程	40	C	N	华南农业大学工程学院
9	范小龙	男	1996-10-12	445381199610122112	E	无	学士	农业工程与信息技术	40	C	N	华南农业大学工程学院
10	何思敏	男	1996-05-01	44132419960501401X	E	无	学士	农业信息化	40	C	N	华南农业大学工程学院
11	杨得帅	男	1999-04-03	622323199904032013	E	无	学士	农业机械化	40	C	N	华南农业大学工程学院
12	郭能明	男	1998-10-02	360730199810022017	E	无	学士	农业工程	40	C	N	华南农业大学工程学院
13	钟劲峰	男	1998-08-18	441424199808182270	E	无	学士	机械	40	C	N	华南农业大学工程学院
14	林臻	男	1997-07-14	362429199707140015	E	无	学士	机械	40	C	N	华南农业大学工程学院
15	李鑫	男	1996-12-03	441802199612037331	E	无	学士	农业信息化	40	C	N	华南农业大学工程学院
		固定研究人员合计							590	/	/	/
		流动人员或临时聘用人员合计							0	/	/	/
		累计							590	/	/	/

十、经费预算

子课题承担单位基本情况表

表 B1

填表说明：1.组织机构代码指企事业单位国家标准代码，单位若已三证合一请填写单位社会信用代码，无组织机构代码的单位填写“000000000”； 2.单位公章名称必须与单位名称一致。					
子课题编号	02			执行周期（月）	60
子课题名称	农机无人作业环境信息感知				
子课题承担单位	单位名称	华南农业大学			
	单位性质	大专院校			
	单位主管部门	广东省教育厅		隶属关系	地方
	单位组织机构代码	124400004554165634			
	单位法定代表人姓名	刘雅红			
	单位所属地区	广东省	广州市	天河区	
	电子邮箱	kycjhk@scau.edu.cn			
	通信地址	广东省广州市天河区五山路 483 号			
	邮政编码	510642			
	银行账号	3602002609000310520			
	单位开户名称	华南农业大学			
	开户银行（全称）	中国工商银行广州市五山支行			
相关责任人	子课题负责人	姓名	姜锐		
		身份证号码	142427199304296310		
		工作单位	华南农业大学工程学院		
		电话号码	020-38676975	手机号码	13424049263
		电子邮箱	ruiojiang@scau.edu.cn	邮政编码	510642
		通信地址	广东省广州市天河区五山路 483 号		
	财务部门负责人	姓名	肖斐		
		电话号码	020-85288032	手机号码	13416122195
		传真号码			
		电子邮箱	feixiao@scau.edu.cn		

子课题预算表

金额单位：万元

序号	预算科目名称	合计	专项经费	自筹经费
	（1）	（2）	（3）	（4）
1	**一、中央财政专项资金**	**100.00**	**10.00**	**0**
2	（一）直接费用	**80.00**	**80.00**	**0**
3	1.设备费	**6.14**	**6.14**	**0**
4	其中：购置设备费	**6.14**	**6.14**	**0**
5	2.业务费	**51.26**	**51.26**	**0**
6	3.劳务费	**22.60**	**22.60**	**0**
7	（二）间接费用（自动计算）	**20.00**	**20.00**	**0**
8	**二、其他来源资金**	**0**	**0**	**0**
9	**三、合计**	**100.00**	**100.00**	**0**

任务书签署

甲、乙、丙三方根据《国务院关于改进加强中央财政科研项目和资金管理的若干意见》（国发[2014]11 号）、《国务院印发关于深化中央财政科技计划（专项、基金）管理改革方案的通知》（国发[2014]64 号）、《科技部财政部关于改革过渡期国家重点研发计划组织管理有关问题的通知》（国科发资[2015]423 号）、《科技部财政部关于印发<中央财政科技计划（专项、基金等）监督工作暂行规定>的通知》（国科发政[2015]471 号）、《财政部科技部关于中央财政科技计划管理改革过渡期资金管理有关问题的通知》（财教[2015]154 号）等有关文件规定，以及有关法律、政策和管理要求，依据项目立项通知、项目任务书、课题任务书，签署本任务书。

课题承担单位（甲方）：（公章）

课题负责人（签字）：

2022 年 12 月 30 日

子课题承担单位（乙方）：（公章）

子课题负责人（签字）：

2022 年 12 月 30 日

项目牵头承担单位（丙方）：（公章）

北京市农林科学院智能装备技术研究中心

项目负责人签字（签字）：

2022 年 12 月 30 日

项目批准号	32301707
申请代码	C1302
归口管理部门	
依托单位代码	51064208A0499-0932

323017071001261

国家自然科学基金

资助项目计划书

（包干制项目）

资助类别：青年科学基金项目

亚类说明：

附注说明：

项目名称：水稻群体长势快速监测的无人机线阵遥感自主感知补偿机制

资助经费：30万元 执行年限：2024.01-2026.12

负 责 人：姜锐

通讯地址：广东省广州市天河区五山路华南农业大学农业工程楼102

邮政编码：510642 电 话：13424049263

电子邮件：ruiojiang@scau.edu.cn

依托单位：华南农业大学

联 系 人：唐家林 电 话：020-85280070

填表日期：2023年08月30日

国家自然科学基金委员会制

Version：1.001.261

简表

项目负责人信息	姓名	姜锐	性别	男	出生年月	1993年04月	民族	汉族
	学位	博士			职称	无		
	是否在站博士后	是		电子邮件	ruiojiang@scau.edu.cn			
	电话	13424049263		个人网页				
	工作单位	华南农业大学						
	所在院系所	工程学院						
依托单位信息	名称	华南农业大学					代码	51064208A0499
	联系人	唐家林		电子邮件	kycjhk@scau.edu.cn			
	电话	020-85280070		网站地址	http://kjc.scau.edu.cn/			
合作单位信息	单位名称							
项目基本信息	项目名称	水稻群体长势快速监测的无人机线阵遥感自主感知补偿机制						
	资助类别	青年科学基金项目		亚类说明				
	附注说明							
	申请代码	C1302:农艺农机学		C1301:农业信息学				
	基地类别	南方农业机械与装备关键技术教育部重点实验室						
	执行年限	2024.01-2026.12						
	资助经费	30万元						

项目摘要

中文摘要：

基于无人机飞行时间轴的线阵遥感技术可快速、无损地获取水稻群体长势信息，促进水稻生长过程中的胁迫监测和产量预测向过程机理化、定量精准化方向发展。以解决无人机线阵遥感数据质量不高和投影配准难所面临的关键科学问题和技术挑战为目标，申请人拟在无人机线阵遥感的研究基础上：1）揭示无人机位姿特征对线阵遥感数据位置误差的形成机理，提出基于无人机位姿特征的实时动态补偿方法；2）设计一套与现有线阵传感器兼容的光照传感器方案，构建基于光照传感器自身位姿特征的自主感知校准模型，实现光照传感器的瞬态姿态估计和天顶方向入射光辐射量的准确测量；3）建立基于光照传感器入射光辐射量的线阵传感器曝光时间智能决策模型，实现地物反射光辐射量和反射率的精准测量。所提出的自主感知补偿新方法，能够提高无人机线阵遥感数据精度，突破水稻群体长势信息的快速获取与定量化解析技术，具有重要的实际应用价值和科学意义。

Abstract：

The linear array remote sensing technology based on the flight time axis of unmanned aerial vehicle (UAV) can quickly and non-destructively obtain rice population growth information, and promote the development of stress monitoring and yield prediction in the process of rice growth to the direction of process mechanism and quantitative precision. In order to solve the key scientific problems and technical challenges faced by the low data quality and difficult projection registration of UAV-based linear array remote sensing technology, the applicant intends to carry out further research on the basis of the exploration on UAV-based linear array remote sensing: 1) reveal the formation mechanism of the position error of linear array remote sensing data caused by the position and pose characteristics of UAV, and propose a real-time dynamic compensation method; 2) design an illumination sensor scheme compatible with the existing linear array sensor, and suggest an autonomous perception calibration model based on the position and pose characteristics of the illumination sensor to realize the transient pose estimation of the illumination sensor and the accurate measurement of the incident light radiation in the zenith direction; 3) establish an intelligent decision-making model of exposure time of linear array sensor based on incident light radiation of illumination sensor to realize accurate measurement of reflected light radiation and reflectivity of ground objects. The proposed new method of autonomous perception compensation can improve the accuracy of UAV-based linear array remote sensing data and break through the rapid acquisition and quantitative analysis technology of rice population growth information, which has important actual application value and scientific significance.

关键词(用分号分开)：大田作物；田间信息自动获取；农业遥感；水稻群体长势；无人机

Keywords(用分号分开)： Field crops; Automatic acquisition of field information; Agricultural remote sensing; Rice population growth; Unmanned aerial vehicle

国家自然科学基金项目负责人、依托单位承诺书

国家自然科学基金项目负责人承诺书

本人郑重承诺：我接受国家自然科学基金的资助，严格遵守中共中央办公厅、国务院办公厅《关于进一步加强科研诚信建设的若干意见》《关于进一步弘扬科学家精神加强作风和学风建设的意见》《关于加强科技伦理治理的意见》等规定，及国家自然科学基金委员会关于资助项目管理、项目资金管理等各项规章，在《计划书》填写及项目执行过程中：

（一）按照《批准通知》《国家自然科学基金资助项目计划书填报说明》的要求填写《计划书》，未自行降低、更改目标任务或约定要求，或缩减研究（研制）内容；

（二）树立“红线”意识，严格履行科研合同义务，按照《计划书》负责实施本项目（批准号：32301707），切实保证研究工作时间，按时报送有关材料，及时报告重大情况变动，不违规将科研任务转包、分包他人，不以项目实施周期外或不相关成果充抵交差；

（三）遵守科研诚信、科技伦理规范和学术道德，认真开展研究工作，对资助项目发表的论著和取得的研究成果按规定进行标注，不在非本项目资助的成果或其他无关成果上标注本项目批准号，反对无实质学术贡献者“挂名”，不在成果署名、知识产权归属等方面侵占他人合法权益，并如实报告本人及项目组成员发生的违背科研诚信要求的任何行为；

（四）尊重科研规律，弘扬科学家精神，严谨求实，追求卓越，反对浮夸浮躁、投机取巧，不人为夸大学术或技术价值，不传播未经科学验证的现象和观点；

（五）将项目资金全部用于与本项目研究工作相关的支出，并结合科研活动需要，科学合理安排项目资金支出进度；

（六）做好项目组成员的教育和管理，确保遵守以上相关要求。

如违背上述承诺，本人愿接受国家自然科学基金委员会和相关部门做出的各项处理决定。

项目负责人（签字）：

年　　月　　日

国家自然科学基金项目依托单位承诺书

我单位同意承担上述国家自然科学基金项目，将保证项目负责人及其研究队伍的稳定和研究项目实施所需的条件，严格遵守国家自然科学基金委员会有关资助项目管理、项目资金管理、科研诚信管理和科技伦理管理等各项规定，并督促实施。

依托单位（公章）

年　　月　　日

受理编号：c24140500000446

项目编号：2024A1515012608

文件编号：粤基金字〔2024〕7号

广东省基础与应用基础研究基金项目

任务书

项目名称： 作物长势监测的单目高分多光谱传感器波段互扰机理及混合光谱分解方法研究

项目类别： 广东省自然科学基金-面上项目

项目起止时间： 2024-01-01　至　2026-12-31

管理单位（甲方）： 广东省基础与应用基础研究基金委员会

依托单位（乙方）： 岭南现代农业科学与技术广东省实验室茂名分中心

通讯地址： 广东省茂名市茂南区茂名市茂南区油城六路5号大院茂名市科学技术局副楼4楼

邮政编码： 525000　　**单位电话：** 020-2263932

项目负责人： 姜锐　　**联系电话：** 13424049263

（广东科技微信公众号）　　（查看任务书信息）　　（受理纸质材料二维码）

广东省基础与应用基础研究
基金委员会
二〇二〇年制

填写说明

一、项目任务书内容原则上要求与申报书相关内容保持一致，不得无故修改。

二、项目承担单位通过广东省科技业务管理阳光政务平台下载项目任务书，按要求完成签名盖章后扫描上传到广东省科技业务管理阳光政务平台。

三、签名盖章说明。请分别在单位工作分工及经费分配情况页、人员信息页、签约各方页等地方按要求签字或盖章，签章不合规或错漏将不予受理。其中，人员信息页要求所有参与人员本人亲笔签名，代签或印章无效，漏签将不予受理。

四、本任务书自签字并加盖公章之日起生效，各方均应负本任务书的法律责任，不应受机构、人事变动影响。

五、根据《广东省科学技术厅广东省财政厅关于深入推进省基础与应用基础研究基金项目经费使用“负面清单+包干制”改革试点工作的通知》（粤科规范字〔2022〕2号），2022年度及以后立项资助的全部省基金项目(包括省自然科学基金、省市联合基金、省企联合基金项目等)均适用“负面清单+包干制”，项目提交申请书和任务书时无需编制费用明细科目预算。

一、主要研究内容和要达到的目标

1. 主要研究内容：

本项目以攻克单目多光谱传感器中各光谱波段之间信息互扰机理不明确，光谱分解难度高所面临的关键科学问题和技术挑战为目标，结合申请人前期的研究基础，拟开展以下研究内容：

（1）单目高分多光谱传感器的影像畸变与渐晕校正模型研究

采用单目单芯（单RGB全局曝光感光芯片）的感知结构，利用高分辨率的RGB感光芯片和低畸变高清镜头，研制单目高分多光谱传感器样机；采用方格标定板和内插法建立单目高分成像系统的畸变校正模型，通过全局优化算法获得畸变校正参数矩阵，实现原始RGB影像的无畸变化；通过设置不同曝光时长获取渐晕校正模型的训练集，对所获得的独立通道（R、G、B）灰度影像进行处理，建立衰减因子图，实现原始影像对均一反光面辐射照度的准确响应，进而降低单目高分多光谱传感器各通道的自身噪声。

（2）单目高分多光谱传感器各光谱波段的互扰机理及解混模型研究

基于单目高分多光谱传感器样机，结合红光（R）、绿光（G）和近红外（NIR） 的独立窄带滤光片和组合窄带滤光片，开展以曝光时间、窄带滤光片和辐射照度为因素的控制波段约束试验；配合使用辐射照度仪，建立单目高分多光谱传感器感光芯片的RGB影像DN值与组合窄带滤光片各波段（R、G、NIR）实际辐射照度的响应模型，实现单目高分三光谱窄带波段影像的准确获取；在辐射分量的精准提取基础上，结合标准反射板进行反射率和植被指数的计算。

（3）单目高分多光谱传感器的多波段混合光谱分解模型试验验证

集成研究内容一、二的成果，创制单目高分多光谱传感器新系统；以水稻为感知对象，设置不同水稻氮素胁迫梯度，在水稻的分蘖、抽穗等关键农时节点，结合无人机平台，将单目高分多光谱传感器与商业化的多镜头型多光谱传感器、地面作物传感器进行多种工况的对比试验；以水稻冠层反射率、遥感数据处理速度和影像分辨率为分析对象，通过比较数据解析时间成本、相关性分析和差异性检验，进一步验证和改进单目高分多光谱传感器中的多波段混合光谱分解模型的正确性和快速响应性。

2. 要达到的目标：

（1）探明作物长势监测的单目高分多光谱传感器波段互扰机理，采用控制波段约束的混合光谱分解法，研发成功用于作物长势监测的单目高分多光谱传感器1套；

（2）单目高分多光谱传感器的遥感影像分辨率达3cm（120m的航拍高度）；

（3）单目高分多光谱传感器对红光R（650nm）、绿光G（515nm）和近红外光NIR（850nm）的响应精度≥95%；

（4）发表高水平的研究论文2篇；

（5）申请发明专利1件。

二、项目预期获得的研究成果及形式

<table>
<tr><td rowspan="3">论文及专著情况</td><td colspan="2">国家统计源刊物以上刊物发表论文（篇）</td><td colspan="2">2</td><td colspan="2">科技报告（篇）</td><td colspan="2">0</td></tr>
<tr><td colspan="2">其中被SCI/EI/ISTP收录论文数（篇）</td><td colspan="2">2</td><td colspan="2">培养人才（人）</td><td colspan="2">2</td></tr>
<tr><td colspan="2">专著（册）</td><td colspan="2">0</td><td colspan="2">引进人才（人）</td><td colspan="2">0</td></tr>
<tr><td rowspan="3">专利情况(项)</td><td colspan="2">发明专利</td><td colspan="2">实用新型专利</td><td colspan="2">外观设计专利</td><td colspan="2">国外专利</td></tr>
<tr><td>申请</td><td>授权</td><td>申请</td><td>授权</td><td>申请</td><td>授权</td><td>申请</td><td>授权</td></tr>
<tr><td>1</td><td>0</td><td>0</td><td>0</td><td>0</td><td>0</td><td>0</td><td>0</td></tr>
</table>

三、项目进度和阶段目标

（一）项目起止时间： 2024-01-01 至 2026-12-31		
（二）项目实施进度及阶段主要目标：		
开始日期	结束日期	主要工作内容
2024-01-01	2024-12-31	分析国内外相关文献资料、数据手册，完成单目高分多光谱传感器样机的研制，实现R、G、B通道对红光R（650nm）、绿光G（515nm）和近红外光NIR（850nm）三波段混合光谱影像的高精度、高分辨率获取；开展校正试验，建立成像系统的畸变校正模型、光学渐晕效应校正模型，实现单目高分多光谱传感器对混合光谱影像的无畸变准确获取。期间，申请发明专利1件。
2025-01-01	2025-12-31	开展光谱波段控制约束试验，建立R、G、B通道影像DN值与组合窄带滤光片各波段（650nm、515nm、850nm）实际辐射照度的响应模型，获得响应系数因子矩阵；建立成像底片绿通道G对515nm、红通道R对650nm和蓝通道B对850nm波段单独对应的混合光谱分解模型，实现基于全局快门高像素RGB单目高分多光谱传感器对515nm、650nm和850nm独立波段影像的准确获取。期间，发表高水平研究论文1篇。
2026-01-01	2026-12-31	结合无人机平台，开展单目高分多光谱遥感新系统与商业化的多镜头型多光谱传感器、地面作物传感器在多种工况下的对比试验，通过比较数据质量、相关性分析和差异性检验，进一步验证和改进混合光谱分解模型。期间，发表高水平研究论文1篇，准备验收材料，完成结题报告，并拟定进一步研究计划。

四、项目总经费及省基金委经费预算

1. 省基金委经费下达总额：（大写）壹拾伍万圆整；（小写 ）15万元；

2. 省基金委经费年度下达计划：

年度	2024 年	年	年	年	年
经费(万元)	15.00				

五、人员信息

项目负责人

姓名	证件号码	年龄	性别	职称	学历	在项目中承担的任务	所在单位	签名
姜锐	142427199304296310	31	男	副教授	博士研究生	项目负责人	岭南现代农业科学与技术广东省实验室茂名分中心	姜锐

项目组主要成员

姓名	证件号码	年龄	性别	职称	学历	在项目中承担的任务	所在单位	签名
周志艳	432923197211230314	52	男	教授	博士研究生	项目策划与技术指导	岭南现代农业科学与技术广东省实验室茂名分中心	周艳
廖娟	430923198705296949	37	女	讲师	博士研究生	试验设计与数据分析	岭南现代农业科学与技术广东省实验室茂名分中心	廖娟
万欢	429004198601015370	38	男	实验师	硕士研究生	解混模型验证与优化	岭南现代农业科学与技术广东省实验室茂名分中心	万欢
欧媛珍	445381199405285748	30	女	未取得	本科	试验数据处理分析	岭南现代农业科学与技术广东省实验室茂名分中心	欧媛珍

黄俊浩	445221199706047258	27	男	未取得	本科	算法设计与验证	岭南现代农业科学与技术广东省实验室茂名分中心	黄俊浩
林键沁	44522119970610657X	27	男	未取得	本科	硬件开发	岭南现代农业科学与技术广东省实验室茂名分中心	林键沁
范小龙	445381199610122112	28	男	未取得	本科	图像处理	岭南现代农业科学与技术广东省实验室茂名分中心	范小龙
陈羽立	422202199511110012	29	男	未取得	硕士研究生	硬件优化	岭南现代农业科学与技术广东省实验室茂名分中心	陈羽立
刘梓博	440106199805291818	26	男	未取得	本科	模型优化	岭南现代农业科学与技术广东省实验室茂名分中心	刘梓博

六、工作分工及财政经费分配

承担/参与单位名称（盖章）	工作分工	省级财政科技资金分配（万元）
岭南现代农业科学与技术广东省实验室茂名分中心 4400025010363	开展作物长势监测的单目高分多光谱传感器波段互扰机理及混合光谱分解方法的研究，探明单目多光谱传感器波段互扰机理，通过控制波段约束分解法构建混合光谱分解模型，创制一种农业遥感专用单目高分多光谱传感器，实现单目多光谱传感器获取高分辨率高精度多光谱影像的目标。	15.00
	合计	15.00

七、任务书条款

第一条 甲方与乙方根据《中华人民共和国民法典》及国家有关法规和规定，按照《广东省科学技术厅关于广东省基础与应用基础研究基金（省自然科学基金、联合基金等）项目管理的实施细则（试行）》《省级科技计划项目任务书管理细则》《广东省省级科技计划项目验收结题工作规程（试行）》等规定，为顺利完成（2024）年作物长势监测的单目高分多光谱传感器波段互扰机理及混合光谱分解方法研究专项项目（项目编号：2024A1515012608）经协商一致，特订立本任务书，作为甲乙双方在项目实施管理过程中共同遵守的依据。

第二条 甲方的权利义务：

1.按任务书规定进行经费核拨的有关工作协调。

2.根据甲方需要，在不影响乙方工作的前提下，定期或不定期对乙方项目的实施情况和经费使用情况进行检查或抽查。

3.根据《广东省科研诚信管理办法(试行)》等规定对乙方进行科技计划信用管理。

第三条 乙方的权利义务：

1.确保落实自筹经费及有关保障条件。

2.按任务书规定，对甲方核拨的经费实行专款专用，单独列账，并随时配合甲方进行监督检查。

3.经费使用按照广东省级财政科研项目经费使用等有关规定进行管理。

4.项目依托单位应制定经费使用“负面清单+包干制”内部管理制度并报甲方备案。

5.使用财政资金采购设备、原材料等，按照《广东省实施〈中华人民共和国招标投标法〉办法》有关规定，符合招标条件的须进行招标。

6.项目任务书任务完成后，或任务书规定的任务、指标及经费投入等提前完成的，乙方可提出验收结题申请，并按甲方要求做好项目验收结题工作。

7.若项目发生需要终止结题的情况，乙方须提出终止结题申请，并按甲方要求做好项目终止结题工作。

8.在每年规定时间内向甲方如实提交上年度工作情况报告，报告内容包含上年度项目进展情况、经费决算和取得的成果等。

9.按照国家和省有关规定，提交科技报告及其他材料。

10.利用甲方的经费获得的研究成果，项目负责人和参与者应当注明获得“广东省基础与应用基础研究基金（英文：Guangdong Basic and Applied Basic Research Foundation）（项目编号）”资助或作有关说明。

11.乙方要恪守科学道德准则，遵守科研活动规范，践行科研诚信要求，不得抄袭、剽窃他人科研成果或者伪造、篡改研究数据、研究结论；不得购买、代写、代投论文，虚构同行评议专家及评议意见；不得违反论文署名规范，擅自标注或虚假标注获得科技计划（专项、基金等）等资助；不得弄虚作假，骗取科技计划（专项、基金等）项目、科研经费以及奖励、荣誉等；不得有其他违背科研诚信要求的行为。

12.确保本项目开展的研究工作符合我国科技伦理管理相关规定。

第四条 在履行本任务书的过程中，如出现广东省相关政策法规重大改变等不可抗力情况，甲方有权对所核拨经费的数量和时间进行相应调整。

第五条 在履行本任务书的过程中，当事人一方发现可能导致项目整体或部分失败的情形时，应及时通知另一方，并采取适当措施减少损失，没有及时通知并采取适当措施，致使损失扩大的，应当就扩大的损失承担责任。

第六条 本项目技术成果的归属、转让和实施技术成果所产生的经济利益的分享，除双方另有约定外，按国家和广东省有关法规执行。

第七条 根据项目具体情况，经双方另行协商订立的附加条款，作为本任务书正式内容的一部分，与本任务书具有同等效力。

第八条 本任务书一式三份，各份具有同等效力。甲、乙方及项目负责人各执一份，三方签字、盖章后即生效，有效期至项目结题后一年内。各方均应负任务书的法律责任，不应受机构、人事变动的影响。

第九条 乙方必须接受甲方聘请的本项目任务书监理单位的监督和管理。监理单位按照甲方赋予的权利对本项目任务书的履行进行审核、进度调查，对项目任务书变更、经费使用情况进行监督管理及组织项目验收。

说明：1. 本任务书中，凡是当事人约定无需填写的内容，应在空白处划（/）。

2. 委托代理人签订本任务书的，应出具合法、有效的委托书。

八、本任务书签约各方

管理单位（甲方）：　　广东省基础与应用基础研究基金委员会　（盖章）

科技项目合同专用章 4401040051250

法定代表人（或法人代理）：　曾路 曾路　（签章）

2024 年　05 月　22 日

依托单位（乙方）：　岭南现代农业科学与技术广东省实验室茂名分中心　（盖章）

4409025010363

法定代表人（或法人代理）：　曾春　＿＿＿＿＿＿（签章）

联系人（项目主管）姓名：　车南青　＿＿＿＿＿＿（签章）

Email：　181028178@qq.com

电话：　0668-2299399　/　18127339373

开户单位名称：　岭南现代农业科学与技术广东省实验室茂名分中心

开户银行名称：　中国农业银行股份有限公司茂名茂东支行

开户银行账号：　44588501040018118

2024 年 5 月 23 日

联系人（项目负责人）姓名：　姜锐　（签名）姜锐

Email：　ruiojiang@scau.edu.cn

电话：　13424049263

2024年 5 月 22日

任务书编号：2024B03J1356

广州市科技计划项目
任务书

项目名称：	基于“端-云”协同计算的无人机机载双目线阵遥感传感器研发与应用
承担单位：	华南农业大学
项目负责人：	姜锐
计划类别：	重点研发计划
专题名称：	2024年度农业和社会发展科技专题
支持方向：	数字农业与现代农业装备技术方向
组织单位：	华南农业大学
起止时间：	2024-01-01 至 2026-12-31
主管处室：	农村和社会发展科技处

广州市科学技术局制

二〇二四年

一、项目基本信息

项目名称	基于“端-云”协同计算的无人机机载双目线阵遥感传感器研发与应用			
计划类别	重点研发计划		专题名称	2024年度农业和社会发展科技专题
支持方向	数字农业与现代农业装备技术方向			
支持内容	2.基于物联网的农业传感器关键技术研发与应用			
指南发布日	2023-04-15			
项目开始时间	2024-01-01		项目结束时间	2026-12-31
资助方式	竞争性前资助		申请市财政科技经费(万元)	50
广东省技术领域	农业技术农业装备(农业机械、设备及材料等);			
承担单位	华南农业大学			
合作单位	广州五山农业服务有限责任公司;			
组织单位	华南农业大学			
	姓名	办公电话	手机号码	电子邮箱
项目负责人	姜锐	020-38676975	13424049263	ruiojiang@scau.edu.cn
项目联系人	欧媛珍	020-38676975	13631295324	1337969174@qq.com
科研财务助理	欧媛珍	020-38676975	13631295324	1337969174@qq.com
项目摘要	快速实时地掌握农情信息是实施精准农作的基础。无人机搭载获取农情信息的重要“探头”工具—遥感传感器，可提供空间和光谱分辨率更高的农情信息地图。然而，目前无人机低空遥感普遍存在气象要求高、时间窗口小、遥感数据量大和拼接出图慢等突出问题，降低了遥感数据的时效性，限制了无人机遥感技术在实际农业生产中的应用推广。基于无人机的线阵遥感技术可改善数据图幅、空间、光谱及时间维度观测能力的问题，但目前无人机线阵遥感仍存在受环境光照变化影响大、数据采集和处理的同步性差以及数据后处理效率低的问题。本项目拟研发基于“端-云”协同计算的无人机机载双目线阵遥感传感器，采用线阵传感器快速精准感知、板载计算机与云服务器协同计算、自适应分片处理相结合的方法，进一步提高无人机线阵遥感数据的处理效率，实现无人机低空遥感数据从“获取处理”到“指导生产”的“无感”化，全面提升无人机高时效			

	遥感获取作物群体长势信息的能力。本项目的目标是成功研发基于“端-云”协同计算的无人机机载双目线阵遥感传感器2套，实现作物长势专题图（NDVI）的解析速率达到600亩/分钟、申请相关发明专利1件、发表高水平论文1篇以及推广推广应用面积达8万亩次。

二、承担单位基本情况

单位名称	华南农业大学	统一社会信用代码	12440000455416563 4
注册时间	1952-01-01	单位类型	高等院校
注册地址	广东省广州市天河区五山路483号		
办公地址	广东省广州市天河区五山路483号		
联系人	姓名	倪慧群	
	手机号码	13711345768	
	电子邮箱	kjcgxk@scau.edu.cn	
开户银行	广东广州工行五山支行		
开户户名	华南农业大学		
银行账号	3602002609000310520		
任务分工	华南农业大学作为《基于“端-云”协同计算的无人机机载双目线阵遥感传感器研发与应用》项目的承担单位，整体负责项目运行的组织、实施、协调与控制，负责参与单位执行进度、运行质量的监督与考核。		
知识产权分配	项目承担单位与合作单位在完成所分配的任务过程中独立完成的研究成果，其知识产权分别归各自所有；由双方合作完成的科研成果（专利、论文等），归双方共有，并按照贡献程度排名。		

三、合作单位基本情况

单位名称1	广州五山农业服务有限责任公司	单位类型	有限责任公司
所属国别或地区	中国	统一社会信用代码	91440101MA5AKHXG1L
联系人	姓名	黄俊浩	
	办公电话	020-38676975	
	手机号码	15813302192	
任务分工	承担的研究任务为：无人机机载双目线阵遥感传感器的田间试验与推广应用。		
知识产权分配	项目承担单位与合作单位在完成所分配的任务过程中独立完成的研究成果，其知识产权分别归各自所有；由双方合作完成的科研成果（专利、论文等），归双方共有，并按照贡献程度排名。		

四、项目组成员信息

项目负责人	姓名	姜锐	证件类型	身份证	证件号码	142427199304296310	性别	男
	出生日期	1993-04-29	民族	汉族	国籍	中国	学历	博士研究生
	学位	博士	学位授予国家（或地区）	中国	职务	无	职称	中级
	所学专业	农业电气化与自动化	手机号码	13424049263	办公电话	020-38676975	电子邮箱	ruiojiang@scau.edu.cn

项目组成员（含项目负责人）

序号	姓名	证件类型	证件号码	年龄	职务	职称	学位	项目分工	所在单位	手机号码
1	姜锐	身份证	142427199304296310	29	无	中级	博士	项目负责人	华南农业大学	13424049263
2	周志艳	身份证	432923197211230314	50	副主任	正高级	博士	项目策划与技术指导	华南农业大学	13560026139
3	黄俊浩	身份证	445221199706047258	26	总经理	无	学士	组织项目试验和推广应用	广州五山农业服务有限责任公司	15813302192
4	欧媛珍	身份证	445381199405285748	29	无	无	学士	试验数据分析	华南农业大学	13631295324
5	万欢	身份证	429004198601015370	37	无	中级	硕士	试验设计与数据分析	华南农业大学	19880898601
6	陈羽立	身份证	4222021995111	27	无	无	硕士	算法设计与验证	华南农业大	19880898602

			10012						学	
7	林键沁	身份证	44522119970610657X	26	无	无	学士	图像处理	华南农业大学	15813312677
8	范小龙	身份证	445381199610122112	26	无	无	学士	硬件开发	华南农业大学	13247660438
9	刘梓博	身份证	440106199805291818	25	无	无	学士	服务器前端设计	华南农业大学	13640839237
10	杨得帅	身份证	622323199904032013	24	无	无	学士	数据库设计与维护	华南农业大学	17752152860
11	何思敏	身份证	44132419960501401X	27	无	无	学士	通信链路测试	华南农业大学	13602725454

五、项目经费信息

本项目总投入：¥（50）万元，其中，市财政科技经费：¥（50）万元，自筹经费：¥（0）万元。

项目经费			
资金来源	小计	市财政科技经费	自筹经费
2024	50	50	0
2025	0	0	0
2026	0	0	0
2027	0	0	0
总计	50	50	0
支出预算明细			
支出科目	小计	市财政科技经费	自筹经费
一、直接费用	43	43	0
（一）设备费	0	0	0
（二）业务费	35.5	35.5	0
（三）直接人力资源成本费	7.5	7.5	0
二、间接费用	7	7	0
合 计	50	50	0

（单位：万元）

注：自筹经费由项目承担单位自身筹措，不包含来自各级政府部门的财政资金。

单位名称	市财政科技经费分配	自筹经费分配	总经费分配
华南农业大学	40	0	40
合作单位1：广州五山农业服务有限责任公司	10	0	10
合计	50	0	50

项目承担单位（乙方）及项目负责人承诺书

承诺书

本单位/本人作为广州市科技计划项目承担单位/项目负责人，将严格遵守广州市科技计划管理相关规定，严格履行自身责任，加强对项目组人员及合作单位的管理，在此郑重承诺：

（一）确保与本项目有关的全部材料真实、合法、有效，未侵犯其他方知识产权等权利，不存在多头申报、重复申报行为；

（二）严格遵守《广州市科技创新条例》《广州市科技计划项目管理办法》《广州市科技计划项目经费管理办法》《广州市科技计划科技报告管理办法》等相关规定，实施项目和经费管理；

（三）严格遵守国家、省、市关于科研诚信和科技伦理的有关法律、法规，相关政策以及各项规定，加强项目实施过程中的科研诚信及科技伦理管理，恪守科研道德准则。

如有违反，本单位/本人愿意接受相关部门做出的各项处理决定，包括但不限于终止项目、停拨经费、核减经费、追回经费，取消一定期限广州市科技计划项目申报资格，记入科研失信行为数据库，将不良行为向社会公开等。

项目承担单位：华南农业大学
日期：年 月 日

项目负责人：姜锐
日期：2023年12月13日

任务书签署

甲乙丙三方根据《广州市科技计划项目管理办法》《广州市科技计划项目经费管理办法》《广州市科技计划科技报告管理办法》等有关文件规定，以及有关法律、政策和管理要求，签署本任务书。

签订地点：广州市越秀区

广州市科学技术局（甲方）：广州市科学技术局
局项目经办人：刘晓辉　　　　　　联系电话：83124045
责任处室负责人：陈洁

4401040029985

2024年01月09日

项目承担单位（乙方）：华南农业大学
二级部门：华南农业大学工程学院
项目负责人：姜锐
项目经费汇入账号
账户名：华南农业大学　　账号：3602002609008810520
开户银行：广东广州工行五山支行
财务负责人：肖斐

4401060369544

2023年12月16日

组织单位（丙方）：华南农业大学
项目经办人：倪慧群

4401060369544

2023年12月16日

计划类别：科技专项
项目类别：吉安市农业及乡村振兴类
主管科室：农社科
项目编号：20211-055312

20211-055312

吉安市科技计划项目
合同书

（2021年度）

项目名称：无人机低空遥感传感器及水稻生长信息动态监测系统研发

申报单位：井冈山大学

项目负责人：刘朝晖　　联系电话：15979666338　　手机：15979666338

项目联系人：刘朝晖　　联系电话：0796-8106067　　手机：15979666338

推荐单位：井冈山大学

起止时间：2022 年 01 月 01 日 至 2023 年 12 月 31 日

申报日期：2021 年 10 月 23 日

吉安市科学技术局制

2019年4月

一、项目基本情况表

项目名称	无人机低空遥感传感器及水稻生长信息动态监测系统研发
专题名称	JAZT-21-14-智能农业
起止年限	2022 年 01 月 01 日 至 2023 年 12 月 31 日
技术领域	农业机械化,农业电气化与自动化,农田测量
所属学科	农业信息学

项目内容摘要

吉安市水稻种植面积约900万亩，快速、无损、准确地监测水稻生长状况，对于及时准确地了解水稻的氮利用率、改善施肥策略、防止肥料过度使用带来的农田环境污染和深入开展精准农业的研究与应用具有重要意义。传统的航天、航空遥感技术是目前水稻长势信息快速获取的主要方法之一，但目前还存在影响因子多、周期长等问题。“无人机低空遥感传感器及水稻生长信息动态监测系统研发”为了突破上述缺陷，无人机低空遥感传感器将采用空中实时计算的方式，在无人机端进行遥感数据采集和解析，实现近实时的遥感影像（数据）解析能力。水稻生长信息动态监测系统研发是一种地面实时的光谱影像（数据）采集分析方法，通过在田间分布安装经过组网的水稻生长信息动态监测系统，在远程端可以24小时全天候进行水稻的光谱影像（数据）的分析和调查，在略低于无人机低空遥感传感器的空间分辨率上提供更高的时间分辨率。空地感测一体化将有效提高水稻生产的智能化和信息化水平。

关键词	农业遥感 ； 智能农业装备 ； 数字农情
立项金额（万元）	50.00

二、项目实施内容

主要研究开发内容

1. 无人机低空遥感传感器

（1）研发新型无人机低空遥感传感器，相比面阵式多光谱相机，成本更低、出图效率更高，可以进行近实时、快速的数据采集和平面建图，且拥有极少的后期处理时间。同时可以提供能够满足实际生产需要的空间分辨率，有效避免监测区域遗漏，对作物群体长势数据的采集效率更高。

（2）使用自稳定云台可以确保无人机低空遥感传感器在不同运动姿态下都始终处于正射拍摄地面状态，以确保采集的光谱数据与地理信息坐标数据正射对应，同时也减少了后期数据与地理位置计算的数据维度，加快建图速度。

（3）为了提高数据处理速度，本项目拟采用五通道并行数据采样方法，同时并行获取多个光谱波段数据，并同步合并成简短完整的专用数据格式。生成的数据格式经过光学余弦校正处理、地理位置配准处理后可以直接快速输出具有地理位置信息的二维栅格化的水稻长势专题图文件。

2. 水稻生长信息动态监测系统

（1）水稻生长信息动态监测系统属于地面数据采集终端，需要分布式地安装在田间，监测系统具有可升降可见光RGB图像传感器和自主补光的近红外光图像传感器，同时具有监测系统间的组网通信能力，按照田块为单位进行组网后统一通过4/5G网络通信技术反馈光谱影像（数据集）到云服务器（或计算机终端）。

（2）各个监测系统可围绕定位点进行360° 的光谱影像（数据）采集，所有采集的影像经过拼接后建立当前定位点的局部群体长势专题图，经过统一回传的局部专题图集经过图形工作站进行统一拼接正射校正和空间插值预测得出整块农田的水稻群体长势专题图。

（3）各个监测系统可支持24小时全天候农田作物群体长势专题图的生成，在略低于无人机低空遥感传感器的空间分辨率上提供更高的时间分辨率。

现有工作基础和优势

1. 研究力量

申请人刘朝晖，机械工程专业博士，井冈山大学机电工程学院副教授，江西省科技特派团成员，从事农业机械、机械工程专业的教学研究。主持完成教育厅科技项目1项，参与国家、省级自然科学基金项目3项，发表论文6篇，获得专利2项，完成其中1项专利的试制。

联合申请人姜锐博士就职于广东省农业人工智能重点实验室，兼任中国农业机械学会农业航空分会副秘书长、国家农业航空产业技术创新战略联盟副秘书长，主要从事水稻长势信息的快速检测以及稻田精确管理智能装备研究，参与国家级课题3项，以第一作者发表SCI/EI论文6篇，合作发表SCI/EI论文11篇，申请发明专利11件，授权4件，申请实用新型专利6件，授权6件。

本项目的研究成员涵盖了农学、信息与通信工程、光学工程、计算机科学与技术、测绘科学与技术等学科，为本项目的软硬件开发、测试和优化提供了强有力的研究力量。

2. 项目申请单位基本情况和具备的研究条件

项目申请单位井冈山大学是江西省人民政府和教育部共同重点支持建设高校，设有各级各类科研平台82个，其中，国家测绘地理信息局重点实验室1个，博士后科研工作站2个，江西省工程实验室2个，江西省工程研究中心1个，江西省重点实验室3个，江西省优势科技创新团队1个，江西省2011协同创新中心1个，江西省教育厅重点实验室 1个，吉安市院士工作站1个等。

本项目合作单位华南农业大学是“双一流”建设高校，项目依托南方农业机械与装备关键技术教育部重点实验室和广东省农业人工智能重点实验室，实验室具备了遥感试验和农田试验必要的仪器设备，包括有ASD高光谱仪、EU2000系列高光谱仪、SPAD计、数字示波器、IBM X3620 机架式服务器、多旋翼无人机数十架等。此外，本项目的依托单位华南农业大学拥有校内农场及增城试验基地，总面积达379公顷，具有便利的田间试验条件。

项目的组织实施与保障措施

项目由井冈山大学和华南农业大学联合完成，双方优势互补，共同协调创新。

井冈山大学是吉安市本地高校，作为项目的主持单位，全面负责项目的组织和实施，具体负责应用示范推广基地的筹建以及适用于吉安市当地水稻种植习惯和农艺要求的无人机低空遥感及水稻生长信息动态监测技术联合攻关。华南农业大学拥有一流的精准农业航空技术研究创新团队，作为项目的参与单位，配合主持单位完成项目任务，具体包括突破技术关键问题、进行样机的改进和制作、项目相关产品的成果推广演示和培训等。

项目实施过程中所产生的知识产权，优先执行任务下达单位的知识产权管理政策，在此前提下，各方独立完成的所有权归各自所有；双方共同完成的由双方共享，具体按照双方的贡献大小进行分配或双方另行商定。

项目成果申报各级奖项，双方单位排名根据具体情况另行商定，人员排名原则上按贡献大小先后排名。

三、考核目标

关键技术与主要创新指标

1. 关键技术

（1）针对水稻长势遥感监测中存在的传感器成本高、数据量大、解析处理效率低、较难满足实际生产的要求等问题，研发适用于农田作物群体长势信息快速获取和解析的装置。

（2）突破无人机低空遥感受天气、光照的环境条件的影响，建立水稻田间原位光谱影像（数据）组网采集系统，实现全天候水稻群体长势信息获取和解析。

2. 主要创新指标

（1）“无人机低空遥感传感器及水稻生长信息动态监测系统研发”的为了突破已有同类产品存在的缺陷，分别以快速遥感和非全局采样的方式加快作物群体长势信息的获取和解析速度。无人机低空遥感传感器将采用空中实时计算的方式，在无人机端进行遥感数据采集和解析，实现近实时的遥感影像（数据）解析能力。

（2）水稻生长信息动态监测系统研发是一种地面实时的光谱影像（数据）采集分析方法，通过在田间分布安装经过组网的水稻生长信息动态监测系统，在远程端可以24小时全天候进行水稻的光谱影像（数据）的分析和调查，在略低于无人机低空遥感传感器的空间分辨率上提供更高的时间分辨率。空地感测一体技术将有力提升水稻群体长势信息的获取效率，提高水稻生产的数字化和信息化水平。

成果转化与产业化经济效益指标或社会效益指标

1. 技术经济指标

（1）制作无人机低空遥感传感器样机一套：1）遥感传感器获得水稻长势专题图（NDVI为例）的解析速率达到50亩/分钟及以上（高于现有的3.3亩/分钟）；2）遥感传感器的空间分辨率在100米的飞行高度时达到1 m/像素；3）与专业多光谱相机的数据各个波段的反射率和植被指数（NDVI、SAVI、EVI）的相关系数$R>0.85$，$P<0.001$。

（2）制作水稻生长信息动态监测系统一套：1）水稻生长信息动态监测系统可24小时全天候获得水稻长势专题图（NDVI为例）；2）与专业多光谱相机的数据的NDVI相关系数$R>0.85$，$P<0.001$。

2. 社会经济效益指标

（1）建立无人机低空遥感传感器与水稻生长信息动态监测系统应用建立示范基地1-2个，核心示范面积≥150 亩，辐射示范面积≥1000 亩。

（2）有效提高水稻群体长势信息的获取和解析效率，降低遥感影像的数据后处理时间，有效提高遥感数据的实时性，增强实时遥感数据对水稻生产中肥料管理的指导作用，逐步改善稻田生态环境。

人才培养、知识产权、技术标准等指标

1. 人才培养

通过项目的执行开展，培养一批从事微小型无人机遥感测量、精准农业生产管理和农业信息化技术研究等方面的专业技术人才，培养博士研究生1-2名，硕士研究生3-4名。

2. 知识产权

国内外学者在作物遥感信息获取技术、养分管理决策支持技术等方面已经取得了一定的研究成果，有相关的专利和软件著作权，但基于微小型无人机遥感技术的水稻群体长势信息快速获取技术领域，相关的专利和软件著作权还未见报道。本项目拟在微小型无人机水稻遥感信息获取技术和近地实时遥感技术等方面开展研究，申请发明专利1-2件，发表SCI/EI学术论文1-2篇。

3. 技术标准

形成技术标准1个。

其他指标

1. 通过研发更高效率的无人机低空遥感传感器，提高水稻群体长势信息的获取效率。“无人机低空遥感传感器”定位于研究解决水稻长势遥感监测中存在的传感器成本高、数据量大、解析处理效率低、其实时性较难满足实际生产的要求等问题，重点研究适用于水稻氮素营养诊断的高效率光谱影像（数据）获取方法，并在水稻生产中进行验证。

2. 通过研发水稻生长信息动态监测系统，提高水稻群体长势信息获取的时间分辨率。“水稻生长信息动态监测系统”采用分布式原位光谱影像（数据）采集策略，实现24小时全天候水稻群体长势专题图的生成。

本项目最终目标是研发出可直接应用于生产实践的、能低成本快速输出水稻长势信息的低空遥感监测系统，技术实现后可弥补现有遥感技术效率低的短板，提高光谱物理方法获取作物信息的实际应用水平，即时生成的水稻群体长势专题图数据有助于改进水稻养分管理策略，提升肥料利用率，降低过量用肥概率，改善农田生态环境。

五、承担/参与单位情况

申请单位信息			
单位名称	井冈山大学		
统一社会信用代码（组织机构代码）	12360000492390024X		
通讯地址	江西省吉安市青原区学苑路28号		
单位所在地(邮编)	343009	注册资本(万元)	5000.00
单位性质	高等院校		
所属行业	普通高等教育	成立时间	1958-10-28
网址	343009		
是否高新技术企业	否		
所属产业链	电子信息		
法人代表	曾建平	联系电话(手机)	15216290510
申报单位人员情况			
员工人数	1600	其中：从事研发人员数	1212
占员工总数比例	76%		
上年度主要经济指标			
销售收入总额（万元）	5000.00	利润总额（万元）	2000.00
年研究开发经费（万元）	2000.00	研发经费占年销售收入比例	40.00%

主要股东/出资人（前5位）

序号	股东/出资人名称	出资金额(万元)	出资方式	出资比例	入股时间

参与单位

序号	单位名称	单位性质	统一社会信用代码（组织机构代码）	联系人	电话	手机
1	华南农业大学	高等院校	124400004554165634	姜锐	02038676975	13424049263

六、项目组人员情况

项目联系人					
姓名	刘朝晖			联系电话	0796-8106067
手机	15979666338			E-mail	jgsucad@126.com
项目负责人					
姓名	刘朝晖	性别	男	出生年月	1979-06-28
证件类型	身份证	证件号码	362429197906281911	民族	汉族
职称	副教授	从事专业	机械	学位	博士
职务	副教授	手机	15979666338	联系电话	15979666338
E-mail	103489234@qq.com	传真	0796-8106067	为本项目工作时间（月/年）	8
在本项目中承担的主要工作					
全面负责项目的组织和实施，具体负责应用示范推广基地的筹建以及适用于吉安市当地水稻种植习惯和农艺要求的无人机低空遥感及水稻生长信息动态监测技术联合攻关。					
项目负责人					
姓名	姜锐	性别	男	出生年月	1993-04-29
证件类型	身份证	证件号码	142427199304296310	民族	汉族
职称	讲师	从事专业	遥感	学位	博士
职务	讲师	手机	13424049263	联系电话	13424049263
E-mail	ruiojiang@scau.edu.cn	传真	020-38676975	为本项目工作时间（月/年）	8
在本项目中承担的主要工作					
配合主持单位完成项目任务，具体包括样机的改进和制作、项目相关产品的成果推广演示和培训等。					
项目负责人					

七、项目经费情况（单位：万元）

预算科目名称	合计	专项经费	自筹经费	说明
一、经费支出	50.00	50.00	0.00	无
（一）直接费用	43.50	43.50	0.00	无
1、设备费	0.00	0.00	0.00	项目组依托的实验室已配备了试验所需的仪器，无需采购。
（1）购置设备费	0.00	0	0	无
（2）试制设备费	0.00	0	0	无
（3）设备改造与租赁费	0.00	0	0	无
2、材料费	2.00	2.00	0	主要用于无人机低空遥感传感器及水稻生长信息动态监测系统所需要的光学镜头（需定制）、光敏器件、芯片处理器、网络通信设备、水稻长势遥感监测样本的培育及其它耗材、试验试剂的费用。
3、测试化验加工费	0.50	0.50	0	主要用于委托加工、模型打样制作、水稻样本农学理化参数化验分析等所产生的费用。
4、燃料动力费	0.00	0	0	
5、差旅费/会议费/国际合作与交流费	2.50	2.50	0	主要用于往返试验农场、开展国内外学术交流及调研等所产生的费用。
6、出版/文献/信息传播/知识产权事务费	1.50	1.50	0	主要用于查新、论文发表、专利申请、资料复印装订等所产生的费用。
7、劳务费	1.00	1.00	0	主要用于参加项目的本科/研究生、临时用工等劳务费用。
8、专家咨询费	1.00	1.00	0	主要用于专家项目咨询所产生的费用。
9、其他支出	35.00	35.00	0	用于华南农大合作研究费用
（二）间接费用	6.50	6.50	0	无
其中：绩效支出	4.00	4.00	0	用于项目组人员的绩效奖励。
二、经费来源	50.00	50.00	0.00	无
1、专项经费	50.00	50.00	/	无
2、自筹经费	0.00	/	0.00	无
（1）其他财政拨款	0.00	/	0	无
（2）单位自有货币资金	0.00	/	0	无
（3）其他资金	0.00	/	0	无

十、任务书签订单位

甲方：吉安市科学技术局（盖章）：

3608000021164

法人代表或授权代表（签章）： 周才俊印

执行科室（盖章）： 科室主要负责人（签字）：周卫华

经办人（签字）：杨洪斌 联系电话：8225273

2022 年 6 月 6 日

乙方：井冈山大学

项目承担单位（盖章）：

法人代表或授权代表（签章）： 联系电话：

项目负责人（签章）： 联系电话：15979666358

财务负责人（签章）： 联系电话：

开户银行： 账号：

年 月 日

丙方：项目推荐单位（盖章）：

法人代表或授权代表（签章）： 联系电话：

经办人（签章）： 联系电话：

年 月 日

3

受理编号：c22JAJH-22-0500000004

项目编号：20222-051252

文件编号：吉市科计字[2022]18号

20222-051252

科技计划项目

合同书

项目名称：南方红壤丘陵区水稻智慧生产关键技术与装备研发及示范应用

业务类型：井冈山农高区省级科技专项“揭榜挂帅”项目

项目起止时间：2022-10-01 至 2025-09-30

管理单位(甲方)：吉安市科学技术局

3608000021184

承担单位(乙方)：华南农业大学

乙方主管部门(丙方)：

通讯地址：广东省-广州市-天河区

邮政编码：510642 **单位电话**：020-85280011

项目负责人：胡炼 **手机**：15915767370

项目联系人：周志艳 **联系电话**：020-38676975

二零一七年一月制

一、项目摘要

针对南方红壤丘陵区水稻田块面积较小、形状复杂、农机作业全覆盖难和水田硬底层不平影响无人农机行驶与作业的精度和效率的问题，开展南方红壤丘陵区水稻智慧生产无人化关键技术、适应南方地块的水稻种植装备、水稻生产智能排灌技术与系统开发研究，研究水稻无人化农机农艺融合生产模式和规范以及水稻无人化智慧生产集成技术，创制无人农场高精度地图构建平台，开发适应南方红壤丘陵区的农机自动驾驶系统，创制小型智能化水稻精量穴直播机和无人机载彩绘水稻种植作业装备，开发适宜于南方红壤丘陵区水稻生产的排灌智能管控系统，通过技术集成在井冈山农高区建立水稻无人化智慧农场开展应用示范，示范面积500亩并制定技术规范，在全市选择3-5基地进行全程或至少2个及以上关键环节示范应用推广，且示范基地和推广应用基地作业数据上传至井冈山农高区智慧农业综合服务平台。

二、项目考核指标

主要技术经济指标及社会效益	
累计新增销售收入（万元）	
累计新增利税（万元）	
其他主要技术经济指标及社会效益说明：	
项目负责人（签章）： 2022年 12月 21日	

三、项目进度和阶段目标

序号	起止时间	项目进度工作内容
1	2022-10-01至2022-12-31	（1）开展秋冬季水田图像采集，优化无人农场高精度地图创制技术路线和实施方案； （2）连片小面积水田无人驾驶农机路径规划和避障技术； （3）开展小型动力底盘选型、搭建多品种兼用型水稻播种器试验台架，优化技术方案； （4）研究制定基于农业无人机水稻定点、精量和成行成穴播种技术方案；（5）研究制定水稻灌溉整体技术方案； （6）选定核心示范基地，制定水稻无人化智慧农场建设方案。
2	2023-01-01至2023-06-30	（1）开展春夏季水田图像采集，开展边界高精度定位信息获取、实地检验、校准优化研究； （2）田埂和田角覆盖作业路径主自规划和避开障碍物绕行路径自主规划方法； （3）开展围绕直播机具的开沟器、仿形底板、传动机构的设计研究； （4）基于农业无人机水稻定点、精量和成行成穴播种技术； （5）开展水层-水分传感器设计与试制，闸门方案优化设计； （6）建设水稻无人化智慧农场，选择耕和种环节开展试验。
3	2023-07-01至2023-12-31	（1）继续采集水田图像，开展面向地图构建需求的边界定位信息的编译和数据库存储。 （2）研究基于农机具位姿估计的抗干扰控制技术、自主路径规划、作业控制技术； （3）创制轻小型水稻直播机具，研究播种状态监测与报警机制；（4）研究异型区域地理信息智能转换的方案； （5）试验水层-水分传感器，开展闸门设计与试制； （6）开展管理和收获环节开展智慧耕种试验，开展推广示范基地选定工作。
4	2024-01-01至2024-06-30	（1）开展面向地图构建需求的数据库可视化，初步验证无人农场地图构建平台技术路线； （2）开发适宜于南方红壤丘陵区水稻智慧生产的自主驾驶系统；（3）优化和集成播种状态监测与报警机制。 （4）研究形成无人机撒播水稻成穴成行技术系统； （5）试验水层-水分传感器、闸门，智能灌溉管控系统设计； （6）在核心示范基地开展耕种管收无人化作业，召开现场观摩会和培训会。
5	2024-07-01至2024-12-31	（1）集成面向无人农场地图构建系统，优化平台技术系统结构和模型方法； （2）研究分布式协同任务规划和控制技术、双季稻连片稻田多农机协同作业控制技术； （3）开展水稻直播机的轻量化设计，完善播种状态监测与报警系统； （4）根据目标图案轮廓实现航线边界，优化彩绘方案设计； （5）优化灌溉管控系统，开展水稻合理管水技术标准流程研究； （6）继续开展无人化作业，在推广基地进行作业示范，召开现场观摩会和培训会。
6	2025-01-01至2025-09-30	（1）面向数据指标和示范指标，全面开展无人农场高精地图构建平台的评价和完善； （2）南方红壤丘陵区水稻智慧生产的自主驾驶系统； （3）对轻小型水稻直播机和播种状态监测系统进行优化定型； （4）完善形成无人机撒播水稻成穴成行技术系统； （5）在核心示范基地进行智能灌溉系统应用； （6）在推广基地进行作业示范，召开现场观摩会和培训会； （7）项目总结与验收。

四、经费分配情况

承担/参与单位名称（盖章）	经费分摊（万元）	工作分工
华南农业大学	280.00	研究农机自动驾驶技术、障碍物识别技术，开发自主驾驶系统；研究无人化彩绘水稻种植技术，研制水稻种植装备；研究水田水层-水分传感技术，研制水层-水分传感器、排灌水闸门，开发水稻生产排灌智能管控系统。
吉安市农作物良种场	100.00	开展应用场景示范，进行水稻无人化智慧生产集成应用示范和推广应用。
井冈山大学	50.00	研究南方红壤丘陵区水稻智慧技术需求，参与水稻智慧生产集成应用示范，编制示范技术规范。
江西农业大学	70.00	研究基于人工智能的南方水稻农场田埂边界、作物和障碍物等对象目标的分类识别和相对定位，开发无人农场高精度地图构建平台，研制地面小型水稻种植装备。
合计	500.00	

五、项目组人员情况

项目负责人							
序号	姓名	职称	E-mail	所在单位	证件号码	工作分工	签名
1	胡炼	副高级-副研究员	lianhu@scau.edu.cn	华南农业大学	430122198405053259	负责项目的技术方案的制定与实施	胡炼

主要参与人员							
序号	姓名	职称	E-mail	所在单位	证件号码	工作分工	签名
1	罗锡文	教授	xwluo@scau.edu.cn	华南农业大学	440106194512021811	项目策划与技术指导	罗锡文
2	何杰	实验师	hooget@scau.edu.cn	华南农业大学	362330198508288311	农机自动驾驶技术及系统开发	何杰
3	周志艳	教授	zyzhou@scau.edu.cn	华南农业大学	432923197211230314	无人化彩绘水稻种植技术	周志艳
4	王国庆	高级农艺师	1243@163.com	吉安市农作物良种场	362421197608043519	水稻智慧生产集成应用示范	王国庆
5	刘兆朋	讲师	314134582@qq.com	江西农业大学	370911198411082011	无人农场高精度地图平台构建	刘兆朋
6	肖根福	副教授	xiaogenfu@163.com	井冈山大学	362136198005100038	示范技术规范编制	肖根福
7	黄培奎	高级工程师	huangpeiku@scau.edu.cn	华南农业大学	445121199003156639	水层-水分传感器研制	黄培奎
8	汪沛	讲师	wangpei@scau.edu.cn	华南农业大学	320321198306242045	障碍物识别技术	汪沛
9	姜锐	讲师	ruiojiang@scau.edu.cn	华南农业大学	142427199304296310	机载水稻点射播种装置	姜锐
10	刘文安	未取得	123456@163.com	吉安市农作物良种场	362401196808144031	水稻智慧生产集成应用示范	刘文安
11	刘新生	技术员	13546@163.com	吉安市农作物良种场	362421196809018315	水稻智慧生产集成应用示范	刘新生
12	杨光华	高级农艺师	13466@163.com	吉安市农作物良种场	362425198510260216	水稻智慧生产集成应用示范	杨光华
13	郑大腾	教授	yizh9026@163.com	井冈山大学	362429197004014355	协助示范基地建设	郑大腾
14	肖忠跃	副教授	306490389@qq.com	井冈山大学	362426197411114813	示范应用推广及技术培训	肖忠跃
15	刘俊安	讲师	806189827@qq.com	江西农业大学	420983198910114416	轻小型水稻直播机装备创制	刘俊安
16	方鹏	讲师	1244860715@qq.com	江西农业大学	360731199301194810	无人农场多地物目标识别与边界提取技术规划	方鹏
17	陈雄飞	副教授	121686212@qq.com	江西农业大学	362330198702278256	直播机技术集成与试验示范	陈雄飞
18	刘木华	教授	714874481@qq.com	江西农业大学	360101196906297519	项目组织与示范建设推进	刘木华
			403614537@		420704198412	直播机排种器结构	

19	余佳佳	讲师	qq.com	江西农业大学	03429X	参数和工作参数优选	余佳佳
20	肖丽萍	教授	16043570@qq.com	江西农业大学	362232197803090423	直播机农艺与农机融合技术规划及装备制备	肖丽萍

六、合同条款

第一条 甲方与乙方根据《中华人民共和国合同法》及国家有关法规和规定，为顺利完成（2022）年**南方红壤丘陵区水稻智慧生产关键技术与装备研发及示范应用** 专项项目（项目编号： 20222-051252）经协商一致，特订立本合同，作为甲乙双方在项目实施管理过程中共同遵守的依据。

第二条 甲方的权利义务：

1.按合同书规定进行经费核拨的有关工作协调。

2.根据甲方需要，在不影响乙方工作的前提下，定期或不定期对乙方项目的实施情况和经费使用情况进行检查或抽查。

3.根据《技计划项目信用管理办法(试行)》对乙方进行科技计划信用管理。

第三条 乙方的权利义务：

1.确保落实自筹经费及有关保障条件。

2.按合同书规定，对甲方核拨的经费实行专款专用，单独列账，并随时配合甲方进行监督检查。

3.使用财政资金采购设备、原材料等，按照《〈中华人民共和国招标投标法〉办法》有关规定，符合招标条件的须进行招标。

4.项目实施完成或实施到一定程度，须按照《科技计划项目结题管理的实施细则（试行）》提出验收或终止结题的申请，并按甲方要求做好项目结题工作。

5.在每年1月向甲方如实提交上年度工作情况报告，报告内容包含上年度项目进展情况、经费决算和取得的效果等。

6.按照国家和省有关规定，每年须提交年度科技报告；项目验收时，须提交验收科技报告。

第四条 在履行本合同的过程中，如出现相关政策法规重大改变等不可抗力情况，甲方有权对所核拨经费的数量和时间进行相应调整。

第五条 在履行本合同过程中，需要对项目起止时间、项目经费使用（包括自筹经费、经费分配及经费支出预算等）、项目内容（包括研发内容、技术指标、经济指标及成果指标等）、项目名称、项目承担单位（包括承担单位更名、承担单位替换）、参与单位、项目负责人和成员等进行变更的，甲乙双方按照《科技计划项目合同书管理的实施细则（试行）》有关规定执行。

第六条 在履行本合同的过程中，当事人一方发现可能导致项目整体或部分失败的情形时，应及时通知另一方，并采取适当措施减少损失，没有及时通知并采取适当措施，致使损失扩大的，应当就扩大的损失承担责任。

第七条 本项目技术成果的归属、转让和实施技术成果所产生的经济利益的分享，除双方另有约定外，按国家有关法规执行。

第八条 属技术保密的项目，甲乙双方应另行订立技术保密条款，作为本合同正式内容的一部分，与本合同具有同等效力。

第九条 根据项目具体情况，经双方另行协商订立的附加条款，作为本合同正式内容的一部分，与本合同具有同等效力。

第十条 本合同的争议应由双方本着协商一致的原则解决，如双方协商不成的，则应向甲方所在地法院提起诉讼。

第十一条 保密条款：

1.本合同保密内容范围为：

各承担单位标明保密的文件。

2.本合同保密期限为：

项目结题后2年或标明保密文件上要求期限。

3.乙方应与可能知悉保密内容的人员签订技术秘密保护协议。

4.各方应建立技术秘密保护制度。

5.属技术保密的项目必须经省负责技术保密部门审查后，确定可否发表或用于国际合作和交流。

第十二条 甲方可根据具体情况决定乙方是否需要单位担保，若需要保证单位，应订立担保条款，作为本合同正式内容一部分。当乙方不履行或不完全履行本合同，以及没有或没有完全承担违约责任时，乙方的保证单位承担连带保证责任。

第十三条 本合同一式六份，各份具有同等效力。甲方存三份，乙方存二份，丙方存一份，本合同自签字之日起生效，有效期至项目结题后一年内。各方均应负合同的法律责任，不应受机构、人事变动的影响。

说明：本合同书中，凡是当事人约定无需填写的内容，应在空白处划（/）。

八、本合同签约各方

管理单位（甲方）：　　（盖章）

安市科学技术局

单位地址：

法定代表人（或授权代表）：________　　（签章）

联系人（经办人）姓名：________　　（签章）

Email：

电话：

2022年12月20日

承担单位（乙方）：　　（盖章）

华南农业大学

单位地址：

法定代表人（或法人代理）：刘雅红　　（签章）

联系人（项目主管）姓名：　　（签章）

Email：

电话：

开户单位名称：

开户银行及帐号：

2022年12月20日

乙方主管部门（丙方）：　　（盖章）

单位地址：

法定代表人（或法人代理）：________　　（签章）

联系人（项目主管）姓名：________　　（签章）

Email：

电话：

开户单位名称：

开户银行及帐号：

年　月　日

课题编号：

S	K	L	R	S	-	2	0	2	4	-	K	F	-	0	8

机器人技术与系统全国重点实验室开放基金
课题任务合同书

课题名称：菠萝采摘机器人立体视觉感知与运动控制

课题委托方（甲方）：哈尔滨工业大学

课题受托方（乙方）：华南农业大学

课题起止年限：2024 年 1 月 1 日 - 2025 年 12 月 31 日

2024 年 1 月

填 写 说 明

一、本合同文本一式四份，并提交电子版。

二、乙方（法人单位）请按单位公章的详细名称填写。

三、所盖公章为单位公章或技术合同专用章。

四、填写内容涉及到外文名称，首次出现时要写全称和缩写字母。凡不填内容的栏目，请用“×”或“无”表示。

五、合同双方可根据课题具体情况，就本合同的未尽事宜协商订立附加条款。附加条款与本合同正文具有同等法律效力。

机器人技术与系统全国重点实验室开放基金课题任务合同书

课题委托方(甲方)：哈尔滨工业大学

法定代表人：韩杰才

机器人技术与系统全国重点实验室负责人：付宜利

固定电话：0451-86403679　　　　移动电话：13936137598

传　　真：0451-86403679　　　　电子邮件：meylfu@hit.edu.cn

课题受托方（乙方）：华南农业大学

法定代表人：薛红卫

课题负责人：李杰浩　　　　　性别：男

身份证号：441225198906280019

通讯地址：广州市天河区五山路483号华南农业大学工程学院

职务：科研秘书　　　　　　　职称：副教授

最高学历：博士研究生　　　　获得学位时间：2022-06

最高学历毕业学校：北京理工大学

固定电话：020-85280783　　　移动电话：15915764624

传真：020-85280783　　　　　电子邮件：jiehao.li@scau.edu.cn

为执行机器人技术与系统全国重点实验室开放基金，甲方委托乙方开展开放课题研究，课题名称为 菠萝采摘机器人立体视觉感知与运动控制 ，甲方和乙方依照《中华人民共和国民法典》等法律法规，以及机器人技术与系统全国重点实验室开放基金管理办法，在充分协商的基础上，就研究开发该课题的有关事宜，签订本合同。

乙方银行信息：

单位名称：华南农业大学

开户银行：中国工商银行（广州工行五山支行）

账　　号：3602002609000310520

一、课题主要研究内容（包括拟解决的主要技术问题、难点、主要创新点等）

1 研究目标

本项目总目标是探明多模态信息融合的采摘机器人立体视觉感知与运动控制的自主运动机理。首先建立非结构化环境下统一编码框架内多模态数据，同模态内和跨模态间特征的高效耦合机制；其次提出多源信息融合下采摘目标的准确识别和定位方法；接着提出受限条件下采摘机械臂运动驱动与控制方法。具体而言，研究目标包括：

（1）建立非结构化环境下立体视觉准确感知的多模态融合机制，充分发挥图像模态和三维模态的互补优势。提出非结构环境下采摘目标的准确识别和定位方法，构建基于果实形态先验下的采摘目标的准确识别模型，实现动态非结构环境下采摘机器人对采摘目标的准确识别和定位。

（2）探明动态非结构环境下采摘机械臂的鲁棒自主控制机理，构建复杂环境扰动的力馈闭环和误差补偿模型，提升采摘机械臂在复杂环境中运动控制的鲁棒性，实现动态非结构环境下采摘机械臂高效自主控制。

2 研究内容

研究内容一：多模态融合的非结构化环境准确感知和采摘点精准定位

针对非结构化环境下，基于单模态数据的采摘目标立体视觉感知和定位精度有限的问题，目前主要采用同坐标系叠加、二维空间卷积和低维向量聚类等多模态数据融合的方法提升感知和定位的准确率。需要指出的是，现有方法仅实现多模态数据的浅层融合，缺乏对同模态内和跨模态间特征关联关系的挖掘，不能实现多模态数据的高效耦合，难以进一步提升非结构化环境下采摘点的定位精度。因此本项目通过建立统一编码框架内多模态数据同模态内和跨模态间特征的高效耦合机制，实现非结构化环境下多模态融合的采摘机器人立体视觉准确感知和采摘点精准定位。具体如下：

① 果实形状先验下图像模态中菠萝果实的精确识别

② 多模态融合的动态非结构化环境三维语义信息准确感知

③ 基于结构化潜在编码空间的无监督采摘点精准定位

研究内容二：受限动态扰动下采摘机械臂鲁棒柔顺控制研究

针对受限动态扰动下采摘机械臂安全稳定到达指定采摘点的鲁棒控制问题，目

前主要采用神经网络逼近的控制方法。需要指出的是，现有的方法是在稳定状态的前提下设计控制器。然而，采摘过程中机械臂状态参数受到外界扰动以及机械臂系统参数的测量误差等因素干扰，使得运动控制器性能下降，影响机械臂的跟踪性能。因此，本项目研究状态受限和动态扰动下采摘机械臂的鲁棒控制方法。具体如下：

① 动态扰动条件下的采摘机械臂自适应鲁棒跟踪控制

② 状态受限条件下的采摘机械臂与环境交互柔性阻抗控制

③ 未知动态环境下采摘机械臂的自适应柔顺交互策略

3 主要创新点

（1）探明统一编码框架内多模态数据同模态内和跨模态间特征的高效融合机制。提出外界因素干扰下采摘目标的准确识别与定位的方法，设计基于果实形态先验的遮挡果实区域关联算法，提出基于结构化潜在编码空间的无监督定位算法，实现在非结构化环境中对采摘目标的准确识别与定位。

（2）设计基于宽度学习的模糊神经网络推理模型，提出状态受限及动态扰动环境下采摘机械臂鲁棒控制方法，实现受限动态扰动环境下采摘机械臂稳定到达目标采摘点。提出基于自适应动态系统理论柔顺交互策略，设计全局渐进稳定势能函数与鲁棒因子，实现采摘机械臂与动态环境柔顺交互。设计边界限制条件避免机械臂与环境交换中发生突变而引起不稳定安全问题。

二、课题预期成果和考核指标（包括应达到的主要技术指标和水平，应获得的发明专利等知识产权，及其他应考核的指标。基金资助的课题至少发表影响因子在 1.0 以上的 SCI 论文 1 篇或者累计影响因子在 2.0 以上。对于超额完成指标的优秀课题，通过评审实验室将会继续支持。）

1）预期成果：

①发表影响因子在 1.0 以上的 SCI 论文 1-2 篇，或者累计影响因子在 2.0 以上；

②申请国家专利 1 项；

③培养研究生 1-2 名；

④组织国内外学术会议/期刊的特邀专题 1 次；

2）考核指标：

①发表影响因子在 1.0 以上的 SCI 论文 1-2 篇，或者累计影响因子在 2.0 以上；

②申请国家专利 1 项；

三、课题的年度计划及年度考核指标

年度计划：

- **2024-01 至 2024.12：**探明动态非结构环境下采摘机器人立体视觉感知方法。建立统一编码框架内多模态数据同模态内和跨模态之间特征的高效耦合机制，实现非结构环境下多模态融合的采摘机器人对环境的精准感知和三维语义地图构建。（年度考核指标：发表 SCI 论文 1 篇或者申请国家专利 1 项）

- **2025.01 至 2025.12：**探明动态非结构环境下采摘机械臂的鲁棒自主控制机理。探明基于策略迭代的最优阻抗学习机制，设计基于宽度学习模糊神经网络的推理模型，实现受限动态扰动环境下采摘机械臂稳定到达目标。按时提交结题材料。（年度考核指标：发表 SCI 论文 1 篇或者申请国家专利 1 项）

四、课题拟采取的研究方法、课题技术路线、实施方案（可多页）

1 课题拟采取的研究方法、技术路线和实施方案

本项目在申请人及其团队已有的相关研究基础上，对菠萝采摘机器人相关机理的研究进行了充分的调研，发挥项目组成员在机器人环境感知、采摘目标准确识别与定位以及机械臂运动规划等方面的优势，对两个方面的关键问题进行由浅入深的攻关，循序渐进地予以解决，达到预期研究目标。

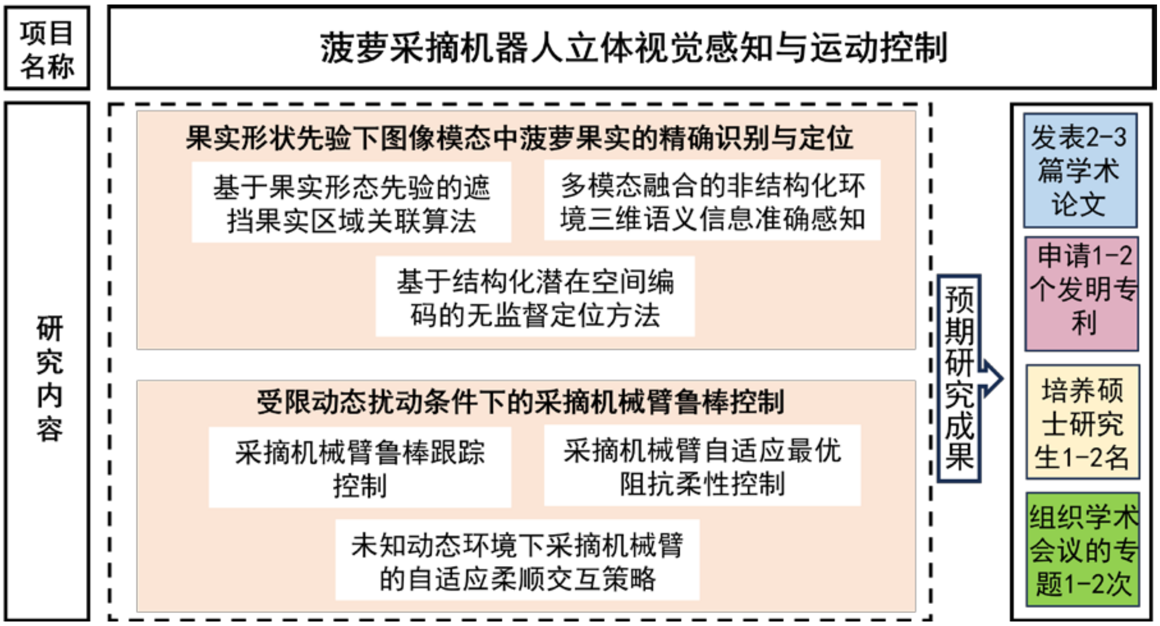

图 3 技术路线总图

（1）非结构化环境下采摘目标的准确识别和采摘点精准定位

针对非结构化环境下多模态融合的立体视觉准确感知和采摘点精准定位，本项目拟首先基于图像模态中采摘目标的识别确定目标区域，然后借助多模态融合获取非结构化环境的三维语义信息，最终实现对于最优采摘点的精准定位。

① 果实形态先验下图像模态中采摘目标的准确识别研究

针对非结构化环境下光照不均对于采摘目标识别准确率的影响，本项目拟构建基于实例-批归一化（Instance-Batch Normalization，IBN）的域自适应模型，该模型的示意图如图 5 所示。实例-批归一化的域自适应模型包含实例归一化和批归一化两种类型的自适应矫正操作，其中实例归一化被用于处理底层视觉任务，批归一化被用于处理高层视觉任务。通过将实例归一化和批归一化集成，同时提高了模型的学习能力和泛化能力，进而可以被用于非结构化环境下不均匀光照的自适应矫正。

整个基于实例-批归一化的域自适应模型由编码器、IBN 矫正模块和解码器组成，首先输入的图像模态数据经过基于卷积神经网络的编码器，被提取成一系列特征图（feature map），该部分网络可以基于大规模图像数据集进行预训练以提升模型的特征提取能力。借助实例归一化和批归一化逐层对编码后的特征进行归一化，可以实现不同光照、对比度等采摘目标外观的自适应矫正，从而消除光照不均的影响。除光照不均对识别精度的影响外，非结构化环境下的枝叶遮挡易导致采摘目标被切分为若干不相连的区域。为此，本项目拟提出基于果实形态先验的遮挡果实区域关联算法。对于不同果实区域掩码，用果实形态先验与其轮廓进行匹配。根据重合区域对果实区域轮廓进行端点选取，从而再次调整形态学先验尺寸以实现最佳匹配，进而确定对应果实区域，实现对于不同果实区域的语义关联关系的确定。

通过将上述基于实例批归一化的域自适应模型和基于果实形态先验的遮挡果实区域关联算法集成到同一端到端网络进行训练，可以实现动态非结构化环境中采摘目标的准确识别。

② 多模态融合的非结构化环境三维语义信息准确感知研究

针对多模态数据在结构、维度和复杂度等方面的显著差异带来的融合困难，拟研究多模态数据的特征提取和嵌入模型，将动态非结构化环境的纹理、轮廓等特征映射到高维语义空间。将图像模态和其实例分割结果进行逐通道堆叠，通过预训练的卷积神经网络提取特征形成图像模态的高维输入。对于三维模态中由遮挡导致的三维结构空洞，采用基于自定义膨胀核的空洞补齐算法进行预处理填充，进而通过基于 PointNet 的三维点云编码网络提取相应空间高维特征。构建基于多头自注意力机制的 Transformer 编码器，自适应为不同模态高维语义特征分配不同的权重，实现对于多模态特征间的加权耦合，并通过建立多尺度特征融合模型，实现非结构化环境下三维语义信息的准确感知。

③ 基于结构化潜在编码空间优化的采摘点精准定位研究

针对非结构化环境下果实区域由于枝叶遮挡带来的采摘点难定位问题，拟采用实例与语义解耦的三维分割算法，基于全局环境三维语义信息对果梗区域进行三维分割，算法的示意图如图 6 所示。通过将全局三维语义信息编码再融合解码，可以实现果实局部遮挡情况下对不可见区域进行三维分割，为采摘点的精准定位提供三维候选区域。在此基础上，拟采用基于结构化潜在编码空间的无监督优化算法，实现对果梗三维区域精细化分段。结合采摘目标的三维坐标信息，本项目拟采用基于果梗段质心的最优采摘点精准定位算法，实现对于最优采摘点的精准定位。

（2）受限动态扰动条件下的采摘机械臂鲁棒控制研究

针对受限动态扰动下采摘机械臂稳定到达指定采摘点的鲁棒控制问题，本部分主要研究状态受限和动态扰动下采摘机械臂的鲁棒控制方法。

① 动态扰动条件下的采摘机械臂鲁棒跟踪控制

采摘机械臂动力学模型建模：假设一个具有 N 自由度的机械臂，其关节角度向量及角速度向量分别为 $\theta = [\theta_1, \theta_2, \cdots, \theta_N]$ 和 $\dot{\theta} = \left[\dot{\theta}_1, \dot{\theta}_2, \cdots, \dot{\theta}_N\right]$，则机器臂的动力学模型可以根据拉格朗日形式 (Lagrange-Euler)描述为:

$$\mathcal{M}(\theta)\ddot{\theta} + C\left(\theta, \dot{\theta}\right)\dot{\theta} + \underbrace{\mathcal{F}_c\left(\dot{\theta}\right) + G(\theta)}_{\mathcal{H}(\theta,\dot{\theta})} + \tau_n = \tau_c \tag{1}$$

其中，$C(\theta, \dot{\theta}) \in \mathbb{R}^{N\times 1}$ 表示离心力和科氏力向量，$\mathcal{F}_c(\dot{\theta}) \in \mathbb{R}^{N\times 1}$ 表示库伦(Coulomb)摩擦项，以及关节的控制力矩。

自适应神经网络设计：径向基神经网络可以看作一个包含隐含层和输出层的两层网络，其中隐层对输入做非线性变换，输出层的作用是对其输入进行线性加权求和。使用高斯径向基函数神经网络对非线性函数进行逼近，其数学描述如下：

$$f(x) = {W^*}^{\mathrm{T}} S(x) + \epsilon(x), \forall x \in \Omega_x \tag{2}$$

其中，$\Omega_x \subset \mathbb{R}^n$为一个紧集，$W^*$为最优权值矩阵，逼近误差$e(x)$ 满足$\| \epsilon(x) \| \leqslant \epsilon^*$，$\epsilon^*$为误差上界。最优权值矩阵 W^* 可以表示为：

$$W^* = \arg\min_{W\in R^{|\times x|}} \left\{ \sup_{x\in\Omega_x} \left| f(x) - W^T S(x) \right| \right\} \tag{3}$$

跟踪控制器的设计：由机械臂的动力学模型设计轨迹跟踪控制器。首先，定义跟踪误差和瞬时性能变量如下：

$$e_i = \theta_i - \theta_{id} \tag{4}$$

$$\rho_i = \dot{e}_i + \Lambda_i e_i \tag{5}$$

其中，Λ_i是一个正实数，$i = 1,2, \cdots, n-m, \theta_i, \theta_{id}$分别为机器人在关节空间的 实际位置和期望位置。则有：

$$M_\theta \dot{\rho} + C_\theta \rho = u \tag{6}$$

则跟踪误差可以写成：

$$\dot{e} = -\Lambda e + \rho \tag{7}$$

式中$e = [e_1, e_2, \cdots, e_{n-m}]^{\mathrm{T}}, \Lambda = \mathrm{diag}\,[\Lambda_1, \Lambda_2, \cdots, \Lambda_{n-m}]$。选取e, ρ作为增广系统的状态变量，对增广系统进行建模，则控制器的状态方程表达式如下:

$$\dot{X}=\begin{bmatrix}\dot{e}\\ \dot{\rho}\end{bmatrix}=\begin{bmatrix}-\Lambda & I\\ 0 & -M_\theta^{-1}C_\theta\end{bmatrix}\begin{bmatrix}e\\ \rho\end{bmatrix}+\begin{bmatrix}0\\ M_\theta^{-1}\end{bmatrix}u(t) \tag{8}$$

② 状态受限条件下的采摘机械臂自适应最优阻抗柔性控制

首先设计一个基于宽度模糊神经网络的状态受限运动控制器，通过引入障碍李雅普诺夫函数，实现系统的状态受限控制，从而保证机器人在交互过程中的安全运行；此外，充分结合宽度神经网络的拓展能力、径向基神经网络的逼近能力和模糊系统的推理能力，提出适用于采摘机械臂控制的宽度模糊神经网络，对控制系统的不确定项进行逼近。

由采摘机械臂的阻抗模型，表达了机械臂末端交互力与交互位置的一个动态关系。

$$D_m(\ddot{x}-\ddot{x}_r)+C_m(\dot{x}-\dot{x}_r)+G_m(x-x_r)=f_e-f_d \tag{9}$$

式中，$x,\dot{x}$和$\dot{x}\in\mathbb{R}^D$ 分别表示机器人末端的位置、速度以及加速度，x_r、$\dot{x}_r$ 和 $\ddot{x}_r\in\mathbb{R}^D$ 表示机器人在目标阻抗情况下的交互期望位置、速度以及加速度，$f_e\in\mathbb{R}^D$ 表示机器人与环境的末端交互力，$f_d\in\mathbb{R}^D$ 表示期望的交互力。

进一步地，为了限制机器人的状态变量，使得机器人在与环境交互的过程中能在安全的范围内运行，引入障碍李雅普诺夫方程来处理状态受限问题：

$$V=\frac{\iota^2}{\pi}\tan\left(\frac{\pi\kappa^2}{2\iota^2}\right) \tag{10}$$

式中，κ表示系统状态变量，此外需要注意为了保证系统的稳定性。

③ 采摘机械臂在动态未知环境交互的自适应柔顺交互策略

本节将阐述基于动态系统的自适应柔顺交互策略的设计原理。首先通过不同的物理示教方法得到期望的任务模型，再通过回归方法得到原始的动态系统模型；然后运动规划环根据机器人与环境交互的力信息以及期望交互力，通过计算鲁棒项以及势能因子两个参数，调节原始动态系统的输出；最后，根据调整后的动态系统输出，利用前文设计的自适应宽度神经网络控制器对机器人运动进行控制，保证机器人的暂态及稳态性能，从而在运动规划层面实现机器人与环境的柔顺交互。设计采摘机械臂避障的非线性函数：

$$\wp(\xi_0,\xi,R_0)=\left(1+\frac{(R_0)^2}{(\xi-\xi_0)^T(\xi-\xi_0)}\right)(\xi-\xi_0) \tag{11}$$

进一步地，为了能实时调节机器人的速度实现避障，设计机器人的动态避障速度为：

$$\dot{\xi}_s=\Xi_p^s(\xi_0,\xi,R_0)f(\xi) \tag{12}$$

然而，本章的目标是研究面向未知环境的机器人-环境柔顺交互，交互物体的中心点、半径

等模型参数是未知的，因此提出的基于动态系统自适应运动规划形式定义如下：

$$\dot{\xi}_a = \Xi_p f(\xi) + \Xi_f \tag{13}$$

其中$\dot{\xi}_a \in \mathbb{R}^D$ 是通过自适应动态规划系统调节后的系统状态，Ξ_p为系统的势能因子，根据期望交互力以及实际交互力调节原始动态系统的交互速度；Ξ_f 为鲁棒项，其作用在于对交互速度进步调节，从而实现更加精确的力跟踪交互。由此，可以得到调整后的期望交互轨迹为：

$$\xi_a(i+1) = \xi_a(i) + \dot{\xi}_a \delta t \tag{14}$$

式中，δt 为时间的积分项。

五、拟解决的关键科学问题

① 非结构化环境下如何实现对环境的准确感知和采摘目标的精准定位？

采摘目标的准确识别和定位是采摘机器人完成采摘任务的前提，如何消除光照强度、果实被遮挡等因素，对果实进行准确识别与定位是目前研究的热点。现有的算法主要针对果实的特征（颜色、纹理、形状等）进行识别，忽略了外界的干扰因素。因此，如何消除非结构化环境中光照不均和果实被遮挡等因素的影响，将基于果实形态先验的遮挡果实区域算法和基于结构化潜在编码空间的无监督定位算法相结合，是实现对采摘目标准确识别和定位的关键科学问题。

② 受限动态扰动环境下如何设计采摘机械臂与动态环境的鲁棒柔顺控制？

采摘机械臂的动态输出通常是期望速度或者加速度，并结合比例积分控制、力/位混合控制、阻抗控制等传统控制器，实现被控对象的运动控制。然而，这类控制器面对受限动态扰动环境的抗干扰能力较弱。目前，采用神经网络逼近的方法对于未知动态扰动的处理取得了不错的效果，但是忽略了被控对象与动态环境之间的力反馈，影响了控制系统在动态受限环境下的稳定性。因此，针对状态受限和动态扰动下采摘机械臂稳定到达采摘点的目标，如何设计采摘机械臂与动态环境的鲁棒柔顺控制是关键科学问题。

六、课题组主要研究人员情况

姓名	性别	出生年月	职务/职称	专业	累计为本课题工作时间(人月)	课题组中职务(组长、副组长或成员)	在本课题中分担的任务	所在单位
李杰浩	男	1989-06	副教授	控制科学与工程	12	组长	项目负责人	华南农业大学
赵立军	男	1972-02	教授	机械电子工程	6	副组长	指导专家	哈尔滨工业大学
罗锡文	男	1945-12	教授/院士	农业工程	6	副组长	指导专家	华南农业大学
杨辰光	男	1982-11	教授	控制科学与工程	6	副组长	指导专家	华南理工大学
曾山	男	1973-09	研究员	农业工程	6	成员	底盘设计	华南农业大学
卢家欢	男	1992-02	副教授	车辆工程	12	成员	能量优化	华南农业大学
姜锐	男	1993-04	副教授	农业机械化	12	成员	图像处理	华南农业大学
施琳琳	女	1994-06	讲师	控制科学与工程	12	成员	控制算法	华南农业大学
李城林	男	1999-08	研究生	农业工程	16	成员	图像识别	华南农业大学

刘宏鲜	男	1993-10	研究生	农业工程	16	成员	机械臂运动控制	华南农业大学
罗群斐	男	2000-01	研究生	控制工程	16	成员	采摘路径规划	华南农业大学
吴浩楠	男	2001-03	研究生	机械工程	16	成员	执行机构设计	华南农业大学
曾德钊	男	2000-10	研究生	机械工程	16	成员	建图导航	华南农业大学
合计： 152 人月								

注：累计为本课题工作时间（人月）是指在课题实施期间该人总共为课题工作的满月度工作量；合计人月是指课题组所有人员投入人月之和。

七、乙方提供的技术与条件保障（包括现有技术基础和承诺提供的支撑条件，如仪器设备、水电、燃料、环保等条件）

本项目依托华南农业大学工程学院的 4 个国家级科研平台：国家精准农业航空施药技术国际联合研究中心，国家精准农业航空应用技术研究学科创新引智基地；以及广东省农业人工智能重点实验室，南方农业机械与装备关键技术教育部重点实验室开展研究工作。项目申请人属于罗锡文院士团队，团队还拥有国家级教学名师 1 人，国家“万人计划”科技创新领军人才 1 人，教授 22 人，副教授 38 人，研究生 50 余名。现有教学、科研用房面积 13000 多平方米，仪器设备 7000 多件。特别在智能无人农场技术，水稻生产机械与装备关键技术，南方特色农作物生产机械与装备关键技术，农业航空应用技术等研究方向特色鲜明。先后形成一批填补国内空白和国际领先的重大成果，实现了技术转让以及产业化生产应用。总而言之，华南农业大学是一所面向国家农业重大战略发展需求的一所实干型高校，为本项目的开展奠定了良好的工作环境。

八、课题经费预算

单位：千元

序号	预算科目名称	经费金额
1	**业务费**	**50**
（1）	材料费	10
（2）	测试化验加工费	0
（3）	燃料动力费	0
（4）	差旅/会议/国际合作与交流费	20
（5）	出版/文献/信息传播/知识产权事务费	20
2	**劳务费**	**30**
合计		**80**

九、其他条款

（一）缔约各方的权利、义务

第一条　缔约双方均应共同遵守《中华人民共和国民法典》、《中华人民共和国著作权法》、《中华人民共和国专利法》等法律及《机器人技术与系统全国重点实验室（哈尔滨工业大学）开放基金管理办法》，严格遵守并认真履行本合同的各项条款。

（一）甲方

甲方有权监督、检查合同履行情况。合同履行期间，甲方有权对乙方履行本合同的情况进行检查、监督。乙方完成课题研究开发任务后，由甲方负责进行验收。

（二）乙方

乙方应为课题的顺利实施提供承诺的技术与条件保障，严格履行合同义务，保证按时完成课题研究开发任务，并履行为课题组提供财务管理、科技档案管理服务等合同约定的义务。

乙方应及时向甲方提供真实准确的信息。乙方应积极配合或参加由甲方召集的有关本课题的监督、管理和评估等活动。

乙方应在课题实施过程中采取措施避免产生可能危及国际关系、造成恶劣政治影响、妨害经济运行等损害国家利益的活动。当出现危及社会利益、影响课题完成和其它可能违反合同条款的事件时，乙方应及时告知甲方。

乙方开展的一切与课题有关的活动如涉及伦理问题（如人体实验、基因重组实验、危害性微生物或病毒实验、动物实验等），应确保有关研究人员遵守相关法律法规。乙方应承担维护实验环境卫生、安全的责任，做好安全防护措施，如因执行本课题而导致人员生命、健康、财产等受到侵害或使环境受到损害，乙方应负完全责任。

第二条　甲方有权根据乙方课题计划进度完成情况决定是否继续支持。乙方使用经费应严格按照课题经费预算和合同约定的支出范围执行，课题完成后，乙方应向甲方提交课题经费使用情况报告，并加盖财务印章，在课题验收时一并验收。

（二）知识产权与成果管理

第三条　属开放基金资助的课题所取得的论文、专利、奖项等成果，归甲方和乙方共有。

第四条　属开放基金资助课题的有关论文、专著、成果等，均应标注“机器人技术与系统全国重点实验室开放基金资助(课题编号)”字样，英文为：Supported by State Key Laboratory of Robotics and Systems (HIT)(课题编号)；至少有1篇论文的第一作者或通讯作者的第一单位署名为“机器人技术与系统全国重点实验室（哈尔滨工业大学)”，英文为“State Key Laboratory of Robotics and Systems (HIT)”。

（三）文档资料管理

第五条　乙方应组织课题组按照合同约定的时间完成分段研究开发工作，按照约定的要求向甲方提交材料；在2024年12月31日前提交项目中期进展报告；在2025年12月31日之前完成全部研究开发工作，并在30日内向甲方提交结题报告；同时应将全部实验报告、数据手稿、图纸、声像等原始技术资料收集整理，交甲方的科技档案部门归档保管。

第六条　甲方可以视需要不限地域、时间和次数，以各种方式无偿使用乙方提交的可供公开发表的研究报告。

（四）违约责任

第七条　甲方未能按合同约定提供经费，导致乙方研究开发工作延误的，应允许合同规定的研究开发工作完成期限相应顺延。

第八条　因乙方的原因导致研究开发工作未能按期完成，或者课题成果未能达到合同约定指标的，经甲方书面同意后，乙方应当采取措施在甲方规定的合理期限内完成研究开发工作或者使课题成果达到合同要求，并承担由此增加的费用。逾期仍未完成的，甲方有权追缴部分或者全部经费，由此造成的经济损失由乙方承担。

第九条　乙方无正当原因未履行合同时，甲方有权追缴部分或全部经费，由此造成的经济损失由乙方承担。

第十条　任何一方因不可抗力不能履行合同义务时，可以免除违约责任，但应及时通知另一方，并在30天内出具因不可抗力导致合同不能履行的证明。在出现不可抗力的情况下，双方均应采取适当措施减轻损失。任何一方因未采取措施或采取措施不当导致损失扩大的，应当对扩大的损失承担责任。

（五）附　则

第十一条　本合同自缔约双方签章后生效。

第十二条　本合同由机器人技术与系统全国重点实验室负责解释。

第十三条　本合同正本一式4份（甲方2份，乙方2份）。

十、合同签署：

甲方：哈尔滨工业大学

（盖章）

机器人技术与系统全国重点实验室负责人：

（签章）

2024年 1 月 1 日

乙方：华南农业大学

（盖章）

课题负责人：

（签名）

2024年 1 月 1 日

检索证明

根据委托人提供的论文材料，委托人**华南农业大学工程学院姜锐**1篇论文收录情况如下表。

序号	论文名称	发表刊物及发表的年月卷期/页码等	作者排名	作者文中单位	收录情况	论文等级	影响因子	中科院大类分区
1	Evaluation Method of Rowing Performance and Its Optimization for UAV-based Shot Seeding Device on Rice Sowing	Computers and Electronics in Agriculture 出版年：2023 卷期：207　文献号：107718 文献类型：Article	共同通讯作者	华南农业大学	SCI	T2类	IF2-year=6.757 IF5-year=6.817 (2021)	农林科学　1区 Top期刊：是 (2022)

说明：论文等级和中科院大类分区按《华南农业大学学术论文评价方案（试行）》划分。

报告免责声明:如未盖章,报告无效

检索员：张进
华南农业大学图书馆
2023-05-23

检索证明

根据委托人提供的论文材料，委托人**华南农业大学工程学院姜锐**1篇论文收录情况如下表。

序号	论文名称	发表刊物及发表的年月卷期/页码等	作者排名	作者文中单位	收录情况	论文等级	影响因子	中科院大类分区
1	Development of UAV-based shot seeding device for rice planting	International Journal of Agricultural and Biological Engineering 出版年：2022 卷期：15　6 页码：1-7 文献类型：Article	共同通讯作者	华南农业大学	SCI	B类	IF2-year=1.885 IF5-year=2.232 (2021)	农林科学　3区 Top期刊：否 (2022)

说明：论文等级和中科院大类分区按《华南农业大学学术论文评价方案（试行）》划分。

报告免责声明:如未盖章,报告无效

检索员：张进
华南农业大学图书馆
2023-05-23

检索证明

根据委托人提供的论文材料，委托人**华南农业大学工程学院姜锐**1篇论文收录情况如下表。

序号	论文名称	发表刊物及发表的年月卷期/页码等	作者排名	作者文中单位	收录情况	论文等级	影响因子	中科院大类分区
1	Laser tracking leader-follower automatic cooperative navigation system for UAVs	INTERNATIONAL JOURNAL OF AGRICULTURAL AND BIOLOGICAL ENGINEERING 出版年：2022 MAR 卷期：15 2 页码：165-176 文献类型：Article	共同通讯作者	华南农业大学	SCI	B类	IF2-year=1.885 IF5-year=2.232 (2021)	农林科学 3区 Top期刊：否 (2022)

说明：论文等级和中科院大类分区按《华南农业大学学术论文评价方案（试行）》划分。

报告免责声明:如未盖章,报告无效

检索员：张进
华南农业大学图书馆
2023-05-23

SCAULIB202519290

检索证明

根据委托人提供的论文材料，委托人**华南农业大学工程学院 姜锐** 3 篇论文收录情况如下表。

序号	论文名称	发表刊物及发表的年月卷期/页码等	作者排名	论文等级	作者文中单位	收录情况	影响因子	中科院大类分区
1	Pomelo-Net: A lightweight semantic segmentation model for key elements segmentation in honey pomelo orchard for automated navigation	COMPUTERS AND ELECTRONICS IN AGRICULTURE 出版年：2025 出版日期：FEB 卷期：229 页码：- 文献号：109760 文献类型：Article	共同通讯作者	T2 类	华南农业大学工程学院	SCI	IF2-year=8.9 IF5-year=9.3 （2024）	农林科学 1 区 Top 期刊：是 （2025）
2	Quantity Monitor Based on Differential Weighing Sensors for Storage Tank of Agricultural UAV	DRONES 出版年：2024 出版日期：MAR 卷期：8 3 页码：- 文献号：92 文献类型：Article	共同通讯作者	B 类	华南农业大学工程学院	SCI	IF2-year=4.8 IF5-year=5.0 （2024）	计算机科学 3 区 Top 期刊：否 （2025）
3	A UAV-Borne Six-Vessel Negative-Pressure Enrichment Device with Filters Designed to Collect Infectious Fungal Spores in Rice	AGRONOMY-BASEL 出版年：2024 出版日期：APR 卷期：14 4 页码：-	共同通讯作者	A 类	华南农业大学工程学院	SCI	IF2-year=3.4 IF5-year=3.8 （2024）	农林科学 2 区 Top 期刊：否 （2025）

	Fields	文献号：716 文献类型：Article						

说明：论文等级和中科院大类分区按《华南农业大学学术论文评价方案（试行）》划分。

报告免责声明:如未盖章,报告无效

检索员：尹银怀

华南农业大学图书馆

2025-07-16

SCAULIB202519341

检索证明

根据委托人提供的论文材料，委托人**华南农业大学工程学院 姜锐** 1 篇论文收录情况如下表。

序号	论文名称	发表刊物及发表的年月卷期/页码等	作者排名	论文等级	作者文中单位	收录情况	影响因子	中科院大类分区
1	Experiment on Weed Seed Germination Rate in Soil under Different Flame Temperature Conditions before Sowing of Direct-Seeded Rice	农业机械学报 出版年：2024 卷期：55 1 页码：134-144 文献号： 文献类型：JA	通讯作者	B 类	华南农业大学工程学院	EI	无	无

说明：论文等级和中科院大类分区按《华南农业大学学术论文评价方案（试行）》划分。

报告免责声明:如未盖章,报告无效

检索员：尹银怀

华南农业大学图书馆

2025-07-16

Computers and Electronics in Agriculture 207 (2023) 107718

Contents lists available at ScienceDirect

Computers and Electronics in Agriculture

journal homepage: www.elsevier.com/locate/compag

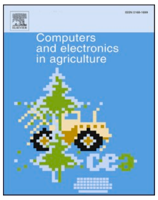

Evaluation method of rowing performance and its optimization for UAV-based shot seeding device on rice sowing

Wei Liu [a,b,c,d,e,f], Zhiyan Zhou [a,b,c,*], Xuelang Xu [a,b,c,d], Qingyu Gu [a,b,c,d], Shuaishuai Zou [a,b,c,d], Weizhuo He [a,b,c,d], Xiwen Luo [a,b,c,d], Junhao Huang [a,b,c,d], Jianqin Lin [a,b,c,d], Rui Jiang [d,1]

[a] *College of Engineering, South China Agricultural University and Guangdong Laboratory for Lingnan Modern Agriculture, Guangzhou 510642, China*
[b] *Guangdong Provincial Key Laboratory of Agricultural Artificial Intelligence (GDKL-AAI), Guangzhou 510642, China*
[c] *Guangdong Engineering Research Center for Agricultural Aviation Application (ERCAAA), Guangzhou 510642, China*
[d] *Key Laboratory of Key Technology on Agricultural Machine and Equipment (South China Agricultural University), Ministry of Education, Guangzhou 510642, China*
[e] *Guangdong Institute of Modern Agricultural Equipment,Guangzhou 510630,China*
[f] *Key Laboratory of Modern Agricultural Intelligent Equipment in South China, Ministry of Agriculture and Rural Affairs, P.R.China,Guangzhou 510630,China*

ARTICLE INFO

Keywords:
Rice seeding
Image recognition
UAV seeding
Rowing performance
Shot seeding

ABSTRACT

In recent years, unmanned aerial vehicle (UAV) has been widely used in the agricultural production. Combined with the promotion of rice direct seeding technology, UAV rice seeding has become an important planting method. In order to quickly obtain the rowing performance on rice sowing, this study proposes an evaluation method based on image recognition technology. In the process of image recognition, a binary method of dynamic threshold based on mean filter difference (BD-MFD) was adopted, and obtained the position coordinates of the seeds. According to the evaluation method, the key structural parameters and operational parameters of the UAV-based shot seeding device are optimized. In the bench test, the size parameters of guide tube were optimized, and the best seeding effect was obtained when the length and diameter of the guide tube were 100 mm and 17 mm, respectively. Experiments were carried out on the seeding effect under different seed discharge rate levels, and the reasonable range of the seed metering wheel rotational speed was 16–24 rpm. In the field seeding test, the appropriate friction wheel rotation speed at different working heights was obtained. In the two-factor comprehensive test of flying speed and seed metering wheel rotational speed, when the flying speed was 1.0–2.0 m/s and the seed metering rotational wheel speed was 22–26 rpm, it has better seeding uniformity. In the five-row seeding experiment, the average width of seed row (B_d) ranged from 66.17 mm to 75.34 mm, and the *C. V.* (coefficient of variation) of seeding uniformity was between 18.44 % and 27.04 %. The study provided a new idea for UAV rice seeding, and optimized the structural parameters and operation parameters through experiments.

1. Introduction

The development of unmanned aerial vehicle (UAV) technology has provided more operating methods for agricultural production (Panagiotis et al., 2020; Rahman et al., 2021). Following the widespread application of spraying UAV, the application scenarios of UAV cover fertilization, seeding, and feed delivery (Ren et al., 2021; Zhu et al., 2021). On the other hand, the rice direct seeding technology is to sow the seeds in the field directly, which can greatly simplify the operation steps (Tao et al., 2016; Zhang et al., 2018; Wang et al., 2020a). Therefore, UAV direct seeding of rice, as an emerging sowing method, has received extensive attention.

With the improvement of UAV technology and rice direct seeding (Farooq et al., 2011; Yang et al., 2015), the application of UAV rice seeding in China was increasing (Song et al., 2018a). UAV seeding was first applied in broadcast sowing (Wan et al., 2021). A pneumatic broadcast sowing device was designed that uses airflow to disperse and blow seeds (Song et al., 2018b). A centrifugal broadcast sowing device was designed, which continuously throws out the contacting seeds through a centrifugal disc (Song et al., 2018c). In addition, a comparative study on the four mainstream broadcast sowing UAV was conducted, and comprehensively evaluated the effect of UAV seeding (Song

---

* Corresponding author at: South China Agricultural University, Guangzhou 510642, China.
E-mail addresses: zyzhou@scau.edu.cn (Z. Zhou), ruiojiang@scau.edu.cn (R. Jiang).

[1] Co-corresponding author.

https://doi.org/10.1016/j.compag.2023.107718
Received 23 August 2022; Received in revised form 14 February 2023; Accepted 16 February 2023

et al., 2020). A centrifugal rice seeding device was designed, and optimized the structural parameters through simulation analysis and orthogonal test (Wu et al., 2020). On the other hand, XAG and DJI were two well-known companies in the field of agricultural UAV, both of which have launched particle spreaders and dominated the Chinese market (Gao et al., 2019; Xiao et al., 2021).

Under the background of the widespread application of UAV broadcast sowing technology, the research on UAV seeding in rows was gradually increasing. Yuren UAV (Zhuhai) Co., ltd. has designed a rice precision seeding drone that can be used for rice seeding in rows. In actual operation, the end of the seed guide tube needs to be within 50 cm of the ground to ensure the good rows effect of seeding. A UAV seeding device for rapeseed was designed, which guides the seeds to the ground through a seed guiding device with a height of 1.5–2.5 m (Huang et al., 2020a; Huang et al., 2020b). In order to reduce the impact of the UAV wind on the accuracy of seed landing, it was necessary to accelerate the seeds or use a conduit to isolate the wind field. In agricultural planting, ground machinery also had devices that accelerate seeds and shoot them into the soil. Li Hongwen’s team from China Agricultural University carried out research on non-contact seeding of wheat. The acceleration methods of wheat seeds involved high-pressure air flow acceleration and rotating centrifugal acceleration (Wang et al., 2020b; Wang et al., 2021).

According to the above research, the existing UAV rice seeding method was mainly broadcast sowing, and the seeds were scattered on the surface. Seedling population distribution was less uniform in broadcast sowing compared to seeding in rows, and the seeds floating on the surface were easily washed away by rainwater and eaten by birds or mice (Feng et al., 2020; Mai et al., 2019). On the other hand, the existing UAV seeding device had the problems of low working height and large structural size, which will reduce the flight safety and operation stability. To overcome the above disadvantages, the authors designed a shot seeding device that uses friction wheels to accelerate the pelleted rice seeds. Different from the ground rice seeding machinery, the rowing performance of UAV seeding was affected by the seeding principle, flight stability and wind field. Therefore, it was important to evaluate the rowing performance of UAV seeding. Based on the development of the shot seeding UAV (Liu et al., 2022), an evaluation method of rowing performance depended on BD-MFD image recognition was applied in bench test, and optimized the structural parameters of the guide tube and the rotation speed of the seed metering wheel. On this basis, field test was carried out to optimize the flying speed, working height, rotation speed of seed metering wheel and friction wheel. Then, according to the test results, the reasons that affect the accuracy of seed landing were discussed and analyzed.

2. Materials and methods

2.1. Evaluation method of rowing performance based on BD-MFD image recognition

The principle of seeding in row performance evaluation method: First, the distribution image of seeds on the ground surface was obtained through the camera and auxiliary equipment. Then, the position coordinates of each seed were obtained through BD-MFD image recognition and processing technology. Finally, the seed coordinates are processed as needed to quantify the row performance. In this study, the evaluation method was divided into two experimental environments: indoor bench test and field aerial seeding test. Combined with the test of shot seeding device in this study, the evaluation method of rowing performance was explained.

2.1.1. Evaluation method of rowing performance in bench test

A bench test device for motion seeding was built (Fig. 1). A slide rail was arranged above the mud tank, and the shot seeding device equipped with the shot seeding module can move linearly along the slide rail. The distance of the seeds from the outlet of the guide tube to the surface of the mud tank was 1.5 m, and the theoretical seed landing point was marked with a line laser. The model of the line laser transmitter was SZ-MT50i (Shantou S&D Business Development Co., ltd, Shantou), the laser wavelength was 650 nm, and the output power was 0.05 W. The movable photo platform was used to assist the photographing of the seed trajectory, so that the imaging plane of the camera was parallel to the plane of the mud tank. During the test, the mobile photo platform was first removed, and then the shot seeding device continued to sow during the movement along the slide rail, which would leave a seed track in the mud trough. The seed trajectory picture was taken in image acquisition section, and the position coordinates of the seeds were calculated based on the BD-MFD image recognition technology (Hou et al., 2022; Zhang et al., 2022).

The test was carried out in an indoor incandescent light, and the original image with a resolution of 2250 × 4000 pixels was collected by mobile phone (Phone model: Smartisan pro 3, camera sensor model: Sony IMX586) as shown in Fig. 2. In order to facilitate the calculation of seed coordinates, a black and white grid calibration plate was placed in the image field of view, and the black grid size of the calibration plate was 40 mm × 40 mm. The actual distance of each pixel in the original

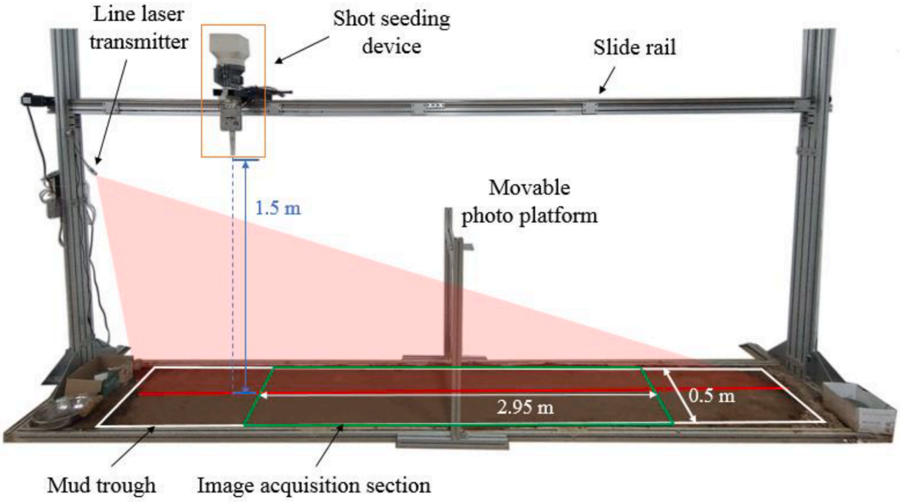

Fig. 1. Bench test device. The red line in the mud trough is the theoretical center line of the seed row marked with the laser line. The green wire frame (2.95 m length) is the uniform motion interval of the shot seeding device, and image acquisition can be performed in this interval. (For interpretation of the references to color in this figure legend, the reader is referred to the web version of this article.)

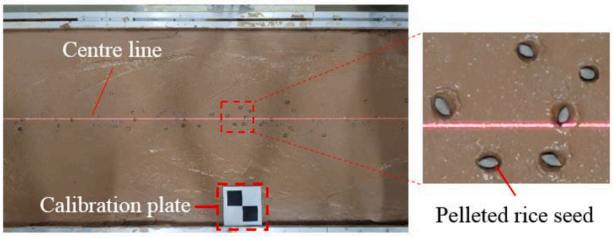

Fig. 2. Seed distribution images captured by move photo platform.

image was calculated with reference to the black grid size of the calibration plate. On the other hand, the center line represented the straight line that would be formed when the seeds land without skewing. The pelleted rice seeds were rugby shaped with a diameter of 4 mm to 5 mm and a length of 9 mm to 10 mm, and the rice variety was Fengtianyou 1999.

Statistics showed that the gray value of the white area of the calibration board was greater than 180, and the gray value of the black area was less than 10. According to this feature and the rectangular shape of the black grid, the outline of the black grid can be extracted. The actual length *c* (mm) of each pixel was calculated according to formula (1) (Luo et al., 2010). The image was divided into three channels R-G-B, and the soil area was grayed and enhanced according to formula (2) (Fig. 3a).

$$c = 40/A \tag{1}$$

$$G_m = 4^*G_r - G_b \tag{2}$$

where, *c* is actual length of a single pixel, mm; *A* is the number of pixels occupied by the black grid border; *Gm* is gray value of the region of interest (ROI); *Gr* is gray value of R-channel image; *Gb* is gray value of B-channel image.

The red laser line was very prominent in Fig. 3a, and its gray value was above 250 according to statistics. The laser line was extracted according to its gray value and length characteristics, and then the vertical line was obtained. The X-Y coordinate system was established based on the laser line and marked by the red line (Fig. 3b).

In the process of seed recognition, a binary method of dynamic threshold based on mean filter difference (BD-MFD) was adopted. First, the image was filtered with a rectangle mask of 50 × 50 pixels (twice the long axis of the seed) (Fig. 4a). Then, the mean value filtered image was subtracted from the ROI of the original enhanced image, so that the darker seeds color could be enhanced, and then the image was binarized based on the dynamic threshold method shown in formula (3) (Yan et al., 2022), seeds were marked by red areas (Fig. 4b). Finally, the pixel coordinates of the center of each seed were obtained, and the position of each seed was completed according to formula (4).

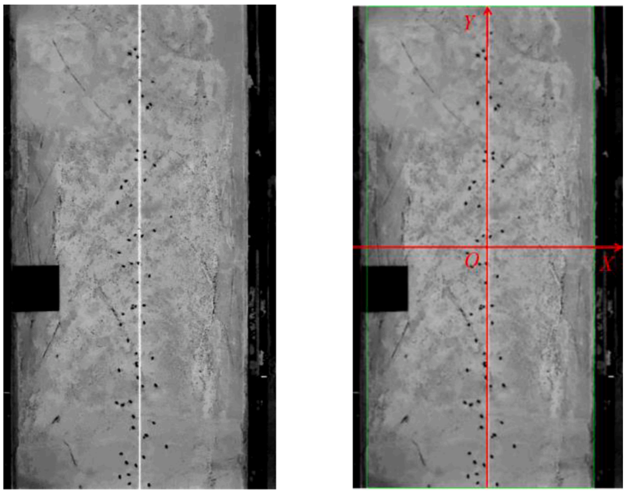

(a) (b)

Fig. 3. Image preprocessing. **(a)** The grayscale and enhanced results of the soil area obtained by the difference between the enhanced red channel and the blue channel. (**b)** The green wireframe is the ROI, and the red line is the coordinate system. (For interpretation of the references to color in this figure legend, the reader is referred to the web version of this article.)

$$\begin{aligned} G_d &= 1, G_{mean} \geq G_m + Offset \\ G_d &= 0, G_{mean} < G_m + Offset \end{aligned} \tag{3}$$

$$\begin{aligned} S_x &= (C_s - C_o)^*c \\ S_y &= (R_s - R_o)^*c \end{aligned} \tag{4}$$

where, *Gd* is gray value of dynamic threshold result; *Gm* is gray value of the ROI; *Gmean* is gray value of the mean value filtered image; *Offset* is dynamic threshold compensation value (Select 50 after testing and comparison); *Sx* is the X-axis coordinate value of the seed, mm; *Sy* is the Y-axis coordinate value of the seed, mm; *Cs* is the X- axis coordinate value of the seed in pixels; *Rs* is the Y- axis coordinate value of the seed in pixels; *Co* is the X-axis coordinate value of the origin in pixels; *Ro* is the Y-axis coordinate value of the origin in pixels; *c* is actual length of a single pixel, mm.

The coordinate data was output as a.txt file, and part of the seed recognition results were shown in Fig. 4c. The relative error of the seed coordinate values in the bench test was calculated by selecting 5 seeds in the image area along the seed row, measuring their X-axis coordinates, and repeating three times. The results were shown in Table 1, and the values of relative error (R_e) was 1.3 % according to formulas (5).

$$R_e = \frac{S_r - S_m}{S_m} \times 100\% \tag{5}$$

where, *Re* is relative error; *Sr* is recognition value; *Sm* is measurement value.

In this study, the seed row effect index was quantified based on the characteristics of seed distribution on the soil surface. The absolute value of the X-axis coordinate of the seed represented the offset distance. Therefore, 2 times the average value of the seed offset distance was defined as average width of seed row (D_X). and the smaller the value of D_X, the better the seed row effect. The percentage of seeds within the width *d* to the total number (W_d) was the qualified rate of seeding in rows, which was used to show the characteristics of seed distribution. The values of D_X and W_d were calculated according to formulas (6) and (7).

$$D_X = \frac{2\sum |X|}{N} \tag{6}$$

$$W_d = \frac{N_d}{N} \times 100\% \tag{7}$$

where, D_X is the average width of seed row, mm; *X* is the seed X-axis coordinate value; W_d is the qualified rate of seeding in rows, %; N_d is the number of seeds with the X coordinate value in the interval (-0.5*d*, 0.5*d*); *N* is the total number of seeds.

2.1.2. Evaluation method of rowing performance in field aerial seeding test

The test was carried out in an outdoor mud field. A smooth sowing area with a length of about 10 m was set up in the field, and the shot seeding UAV sowed the seeds in this area (Fig. 5). The UAV was a self-built test prototype, which was based on DJI A3 flight controller and DJI D-RTK GNSS (Shenzhen DJI Technology Co., ltd.), and its horizontal flight positioning accuracy was within 10 cm. During the test, each group of tests flew once and took pictures of the seed distribution, and the length of the photo collection was 8.0–9.0 m. In order to reduce the difficulty of image acquisition, except for the five-row simultaneous seeding test, only the middle row was opened for each seeding in other tests. After planning the flying route, set the flight and operation parameters through the remote control, and then the automatic flight

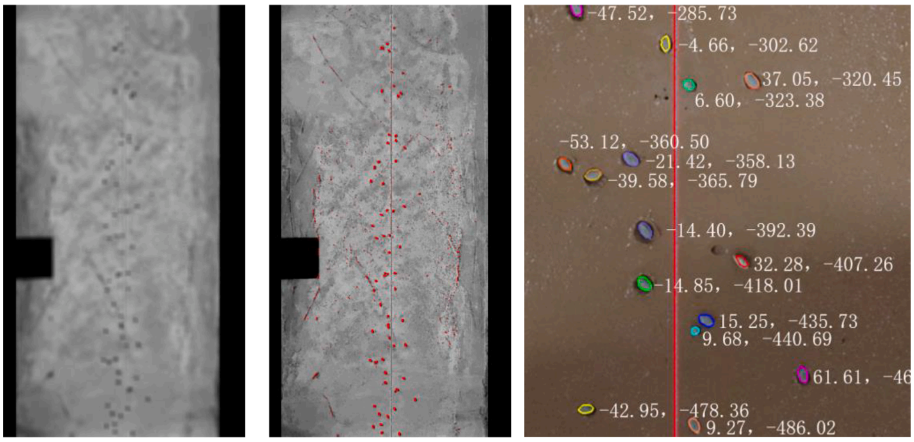

(a) (b) (c)

Fig. 4. Seed identification. **(a)** Image result obtained by mean filter difference. **(b)** Seed recognition result after binarization by formula (3). **(c)** Partial seed coordinates calculated according to formula (4).

Table 1
Recognition value (S_r) and measurement value (S_m) of X-axis of seed in error measurement of bench test.

Repeat	Type	X-axis coordinate value of seeds				
1	S_r	34.3533	−40.4253	24.3326	26.7357	−35.4808
	S_m	33.34	−41.02	24.48	27.04	−34.36
2	S_r	−15.7972	−64.3983	4.05985	54.7581	17.0867
	S_m	−16.02	−61.84	3.88	52.88	16.96
3	S_r	−61.2263	15.5533	−20.1101	21.9914	−57.1975
	S_m	−63.42	14.84	−20.02	21.38	−56.88

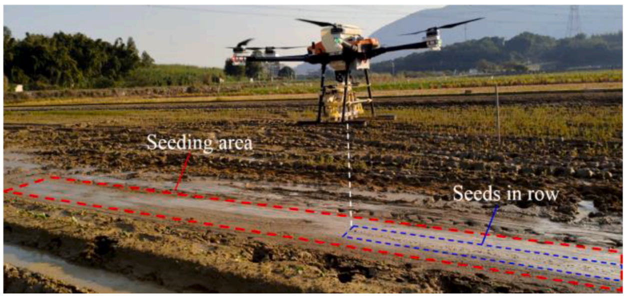

Fig. 5. In the field test,the UAV sowed seeds inside the red dotted box, and the blue dotted box was the track of the seeds that had landed. (For interpretation of the references to color in this figure legend, the reader is referred to the web version of this article.)

operation can be carried out. During the test, clear weather, natural wind speed of 0–2.5 m/s, strong and stable satellite signals and an environment without strong magnetic fields ensure the basic stability of the UAV flight. In this study, the capacity of the seed tank was 20 L, which could carry 12.3 kg rice seeds under full load. In general, each filled seed tank can cover 0.27–0.53 hm^2. In practice, each flight operation is usually loaded with 2.0–3.0 kg of seeds, depending on the battery life.

Since the typical trajectory of the UAV flight was not straight in the field test, it was hard to obtain a projection of the UAV ground flight trajectory. Therefore, the in-situ method of image acquisition and the calculation of the average width of seed row was different from the bench test. In the field test, the string was straightened and placed in the middle of the seeds distributed in rows, as show in Fig. 6. Since this string is used to provide a reference for the position of the sampling frame, it only needs to be placed roughly in the middle of the seed row to ensure that the seeds are inside the sampling frame. When capturing the seed image in the sampling frame, the position of the rectangular sampling frame is moved and photographed frame by frame from the beginning of the seed row. The camera was the same as in bench test and its own horizontal shooting function could ensure the level of the photos.

The sample images and the recognition results of seed position

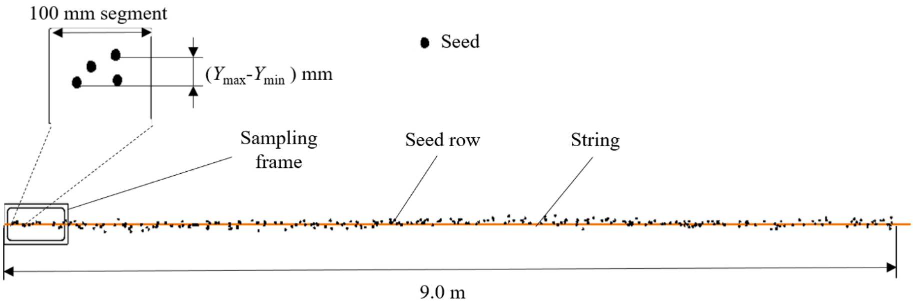

Fig. 6. The image acquisition method and the measurement principle of the average width of segment.

coordinates as show in Fig. 7. The internal size of the sampling frame was 250 mm × 500 mm, and there were rulers on the narrow sides on both sides to locate the position of the sampling frame relative to the string. When calculating the seed distribution coordinates, the sampling frame was used as the reference for seed coordinate conversion, and the coordinate system was established with the centerline of sampling frame. Due to the poor color stability of the image in the field environment, the seeds cannot be identified in some cases. To ensure data integrity, the seed location can be manually selected, so it can be considered that the seed recognition rate was 100 %.

The relative error of the seed coordinate values in the field test was calculated, and the calculation method was the same as that in bench test. The Y-axis coordinates of the seeds reflect the offset distance, so the Y-axis coordinates are measured, and the results were shown in Table 2. The average relative error of seed coordinate recognition was 2.4 %, which can meet the needs of rapid analysis of seed distribution in the experiment.

The calculation method of the average width of seed row (B_d) in field test was different from that in bench test. In the field trial, the seed rows were divided into successive 100 mm segments, and the average of the maximum widths obtained from the measurements of each segment was used as the average width of the seed rows (B_d), as show in Fig. 6. The seed rows were divided into small segments to facilitate the weakening of the effect of the uncertainty of the complete trajectory straightness of the UAV on B_d. According to the technical specification of quality evaluation for aerial broadcast seeder by remote control (NY/T 3881–2021), the coefficient of variation of seeding uniformity ($C.V$) was used as an index to measure the uniformity of seeding. B_d and $C.V$ were calculated according to formulas (8) and (9).

$$B_d = \frac{\sum (Y_{\max} - Y_{\min})}{N_d} \tag{8}$$

$$C.V = \frac{1}{\overline{n}} \sqrt{\frac{1}{N_a - 1} \sum (n_i - \overline{n})} \times 100\% \tag{9}$$

where, B_d is average width of seed row, mm; $C.V$ is variation coefficient of seeding uniformity, %;$Y_{\max}$ is the maximum value of the Y-axis of the seed within the 100 mm segment, mm; $Y_{\min}$ is the minimum value of the Y-axis of the seed within the 100 mm segment, mm; N_d is number of 100 mm segments; n_i is number of seeds in 300 mm segment; $\overline{n}$ is average number of seeds in 300 mm section; N_a is number of 300 mm segments.

2.2. Optimization test scheme of shot seeding device

2.2.1. Bench test on optimization of structural parameters of shot seeding device

The function of the shot seeding module was to accelerate the seeds and was the last part before the seeds leave the machine, which directly affects the accuracy of the seeds' landing positions (Fig. 8). When working, the seeds first enter the vibrating cone, and then the seeds enter the gap between two friction wheels. The cone was equipped with a vibration motor, which can prevent the seeds from blocking in the cone. The vibration motor is a miniature motor with a semicircular eccentric block mounted on the rotating shaft, model XFF-030 (Huizhou Xinli Motor Co., ltd, Huizhou). The friction wheels rotated in the direction of the red arrow, and the seeds were accelerated under the action of friction, and finally shot to the ground through the guide tube. As an important part for correcting the direction of seed ejection, the guide tube was necessary to carry out parameter optimization experiments on its diameter and length. On the other hand, the seed discharge rate that the shot seeding module can withstand has a maximum value, and it was necessary to determine the optimal discharge rate range to provide a reference for field experiments.

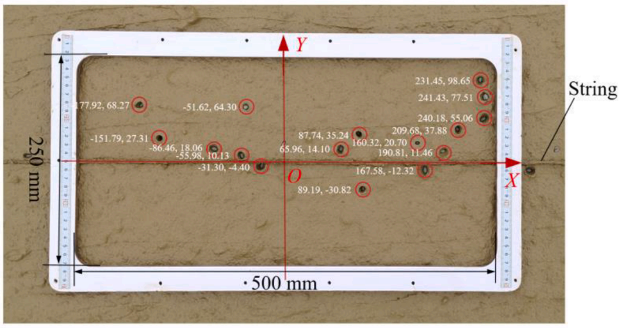

Fig. 7. The sample images and the recognition results of seed position coordinates.

Three groups of tests were set up in this study, namely the guide tube length test (A), the guide tube diameter test (B) and the seed discharge rate test (C). The seed discharge rate was controlled by the rotation speed of the seed metering wheel (RSS), and the number of seeds discharged per second under different *RSS* levels was obtained (Fig. 9).

The levels arrangement of each factor was shown in Table 3. In test A, the R_{SS} and the guide tube diameter were 20 rpm and 16 mm, respectively; In test B, the R_S and the guide tube length were 20 rpm and 100 mm, respectively; In test C, the guide tube length and diameter were 100 mm and 16 mm, respectively.

2.2.2. Field test on optimization of operating parameters of shot seeding UAV

On the basis of the bench test, in order to obtain the optimal operating parameters of the shot seeding UAV and the effect of field aerial sowing, a field flying seeding test was carried out. In this paper, a comprehensive test of working height and rotation speed of friction wheel (R_{SF}), a comprehensive test of flying speed and rotation speed of seed metering wheel (R_{SS}), and a five-row simultaneous seeding test were carried out. Taking the average width of seed row and the coefficient of variation of sowing uniformity as the index to measure the seeding effect.

At different working heights, the shooting speed of seeds will affect the accuracy of the seeds landing. Theoretically, the higher the shooting speed, the less the seeds were affected by the UAV wind, but the higher shooting speed will increase the wear of the friction wheel and the energy consumption. In this test, a comprehensive test was carried out with the working height and the RSF (Table 4). During the test, the flying speed of the UAV was 1.2 m/s, and the rotation speed of seed metering wheel (RSS) was 20 rpm.

The uniformity of sowing was determined by the stability of flying speed and the RSS. In this test, a comprehensive test was carried out with the flying speed and the *RSS* (Table 5). During the test, the working height of the UAV was 1.0 m, and the RSF was 7000 rpm.

In order to verify the consistency of the sowing effect of each row, the seeding test was carried out by the method of simultaneous sowing in five rows. In the test, the working height was 1.5 m, the RSS was 18 rpm, the flying speed was 1.3 m/s, and the RSF was 8000 rpm. The test site, image collection and processing methods were the same as the previous test, and the data acquisition length was 6.0 m.

3. Results

3.1. Influence of guide tube parameters and R_{SS} on average width of seed row

According to the seed coordinate value, calculate the average width of seed row (D_X) and the qualified rate of seeding in rows (W_d) within the range of width d, where d takes three levels of 80 mm, 90 mm and 100 mm (Fig. 10). According to the analysis of variance, it could be seen that the length of the guide tube (L), the diameter of the guide tube (D) and the rotation speed of the seeding wheel (R_{SS}) have a very significant

Table 2
Recognition value (S_r) and measurement value (S_m) of Y-axis of seed in error measurement of field test.

Repeat	Type	Y-axis coordinate value of seeds				
1	S_r	−31.669	33.4232	−17.8903	−45.4476	9.66692
	S_m	−31.14	32.32	−16.88	−46.28	8.72
2	S_r	−33.0989	−17.0807	36.1565	26.734	−44.877
	S_m	−32.92	−16.56	36.82	26.36	−44.54
3	S_r	27.189	76.8683	−13.0276	−43.7815	−19.6515
	S_m	27.04	73.82	−13.28	−41.16	−19.02

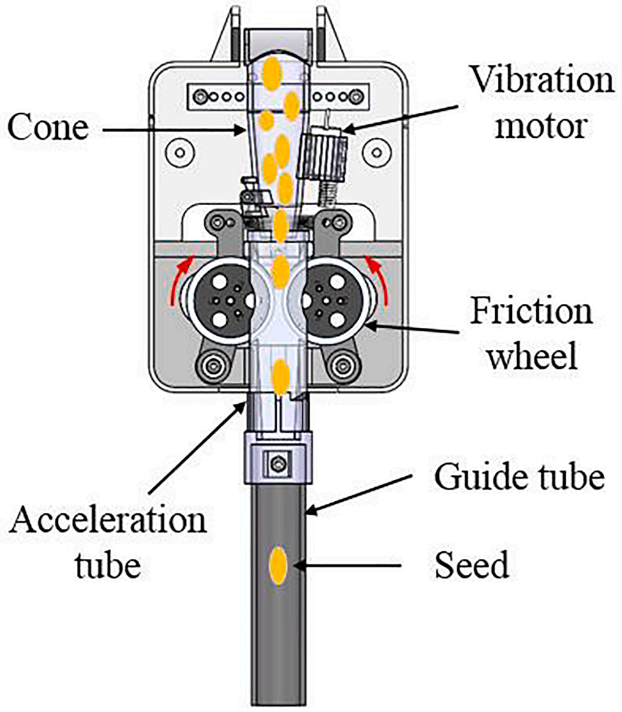

Fig. 8. The structure and working principle of the shot seeding module. The yellow oval is the pelleted rice seed, and the red arrow is the rotation direction of the friction wheel. (For interpretation of the references to color in this figure legend, the reader is referred to the web version of this article.)

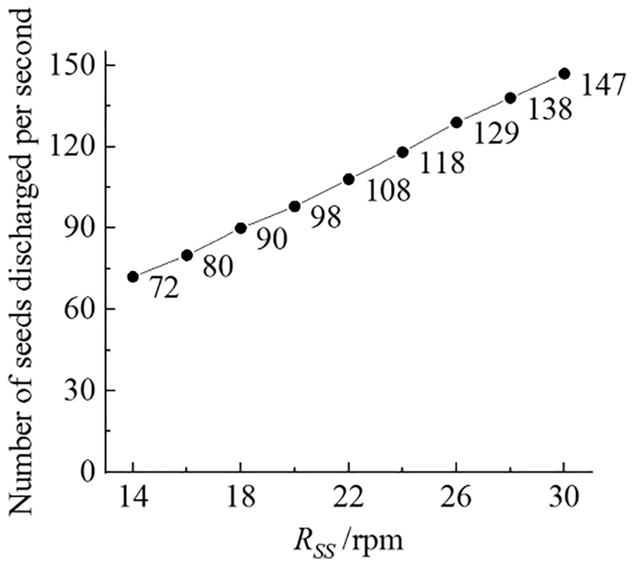

Fig. 9. Number of seeds per second at different rotation speeds of the seed metering wheel.

effect on the row effect of seeding.

From the results of the guide tube length test (Fig. 10a and Fig. 10d), it can be seen that with the increase of the guide tube length, D_X shows a gradually decreasing trend, and W_d shows a gradually increasing trend. The test results showed that with the increase of the length of the guide tube, the effect of seeding in rows was better. In this study, due to the limitation of equipment space, the maximum length of the guide tube can only be set to 100 mm.

According to the results of the guide tube diameter test (Fig. 10b and Fig. 10e), when the guide tube diameter $D = 12$ mm, 13 mm, and 14 mm, the D_X value was between 53.76 mm and 54.78 mm; When the guide tube diameter $D > 14$ mm, the D_X value showed obvious downtrend and get minimum value at $D = 17$ mm. According to the variation curve of the seeding qualification rate W_d, it could be seen that within the guide tube diameter $D = 12$–15 mm, the seeding qualification rate W_d was stable; when the guide tube diameter $D > 15$ mm, the seeding qualification rate W_d gradually increases and then slows down. The W_d reached a maximum value at $D = 17$ mm. Considering the changing trends of D_X and W_d, when the guide tube diameter $D = 17$ mm, the shot seeding module had a better seeding effect.

From the results of the $\boldsymbol{R_{SS}}$ test (Fig. 10c and Fig. 10f), it could be seen that the D_X ranges from 47.15 mm to 56.57 mm, and it increases with the increase of the R_{SS}. According to the change curve of W_d, when the seed row width $d = 80$–100 mm, the W_d was between 76.94 % and 89.90 %, and with the increase of R_{SS}, the W_d gradually decreases. In this study, lower R_{SS} decreased seeding efficiency, while higher R_{SS} increased the risk of seed blockage. Based on the above analysis, it was recommended to set the rotation speed of the seed metering wheel (R_{SS}) within the range of 18–24 rpm.

3.2. *Influence of seeding parameters and flying parameters on seeding effects in field*

According to the field test results, 3D surface graphs of the influence of the working height and the rotation speed of the friction wheel (R_{SF}) on the index were drawn (Fig. 11). According to the standard NY/T 3881–2021, the coefficient of variation of seeding uniformity ($C.V$) should be less than 45 %, and the test results of each group meet the requirements. When the R_{SF} was 6000 rpm to 8000 rpm, the $C.V$ had smaller values when the working height was 0.5–1.5 m, and had larger values when the working height was 1.5–2.0 m. When the R_{SF} was 8000 rpm to 12000 rpm, the $C.V$ had larger values when the working height was 0.5–1.5 m, and had smaller values when the working height was 1.5–2.0 m.

According to the influence of the working height and the RSF on the average width of the seed row (B_d) in the figure, the B_d ranged from 27 mm to 123 mm. According to the surface change trend of the B_d, it could be seen that the B_d was mainly affected by the working height, and the B_d increased with the increase of the working height. When the working height was 2.0 m and the *RSF* was 6000 rpm, the B_d was 122.32 mm; when the working height was greater than 1.0 m, the B_d could be reduced by appropriately increasing the *RSF* as the working height increases.

Based on the above analysis of the $C.V$ and the B_d, and according to the requirement of selecting the smaller value of the R_{SF}, the

Table 3
Levels arrangement in each factor experiment.

Project	Factors	Levels								
A	Guide tube length /mm		0		50		100		150	
B	Guide tube diameter/mm	12	13	14	15	16	17	18	19	20
C	Rotation speeds of the seed metering wheel /rpm	14	16	18	20	22	24	26	28	30

Table 4
Working levels of R_{SF} and working height in comprehensive test.

Factors	Levels						
R_{SF} /rpm	6000	7000	8000	9000	10,000	11,000	12,000
Working height /m	0.5		1		1.5		2

Table 5
Working levels of flying speed and R_{SS} in comprehensive test.

Factors	Levels					
R_{SS} /rpm	16	18	20	22	24	26
Flying speed/m·s^{-1}	1.0	1.5		2.0	2.5	3

recommended R_{SF} within the range of different working heights was given, as shown in Table 6.

According to the comprehensive test results of the flying speed and the rotation speed of the seed metering wheel (R_{SS}), 3D surface graphs of the influence on the index under different combinations of flying speed and R_{SS} were drawn (Fig. 12). According to the 3D surface graph of the effect of flying speed and R_{SS} on $C.V$, the $C.V$ in each group of

Table 6
Recommended R_{SF} values at different working heights.

Height of working/m	friction wheel rotation speed/rpm
0.5–1.0	6000–7000
1.0–1.5	7000–8000
1.5–2.0	8000–9000

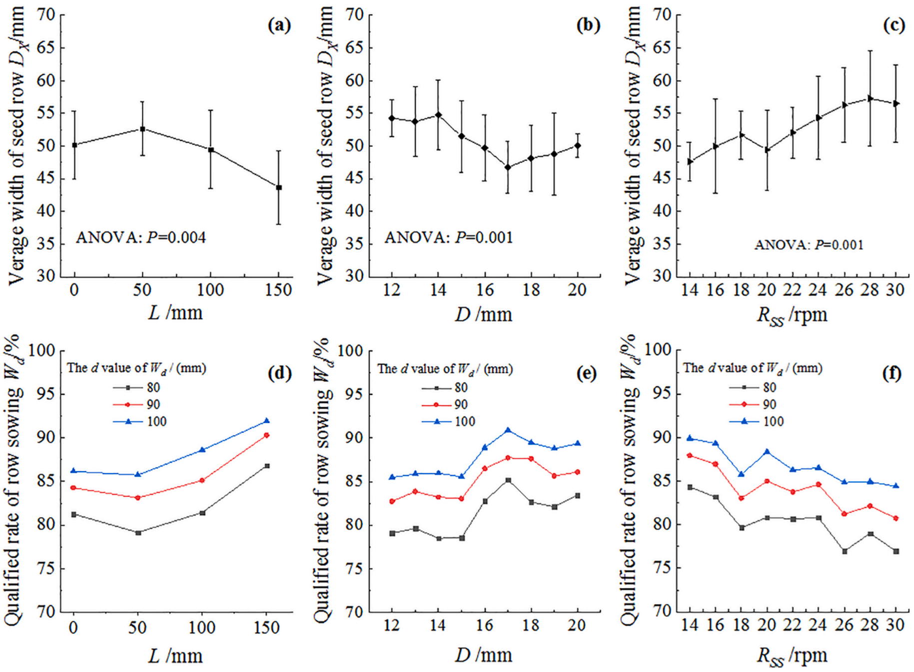

Fig. 10. The bench test results.**(a)~(c)** are the variation curves of the D_X in the experiments with different factors. **(d)~(f)** are the variation curves of the W_d in the experiments with different factors.

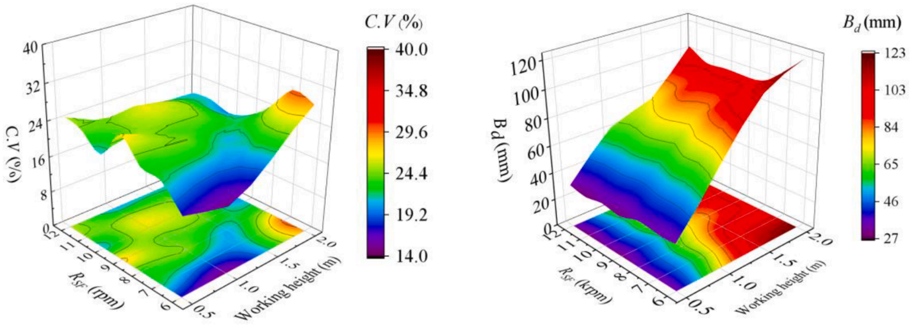

Fig. 11. Effects of working height and R_{SF} on the coefficient of variation of seeding uniformity ($C.V$) and the average width of the seed row (B_d).

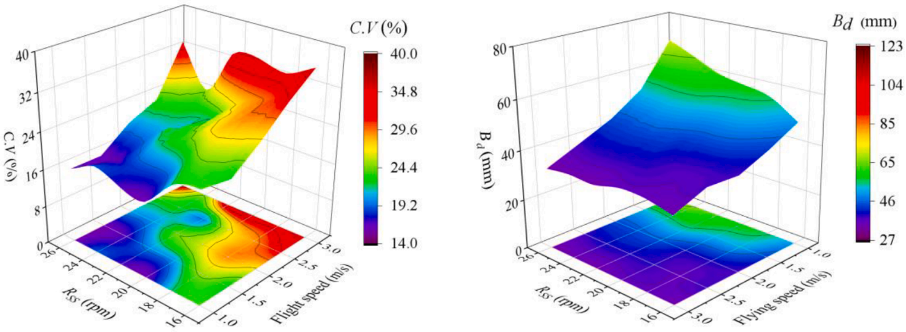

Fig. 12. Effect of flying speed and R_{SS} on the coefficient of variation of seeding uniformity ($C.V$) and the average width of the seed row (B_d).

experiments was less than 45 %, which met the requirements of the standard NY/T 3881–2021. When the flying speed was 2.0–3.0 mm/s and the R_{SS} was 16–20 rpm, the $C.V$ had larger values; when the flying speed was 1.0–2.0 mm/s, the R_{SS} was 22–26 rpm, the $C.V$ had smaller values. The $C.V$ decreased gradually with the increase of the R_{SS} and the decrease of the flying speed.

According to the results of the effect of the flying speed and the R_{SS} on B_d, the range of the B_d was 32–71 mm. When the flying speed was 1.0 m/s, the B_d was greater than 49 mm at all levels of the R_{SS}. With the increase of flying speed, the B_d decreased gradually; on the other hand, with the increase of the R_{SS}, the B_d decreased slowly.

According to the above analysis, when paying attention to the uniformity of seeding, the flying speed below 2.5 m/s was preferred. When focusing on seed row width, lower R_{SS} and higher-flying speed could reduce the B_d.

Through the five-row simultaneous seeding test, the consistency of the seeding effect of each row was verified. When the seeding row spacing was 30 cm, the seeds were clearly divided between the rows (Fig. 13). The distance between the two dotted lines in the seed row in scatter diagram was 100 mm, and it could be seen that most of the seeds were within the 100 mm width (Fig. 14).

The B_d and the $C.V$ for each row of seeds were calculate (Table 7). At the working height of 1.3 m, the average width of the seed row was between 66.17 and 75.34 mm. According to the test results of the working height and the R_{SF}, when the R_{SF} was 8000 rpm and the working height was between 1.0 and 1.5 m, the B_d should be in the range of 65–96 mm, indicating that the test results were in line with the theory value. The minimum value of the $C.V$ was 18.44 % in the fourth row; the maximum value of the $C.V$ was 27.04 % in the third row. All $C.V$ values were below 45 %, which meet the uniformity requirements of rice seeding.

Fig. 13. Shot seeding effect with five rows.

4. Discussion

4.1. Analysis on the influencing factors of guide tube and rotation speed of the seed metering wheel

In the study of UAV rice seeding in rows, the requirement for the width of the seed row was less than 8.0 cm (Diao et al., 2020). According to the results of the bench test, within the width of 8.0 cm, the qualified rate of seeding was 75 %-85 %. In this study, the shape of the seed was not spherical and the surface was rough. Combined with the principle of seed acceleration, the direction of the seed will be random within a certain range. Based on the bench test results, the following two aspects were discussed:

(1) The influence of the guide tube on the accuracy of seed landing

The results of test A proved that the effect of the guide tube was positive, and increasing the length of the guide tube was obvious to improve the seeding effect. Comparing the D_X values of the two groups of tests A and B, the D_X values of $D \leq 15$ mm were greater than the D_X value of $L = 0$ mm, it means that when the diameter of the guide tube was less than 15 mm, the seed row effect will be worse. In the same way, it could be concluded that when the D was in the range of 16 mm-19 mm, the guide tube could improve the seed row effect; when the D was 20 mm, it could be considered that the guide tube had lost its corrective effect on the direction of the seed movement. The reason for the above phenomenon was that under the condition of a certain length of the guide tube, if the diameter of the guide tube was too small, the movement space of the seeds will be insufficient, which will increase the probability of collision between the seeds and the inner wall of the guide tube, and between the seeds and the seeds.

(2) The influence of R_{SS} on the accuracy of seeding

According to the results of test C, when the range of R_{SS} was 14 rpm-26 rpm, the D_X showed a gradual upward trend, which could be analyzed from two aspects. First, the increase of the R_{SS} will increase the probability of the seeds colliding in the guide tube, so that the D_X value will gradually increase. On the other hand, an increase in R_{SS} would make more seeds unable to accelerate sufficiently, and the speed difference between seeds would cause collisions between seeds. When the R_{SS} was greater than 26 rpm, the D_X value showed a maximum value and tended to be stable. The reason why D_X tends to be stable could be

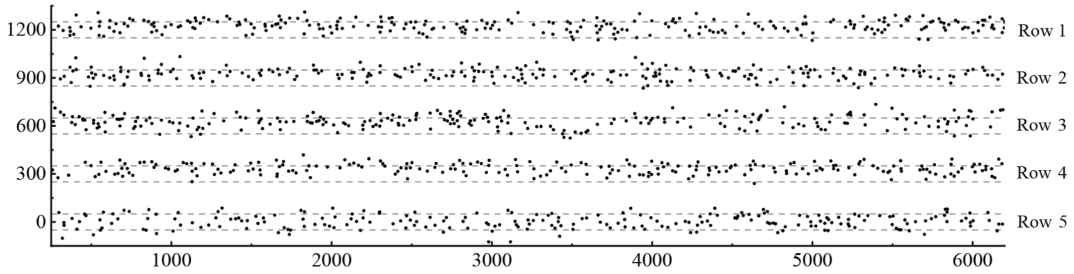

Fig. 14. Scatter diagram of seed distribution with five rows.

Table 7
Test result of shot seeding with five rows.

Result	Rows				
	1	2	3	4	5
B_d /mm	74.63	67.35	75.34	66.17	74.48
$C.V$ /%	24.39	20.25	27.04	20.67	18.44

explained that with the increase of the R_{SS}, the pulsating effect of seed discharging rate was weakened, which made the seed flow into the friction wheel gap tend to be stable, and accordingly the collision probability of the seeds in the guide tube was stabilized.

4.2. Analysis on the influencing factors of seeding parameters and flying parameters

Theoretically, the seeding uniformity was mainly determined by the stability of flying speed and RSS. According to the results of field test that the lower flying speed and the larger *RSS*, the better the seeding uniformity. The external groove wheel seed metering device was used in this study, and related research showed that with the increase of the seed discharging rate, the better the seeding uniformity was, which was consistent with the conclusion of this test (Wang et al., 2004; Yang et al., 2020). The research on UAV seeding of felt seeds shows that within the flying speed range of 1.0–2.0 m/s, the higher the flying speed, the worse the seeding uniformity, which was consistent with this study (Zhang, 2019). In the comprehensive test of working height and RSF, the $C.V$ showed the maximum value under the condition of 2.0 m working height and 6000 rpm *RSF*, this was because the reduction of seed landing accuracy reduces the seeding uniformity.

According to the results of the field test, the average width of the seed row (B_d) was mainly affected by the working height, flying speed and RSS. With the increased of working height, the B_d value increased, indicating that the seed row effect was worse. In other words, when the angle of seed emission was fixed, the higher the seeds were from the ground, the greater the deviation of the seed landing position. With the increase of flight speed, the effect of seeding in rows becomes better. The reasons for this change trend was: At high flying speeds, the density of seeds falling to the ground was low. At the same time, the calculation method of the B_d in this study will reduce when the number of seeds decreases in the 100 mm length segment. Compared with the working height and flying speed, the *RSS* has little effect on B_d, which was consistent with the effect of the *RSS* on the accuracy of seeding in the bench test.

5. Conclusion

In this study, the Pelleted rice seeds were accelerated by a pair of friction wheels, so that the UAV can seed the rice in rows. Through bench test and field test, the key factors affecting the seeding effect were studied, and the structural parameters and operating parameters of the seeding device were optimized. The conclusions of this paper mainly include the following aspects:

(1) In the guide tube length test, it was proved that the guide tube has an effect on improving the accuracy of seed landing, and with the increased of the length of the guide tube, the seed row effect was better. In this study, the length of the guide tube was 100 mm due to the limitation of the installation space of the parts.
(2) In the guide tube diameter test, it was proved that the diameter of the guide tube has an optimal value under a certain length. When the diameter of the guide tube was too small, the collision probability of the seeds in the guide tube was increased, and the seed row effect will become worse. Under the experimental conditions of this study, the optimal guide tube diameter was 17 mm.
(3) In the test of the rotation speed of the seed metering wheel (R_{SS}), it was proved that the increase of the seed discharging rate will reduce the seed row effect. In this study, the maximum R_{SS} value that the shot seeding device can withstand was 30 rpm, and the recommended range of R_{SS} was 18–24 rpm.
(4) In the field test, the working height had the most obvious effect on the seed row effect, and the lower the working height, the better the seed row effect. In addition, at different working heights, the appropriate friction wheel rotation speed was optimized.
(5) In the field test, the main factors affecting the seeding uniformity were the flying speed and the R_{SS}, and the two control the seeding density together. The higher the seeding density, the better the seeding uniformity.

Through BD-MFD image recognition and processing technology, this research provided a method to quickly evaluate the rice seeding effect of UAV, and optimized the shot seeding device. However, in the field experiment, the seed recognition rate was affected by such factors as soil color, environmental light and soil hardness, which requires manual selection of unrecognized seeds, and increasing the workload. In addition, how to reduce the impact of UAV flight stability on seeding effect requires more in-depth research, and the straightness of seed row was also a very important seeding indicator, and no relevant measurement was involved in this study. The above issues should be further studied in future.

CRediT authorship contribution statement

Wei Liu: Conceptualization, Methodology, Validation, Formal analysis, Writing – original draft. **Zhiyan Zhou:** Conceptualization, Funding acquisition, Resources, Supervision, Writing – review & editing. **Xuelang Xu:** Visualization, Investigation. **Qingyu Gu:** Resources, Investigation. **Shuaishuai Zou:** Software, Validation. **Weizhuo He:** Software, Data curation. **Xiwen Luo:** Supervision, Project administration. **Junhao Huang:** Data curation, Methodology. **Jianqin Lin:** Data curation, Validation. **Rui Jiang:** Conceptualization, Supervision, Writing – review & editing.

Declaration of Competing Interest

The authors declare that they have no known competing financial interests or personal relationships that could have appeared to influence the work reported in this paper.

Data availability

Data will be made available on request.

Acknowledgments

This research was funded by the Laboratory of Lingnan Modern Agriculture Project (Grant No.NT2021009); the Project of key R & D program of Guangzhou of China (Grant No. 202206010149); in part by Jiangxi Provincial Science and Technology Special Project of Jinggangshan Agricultural High-tech Zone (Grant No.20222-051252), Science and Technology Plan of Jian City of China (Grant No. 20211-055316 and [2020]83), Rural Revitalization Strategy in Guangdong Province (2020KJ261) and Science and Technology Plan of Guangdong Province of China (2021B1212040009). We also thank the anonymous reviewers for their critical comments and suggestions for improving the manuscript.

References

Diao, Y., Zhu, C., Ren, D., Yu, J., Luo, X., Ou, Y., Zheng, J., Li, X., 2020. Key Points and Prospect of Rice Direct Seeding Technology by Unmanned Aerial Vehicle. China Rice 26 (5), 22–25. https://doi.org/10.3969/j.issn.1006-8082.2020.05.005.

Farooq, M., Siddique, K.H.M., Rehman, H., Aziz, T., Lee, D., Wahid, A., 2011. Rice direct seeding: Experiences, challenges and opportunities. Soil Tillage Res. 111 (2), 87–98. https://doi.org/10.1016/j.still.2010.10.008.

Feng, Y., Wang, Q., Zhao, H., Song, Q., Sun, Y., Ceng, X., 2020. Research Status and Prospect of the Direct Seeding Technology of Rice in China. China Rice 26 (01), 23–27. https://doi.org/10.3969/j.issn.1006-8082.2020.01.005.

Gao, Z., Peng, X., Lin, G., Zhang, Q., Lu, S., Ou, Y., 2019. Application of broadcast sowing by unmanned aerial vehicle in agriculture: a review. Jiangsu Agric. Sci. 47 (06), 24–30. https://doi.org/10.15889/j.issn.1002-1302.2019.06.006.

Hou, Z., Zhang, X., Chen, Z., Dai, N., Ma, X., Liu, M., 2022. Design and Experiment of Identification and Detection System for Pelleted Coated Seeds. Trans. Chin. Soc. Agric. Mach. 53 (06), 62–69. https://doi.org/10.6041/j.issn.1000-1298.2022.06.006.

Huang, X., Zhang, S., Luo, C., Li, W., Liao, Y., 2020a. Design and Experimentation of an Aerial Seeding System for Rapeseed Based on an Air-Assisted Centralized Metering Device and a Multi-Rotor Crop Protection UAV. Appl Sci-basel 10 (24). https://doi.org/10.3390/app10248854.

Huang, X., Xu, H., Zhang, S., Li, W., Luo, C., Deng, Y., 2020b. Design and experiment of a device for rapeseed strip aerial seeding. Trans. Chin. Soc. Agric. Eng. 36 (5), 78–87. https://doi.org/10.11975/j.issn.1002-6819.2020.05.009.

Liu, W., Zou, S., Xu, X., Gu, Q., He, W., Huang, J., Huang, J., Lyu, Z., Lin, J., Zhou, Z., Jiang, R., Luo, X., 2022. Development of UAV-based shot seeding device for rice planting. Int. J. Agric. Biol. Eng 15 (6), 1–7. https://doi.org/10.25165/j.ijabe.20221506.7301.

Luo, Z., Xue, L., Sun, F., Lu, S., Li, Z., 2010. Camera Calibration Based on HALCON. Video Eng. 34 (04), 100–102. https://doi.org/10.16280/j.videoe.2010.04.008.

Mai, W., Ablez, B., Zhang, B., Ceng, F., Tian, Z., 2019. Rice Yield Under Different Cultivation Patterns. Chin. Agric. Sci. Bull. 35 (36), 1–5.

Panagiotis, R., Panagiotis, S., Thomas, L., Ioannis, M., 2020. A compilation of UAV applications for precision agriculture. Comput. Netw. 172 https://doi.org/10.1016/j.comnet.2020.107148.

Rahman, M.F.F., Fan, S., Zhang, Y., Chen, L., 2021. A Comparative Study on Application of Unmanned Aerial Vehicle Systems in Agriculture. Agriculture (Basel. Switz.) 11 (1). https://doi.org/10.3390/agriculture11010022.

Ren, W., Wu, Z., Li, M., Lei, X., Zhu, S., Chen, Y., 2021. Design and Experiment of UAV Fertilization Spreader System for Rice. Trans. Chin. Soc. Agric. Mach. 52 (03), 88–98. https://doi.org/10.6041/j.issn.1000-1298.2021.03.009.

Song, C., Zhou, Z., Luo, X., Lan, Y., He, X., Ming, R., Hassan, G.S., 2018a. Design and test of centrifugal disc type sowing device for unmanned helicopter. Int. J. Agric. Biol. Eng. 11 (2), 55–61. https://doi.org/10.25165/j.ijabe.20181102.3757.

Song, C., Zhou, Z., Jiang, R., Luo, X., He, X., Ming, R., 2018b. Design and parameter optimization of pneumatic rice sowing device for unmanned aerial vehicle. Trans. Chin. Soc. Agric. Eng. 34 (06), 80–88. https://doi.org/10.11975/j.issn.1002-6819.2018.06.010.

Song, C., Zhou, Z., Luo, X., Jiang, R., Lan, Y., Zhang, H., 2018c. Review of Agricultural Materials Broadcasting Application on Unmanned Helicopter. J. Agric. Mech. Res. 40 (09), 1–9. https://doi.org/10.13427/j.cnki.njyi.2018.09.001.

Song, C., Zang, Y., Zhou, Z., Luo, X., Zhao, L., Ming, R., Zi, L., Zang, Y., 2020. Test and Comprehensive Evaluation for the Performance of UAV-Based Fertilizer Spreaders. IEEE Access 8, 202153–202163. https://doi.org/10.1109/ACCESS.2020.3034593.

Tao, Y., Chen, Q., Peng, S., Wang, W., Nie, L., 2016. Lower global warming potential and higher yield of wet direct-seeded rice in Central China. Agron. Sustain. Dev. 36 (24) https://doi.org/10.1007/s13593-016-0361-2.

Wan, J., Qi, L., Zhang, H., Lu, Z., Zhou, J., 2021. Research status and development trend of UAV broadcast sowing technology in China. In ASABE 2021 Annual International Meeting. Michigan.

Wang, Y., Guo, J., Nie, Y., Dong, Y., 2004. Detecting and Analyzing on Performance of External Force Feed. J. Shanxi Agric. Univ. Nat. Sci. Ed. 03, 256–258. https://doi.org/10.13842/j.cnki.issn1671-8151.2004.03.017.

Wang, X., He, Q., Ma, H., Li, H., Yin, Y., 2020a. Key Points and Prospects of Rice Precision Dry Direct Seeding Technique. China Rice 26 (05), 26–29. https://doi.org/10.3969/j.issn.1006-8082.2020.05.006.

Wang, Y., Li, H., Hu, H., He, J., Wang, Q., Lu, C., Liu, P., He, D., Lin, X., 2021. DEM-CFD coupling simulation and optimization of a self-suction wheat shooting device. Powder Technol 393, 494–509. https://doi.org/10.1016/j.powtec.2021.08.013.

Wang, C., Lu, C., Li, H., He, J., Wang, Q., Cheng, X., 2020b. Preliminary bench experiment study on working parameters of pneumatic seeding mechanism for wheat in rice-wheat rotation areas. Int. J. Agric. Biol. Eng. 13 (1), 66–72. https://doi.org/10.25165/j.ijabe.20201301.4906.

Wu, Z., Li, M., Lei, X., Wu, Z., Jiang, C., Zhou, L., Ma, R., Chen, Y., 2020. Simulation and parameter optimisation of a centrifugal rice seeding spreader for a UAV. Biosyst. Eng. 192, 275–293. https://doi.org/10.1016/j.biosystemseng.2020.02.004.

Xiao, H., Li, Y., Yuan, L., Zhang, Z., 2021. Application and Prospect of China Agricultural Unmanned Aerial Vehicle in Rice Production. Guangdong Agric. Sci. 48 (08), 139–147. https://doi.org/10.16768/j.issn.1004-874X.2021.08.017.

Yan, N., Zhang, H., Dong, H., Kang, K., Luo, B., 2022. Wheat variety recognition method based on same position segmentation of transmitted light and reflected light images. Acta Agric. Zhejiangensis 34 (03), 590–598. https://doi.org/10.3969/j.issn.1004-1524.2022.03.20.

Yang, W., Kim, J., Lee, M., Chen, S., Han, H., 2015. Status and Prospect on Rice Direct Seeding Technology of Farmers. Korean J. Int. Agric. 27 (3), 342–347. https://doi.org/10.12719/KSIA.2015.27.3.342.

Yang, Z., Zhang, Y., Wang, H., Yi, S., Guo, S., Ma, Y., 2020. Experimental Study on Seeding Performance of the Millet Drill Seed-metering Device. J. Agric. Mech. Res. 42 (07), 197–202. https://doi.org/10.13427/j.cnki.njyi.2020.07.032.

Zhang, H., 2019. Study on Sowing Device of Mao ye peas Based on Unmanned Aerial Vehicle Carrier. Tarim university, Xinjiang. 30–31. https://doi.org/10.27708/d.cnki.gtlmd.2019.000027.

Zhang, M., Wang, Z., Luo, X., Zang, Y., Yang, W., Xing, H., Wang, B., Dai, Y., 2018. Review of precision rice hill-drop drilling technology and machine for paddy. Int. J. Agric. Biol. Eng. 11 (3), 1–11. https://doi.org/10.25165/j.ijabe.20181103.4249.

Zhang, H., Yan, N., Wu, X., Wang, C., Luo, B., 2022. Design and Experiment of Online Maize Single Seed Detection and Sorting Device. Trans. Chin. Soc. Agric. Mach. 53 (06), 159–166. https://doi.org/10.6041/j.issn.1000-1298.2022.06.016.

Zhu, H., Ma, Z., Xu, D., Ling, Y., Wei, H., Gao, H., Xing, Z., Hu, Q., Zhang, H., 2021. Discussion and Expectation of “Unmanned”Cultivation Technology System for Rice with High Quality and Yield Suitable for UAV Seeding. China Rice 27 (05), 5–11. https://doi.org/10.3969/j.issn.1006-8082.2021.05.002.

Development of UAV-based shot seeding device for rice planting

Wei Liu[1,2,3,4], Shuaishuai Zou[1,2,3,4], Xuelang Xu[1,2,3,4], Qingyu Gu[1,2,3,4], Weizhuo He[1,2,3,4],
Jun Huang[1,2,3,4], Junhao Huang[1,2,3,4], Zichen Lyu[1,2,3,4], Jianqin Lin[1,2,3,4], Zhiyan Zhou[1,2,3*],
Rui Jiang[4*], Xiwen Luo[1,2,3,4]

(1. *College of Engineering, South China Agricultural University and Guangdong Laboratory for Lingnan Modern Agriculture, Guangzhou 510642, China*;
2. *Guangdong Provincial Key Laboratory of Agricultural Artificial Intelligence* (*GDKL-AAI*), *Guangzhou 510642, China*;
3. *Guangdong Engineering Research Center for Agricultural Aviation Application (ERCAAA), Guangzhou 510642, China;*
4. *Key Laboratory of Key Technology on Agricultural Machine and Equipment* (*South China Agricultural University*),
Ministry of Education, Guangzhou 510642, China)

Abstract: In order to realize the high-quality row seeding operation with unmanned aerial vehicle (UAV) in paddy field, a shot seeding device that can sow five rows of pelleted rice seeds at the same time was designed. The shot seeding device mainly consists of an external grooved wheel seed metering device and five shot seeding modules. The designed external grooved wheel seed metering device can take the seeds out of the seed box and divide the seeds into five parts. The shot seeding module can accelerate the pelleted rice seeds to reduce the impact of the UAV wind on the direction of seed movement. Furthermore, an angle adjustment mechanism for the shot seeding module was used to change the row spacing. The seed metering device test verified that when the speed of the seed metering wheel was 15 r/min, the coefficient of variation of the discharge rate of each row ($C.V_1$) and total seed discharge rate stability ($C.V_2$) were 1.70% and 1.04%, respectively. Image processing technique was used to test the UAV seeding performance. The distribution characteristics of seeds on the ground showed that the number of seeds in each row gradually increased from both sides to the middle in the width direction. According to the statistics, there were 60%-70% of the seeds in each row in the 100 mm width range. The field test showed that when the working height was 1.5 m and the seeding quantity was 38.56 kg/hm^2, the performance of sowing in rows was obvious, the deviation rate of seeding quantity was 1.89%. After 16 d of sowing, the seeds' emergence rate was stable, and the average emergence rate was 82.63% and the yield was 6775.50 kg/hm^2.

Keywords: unmanned aerial vehicle, rice direct seeding, row seeding, pelleted rice seeds
DOI: 10.25165/j.ijabe.20221506.7301

Citation: Liu W, Zou S S, Xu X L, Gu Q Y, He W Z, Huang J, et al. Development of UAV-based shot seeding device for rice planting. Int J Agric & Biol Eng, 2022; 15(6): 1–7.

1 Introduction

As an effortless and convenient seeding method, rice direct seeding has received extensive attention in recent years[1,2]. The level of mechanized rice direct seeding in China has been improving year by year[3]. In addition, with the development of agricultural unmanned aerial vehicle (UAV), UAV seeding of rice has become an emerging operation method[4-6]. Compared with ground seeding machinery, UAV seeding has the advantages of flexibility, high efficiency and labor saving[7,8]. But most seeding UAVs are more used in broadcast seeding, and the uniformity of the sowing seeds is not as good as that of the row seeding[9,10]. Research shows, broadcast seeding is more prone to uneven growth density of rice seedlings, which will lead to poor ventilation and be susceptible to lodging[11]. Row seeding can improve the uniformity of seeds, which can overcome the shortcomings of broadcast seeding[12]. Therefore, this paper used the pelleted seeds as the seeding object, and designed a seeding device suitable for UAV operations, which can achieve the row seeding.

At present, some scientific research institutions and companies have carried out relevant researches on UAV seeding. Wu et al.[13] designed a centrifugal rice broadcast seeding, determined the optimal working parameters through simulation tests, and further verified the feasibility of the broadcast seeding device through bench tests and field tests. Song et al.[14-16] conducted research on broadcast seeding UAVs, and designed two broadcast seeding devices, one was centrifugal disc-type, the other was pneumatic-type. Centrifugal disc-type seeding device relied on

---

Received date: 2021-12-28 **Accepted date:** 2022-05-21

Biographies: **Wei Liu**, PhD candidate, research interest: agricultural mechanization and agricultural aviation, Email: 1341011201@qq.com; **Shuaishuai Zou**, MS candidate, research interest: agricultural mechanization, Email: 1366952389@qq.com; **Xuelang Xu**, MS candidate, research interest: agricultural mechanization, Email: 813259695@qq.com; **Qingyu Gu**, MS candidate, research interest: agricultural mechanization and automation, Email: 272968365@qq.com; **Weizhuo He**, MS candidate, research interest: agricultural electrification and automation, Email: 957723414@qq.com; **Jun Huang**, MS candidate, research interest: agricultural mechanization, Email: 1845218655@qq.com; **Junhao Huang**, MS candidate, research interest: agricultural engineering and information technology, Email: boulete@qq.com; **Zichen Lyu**, MS candidate, research interest: agricultural engineering and information technology, Email: zichen_lv@qq.com; **Jianqin Lin**, MS candidate, research interest: agricultural engineering and information technology, Email: 602015148@qq.com; **Xiwen Luo**, Professor, research interest: agricultural Equipment, precision agriculture and agricultural aviation, Email: xwluo@scau.edu.cn.

***Corresponding author: Zhiyan Zhou**, Professor, research interest: agricultural aviation. College of Engineering, South China Agricultural University, Guangzhou 510642, China. Tel: +86-13560026139, Email: zyzhou@scau.edu.cn; **Rui Jiang**, Post-doctoral, research interest: precision agriculture and agricultural aviation. Tel: +86-13424049263, Email: ruiojiang@scau.edu.cn.

centrifugal force to spread the seeds, and the pneumatic-type seeding device relied on airflow of the fan to blow the seeds out from different directions, which improved the uniformity of the broadcast seeding. Some UAV companies have also released a variety of models of seeding UAVs, most of which used centrifugal disc or pneumatic broadcast seeding systems, which cannot achieve row seeding operations[17,18]. In order to realize UAV-based row seeding, Huang et al.[19] designed and tested an auxiliary seeding device based on a centrifugal rape seeding device. The seeding row width can reach 6-7 cm, but the whole machine the structure was huge, and the end of the seed guide device was 20 cm away from the ground, which posed a large flight security risk. Yuren UAV (Zhuhai) Co., Ltd. designed a blowing type precision seeding UAV that used high-speed airflow to send seeds to the ground along the pipeline. But when the working height exceeded 50 cm, the seed drifts seriously and the seed rows were not obvious[20]. The Li's research team of China Agricultural University carried out research on non-contact seeding of wheat, accelerating wheat seeds and shooting them into the soil, and designed a device to jet seeds into the soil through high-pressure airflow[21-24]. In addition, researches have also been carried out on the use of centrifugal force to accelerate seeds. But both methods were aimed at ground machinery and were not suitable for UAV rice seeding.

The above researches on UAV seeding had the following shortcomings: (1) Part of the researches only improved the uniformity of the broadcast seeding, but still cannot realize sowing in rows; (2) For reducing the influence of UAV wind on seeding accuracy, the seed outlet was closer to the ground, which posed a greater safety hazard; (3) In order to achieve multi-row seeding, the size of the whole machine was large, which was not convenient for transportation; (4) The seed acceleration ability was limited or the structure was not suitable for UAV row seeding. In order to overcome the above problems, this research designed a new type of shot seeding device for rice that can be carried on a UAV. The device accelerated the pelleted rice seeds through two counter-rotating friction wheels. The whole machine adopted a compact structure to realize the simultaneous sowing in five rows parallel to flight route, even if the working height of the UAV is above 1 m, it still had an obvious line effect.

2 Materials and methods

2.1 Structure design of the seeding device and working principle

The study used the existing UAV (AGRS T16, Shenzhen DJI Technology Co., Ltd.) as a carrier, and designed a new shot seeding device for rice. The structure of the seeding device is shown in Figure 1. It is mainly composed of T16 UAV, seed box, seed metering device, seed distributor, shot seeding module and angle adjustment mechanism. The five shot seeding modules were arranged on a fan-shaped surface which can achieve five-line simultaneous seeding for each route. During operation, the seeds from the seed box passed through the seed metering device, the seed distributor and the shot seeding modules in sequence. The shot seeding module used two high-speed rotating friction wheels to accelerate the seeds to weaken the influence of wind field on seed movement[25,26].

Pelletized rice seeds were used in the UAV seeding operation. Seed pelletizing was a kind of seed coating technology[27]. The seed was wrapped with a special powder, which significantly increased the size and weight of the seed[28,29]. The pelleted rice seeds had better fluidity and strength, which was beneficial to the seed acceleration by the friction wheel and effectively reduced the rate of injury seeds. In this study, the diameter of the pelletized seeds was between 4 mm and 5 mm, the length was in the range of 9 mm to 11 mm.

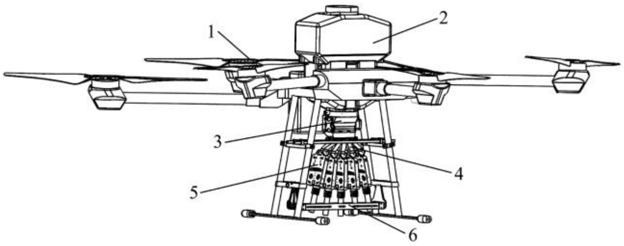

1. UAV platform 2. Seed box 3. Seed-metering device 4. Seed distributor 5. Shot seeding module 6. Angle adjustment mechanism

Figure 1 Shot seeding device

2.1.1 Seed metering device

In this study, the external grooved wheel seed metering device was used to transport the seeds to shot seeding module from the seed box. This kind of seed metering device has simple structure and good working stability, and can be used for pelleted rice seeds. According to the design requirements of five-line simultaneous seeding, the seed metering wheel was designed adaptively at first as shown in Figure 2a. For achieving precise metering, the seed metering wheel was evenly divided into five parts along the axial direction and nine chambers evenly distributed around the outer circle at each part. In order to ensure that the seeds were easy to enter and exit the chamber, the size of the chamber was designed based on the size of the seed. Therefore, according to the range of seed length and diameter in this study, the dimension parameters of the seed metering wheel are indicated in Figure 2a.

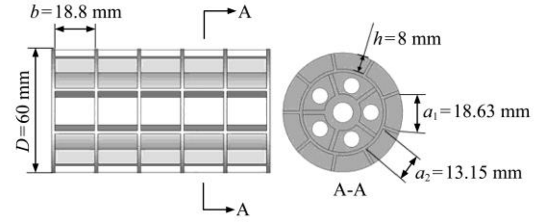

Note: D is the diameter of seed metering wheel, mm; b is the width of seed metering wheel chamber, mm; h is the depth of seed metering wheel chamber, mm; a_1 is the top length of seed metering wheel chamber, mm; a_2 is the bottom length of seed metering wheel chamber, mm

a. Seed metering wheel

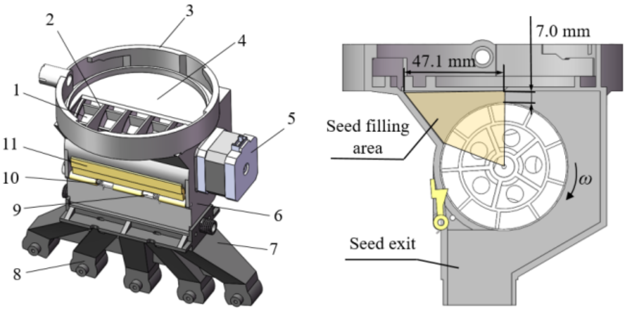

1. Seed metering wheel 2. Division plate 3. Seed box interface 4. Seed baffle 5. Motor 6. Seed metering device shell 7. Seed distributor 8. Seed outlet 9. Shaft 10. Torsion spring 11. Movable baffle

b. Seed metering device and internal structure

Figure 2 Seed metering device

The overall structure of the seed metering device was designed based on the structure parameters of the seed metering wheel, as shown in Figure 2b. Corresponding to the seed metering wheel, the four division plates evenly divided the interior of the seed metering device shell into five parts, so that the seeds can be separated when they enter the seed metering device. When working, with the rotation of the metering wheel in the ω direction, seeds were transported from seed filling area to seed exit, and discharged from five seed outlets of the seed distributor. There is a 5.3 mm gap between the seed metering wheel and the seed baffle, which can prevent the seed metering wheel from being stuck by the seeds. Besides, the seeds were discharged in the upper part of the seed metering device which can avoid seeds leakage caused by vibration.

2.1.2 Shot seeding module

The shot seeding module was used to accelerate the seeds, and its structure is shown in Figure 3a. The whole module can be divided into two parts according to function: (1) Seed vibration queue device, which consisted of a cone and a vibration motor. It can guide the seeds to enter the friction wheel acceleration device and prevent the seeds from jamming in the cone; (2) Friction wheel acceleration device. The two friction wheels with a diameter of 34 mm were symmetrically distributed on both sides of the acceleration tube, and were partially embedded in it; The friction wheel was installed on the outer rotor of the acceleration motor, and the acceleration motor was installed on the movable motor base; The top of the two movable bases were connected by tension spring, and the bottom were hinged on the mounting plate. The gap between the two friction wheels was set to 3 mm to ensure that the seeds are in contact with the friction wheels. The guide tube was installed at the bottom of the accelerating tube. The main structural parameters of the shot seeding module are shown in Figure 3b.

The acceleration motor adopted an external rotor brushless motor, the motor model was DJI2008-1400KV (Shenzhen DJI Technology Co., Ltd., Shenzhen, China), the motor diameter was 24 mm, the weight was 23 g, and the maximum speed can reach 14 000 r/min. The elastic wrapping material of the friction wheels were polyurethane (PU) and the shore hardness was 60 A.

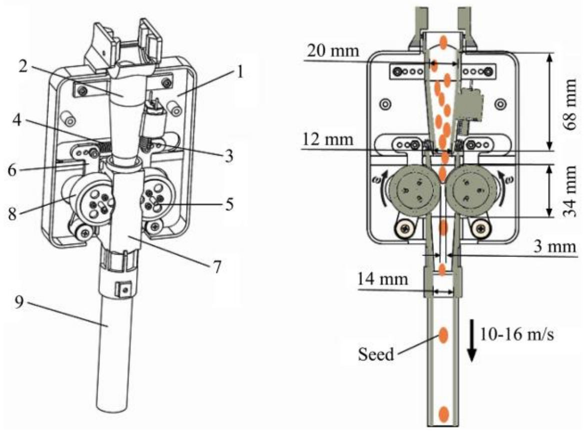

a. Axonometric drawing b. Sectional drawing

1. Mounting plate 2. Cone 3. Vibration motor 4. Tension spring 5. Acceleration motor 6. Movable motor base 7. Acceleration tube 8. Friction wheel 9. Guide tube

Figure 3 Shot seeding module

When working, the directions of rotation of the two friction wheels are shown in Figure 3b. When the seed enters the friction wheel gap, the friction wheel will speed up the seed, and seed will push two friction wheels to the side. After the seed passed, the friction wheels return to their original position under the action of the tension spring. The structure can accelerate the seeds whose size changes within a certain range, effectively reduce the seed damage rate, and can slow down the surface abrasion of the friction wheel.

2.1.3 Angle adjustment mechanism

The angle adjustment mechanism was used to adjust seeding row spacing in accordance with the working height of the UAV. Figure 4 was the structural diagram of the angle adjustment mechanism, which was composed of a plurality of angle adjustment rings, splint, splint fastener and fastening bolt. Two splints and their fastener formed a rectangular frame, which is fixed on the UAV’s body. When the fastening bolts are relaxed, the five angle adjustment rings can rotate around the fastening bolts and slide between the clamping plates. With reference to Figure 1, the angle adjustment ring was sleeved on the guide tube, and the shot seeding module were hinged on the seed distributor. Therefore, the shooting direction can be changed by adjusting the position of the angle adjustment rings.

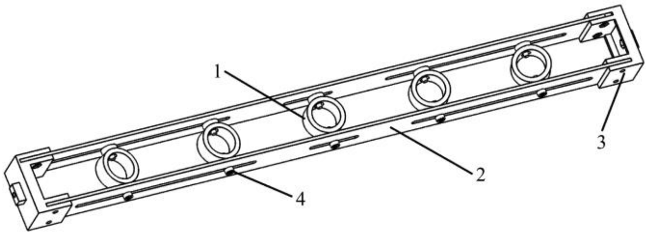

1. Angle adjustment ring 2. Splint 3. Splint fastener 4. Fastening bolt

Figure 4 Angle adjustment mechanism

2.2 Experiments of seed metering and shot seeding

2.2.1 Seed metering device stability test

The test device is shown in Figure 5. Before the test, filled the seed box with clean seeds, and used seed collection bags to collect the discharged seeds. The test of the seed metering device consisted of the following two parts:

(1) The seed discharging rate under different rotating speeds of the seed metering wheel. In this test, the rotation speed range of the seed metering wheel was 14-20 r/min. After setting the rotation speed of the seed metering wheel, the seed metering device ran for 30 s and weighed the total weight of the seeds discharged from the five outlets. The measurement was repeated three times at each speed level and calculated the average seed discharge rate.

(2) The stability of the seed discharging rate. According to the description of the stability of the seed metering device in the standard GB/T 9478-2005 (Testing methods of sowing in lines), the coefficient of variation of the discharge rate of each row ($C.V_1$) and total seed discharge rate stability ($C.V_2$) were computed. Under the condition that the seed metering wheel was 15 r/min and the running time was 30 s, the weight of the seed discharged by the seed metering device was counted. The measurement was repeated five times and according to Equations (1) and (2) to calculate the $C.V_1$ and $C.V_2$.

$$S=\sqrt{\frac{1}{n-1}\sum(x_i-\bar{x})^2} \tag{1}$$

$$C.V=\frac{S}{\bar{x}}\times 100\% \tag{2}$$

where, in the calculation of $C.V_1$, S is the standard deviation of the weight of seeds discharged in five rows; n is the number of rows, n=5; x_i is the average weight of the five repeated tests in the row i, g; $\bar{x}$ is the average value of x_i, g. In the calculation of $C.V_2$, S is the standard deviation of the total weight of seeds discharged in five tests; n is the number of tests, n=5; x_i is the total weight of seeds discharged from 5 rows in test i, g; $\bar{x}$ the average value of the x_i, g.

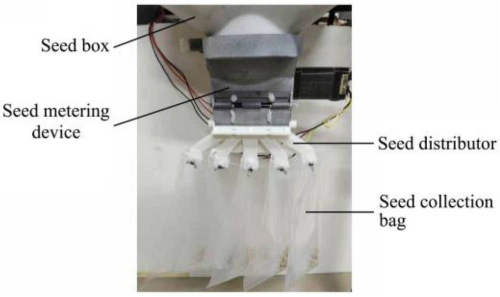

Figure 5 Seed metering device test

2.2.2 UAV seeding performance and field test

Take the AGRS T16 UAV (Shenzhen DJI Technology Co., Ltd.) as a carrier to build a test prototype, as shown in Figure 6. The main technical parameters are shown in Table 1.

Figure 6 Shot seeding UAV

Table 1 Operation parameters of shot seeding UAV

Working height/m	Flying speed/km h^{-1}	Row spacing /cm	Single row seed discharge rate/g s^{-1}	Sowing speed /hm^2 h^{-1}
0.5-2.0	3.6-10.8	15.0-30.0	3.0-5.0	0.6-1.5

(1) UAV seeding performance test

In order to obtain the distribution characteristics of the seeds, a UAV seeding test was carried out above the self-made mud trough (2.5 m×2.0 m, 5 cm in depth). The test site is shown in Figure 7a. The image recognition method was used to obtain the position coordinates of each seed, so as to digitize the position of the seed. The working height of the UAV was 1.5 m, the flying speed was 3.6 km/h, the speed of the friction wheel was 8000 r/min, and the speed of the metering wheel was 15 r/min. The test was repeated three times. Take pictures at a height of 3 m from the mud trough under natural lighting conditions, and the resolution of the collected color image was 2250×4000, as shown in Figure 7b.

a. Sowing in the mud trough

b. Original image of seed trajectory

Figure 7 Experiment of UAV seeding performance

In this study, HALCON 20.11 (MVTec Software GmbH, Munich, Germany) was used for image processing. After dividing the image into R-G-B three channels, the enhanced red channel and blue channel were used for subtraction to gray and enhance the soil area, and then selected the area with the largest area to obtain the image processing region of interest (ROI). Use the center line of the seed row as the vertical *Y* axis to correct the direction of the image and establish an *X*-*Y* coordinate system. The result is shown in Figure 8a. In order to accurately obtain the position of each seed, the image of the region of interest was enhanced with the seed region, as shown in Figure 8b, and the adhesion seeds regions were segmented, as shown in Figure 8c. During the image acquisition process, the actual length represented by each pixel in the image may be uneven in the entire image due to the distortion of the camera. Therefore, according to the five calibration plates (the size of the black grid: 40 mm×40 mm) in Figure 7b, the actual distance represented by each pixel in different areas of the image was calculated respectively. According to the coordinates of the seed pixel and the actual size of the pixel, the actual position coordinates of the seed can be calculated.

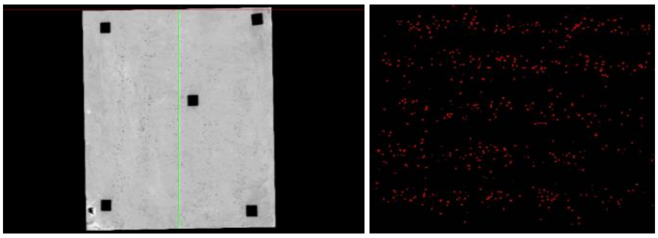

a. ROI image after orientation correction b. ROI recognition result

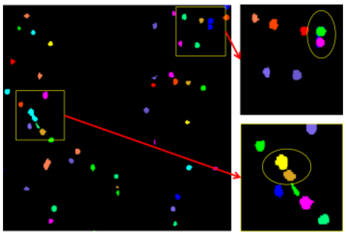

c. Seeds segmentation result

Figure 8 Seed recognition and segmentation

(2) Field test

Field seeding test was carried out on May 21, 2021, at the Zengcheng Teaching and Research Bases, South China Agricultural University. According to the agronomic requirements of direct seeding of rice, completed the field rotary tillage, beating and leveling operations before planting. After the route planning was completed, the shot seeding operation was carried out in the autonomous flight mode, and the actual operation area was 0.252 hm^2. The seeding scene is shown in Figure 9a.

In this test, the rice variety was 19 Xiang, and the thousand-grain weight of the seed was 21.4 g. After the seeds are pelletized, the thousand-grain weight was 70.0 g, the seedling emergence rate of pelletized seeds measured under laboratory conditions was 86.20%. The flying speed was set to 3.6 km/h, the rotation speed of the seed metering wheel was 15 r/min, the working height was 1.5 m, the row spacing was 25 cm, and the friction wheel speed was 8000 r/min. The theoretical seeding quantity can be calculated as 38.56 kg/hm^2. The five-point sampling method was used to count emergence rate. Use a rectangular frame (0.5 m×1 m) to delineate the sampling area, and take two adjacent rows in each sampling area, as shown in Figure 9b. The number of seeds in the sampling area was counted and the number of rice seedlings was recorded from the sixth day after sowing. The seedling emergence rate was calculated according to Equation (3). The damage rate of the pelleted seeds in the sampling area is calculated by Equation (4).

$$A=\frac{N_A}{N}\times 100\% \tag{3}$$

$$D=\frac{N_D}{N}\times 100\% \tag{4}$$

where, A is the seedling emergence rate; D is the damage rate of the pelleted seeds; N_A is the number of seedlings; N_D is the number of damage pelleted seeds; N is the total number of the pelleted seeds.

After sowing, conventional methods were used for field management, and the yield was measured after the rice was mature. When measuring the yield, the rice harvester was used for harvesting, and the fresh grains were weighed. A grain moisture analyzer (Model: LDS-1G, Quzhou Aipu Measuring Instrument Co., Ltd.) was used to measure the moisture content of rice, and converted the measured weight of fresh grain to the weight under the condition of 13.5% moisture content, and then deducted impurities at 1% to obtain the final dry grain quality.

a. Seeding operation in field

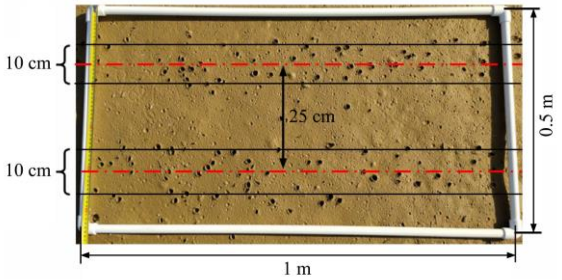

b. Seed traces on the ground and sample area

Figure 9 UAV in seeding and seeds on the mud surface

3 Result and discussion

3.1 The performance of seed metering device

3.1.1 Measurement of seed discharge rate

As shown in Figure 10, according to the measurement results, the seed discharge rate under different rotation speed of seed metering wheel levels was calculated. According to the fitting curve, it can be seen that the rotation speed of seed metering wheel and the seed discharge rate had a linear relationship.

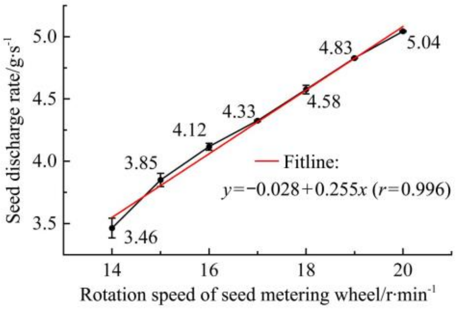

Figure 10 Seed discharge rate under different rotation speeds of seed metering wheel

3.1.2 Stability of seed metering device

The results are shown in Tables 2 and 3. According to the standard NY/T739-2003 (Operation quality of grain drill), the $C.V_1$ should be less than 3.9%, and $C.V_2$ should be less than 1.3%. In this study, $C.V_1$=1.70%, $C.V_2$=1.04%, both meet the requirement.

Table 2 Coefficient of variation of the discharge rate of each row

$\bar{x}_1$	$\bar{x}_2$	$\bar{x}_3$	$\bar{x}_4$	$\bar{x}_5$	$\bar{x}$	S_1	$C.V_1$
111.72	117.16	114.44	114.04	113.92	114.26	1.94	1.70%

Note: $\bar{x}_i$ is the average weight of the five repeated tests in row i, g; $\bar{x}$ is the average value of $\bar{x}_i$, g; S_1 is the standard deviation of the average row weight of each row.

Table 3 Coefficient of variation of total seed discharge rate stability

X_1	X_2	X_3	X_4	X_5	$\bar{X}$	S_2	$C.V_2$
575.9	568.8	561.9	575.1	574.7	571.28	5.95	1.04%

Note: X_i is the total weight of seeds discharged from 5 rows in test i, g; $\bar{X}$ is the average value of X_i, g; S_2 is the standard deviation of the total weight of seeds discharged in five tests.

3.2 The performance of UAV seeding

3.2.1 Seeds distribution characteristics

After the seed coordinates were obtained through image processing, the recognition accuracy was measured. According to the comparison between the X coordinate of the image recognition seed and the actual measured value, it was concluded that the average relative error of the image recognition distance to the manual measurement was 4.25%, and the seed recognition success rate was 95%-98%. According to the data obtained by image processing, drew a map of seed distribution characteristics, as shown in Figure 11.

In order to observe the seed distribution clearly, superimposed the seed scatter plots of the three trials and drew the frequency histogram of each row of seeds in the X-axis direction, as shown in Figure 11a. It can be seen from scatter plot that the distinction between the seed rows was obvious, and the seed density gradually decreased from the center of the row to the edge. According to the frequency distribution histogram of the seeds, the seeds were concentratedly distributed near the center line of the row, and the number of seed gradually decreased toward the edge. In order to further describe the seed row width, the proportion of the number of seeds in different widths was counted, as shown in Figure 11b. As the width increased, the proportion of the number of seeds in the row gradually increased. At 100 mm width, there were 60%-70% of the seeds distributed in this width range.

There are many reasons for the error of the seed landing position within the same row. The irregular shape of pelleted seeds will lead to different directions of force on the seeds, which will affect the initial movement direction of the seeds. Secondly, the wind field generated by the UAV will affect the movement of the seeds in the air. The jitter of the body when the UAV is flying will also affect the stability of the initial shot direction of the seeds.

3.2.2 Evaluation of field seeding effect

After seeding, the seed discharge weight was 9.9 kg, and the actual seeding quantity was 39.29 kg/hm^2. According to Equation (3), the deviation rate of seeding quantity was 1.89%.

$$P_{zz}=\frac{Q_{zs}-Q_{zy}}{Q_{zy}}\times 100\% \tag{3}$$

where, P_{zz} is the deviation rate of the seeding quantity, %; Q_{zs} is the actual seeding quantity, kg/hm^2; Q_{zy} is the theoretical seeding quantity, kg/hm^2.

The standard NY/T739-2003 states that the deviation rate should be within ±2%, In this test, the deviation of the seeding quantity was acceptable.

According to statistics, the total number of pelleted seeds in the five sampling areas was 553, of which the number of damaged pelleted seeds was 4, the damage rate of pelleted seeds was 0.72%. It should be noted that the damage only represents the damage of the pelletized material, and no broken seeds were found. The seedling emergence rate statistics were started on the 6th day after seeding. The emergence rate increased rapidly from 62.16% to 79.82% within 6 days, and slowly after the 12th day. After the 14th day, the seedling emergence rate stabilized, and eventually reaching 82.63% which was close to the laboratory result of 86.20%. The seedling emergence rate changed with time are shown in Figure 12a.

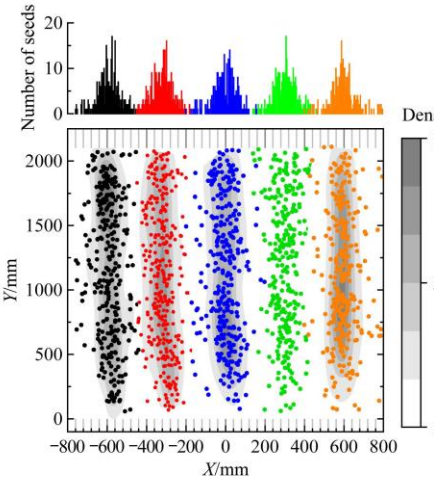

Note: Figure 11a is the result of superimposing the scatter plots obtained from three experiments. Different color points are used to distinguish different rows. The background of the scatter plot is the seed distribution density cloud image obtained by the two-dimensional kernel density estimation method. The top of the figure is a histogram of the frequency distribution of seeds in the width direction. Its horizontal axis is the same as the scatter plot, and the vertical axis is the number of seeds.

a. Seed distribution scatter plot with density and histogram of seed frequency distribution in each row

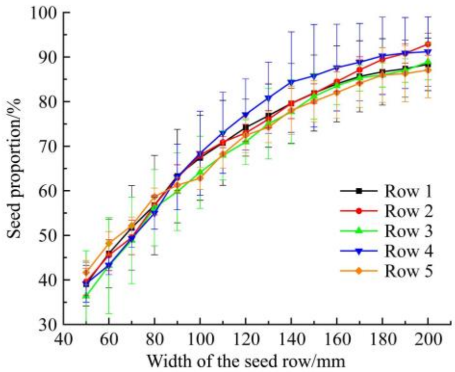

Note: In Figure 11b, the horizontal axis is the width of the seed row, and the vertical axis is the proportion of the seed within the width range, and different colors are used to distinguish different seed rows. For example, 100 mm on the horizontal axis represents the range (μ-50, μ+50), where μ is the average value of the X-axis values of the row of seeds in the scatter chart. The number of seeds in the range (μ-50, μ+50) divided by the total number of seeds in the row is the ordinate value, and it is expressed as a percentage.

b. Proportion of each row of seeds under different seed row widths

Figure 11 Seed distribution characteristics of UAV seeding

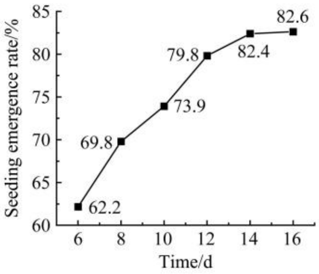

a. Emergence rate with time

b. Rice seedlings on 14 d

Figure 12 The seedling emergence rate

Figure 12b was the field conditions on the 14th day after seeding, and the rows were obvious. The straightness of the row was greatly affected by the flight stability of the UAV, and it was affected by the lateral wind during the operation, which will reduce the straightness of the rows.

The rice was harvested on September 6, 2021, and the yield was measured. The actual harvested area was 0.023 hm^2, the fresh weight of grain was 177.22 kg, and the measured moisture content was 22.01%. The actual yield can be calculated to be 6775.50 kg/hm^2.

4 Conclusions

A novel UAV-based shot seeding device with the advantage of the compact structure of the whole machine, the five rows seeding operation simultaneously, adjustable seed discharging rate, and stably seeding was designed. The following conclusions were obtained through the experiments in laboratory and in field:

(1) Stability of the seed metering device

On the basis of determining the relationship between the rotation speed of the seed metering wheel and the seed discharging rate, the stability of the seed metering device in the total displacement and the displacement of each row was studied. The results of discharge rate showed that when the rotation speed of seed metering wheel was 15 r/min, the coefficient of variation for the consistency of each row's displacement and the coefficient of variation of the total displacement were 1.70% and 1.04%, respectively.

(2) Distribution characteristics of pelleted rice seed sowed by the shot seeding UAV

In the mud trough experiment, the method of image recognition and processing was used to measure the position coordinates of the pelleted rice seeds. A scatter plot of the distribution of seeds on the ground was established, and the rowing effect of seeds was significant. The number of seeds presented a distribution characteristic of increasing gradually from both sides to the center in the width direction of the seed row, and the number of seeds within the width of 100 mm accounted for 60%-70% of the total number of seeds in the row.

(3) Field UAV seeding and the yield

The feasibility of this seeding method was verified by in-field UAV seeding test. By counting the number of pelleted seeds in the sampling area, it was found that the damage rate of the pelleted seeds was 0.72%, and no damaged rice seeds were found. According to the theoretical seeding quantity and the actual seeding quantity, the deviation of seeding quantity was 1.89%. The seedling emergence rate was 82.63%, and the yield was 6775.50 kg/hm^2 after 108 days of seeding.

This study was exploratory research in the field of UAV seeding, and there are still many related researches to be carried out, especially the problems of seed row effect, structural parameter optimization and life of wear parts need to be further studied.

Acknowledgements

This research was funded by the Laboratory of Lingnan Modern Agriculture Project (Grant No. NT2021009); the Project of key R & D program of Guangzhou of China (Grant No. 202206010149); in part by the Science and Technology Plan of Jian City of China (Grant No. 20211-055316 and [2020]83), Rural Revitalization Strategy in Guangdong Province (2020KJ261) and Science and Technology Plan of Guangdong Province of China (2021B1212040009). We also thank the anonymous reviewers for their critical comments and suggestions for improving the manuscript.

[References]

[1] Farooq M, Siddique K H M, Rehman H, Aziz T, Lee D-J, Wahid A. Rice direct seeding: Experiences, challenges and opportunities. Soil and Tillage Research, 2011; 111(2): 87–98.

[2] Yang W H, Kim J K, Lee M H, Chen S C, Han H S. Status and prospect on rice direct seeding technology of farmers. The Journal of the Korean Society of International Agriculture, 2015; 27(3): 342–347.

[3] Zhang M H, Wang Z M, Luo X W, Zang Y, Yang W W, Xing H, et al. Review of precision rice hill-drop drilling technology and machine for paddy. Int J Agric & Biol Eng, 2018; 11(3): 1–11.

[4] Diao Y, Zhu C H, Ren D H, Yu J Q, Luo X, Ouyang Y Y, et al. Key points and prospect of rice direct seeding technology by unmanned aerial vehicle. China Rice, 2020; 26(5): 22–25. (in Chinese)

[5] Xiao H X, Li Y F, Yuan L Y, Zhang Z F. Application and prospect of china agricultural unmanned aerial vehicle in rice production. Guangdong Agricultural Sciences, 2021; 48(8): 139–147. (in Chinese)

[6] Rahman M F F, Fan S R, Zhang Y, Chen L. A comparative study on application of unmanned aerial vehicle systems in agriculture. Agriculture-Basel, 2021; 11(1): 22. doi: 10.3390/agriculture11010022.

[7] Zhou Z Y, Zang Y, Luo X W, Lan Y B, Xue X Y. Technology innovation development strategy on agricultural aviation industry for plant protection in China. Transactions of the CSAE, 2013; 29(24): 1–10. (in Chinese)

[8] Radoglou-Grammatikis P, Sarigiannidis P, Lagkas T, Moscholios I. A compilation of UAV applications for precision agriculture. Computer Networks, 2020; 172: 107148. doi: 10.1016/j.comnet.2020.107148

[9] Song C C, Zhou Z Y, Luo X W, Jiang R, Lan Y B, Zhang H Y. Review of agricultural materials broadcasting application on unmanned helicopter. Journal of Agricultural Mechanization Research, 2018; 40(9): 1–9. (in Chinese)

[10] Gao Z Z, Peng X D, Lin G C, Zhang Q Y, Lu S L, Ouyang F. Application of broadcast sowing by unmanned aerial vehicle in agriculture: a review. Jiangsu Agricultural Sciences, 2019; 47(6): 24–30. (in Chinese)

[11] Feng Y J, Wang Q, Zhao H L, Song Q L, Sun Y, Ceng X N. Research status and prospect of the direct seeding technology of rice in China. China Rice, 2020; 26(1): 23–27. (in Chinese)

[12] Mai W X, Ablez B, Zhang B, Zeng F J, Tian C Y. Rice yield under different cultivation patterns. Chinese Agricultural Science Bulletin, 2019; 35(36): 1–5. (in Chinese)

[13] Wu Z J, Li M L, Lei X L, Wu Z Y, Jiang C K, Zhou L, et al. Simulation and parameter optimisation of a centrifugal rice seeding spreader for a UAV. Biosystems Engineering, 2020; 192: 275–293.

[14] Song C C, Zhou Z Y, Luo X W, Lan Y B, He X G, Ming R, et al. Design and test of centrifugal disc type sowing device for unmanned helicopter. Int J Agric & Biol Eng, 2018; 11(2): 55–61.

[15] Song C C, Zhou Z Y, Jiang R, Luo X W, He X G, Ming R. Design and parameter optimization of pneumatic rice sowing device for unmanned aerial vehicle. Transactions of the CSAE, 2018; 34(6): 80–88. (in Chinese)

[16] Song C C, Zang Y, Zhou Z Y, Luo X W, Zhao L L, Ming R, et al. Test and comprehensive evaluation for the performance of UAV-based fertilizer spreaders. IEEE Access, 2020; 8: 202153–202163.

[17] Zhu H B, Ma Z T, Xu D, Ling Y F, Wei H Y, Gao H, et al. Discussion and expectation of "unmanned" cultivation technology system for rice with high quality and yield suitable for UAV seeding. China Rice, 2021; 27(5): 5–11. (in Chinese)

[18] Wan J J, Qi L J, Zhang H, Lu Z A, Zhou J R. Research status and development trend of UAV broadcast sowing technology in China: ASABE 2021 Annual International Meeting, Michigan, 2021. doi: 10.13031/aim.202100017.

[19] Huang X M, Xu H W, Zhang S, Li W C, Luo C M, Deng Y F. Design and experiment of a device for rapeseed strip aerial seeding. Transactions of the CSAE, 2020; 36(5): 78–87. (in Chinese)

[20] Yuren UAV (Zhuhai) Co., Ltd. Agri precise rice seeds seeding drone sprayer. http://www.nongyehangkong.com/en/. Accessed on [2021-12-28].

[21] Wang C, Li H W, He J, Wang Q J, Lu C Y, Wang J X. Design and experiment of pneumatic wheat precision seed casting device in rice-wheat rotation areas. Transactions of the CSAM, 2020; 51(5): 43–53. (in Chinese)

[22] Wang C, Li H W, He J, Wang Q J, Cheng X P, Wei Z C, Liu J X. Effect of incident angle on wheat soil-ripping parameters by pneumatic seeding. Transactions of the CSAE, 2019; 35(16): 32–39. (in Chinese)

[23] Wang Y B, Li H W, Wang Q J, He J, Lu C Y, Liu K H. Design and experiment of wheat mechanical shooting seed-metering device. Transactions of the CSAM, 2020; 51(S1): 73–84. (in Chinese)

[24] Wang Y B, Li H W, Hu H N, He J, Wang Q J, Lu C Y, et al. DEM-CFD coupling simulation and optimization of a self-suction wheat shooting device. Powder Technology, 2021; 393: 494–509.

[25] Shi Q, Liu D, Mao H P, Shen B G, Li M Q. Wind-induced response of rice under the action of the downwash flow field of a multi-rotor UAV. Biosystems Engineering, 2021; 203: 60–69.

[26] Liu X, Zhang W, Fu H B, Fu X M, Qi L Q. Distribution regularity of downwash airflow under rotors of agricultural UAV for plant protection. Int J Agric & Biol Eng, 2021; 14(3): 35–42.

[27] Chang Y, Wei T B, Zang Gu P, Wang X, Li Y R. Research and application of seed pelleting technology in small seed. China Seed Industry, 2020; 11: 18–21. (in Chinese)

[28] Han B H, Chen K, Lv X L, Lu D P, Tang Y X. Current status and existing problems for seed pelleting equipment at home and abroad. Journal of Chinese Agricultural Mechanization, 2018; 39(11): 51–55, 71. (in Chinese)

[29] Mei J H, Wang W Q, Peng S B, Nie L X. Seed pelleting with calcium peroxide improves crop establishment of direct-seeded rice under waterlogging conditions. Scientific Reports, 2017; 7(1): 4878. doi: 10.1038/s41598-017-04966-1.

Laser tracking leader-follower automatic cooperative navigation system for UAVs

Rui Ming[1,2], Zhiyan Zhou[1,3,4*], Zichen Lyu[1,3,4,5], Xiwen Luo[1,3,4,5], Le Zi[1,3,4,5], Cancan Song[1,3,4,5], Yu Zang[1,3,4,5], Wei Liu[1,3,4,5], Rui Jiang[5*]

(1. *College of Engineering, South China Agricultural University / Guangdong Laboratory for Lingnan Modern Agriculture, Guangzhou 510642, China*;
2. *College of Computer and Control Engineering, Minjiang University / Fujian Provincial Key Laboratory of Information Processing and Intelligent Control, Fuzhou 350108, China*;
3. *Guangdong Provincial Key Laboratory for Agricultural Artificial Intelligence (GDKL-AAI), Guangzhou 510642, China*;
4. *Guangdong Engineering Research Center for Agricultural Aviation Application (ERCAAA), Guangzhou 510642, China*;
5. *Key Laboratory of Key Technology on Agricultural Machine and Equipment, South China Agricultural University, Ministry of Education of P.R. China, Guangzhou 510642, China*)

Abstract: Currently, small payload and short endurance are the main problems of a single UAV in agricultural applications, especially in large-scale farmland. It is one of the important methods to solve the above problems of UAVs by improving operation efficiency through multi-UAV cooperative navigation. This study proposed a laser tracking leader-follower automatic cooperative navigation system for multi-UAVs. The leader in the cluster fires a laser beam to irradiate the follower, and the follower performs a visual tracking flight according to the light spot at the relative position of the laser tracking device. Based on the existing kernel correlation filter (KCF) tracking algorithm, an improved KCF real-time spot tracking method was proposed. Compared with the traditional KCF tracking algorithm, the recognition and tracking rate of the optimized algorithm was increased from 70% to 95% in indoor environment, and was increased from 20% to 90% in outdoor environment. The navigation control method was studied from two aspects: the distance coordinate transformation model based on micro-gyroscope and navigation control strategy. The error of spot position was reduced from the maximum (3.12, −3.66) cm to (0.14, 0.12) cm by correcting the deviation distance of the spot at different angles through a coordinate correction algorithm. An image coordinate conversion model was established for a complementary metal-oxide-semiconductor (CMOS) camera and laser receiving device at different mounting distances. The laser receiving device was divided into four regions, S0-S3, and the speed of the four regions is calculated using an uncontrollable discrete Kalman filter. The outdoor flight experiments of two UAVs were carried out outdoors using this system. The experiment results show that the average flight error of the two UAVs on the *X*-axis is 5.2 cm, and the coefficient of variation is 0.0181. The average flight error on the *Z*-axis is 7.3 cm, and the coefficient of variation is 0.0414. This study demonstrated the possibility and adaptability of the developed system to achieve multi-UAVs cooperative navigation.

Keywords: two-UAVs cooperative, visual navigation, laser tracking
DOI: 10.25165/j.ijabe.20221502.6350

Citation: Ming R, Zhou Z Y, Lyu Z C, Luo X W, Zi L, Song C C, et al. Laser tracking leader-follower automatic cooperative navigation system for UAVs edited. Int J Agric & Biol Eng, 2022; 15(2): 165–176.

1 Introduction

Unmanned Aerial Vehicles (UAVs) have been playing an increasingly important role in civilian use in recent decades[1]. Compared with traditional ground machinery, UAVs can be used in chaotic scenes and environments, such as fire and rescue scenes. It can also be used to protect areas from environmental damage and reduce the labor intensity of farmers, such as farmland spray[2,3].

When working on large-scale farmland, UAVs needs to increase their payload and endurance capacity to improve operation efficiency. However, due to the current technical development and regulations, the overall dimensions of UAV have received greater restrictions, making it difficult to increase endurance time and payload[4,5].

In order to solve the payload and endurance problems of a single UAV, two or more UAVs can be used to achieve cluster operations and expand the UAV operating area to improve operating efficiency. So, it is one of the important methods to solve the above problems of UAVs by improving operation efficiency through multi-UAVs cooperative navigation.

Existing cluster methods of multi-UAVs are mainly divided into absolute navigation and relative navigation[6]. The absolute navigation method operates according to the established mission

---

Received date: 2020-12-08 **Accepted date:** 2021-09-02

Biographies: Rui Ming, Associate Professor, research interests: agricultural aviation, Email: rming@mju.edu.cn; **Zichen Lyu**, Master candidate, research interests: agricultural aviation, Email: zichen_lv@qq.com; **Xiwen Luo**, Professor, research interests: agricultural Equipment, precision agriculture and agricultural aviation, Email: xwluo@scau.edu.cn; **Le Zi**, Master candidate, research interests: information transmission, and intelligent control system, Email: 891750786@qq.com; **Cancan Song**, PhD candidate, research interests: precision agriculture and agricultural aviation, Email: songcc@stu.scau.edu.cn; **Yu Zang**, PhD, research interests: agricultural aviation, Email: zangyu@scau.edu.cn; **Wei Liu**, PhD candidate, research interests: precision agriculture and agricultural aviation, Email: 1341011201@qq.com.

***Corresponding author: Zhiyan Zhou**, Professor, research interests: agricultural aviation. College of Engineering, South China Agricultural University, Guangzhou 510642, China. Tel: +86-13560026139, Email: zyzhou@scau.edu.cn; **Rui Jiang**, Post-doctoral, research interests: precision agriculture and agricultural aviation. College of Engineering, South China Agricultural University, Guangzhou 510642, China. Tel: +86-20-38676975, Email: ruiojiang@scau.edu.cn.

objectives and uses the Global Navigation Satellite System (GNSS) or Real-Time Kinematic (RTK) system for multi-UAV formation flight[7,8]. Due to the narrow bandwidth of the GNSS loop, the vulnerability to interference, and the low receiver data update rate, it is difficult to meet the requirements of real-time measurement and control. The RTK system can meet the requirements of flight in multi-UAV coordination, and it has the advantages of strong autonomy, small size, and continuous output information. However, the cost is relatively high, and the corresponding ground base station and air positioning equipment should be equipped at the same time.

There are two main ways of relative navigation: communication navigation and visual navigation. In communication navigation, that is, the UAV acquires position and attitude information based on its high-precision sensors and uses wireless transmission modules to conduct relevant information interaction to fulfill the user's task requirements[9,10]. Typical communication navigation is based on the leader-follower-based method[11], which advantage is that strong damage resistance and high intelligence. However, the disadvantage of communication navigation is that when the number of UAVs increases, the computational load of information and the communication delay between UAVs will also increase at the same time, finally reducing the robustness of the UAV cluster.

Visual navigation has become a hot research topic in the UAV cluster because visual sensors can provide abundant information[12]. Tang et al.[13,14] used thermal imaging cameras and visible light cameras to track the UAV under different lighting and brightness conditions, respectively. Lin et al.[15] used the monocular camera to extract the UAV features and used the algorithm cascade classifier to classify the features in different situations. Vetrella et al.[16] combined visual navigation and carrier phase differential navigation to improve UAV attitude estimation in real-time or post-processing. In the study of Gassner et al.[17], a leader-follower mode of dual UAV carrier flight was proposed by using a monocular camera without explicit communication. The above visual tracking system takes UAV as the target feature, which can achieve good tracking effects in various applicable scenarios, but it is difficult to effectively track the target in the case of large illumination changes or complex environmental characteristics.

The laser has been widely used in military, medical, navigation, and other fields due to its advantages of high energy, accurate orientation, and high uniformity[18]. Walter et al.[19] proposed an onboard relative localization method, based on ultraviolet light, used for real-time control of a leader-follower formation of multi-UAVs. This method realizes the cooperative flight of multi-UAVs through ultraviolet light and camera, but it has obvious shortcomings. According to the experiment results, the followers make simple harmonic motions according to the leader's position during the tracking process, and the maximum error distance between the two UAVs is 6 m. When the number of followers increases, simple harmonic motion among followers may cause collisions, and thus security needs to be improved, it is difficult to deploy in practical applications. Park et al.[20] used infrared light (850 nm) emitting diode to strengthen the reflection of the guide label installed on the leader, installs an infrared camera from the follower and follows the movement of the guide label on the leader. The infrared light used in this method can effectively reduce the impact of sunlight. However, because it is a low-power LED, it can only track two units at a short distance. Therefore, in view of the above problems of large flight error distance and low power of emission light source, combining the existing visual navigation technology and the advantages of laser tracking navigation, we proposed a multi-UAV visual navigation device based on laser tracking.

In order to reduce the tracking error caused by communication navigation, a visual camera was used in this study to measure the relative distance between two UAVs. To reduce the failure rate of visual tracking, the laser is used instead of the UAV as the tracking feature in visual perception. To achieve robust visual tracking of an autonomous system, an improved kernel correlation filter (KCF) real-time spot tracking method is designed. The tracking method can estimate laser spot position coordinates under reliable visual feedback, and convert them into the flying speed of the UAV, so as to realize the synchronous tracking flight of two UAVs.

Figure 1 illustrates the laser tracking leader-follower automatic cooperative navigation system. In this system, the UAV equipped with the laser transmitting device serves as the team leader, which provides a laser spot as the follower's tracking target. The rest of the UAV is a follower, which follows the laser spot's location and flies synchronously with the leader. To avoid danger, a minimum safe distance was set between the two UAVs. During the flight, airborne sensors such as optical flow and ultrasound only play space positioning, and there was no communication between the two UAVs, all the calculations are performed separately on the two UAVs.

1. Leader UAV 2. Follower UAV 3. Laser emitting device 4. Laser receiving device 5. CMOS camera 6. Visual processing device 7. Laser beam
Note: COMS: Complementary metal-oxide-semiconductor.

Figure 1 Schematic diagram of Two-UAV automatic navigation device based on optical tracking

Based on the existing visual navigation technology and laser navigation, a visual tracking method and device based on laser tracking were proposed. The differences between the navigation of this study and the existing navigation are listed in Table 1.

In addition to the above differences with the existing navigation methods, this study also proposed an improved real-time KCF spot tracking method, which can accurately identify the spot position under different illumination conditions. And a navigation control method was proposed to automatically correct the position coordinates of the light spot according to the angle information provided by the micro gyroscope and convert the image coordinates into flight coordinates. Compared with the existing visual navigation system, the laser tracking automatic navigation system has higher tracking accuracy and more robust visual method in multi-UAV cooperative navigation.

2 Framework of the system

The system proposed in this study is mainly composed of three parts: the first part is the laser transmitting device on the leader, the second part is the laser receiving device on the follower, and the third part is the laser recognition device on the follower as shown in Figure 1.

Table 1 Differences between the navigation of this study and the existing navigation

Navigation methods	Characteristic
Absolute navigation[7,8]	1) Strong autonomy, small size, and continuous output information; 2) Narrow band width of the GNSS loop, the vulnerability to interference, and the low receiver data update rate; 3) Cost is relatively high, and the corresponding ground base station and air positioning equipment should be equipped at the same time.
Communication navigation[11]	1) Strong damage resistance and high intelligence; 2) Low robustness due to the limited communication transmission bandwidth and a large amount of data interaction; 3) The tracking error will be propagated backward step by step and amplified.
Visual navigation[12]	1) The number of UAVs in the cluster can be expanded and low communication; 2) Visual sensors can provide more abundant information; 3) It is difficult to effectively track the target when the illumination brightness changes greatly or the surrounding environment is complex.
Laser navigation[19,20]	1) High energy, accurate orientation, and high uniformity; 2) Security needs to be improved and hard to deploy in practical applications. 3) Maximum error distance is 6 m and makes simple harmonic motion between the two UAVs
The navigation proposed in this study	1) Do not rely on GPS/RTK for positioning, and realize tracking flight through onboard sensors; 2) There is no communication between the two UAVs, which effectively avoids the movement deviation caused by limited communication navigation bandwidth and massive data interaction; 3) Using laser spot as visual recognition target can effectively avoid the influence of complex environment; 4) High tracking accuracy.

During the flight, the UAV equipped with laser transmitting device is named a team leader, while the UAV equipped with laser receiving device is called ‘follower’. The flying mode of the leader can be controlled manually or fly according to the preset route. Before take-off, the laser tracking system on the follower needs to complete initialization. After the two UAVs take off, the leader turns on the laser transmitting device and fires a laser beam to the followers’ laser receiving device. The laser recognition device on the follower starts to collect the spot image on the laser receiving device and obtains the position information of the laser spot. The onboard computer uses the navigation control method to convert the laser spot position information into the UAV’s flying speed and transmits it to the flight controller. The follower flies according to the flying speed, and realizes the simultaneous flight of the two UAVs through laser tracking. The working principle of the device is shown in Figure 2. The main control parameters of the device are listed in Table 2.

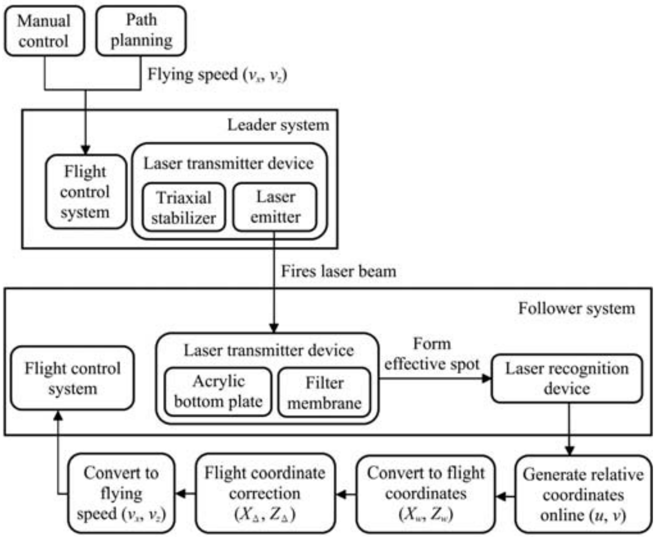

Figure 2 Working principle of the laser tracking navigation system

The laser transmitting device mainly includes a laser stabilization module and a laser-beam module. The laser stabilization module uses the STORM32BGC three-axis brushless stabilizer, effectively reducing the laser emission module’s jitter during the UAV flight. The laser-beam module is installed on the stabilizer, equipped with a 500 mW power red laser transmitter, and the battery is equipped with a 3.7 V (1800 mAh) lithium battery. The laser-transmitting device’s function is to transmit a laser beam perpendicular to the flying direction of the leader. The leader guides the follower to follow the flight through the laser beam to realize the leader-follower simultaneous flight.

Table 2 Main control parameters of the laser tracking navigation system

Variables	Meaning
u	X-axis pix coordinates of the laser spot
v	Z-axis pix coordinates of the laser spot
X_w	X-axis flight coordinates of UAV
X_z	Z-axis flight coordinates of UAV
X_Δ	X-axis flight coordinates of UAV after correction
Z_Δ	Z-axis flight coordinates of UAV after correction
v_x	X-axis flying speed of UAV
v_z	Z-axis flying speed of UAV

The laser receiving device includes a laser receiving plate and a light-transmitting film. The laser receiving board is a 2 mm polyvinyl chloride (PVC) board, and the laser can form effective reflection and transmission on the receiving board. SunMaster’s sr-space silver high-definition filter film was selected as the light-transmitting film and pasted on the PVC board to form a clear and effective light spot on the PVC board. The laser receiving device’s function is to receive the laser beam transmitted from the leader and form an effective recognizable spot on the receiving board, waiting for the laser tracking device’s recognition and tracking.

The laser recognition device consists of a complementary metal-oxide-semiconductor (CMOS) camera and an onboard computer. Choose OpenMV4 H7 for the CMOS camera. The Raspberry Pi 3B+ was selected as the micro airborne computer. Since the CMOS camera uses a fixed focus lens, different installation positions can affect the laser receiving device’s spot acquisition range. To achieve the most complete and comprehensive collection of the spot information on the laser receiving device by the CMOS camera, the best installation position is chosen between the camera and the laser receiving device. The laser recognition device’s function is to first collect the effective light spot on the laser receiving device in the form of a video stream and then obtain the image coordinates of the light spot through a visual processing algorithm. The second step uses the coordinate conversation model to convert the image coordinates of the laser spot into the flying speed of the follower. Finally, the navigation system controls the follower to fly synchronously according to the acquired flying speed. Table 3 provides details of the materials and equipment used in the system.

Table 3 Details of the materials and equipment for laser tracking navigation system

Material	Parameters
STORM32BGC	Processor: STM32F103RC Maximum jitter Angle: 1 degree Gyroscope sampling frequency: 700 Hz
Red laser	Power: 500 MW Working voltage: 2.8-5.2 V (DC) Wavelength: 650 nm
PVC plate	Thickness: 2 mm
Filter film	Transmittance: 18% Reflectivity: 85%
OpenMV4 H7	OV7725 sensor 640×480 16-bit RGB565
Raspberry Pi 3B+	CPU: ARM Cortex-A53 1.4 GHz SOC: Broadcom BCM2837

It can be seen from the above that the main research content of this article has three points: Firstly, when the laser spot is irradiated on the laser receiving device, the method of identifying and obtaining the position of the spot. Secondly, after obtaining the position of the light spot, the method of accurately converting the position of the light spot into the flight coordinates of the UAV. Thirdly, the method of converting the UAV's flight coordinates into the flying speed of the UAV. Through the research of these three parts, the position of the laser spot transmitted from the leader can be converted into the follower's flying speed, realize the tracking of the spot position by the follower, and finally achieve the simultaneous flight of two UAVs.

3 Visual tracking method

When the laser irradiates the laser receiving device from a laser spot, the CMOS camera needs to locate and track the spot position after obtaining the image. In most cases, images acquired by a CMOS camera adopt the RGB color space, but it is sensitive to light brightness and is not suitable for image analysis with a large range of illumination variations[21]. However, the HSV color space is relatively intuitive and has a strong anti-interference ability to light and other effects[22]. Therefore, the color space conversion of the video image from RGB to HSV is carried out first.

With the maturity of machine learning algorithms, discriminant methods are becoming more and more common in the field of target tracking[23]. To achieve high robustness and longtime tracking, an improved KCF real-time spot tracking method is proposed. The discriminant method's main idea is to score the confidence of different sub-areas in the search area by the classifier and identify the target's location by analyzing the response strength layer. As a discriminant tracking method of typical nuclear correlation filtering, KCF has achieved remarkable accuracy and efficiency[24]. However, in the process of using KCF, if the target is affected by the change of illumination brightness, interference of similar targets, and other factors, the target will still be lost.

The KCF tracking algorithm's main idea to train the displacement filter is to learn a discriminant correlation filter to locate a new frame's target. In this study, a scale filter was added based on a displacement filter, and the scale pyramid was used to extract target samples. The sparse matrix was used to carry out cyclic sampling in the target region to improve the algorithm's computational efficiency and tracking accuracy. In the algorithm, ridge regression was used to obtain the optimal correlation filter h_i (Equation (1)).

$$\varepsilon = \sum_{i=1}^{t} \| h_i \times x_i - g_i \|^2 + \lambda \| h_i \|^2 \tag{1}$$

where, x_i is the extraction of the number i training sample; g_i is the target output of the number i training sample; λ is a regular term of a polynomial to prevent overfitting; h_i is the optimal correlation filter of the number i training sample.

According to Parseval's theorem, the operation is converted to the frequency domain as Equation (2).

$$\min \frac{1}{MN} \{[\sum_{i=1}^{t} \| \overline{\boldsymbol{H}_t} X_i - G_i \|^2] + \lambda \sum_{i=1}^{t} \| H_i \|^2\} \tag{2}$$

where, $\overline{\boldsymbol{H}_t}$ is a complex conjugate matrix; X_i is the frequency domain of the number i training sample; G_i is the target frequency domain output of the number i training sample; H_i is the frequency domain expression of the optimal correlation filter of the number i training sample.

By combining Equations (1) and (2), Equation (3) was obtained.

$$H_t = \frac{\sum_{i=1}^{t} \overline{G_l} X_i}{\sum_{i=1}^{t} \overline{X_l} X_i + \lambda} \tag{3}$$

where, H_t is the optimal correlation filter.

It can be seen from Equation (3) that the original sample extracted from the detector's target is the total set sampling. Due to a large amount of calculation in the total set sampling, the algorithm's real-time performance is greatly affected. Therefore, a sparse matrix for the cyclic sampling of the target region was used, which can effectively improve the algorithm's computational efficiency. The transform sparse matrix $\boldsymbol{P}$ was used to conduct cyclic sampling on one-dimensional target image $x_i=[x_{i1}, x_{i2}, x_{i3}, \dots, x_{in}, n\in[1,+\infty)]$. Therefore, the X_i in Equation (3) can be expressed as

$$\boldsymbol{X_i} = \begin{bmatrix} x_{i1} & x_{i2} & \cdots & x_{in} \\ x_{in} & x_{i1} & \cdots & x_{in-1} \\ \vdots & \vdots & \ddots & \vdots \\ x_{i2} & x_{i3} & \cdots & x_{i1} \end{bmatrix} \tag{4}$$

In the process of target tracking, the optimal correlation filter H_t in Equation (3) will constantly update and iterate. For the convenience of expression, the numerator expression in Equation (3) is F_i, while the denominator is L_i. Therefore, the updated expressions of F_i and L_i are as follows:

$$F_i = (1-\theta)F_{i-1} + \theta \sum \overline{G_l} X_i \tag{5}$$

$$L_i = (1-\theta)L_{i-1} + \theta \sum \overline{X_l} X_i \tag{6}$$

where, θ is the learning rate. Therefore, in the next frame of the image, the target position can be obtained by solving the maximum correlation filter response y, and the obtained result is (u, v, w, h). (u, v) is the central pix coordinates of the target; (w, h) is the width and height of the minimum border of the target.

$$y = F^{-1}\left\{\frac{\sum \bar{F}\boldsymbol{Z}}{L+\lambda}\right\} \tag{7}$$

where, F^{-1} represents the Fourier transform; $\boldsymbol{Z}$ represents the feature matrix of the previous frame.

To keep the tracking for a long time, a support vector machine (SVM) classifier is added to train the effective target samples based on the fusion filter[25] and as an online learning classifier based on this existing KCF algorithm. After the target result is obtained in each frame, the target confidence level is judged: when the target detection threshold is larger than threshold 1 (th1), it means that the target sample of the frame is positive, and the sample is used as a training sample to train the SVM classifier; When the confidence of the target is smaller than threshold 2 (th2), it means that the target sample of the frame is invalid. At this time, the SVM does not use this sample for training and re-detects the image target. The flow of the improved KCF real-time spot tracking method is shown in Figure 3.

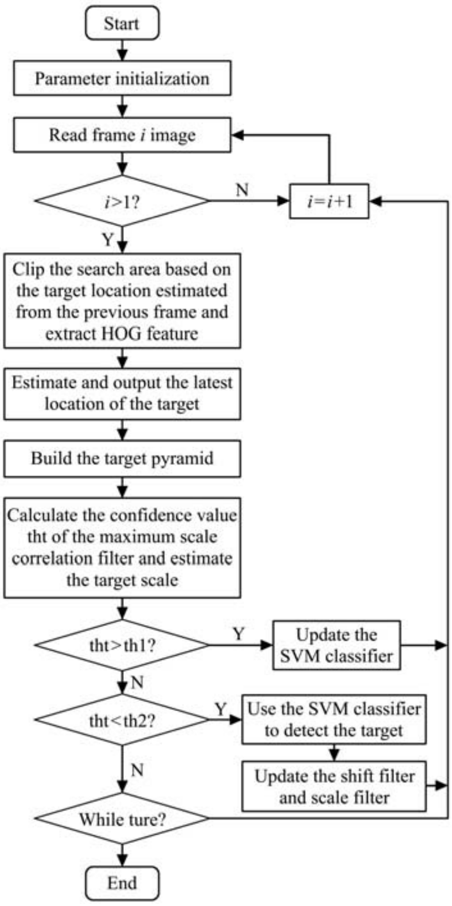

Figure 3 Flow of the improved KCF spot tracking method

When using a pix as a feature, the image is scanned in lexicographical order to form the feature vector. Given N column vector $x_i \in R^d$ and class label $t_i \in \{-1, 1\}$□$i \in \{1, 2, 3, \ldots, N\}$, the SVM classifier will find a hyperplane satisfying Equation (8).

$$\begin{gathered}\min_{w,b} \boldsymbol{w}^{\boldsymbol{T}}\boldsymbol{w} + C\sum_{i=1}^{N}\varepsilon_i \\ s.t.t_i(x_i^T w + b) \geq 1 - \varepsilon_i\end{gathered} \tag{8}$$

where, $\boldsymbol{w}^{\boldsymbol{T}}$ represents the transpose matrix of the matrix $\boldsymbol{w}$; $\boldsymbol{w}$ represents the normal line of the hyperplane; b represents the bias of the hyperplane; ε_i is the relaxation variable; C is the penalty parameter.

4 Navigation control method

4.1 Distance coordinate transformation model

The position coordinate of the spot collected by the CMOS camera is a pix coordinate, which cannot be directly used in actual flight control. Therefore, after obtaining the position information of the target spot in the image plane of the CMOS camera, it is necessary to establish an image coordinate transformation model to convert the pix coordinate (u_0, v_0) of the image into the flight coordinate (X_w, Z_w). Figure 4 is the relationship between pix coordinates and geodetic coordinates.

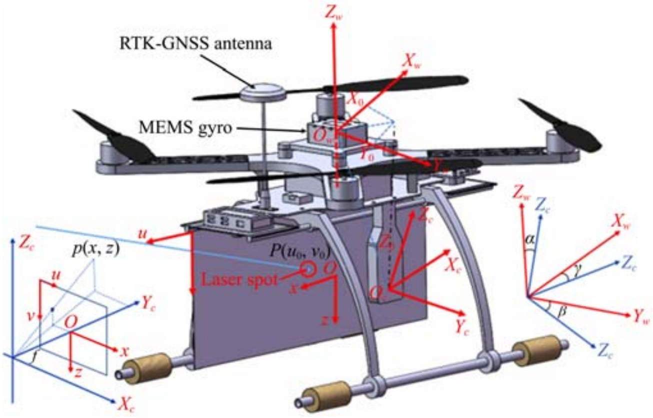

Note: *o-uv* is the pix coordinate system; *o-xz* is the image coordinate system; O_c-$X_cY_cZ_c$ is the camera coordinate system; O_w-$X_wY_wZ_w$ is the world coordinate system; *P* is the laser spot; (u_0, v_0) is the pix coordinates of laser spot.

Figure 4 Image coordinate transformation model diagram

The transformation equation from the image coordinate system to the pix coordinate system is,

$$\begin{bmatrix} u \\ v \\ 1 \end{bmatrix} = \begin{bmatrix} \frac{1}{d_x} & 0 & u_0 \\ 0 & \frac{1}{d_z} & v_0 \\ 0 & 0 & 1 \end{bmatrix} \begin{bmatrix} x \\ z \\ 1 \end{bmatrix} \tag{9}$$

where, u, v are the pix coordinates; d_x is the sum of image units per line; d_z is the sum of image units per column; *o-uv* is the pix coordinate system; *o-xz* is the image coordinate system.

The transformation equation from 2D to 3D is,

$$Y_c \begin{bmatrix} x \\ z \\ 1 \end{bmatrix} = \begin{bmatrix} f & 0 & 0 \\ 0 & f & v_0 \\ 0 & 0 & 1 \end{bmatrix} \begin{bmatrix} X_c \\ Z_c \\ Y_c \end{bmatrix} \tag{10}$$

where, X_c, Y_c, and Z_c are the camera coordinates; f is the internal parameter of the camera; x, z is the image coordinate; O_c-$X_cY_cZ_c$ is the camera coordinate system.

The camera coordinate system's transformation to the world coordinate system is mainly the rotation and translation of the camera relative to the ground. The conversion equation is,

$$R = \begin{bmatrix} 1 & 0 & 0 \\ 0 & \cos\alpha & \sin\alpha \\ 0 & -\sin\alpha & \cos\alpha \end{bmatrix} \begin{bmatrix} \cos\beta & 0 & -\sin\beta \\ 0 & 1 & 0 \\ \sin\beta & 0 & \cos\beta \end{bmatrix} \begin{bmatrix} \cos\gamma & -\sin\gamma & 0 \\ \sin\gamma & \cos\gamma & 0 \\ 0 & 0 & 1 \end{bmatrix} \tag{11}$$

$$\begin{bmatrix} X_w \\ Z_w \\ Y_w \end{bmatrix} = R \begin{bmatrix} X_c \\ Z_c \\ Y_c \end{bmatrix} + \begin{bmatrix} X_0 \\ Z_0 \\ Y_0 \end{bmatrix} \tag{12}$$

where, α, β, and γ are the angle of rotation around x, y, and z, respectively; X_w, Y_w, Z_w are the world coordinate; X_0, Y_0, Z_0 are the offsets of the camera for the flight control, O_w-$X_wY_wZ_w$ is the world coordinate system.

Combining Equations (9)-(12), the following is obtained:

$$X_w = |R| \cdot d_x \cdot \frac{Y_c}{f} \cdot (u - u_0) + X_0 \tag{13}$$

$$Z_w = |R| \cdot d_z \cdot \frac{Y_c}{f} \cdot (v - v_0) + Z_0 \tag{14}$$

$$Y_w = |R| \cdot Y_c + Y_0 \tag{15}$$

where, $\frac{Z_c}{f}$ is a CMOS camera internal reference, it is assumed that $d_x \cdot \frac{Y_c}{f}$ and $d_z \cdot \frac{Y_c}{f}$ are the distance coefficients on x, z, respectively.

Since the spot information of the laser receiving device has only information on two positions, X_w and Z_w, the Y_w position information is ignored. There are Equations (16) and (17) as follows:

$$d_x \cdot \frac{Z_c}{f} = k(d_x) \tag{16}$$

$$d_y \cdot \frac{Z_c}{f} = k(d_y) \tag{17}$$

Substitute Equations (16) and (17) into (13) and (14), Equations (18) and (19) were obtained.

$$X_w = |R| \cdot k(d_x) \cdot (u - u_0) + X_0 \tag{18}$$

$$Z_w = |R| \cdot k(d_z) \cdot (v - v_0) + Z_0 \tag{19}$$

4.2 Gyro-based coordinate information correction algorithm

During the UAVs flight, the laser receiving device will change angle due to the UAVs' attitude angle change. Therefore, the coordinate information correction algorithm based on the gyroscope is proposed to correct the fuselage's tilt interference. The gyroscope used the BMI088 high-performance inertial measurement unit (IMU) produced by Bosch Sensortec. The gyroscope has good paranoid stability (less than 2°/h) and low-temperature coefficient offset (TCO) below 15 mdps/k. While measuring the camera attitude, MEMS gyro-only based system suffers from drift and bias. Therefore, the gyroscope needs to be calibrated. The calibration method of the gyroscope is to place the gyroscope on flat ground and record 5000 sets of data continuously, and calculate the average value of the recorded data as the three-axis zero deviation of the gyroscope. And the gyroscope data with zero offset correction can meet the requirements of camera attitude measurement.

The principle of the body tilt correction algorithm based on the micromachined gyroscope is as follows. The spot position coordinates (X_0, Z_0) output by the CMOS camera are used as the main variables, and the angle of the body (laser receiving device) measured by the UAVs' flight controller gyroscope is used as the correction parameter. The values of (X_w, Z_w) are calculated according to Equations (13) and (14), and then the new coordinate values (X_Δ, Z_Δ) are obtained after the gyroscope angle correction, and the corrected coordinate values are used to participate in the flight control.

Figure 5 depicts conditions of UAVs that have a level or tilted laser receiving device location map; point P is for the laser receiving device that is level in terms of the actual point; P_Δ is the point where the fuselage is tilted and is a laser receiving device to receive the actual point of the same position. As seen from the figure, the fuselage's inclination angle is equal to that of the actual and measured points. Therefore, the relationship between the measured point coordinates and the actual point coordinates is,

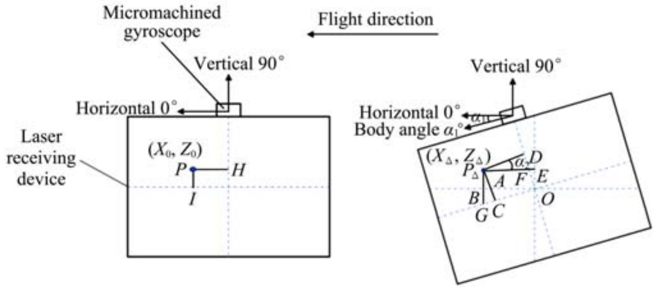

Note: P is the laser spot with angle 0°; (X_0, Z_0) is the position coordinates of spot with angle 0°; P_Δ is the laser spot with angle α_1°; (X_Δ, Z_Δ) is the position coordinates of spot with angle α_1°.

Figure 5 Location of the laser receiver when the UAV is horizontal or tilted

$$X_\Delta = X_0\cos\alpha_1 -+ Z_0\sin\alpha_1 \tag{20}$$

$$Z_\Delta = Z_0\cos\alpha_1 + X_0\sin\alpha_1 \tag{21}$$

where, α_1 is the body angle of the UAV.

4.3 Decision control strategy

After the image coordinate conversion and coordinate information correction, it is necessary to establish the relevant flight control method model.

The laser receiving device is divided into four regions: S0, S1, S2, and S3. Figure 6 is the laser receiving device area division diagram. S0 is a non-adjustment zone. When the light spot is on S0, the UAV is in a hovering and self-stabilizing state and does not follow the light spot's position to move. S1 is a buffer zone, which the main function is to gently transition the change of flying speed. When the light spot is above S1, the distance between the nonregulated zones of the light spot is calculated to determine the speed factor and calculate the real-time speed of the UAV at this time. S2 is the adjustment region. When the spot is in this position, the relevant speed calculation formula will be adopted to calculate the speed according to the spot's specific position to realize UAVs' laser tracking. S3 is the off-target adjustment zone. When the spot is in the zone, the spot's specific position cannot be acquired by the laser recognition device. At this time, the UAVs will accelerate flight for 2 s at the previous heading angle.

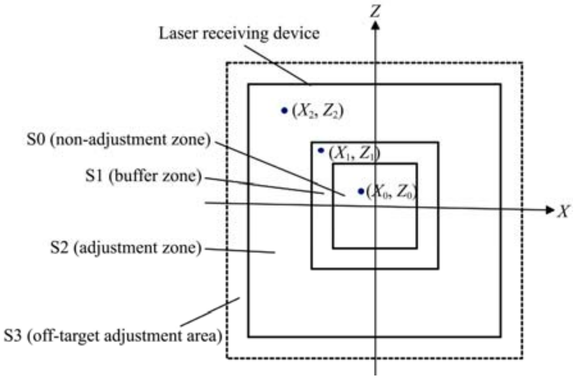

Figure 6 Laser receiving device area division diagram

Different from ordinary filtering, the Kalman filtering method has the advantage of a small delay and can estimate the state of the object in real-time without generating lag. It is widely used in motion estimation, especially in UAV[26]. In this study, the uncontrolled discrete Kalman filter method is adopted to calculate and control UAVs' flying speed when the light spot is in different areas[27].

When the spot is at S1, the coordinate point of the spot at this time is $P_0(X_0, Z_0)$:

$$\overrightarrow{v_{k+1}} = \overrightarrow{v_k} = 0 \tag{22}$$

where, $\overrightarrow{v_k}$ is the velocity at time k; $\overrightarrow{v_{k+1}}$ is the velocity at time k+1.

When the spot is at S2, the coordinate point of the spot is P1 (X_1, Z_1). First, calculate the distance factor Q_x, Q_y:

$$Q_x = \frac{|X_1|}{|X_A|} \tag{23}$$

$$Q_y = \frac{|Z_1|}{|Z_A|} \tag{24}$$

where, (X_A, Z_A) represents the four vertices of the S1 region.

Further, use the uncontrolled discrete Kalman filter method for speed calculation:

$$\overrightarrow{v_1} = \frac{\sqrt{(X_w - X_1)^2 + (Z_w - Z_1)^2}}{T} \tag{25}$$

$$\overrightarrow{v_2} = \overrightarrow{v_k} + \vec{a}T \tag{26}$$

$$k_g = \sqrt{\frac{(v_1 - v_k)^2}{(v_1 - v_k)^2 + (v_2 - v_k)^2}} \tag{27}$$

$$\overrightarrow{v_{k+1}} = \overrightarrow{v_k} + k_g \cdot |\overrightarrow{v_2} - \overrightarrow{v_1}| \tag{28}$$

where, v_1 is the mean square error prediction speed; v_2 is the state prediction speed; k_g is the gain factor; T is the unmanned accelerometer acquisition cycle. (X_w, Z_w) is the position of the spot in an acquisition cycle. a is the UAV acceleration.

Therefore, when the spot is at S2, the speed of the UAV is,

$$v_{k+1(x)} = Q_x \cdot |v_{k+1}| \cdot \frac{x}{\sqrt[2]{x^2 + z^2}} \tag{29}$$

$$v_{k+1(y)} = Q_y \cdot |v_{k+1}| \cdot \frac{y}{\sqrt[2]{x^2 + z^2}} \tag{30}$$

$$v_{k+1(z)} = 0 \tag{31}$$

When the spot is at S2, the coordinate point of the spot is P_2 (X_2, Z_2). At this time, the UAV moves completely following the spot, and P_2 is brought into Equations (25)-(28).

$$v_{k+1(x)} = \left|v_{k+1}\right| \cdot \frac{x}{\sqrt[2]{x^2 + z^2}} \tag{32}$$

$$v_{k+1(z)} = \left|v_{k+1}\right| \cdot \frac{z}{\sqrt[2]{x^2 + z^2}} \tag{33}$$

When the spot is at S3, the laser receiving device has lost the spot at this time, and the spot has no coordinates. At this point, the follower continues to fly at the heading angle and acceleration before the light spot disappears to find the laser spot. At this time, the UAV speed is,

$$v_{k+1} = v_k + aT \tag{34}$$

If no spot is found, the speed drops to 0 and enters the hovering state. The speed is now,

$$v_{k+1} = 0 \tag{35}$$

5 Experiment and results

5.1 UAVs for test

As the F450 quad-axis UAV is flexible and small, capable of carrying a large load, and has a long endurance, this study chose the F450 quad-axis UAV as the test UAV platform. Its main parameters are listed in Table 4. In navigation and positioning devices, both leader and follower use airborne optical flow sensors and ultrasonic sensors for auxiliary positioning. The leader uses manual operation to control the flight, and the follower realizes the automatic flight function according to the laser tracking system. To accurately describe UAV's trajectory, RTK was used to record UAVs' position. RTK is a NEO-M8P RTK-GNSS module produced by Ublox. The base station is a mobile base station, and the positioning accuracy of the airborne mobile station is centimeter-level and relative coordinates.

Table 4 Main specifications of test UAV

Parameter	Unit	Value
Supply mode	mAh	3S lithium battery, 5300 mAh
Dimensions	mm	370 mm×370 mm×240 mm
payload	kg	1 kg
endurance	min	20 min
Number of propellers		4
Location mode (follower)		Optical flow sensor and ultrasonic sensor
Location mode (leader)		Optical flow sensor and ultrasonic sensor
RTK		Centimeter accuracy
MEMS gyro		6-axis, Sensitivity:16.4 LSB/(°)·s^{-1}

According to the previous design scheme, an automatic navigation device for a UAV based on laser tracking is fabricated. Figure 7 shows a physical diagram of the overall device.

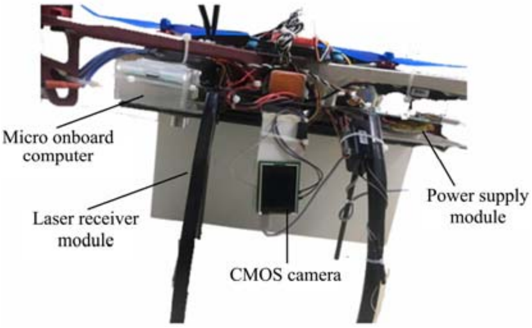

a. Follower UAV equipped with laser tracking system

b. Leader UAV equipped with laser tracking system

Figure 7 Physical diagram of the overall device

5.2 Distance model calibration experiment

The calibration experiment procedure is as follows: taking the intersection of the laser receiving device and the CMOS camera as the origin, vertical lines and horizontal dotted lines are formed on the laser receiving device, and the distance Δx between the adjacent two points is 0.5 cm. The laser receiving device and the CMOS camera are fixed on the ground, and the laser transmitting device fires laser beam at different positions to irradiate the laser receiving device. The pix coordinates $O(0, v)$ of the vertical point of the pix coordinate $A(u, 0)$ of the lateral point and the actual camera coordinate $W(x, z)$ are recorded, and the above experimental steps are repeated thirty times. The average pix coordinates and the average camera coordinates corresponding to each point are substituted into Equations (13) and (14) to solve the corresponding parameters. Figure 8 shows the calibration experiment diagram of the distance relationship between pixel coordinate and image coordinate.

As shown in Figure 9, the difference in the position change of the spot changes correspondingly with the distance between the laser receiving device and the CMOS camera. When the distance is 8 cm, the average difference of the horizontal pix coordinates is 118.2 pix/cm, and the average difference of the vertical pix coordinates is 114.2 pix/cm. When the distance is 24 cm, the average difference of the horizontal pix coordinates is 45.5 pix, and the average difference of the vertical pix coordinates is 46.5 pix. Therefore, linear, logarithmic, quadratic, and exponential curves fit the distance between the laser receiving device and the CMOS camera in horizontal and vertical coordinates. In the horizontal pix coordinate curve fitting, the quadratic curve has R^2=0.9969, and the matching degree and saliency are better than other curves. The fitting curve is $k(d_x)=0.415d^2-19.1d+261.5$. In the vertical pix coordinate curve fitting, the quadratic curve has R^2=0.9729, and the matching degree and saliency are better than other curves. The fitting curve is $k(d_z)=0.231d^2-11.9d+200.8$. Figure 10 is a curve fit diagram of horizontal and vertical pix. The fitted curve and the known parameters u_0=320, v_0=240, and the mounting dimension α=90°, β=0°, γ=0°, X_0=5 cm, Z_0=3 cm are substituted into Equations (18) and (19), and the equations as follows were obtained:

$$X_w=(0.14d^2-6.58d+103.18)\cdot(u-320)+5 \tag{36}$$

$$Z_w=(0.11d^2-5.34d+90.96)\cdot(v-240)+3 \tag{37}$$

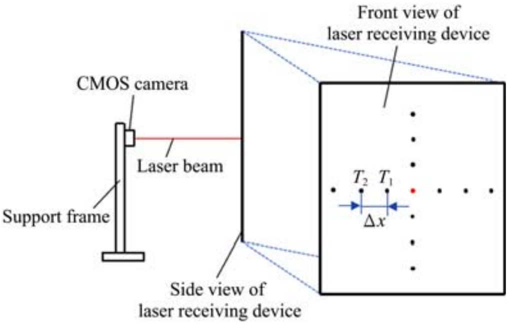

a. Experiment hint diagram

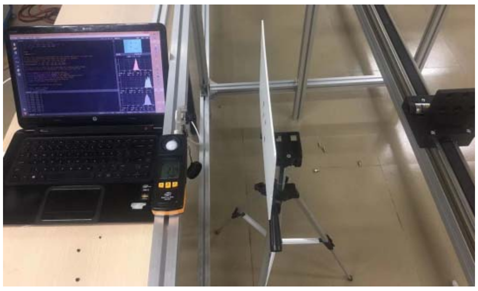

b. Experiment entity diagram

Figure 8 Calibration experiment diagram of distance relationship between pixel coordinate and image coordinate

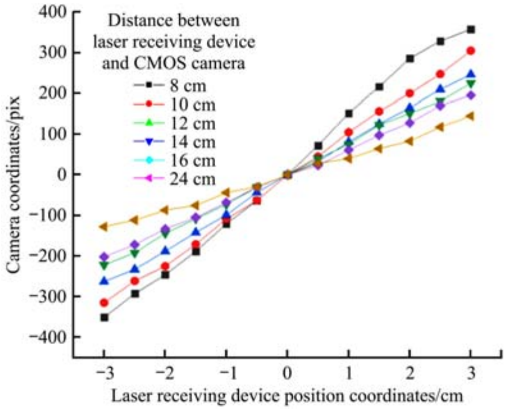

a. Horizontal coordinate

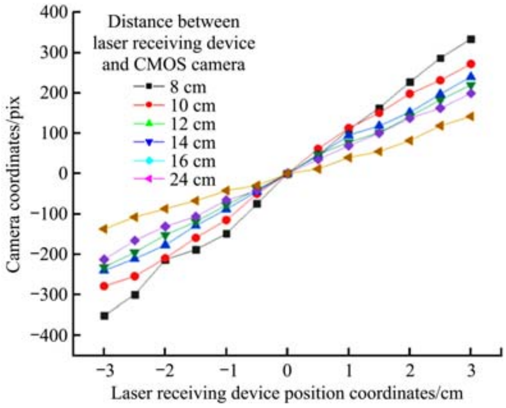

b. Vertical coordinate

Figure 9 Relationship between spot coordinates and actual coordinates at different distances

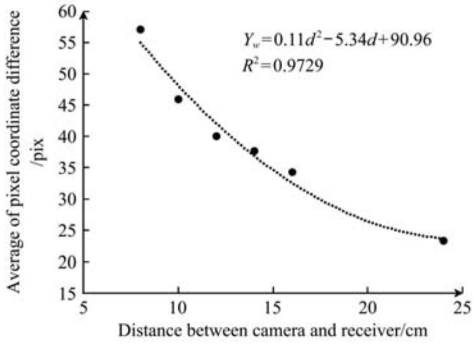

a. Horizontal coordinate

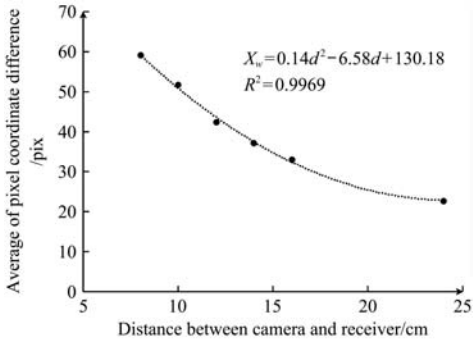

b. Vertical coordinate

Figure 10 Curve fitting map of adjacent coordinate pix under different distances

5.3 Spot recognition experiment with different illumination brightness

The experiment procedure is as follows: Install the fixed support frame and fix the CMOS camera and the laser receiving device in a relative position. Add impurities with the same or similar color as the laser spot on the laser receiving device and within the visible range of the CMOS camera as the interference source 1, and add impurities with the same or similar color as the soil as the interference source 2, as shown in Figure 11. The laser receiving device was placed under 12 luminance levels of 15.4 lx, 27.6 lx, 37.8 lx, 39.4 lx, 71.4 lx, 149.6 lx, 161.8 lx, 192.2 lx, 199.8 lx, 213.2 lx, 35 600 lx, and 48 500 lx. The first ten of them were indoor illumination, and the last two were outdoor illumination. The laser transmitting device is used to illuminate the laser receiving device and remains stationary. The classical KCF algorithm is used to compare the recognition effect with the improved KCF algorithm. After completing the stationary recognition, control the light spot to move between (−3, 0), (3, 0) and (0, −3), (0, 3) and the moving speed is set to 0.2 m/s, 0.4 m/s, 0.6 m/s, 0.8 m/s, 1.0 m/s. Use the classic KCF algorithm to compare the tracking effect with the improved KCF algorithm in this study, record the recognition of light spots in the video stream every second within 1 min, and count the light spot's recognition rate.

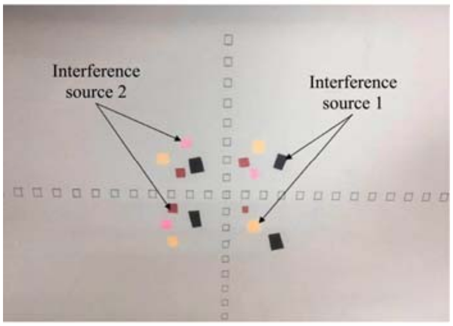

Figure 11 Laser receiving device with interference source

As shown in Figure12a, when the illumination brightness is low, the classical KCF algorithm shows incomplete target contour detection and over-segmentation of the target in different degrees. When the illumination brightness is 71.4 lx, the classical KCF algorithm recognizes the artificially added interference source in the target contour. When the light intensity is 149.6 lx, and the indoor light is above this value, the classical KCF can identify the target contour more accurately. When the laser receiving device and transmitting device are placed in the outdoor light, the classical KCF algorithm will lose the target due to the high outdoor light intensity and the influence of outdoor natural light. It can be seen from Figure 12b that when the ambient light intensity is low, the optimized recognition algorithm can effectively recognize the light spot. As the brightness increases, the algorithm can effectively reduce the impact of light intensity and identify the location of the light spot. Simultaneously, when the lighting conditions are outdoor natural light, the recognition algorithm can accurately identify the target spot and maintain good target detection ability.

As shown in Figure13a, when the classical KCF algorithm is adopted, the contrast between the laser spot and the laser receiving device is relatively bright at the low illumination luminance of 15.4 lx and 27.6 lx, so its recognition rate is relatively high, with the highest recognition rate reaching 75%. When the laser receiving device is in high outdoor light intensity, the highest target tracking rate is only 20% because the laser spot cannot be correctly identified. Due to the influence of natural light, the identification results will be wrong. As shown in Figure 13b, under different illumination luminances, the laser transmitting device adopts different moving speeds. The algorithm of this study can maintain relatively high tracking accuracy, with an average tracking accuracy above 95%. Therefore, by comparing the above two experiments, the improved algorithm has strong robustness regarding the influence of illumination brightness and target movement speed. The tracking effect in the process of color target movement is better than the classical KCF algorithm.

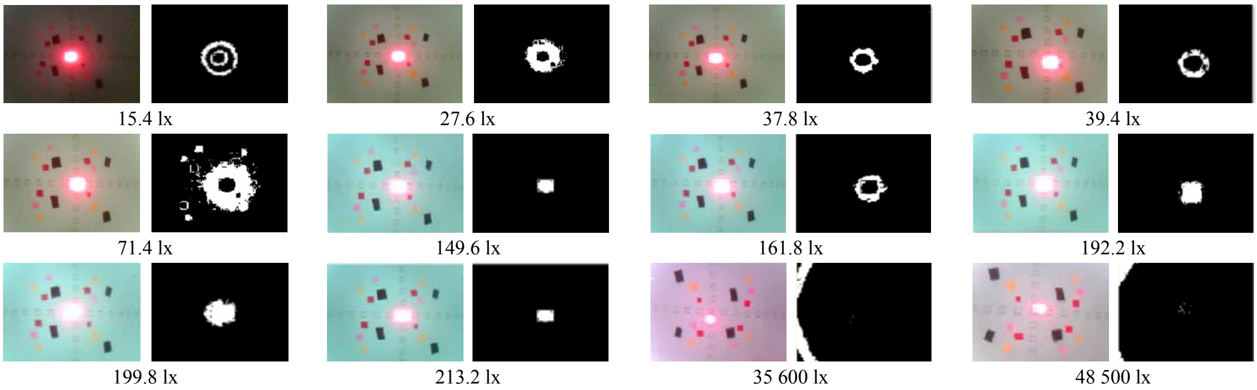

a. Original and identification diagrams of classical algorithms

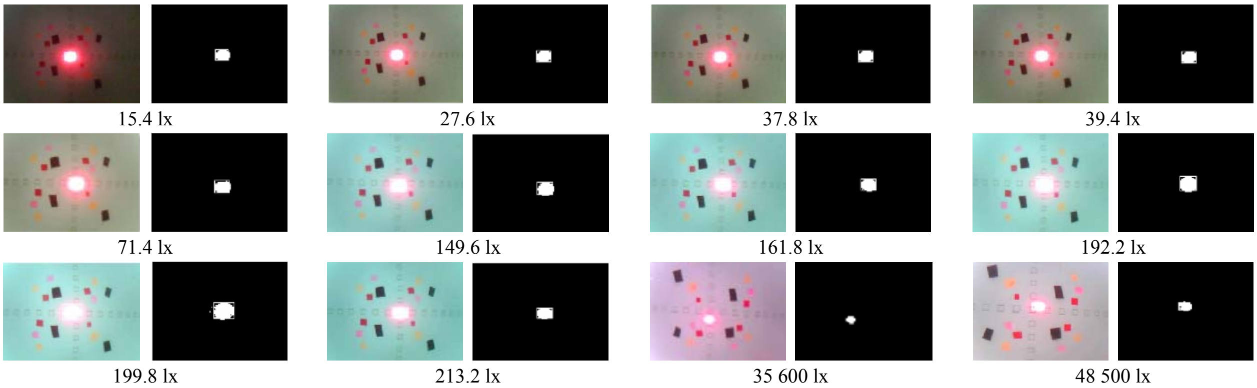

b. Original and identification diagrams of optimization algorithms

Figure 12 Two algorithms of identification and contrast under different brightness conditions

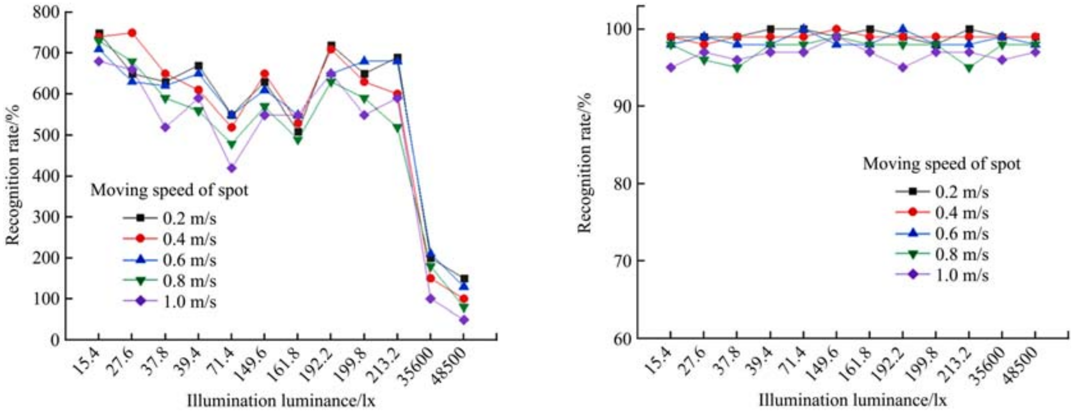

a. Classical algorithm b. Optimization algorithms

Figure 13 Recognition rate of dynamic spots

5.4 Calibration experiment for static body tilt interference

An interference correction experiment in a static environment is conducted to verify the micro-gyroscope coordinate algorithm's accuracy. The experiment procedure is as follows: firstly, fix the laser transmitting device on the flat ground and fix the laser receiving device and CMOS camera in relative positions. Secondly, adjust the relative positions of the transmitting device and receiving device so that the CMOS camera can collect the spot's position information on the receiving device during the angle adjustment. Finally, compare the coordinate errors before and after correction. Figure 14 is the angle (α) of laser receiving device. A total of 7 tilting laser receiving devices at different angles of 5°, 10°, 15°, 20°, 25°, and 30° were simulated, and the position information of light spots collected by the laser recognition device was recorded, as listed in Table 5. The calculation equation of coordinate error is as follows:

$$\Delta X = X_\alpha - X_0 \tag{38}$$

$$\Delta Z = Z_\alpha - Z_0 \tag{39}$$

Table 5 Data comparison before and after tilting interference correction of UAV

Angle /(°)	Actual location /cm	Precorrection error/cm	Correction value/cm	Corrected error/cm
0	(8.40,4.00)	(0, 0)	(8.40,4.00)	(0, 0)
5	(8.02,4.71)	(0.38, 0.71)	(8.37,4.12）	(−0.13,0.12)
10	(7.57,5.39)	(0.83, −1.40)	(8.41,4.05）	(0.11,0.15)
15	(7.08,6.04)	(1.32, -2.04)	(8.43,3.98）	(0.13, 0.12)
20	(6.53,6.63)	(1.87, −2.63)	(8.42,4.01）	(0.12,0.11)
25	(5.92,7.17)	(2.47, −3.17)	(8.42,4.03）	(0.12,0.13)
30	(5.27,7.66)	(3.12, −3.66)	(8.44,3.98）	(0.14, 0.12)

As seen in Table 5, when the laser receiving device is not subject to tilt interference (inclination angle is 0°), the spot's position information is (8.40, 4.00) cm. After the tilt interference, the position information of the spot changes and gradually decreases. After calibration according to the gyroscope angle, the maximum error of the spot position is reduced from the pre-correction (3.12, −3.66) cm to the post-correction (0.14, −0.12) cm. It can be seen that an improved algorithm can better eliminate the interference error caused by the tilt of the laser receiving device caused by the tilt of the fuselage of the UAVs during flight.

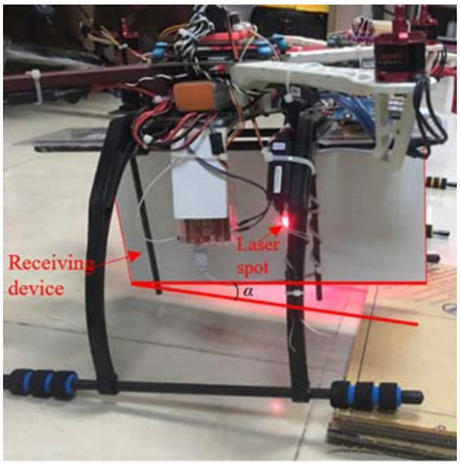

Figure 14 Angle (α°) of laser receiving device

5.5 Automatic collaboration of two UAVs

After the above experiments, it is necessary further to test the tracking device's space tracking effect. A flight experiment is conducted in the school playground at 4 pm, and the weather was a breeze. The laser transmitting device is installed in the leader; the laser receiving device and laser recognition device are installed in the follower. During the flight, the two UAVs' horizontal distance is kept to 2 m and locked in the horizontal position. After completing the laser tracking system's calibration, the leader and follower take off to 1.5 m. Waiting for two UAVs to stably hover, the leader turns on the laser transmitting device and fires a laser beam, the laser receiving device receives the leader's laser and forms a spot, laser recognition device begins gathering spot location information. The leader starts to fly according to the pre-designed flight path, and the maximum flying speed is 2 m/s. The follower fly tracked according to the location of the spot. Figure 15 is the actual flying diagram of leader and follower tracking.

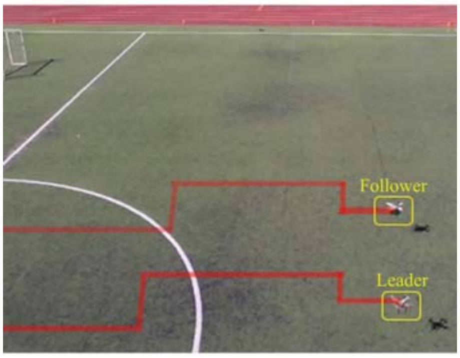

Figure 15 Leader and follower tracking flight

Figure 16a is the three-dimensional trajectory of the leader and follower tracking flight and the leader's preplanned flight path. Figure 16b is the projection of the flight trajectory in the X-Z plane. It can be seen from Figure 16b that when the leader flies in a straight line, the follower can better track the flight of the leader. However, when the current leader turns, the follower's movement trajectory error is relatively large, such as point 1-7. During the hover at point 1, the follower deviated in both the X- and Z-directions, possibly due to wind interference in the sky. When it comes to point 2-7, the deviation is mainly caused by the flying speed control method adopted in the tracking flight in this paper, instead of using the coordinates of geographical position information to control the UAV for tracking the flight. Therefore, in fast flight, the movement distance of followers will exceed the leader's position due to the UAV's fast braking. However, the average return time of the seven inflection points was 0.83 s.

Figure 17 shows the absolute error change of the trajectory of the follower relative to the trajectory of the master during the entire tracking process. It can be seen that during the flight, the absolute error reaches the maximum error at 140 s, which is 17.2 cm. However, the absolute error of the flight trajectory has some jump noise. The main reason is the jump noise generated by the flight decision mode of the light spot in different regions of the laser receiving device. When the light spot is in the non-adjustment zone of the rectangle, the follower uses the airborne sensor to adjust the hover stably. And due to the small size of the UAV frame, there is interference from the natural wind during the flight, which causes the tracking trajectory parameters to drift, and the trajectory error has jumping noise. When the leader is flying straight from point 1 to point 2 in Figure 16b, the follower will fly synchronously according to the position of the light spot. Due to the change of the attitude angle during the flight, the UAV has a height change in the vertical direction. When the accumulated height deviation exceeds the boundary of the non-adjustment zone, the light spot will enter the buffer zone in the vertical direction. At this time, the laser tracking system will adjust the corresponding speed in the vertical direction, so that the light spot returns to the no-adjustment zone in the laser receiving device. Due to the change of the attitude of the follower and the existence of factors of flight decision during the flight, the tracking error of the follower is caused as shown in Figure 17. However, it can be seen from the figure that the average tracking error of the follower remains around 6 cm. Compared with the existing visual tracking methods[13,15], the method proposed in this study has better tracking ability.

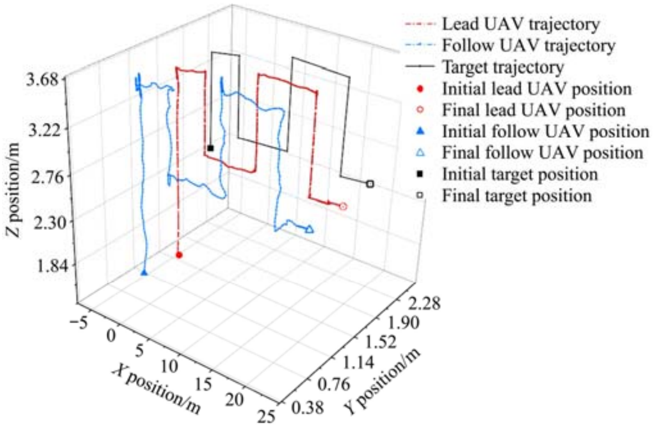

a. Three-dimensional trajectory

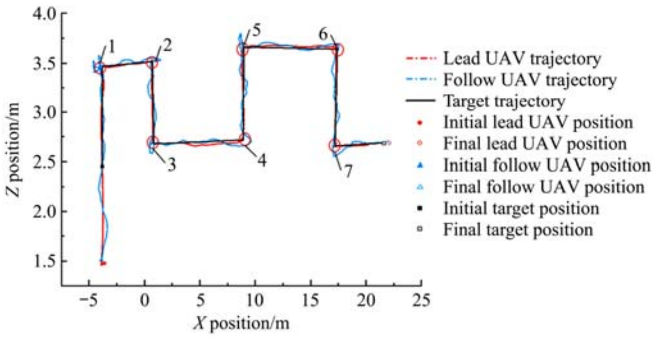

b. Two-dimensional trajectory

Figure 16 Leader and follower tracking flight trajectory

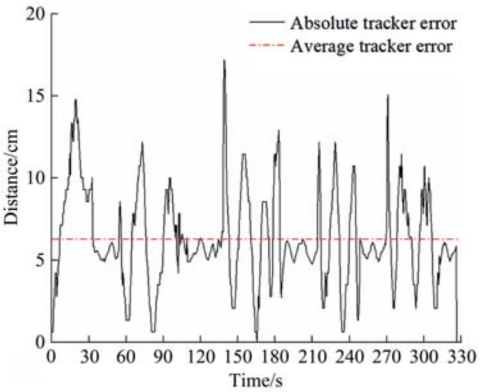

Figure 17 Error variation in the whole process

As listed in Table 6, the relative offset between the follower tracker and the leader tracker is analyzed, from which it can be seen that in the *X*-axis direction, the average offset is 5.2 cm, and the coefficient of variation is 0.0181. In the *Z*-axis direction, the average offset is 7.3 cm, and the coefficient of variation is 0.0414. Compared with the *X*-axis offset, the *Z*-axis direction of the average deviation, maximum deviation, and variation coefficient were greater than in the *X*-direction. The main reason is that there has a natural lateral drift effect of UAVs in the *Z*-direction during flight, and in the *X*-direction, flying UAVs have inertia; therefore, the natural wind has a smaller influence on the flight in the *X*-direction. From the analysis of the whole trajectory, it can be concluded that the average deviation of the whole trajectory is 6.3 cm, and the variation coefficient is 0.0297. Therefore, the device in this study has high reliability when applied to UAVs.

Table 6 Trajectory analysis parameters

Direction	Average offset /cm	Maximum offset/cm	Coefficient of variation
X-direction	5.2	8.8	0.0181
Z-direction	7.3	17.2	0.0414
Full track	6.3	13.0	0.0297

6 Conclusions

In this study, a novel cooperative navigation method was proposed for two UAVs based on laser tracking and the design of a laser tracking system, which successfully combines laser tracking and visual navigation. According to the function requirement, each part of the system was designed and researched. Based on the above experimental analysis results, the following conclusions can be made:

1) In view of the difference in the unit displacement of the light spot between the camera and the laser receiving device at different installation distances, a correlation between the installation distance and the unit displacement was established on the *X*-axis and the *Z*-axis. The coefficients R^2 of the quadratic fitting curve of the *X*-axis and *Z*-axis are 0.9969 and 0.9729 respectively, which can effectively eliminate the influence of the installation distance on the actual movement distance of the light spot.

2) Aiming at the problem of unstable spot recognition due to changes in lighting conditions, and improved KCF real-time spot tracking method was proposed. A scale filter was added based on the displacement filter, sparse matrix cyclic sampling was used instead of full sampling, and SVM was added for online learning of target samples. The improved recognition algorithm can accurately identify the position coordinates of the related light spots when there are multiple interference sources. At the same time, compared with the traditional KCF recognition algorithm, the recognition algorithm in this study can effectively track the light spot under 12 different illumination conditions. Under indoor lighting conditions, the tracking recognition rate of the light spot has increased from 70% to 95%. Under outdoor conditions, the tracking recognition rate of the light spot has increased from 20% to 90%. The experimental results show that the identification and tracking algorithm can effectively reduce the influence of light conditions and interference sources, and has strong robustness.

3) Aiming at tilt interference, a correction algorithm based on a micromachined gyroscope was designed. When the fuselage is tilted 30°, the error is reduced from (3.12, −3.66) cm before correction to (0.14, 0.12) cm after correction. It can better eliminate the interference error of the laser receiving device tilt caused by the tilt of the fuselage of the UAV during the flight.

4) In the outdoor flight experiment of two UAVs, the follower can accurately track the leader for synchronized flight. Comparing the flight trajectories of leader and follower, the average deviation of the two UAVs on the *X*-axis is 5.2 cm, and the coefficient of variation is 0.0181; the average deviation on the *Z*-axis is 7.3 cm, and the coefficient of variation is 0.0414. The experiment results show that the system can accurately realize the

synchronous flight of two UAVs.

The outdoor flight experiment has proved that the tracking system is effective and can reduce the impact of complex lighting conditions and changeable illumination conditions on the visual tracking of UAVs, and achieve stable simultaneous flight of two UAVs. Compared with the existing multi-UAV vision collaboration navigation[13,15], the system in this study has higher accuracy and higher robustness and provides a new navigation method based on optical tracking for multi-UAVs cooperative navigation. But in the process of tracking the flight of the system the follower's trajectory still has jumping noise, and the flight stability of the follower needs to be improved. Therefore, more work would be done in optimizing the method of receiving light spots and flight strategy after receiving the laser. In the following research, the agricultural UAV will be used to carry out a large region of outdoor flight experiments.

Acknowledgments

This work was supported in part by the Laboratory of Lingnan Modern Agriculture Project (Grant No.NT2021009), in part by the Science and Technology Plan of Jian City of China (Grant No. 20211-055316); in part by the National Natural Science Foundation of China (Grant No. 31871520); in part by the Science and Technology Plan of Guangdong Province of China (Grant No. 2021B1212040009,2017B090903007), in part by the Guangdong Basic and Applied Basic Research Foundation under (Grant No. 2020A1515110214), and in part by Innovative Research Team of Agricultural and Rural Big Data in Guangdong Province of China under (Grant No. 2019KJ138). The authors wish to thank sincerely the editors and anonymous reviewers for their critical comments and suggestions to improve the manuscript.

[References]

[1] Fan B K, Li Y, Zhang R Y, Fu Q Q. Review on the technological development and application of UAV systems. Chinese Journal of Electronics, 2020; 29(2): 199–207.

[2] Xue X Y, Lan Y B, Sun Z, Chang C, Hoffmann W C. Develop an unmanned aerial vehicle based automatic aerial spraying system. Computersand Electronics in Agriculture, 2016; 128: 58–66.

[3] Faical B S, Freitas H, Gomes P H, Mano L Y, Pessin G, de Carvalho A C P L, et al. An adaptive approach for UAV-based pesticide spraying in dynamic environments. Computersand Electronicsin Agriculture, 2017; 138: 210–223.

[4] Saeed A S, Younes A B, Islam S, Dias J, Seneviratne L, Cai G. A review on the platform design, dynamic modeling and control of hybrid UAVs. In: 2015 International Conference on Unmanned Aircraft Systems (ICUAS), Denver, USA: IEEE, 2015; pp.806–815. doi: 10.1109/ICUAS.2015.7152365.

[5] Xu C C, Liao X H, Tan J M, Ye H P, Lu H Y. Recent research progress of unmanned aerial vehicle regulation policies and technologies in urban low altitude. IEEE Access, 2020; 8: 74175–74194.

[6] Causa F, Vetrella A R, Fasano G, Accardo D. Multi-UAV formation geometries for cooperative navigation in GNSS-challenging environment. In: 2018 IEEE/ION Position, Location and Navigation Symposium (PLANS), Monterey, USA, 2018; pp.775–785. doi: 10.1109/PLANS.2018.8373453.

[7] Karrer M, Agarwal M, Kamel M, Siegwart R, Chli M. Collaborative 6DoF relative pose estimation for two UAVs with overlapping fields of view. In 2018 IEEE International Conference on Robotics and Automation (ICRA), Brisbane, Australia: IEEE, 2018; pp.6687–6693. doi: 10.1109/ICRA.2018.8461143.

[8] Spurny V, Baca T, Saska M, Penicka R, Krajnik T, Thomas J, et al. Cooperative autonomous search, grasping, and delivering in a treasure hunt scenario by a team of unmanned aerial vehicles. Journal of Field Robotics, 2019; 36(1): 125–148.

[9] Pan R H, Xu S H. Multi-UAV cooperative navigation algorithm based on geometric characteristics. Journal of Ordnance Equipment Engineering, 2017; 10: 55–59. (in Chinese)

[10] Guo K X, Li X X, Xie L H. Ultra-wideband and odometry-based cooperative relative localization with application to multi-UAV formation control. IEEE Transactions on Cybernetics, 2020; 50(6): 2590–2603.

[11] Jongug C, Yudan K. Fuel-efficient three-dimensional controller for leader-follower UAV formation flight. In: 2007 International Conference on Control Automation and Systems, Seoul: IEEE, 2007; pp.806–811. doi: 10.1109/ICCAS.2007.4407011.

[12] Ivanov L I, Obukhova N A, Baranov P S. Review of modern UAV detection algorithms using methods of computer vision. In: 2020 IEEE Conference of Russian Young Researchers in Electrical and Electronic Engineering (EIConRus), St. Petersburg and Moscow: IEEE, 2020; pp.322–325. doi: 10.1109/EIConRus49466.2020.9039352.

[13] Tang Y Z, Hu Y C, Cui J Q, Liao F, Lao M J, Lin F, et al. Vision-aided multi-UAV autonomous flocking in GPS-denied environment. IEEE Transactions on Industrial Electronics, 2019; 66(1): 616–626.

[14] Kalal Z, Mikolajczyk K, Matas J. Tracking-learning-detection. IEEE Transactions on Software Engineering, 2011; 34(7): 1409–1422.

[15] Lin F, Mao P K, Xu D X, Yu Z S, M C B. Vision-based formation for UAVs. Taichung: IEEE, 2014; pp.1375–1380. doi: 10.1109/ICCA.2014.6871124.

[16] Vetrella A R, Causa F, Renga A, Fasano G, Accardo D, Grassi M. Flight demonstration of multi-UAV CDGPS and vision-based sensing for high accuracy attitude estimation. In: 2017 International Conference on Unmanned Aircraft Systems (ICUAS), Miami: IEEE, 2017; pp.237–246. doi: 10.1109/ICUAS.2017.7991378.

[17] Gassner M, Cieslewski T, Scaramuzza D. Dynamic collaboration without communication: Vision-based cable-suspended load transport with two quadrotors. In: 2017 IEEE International Conference on Robotics and Automation (ICRA), Singapore: IEEE, 2017; pp.5196–5202. doi: 10.1109/ICRA.2017.7989609.

[18] Yan L, Fang L F, Wei Z. A study on the sync guidance of the multi-lasers with the micro-vision. In: The 26th Chinese Control and Decision Conference (2014 CCDC), Changsha: IEEE, 2014; pp.1449–1453. doi: 10.1109/CCDC.2014.6852395.

[19] Walter V, Staub N, Franchi A, Saska M. UVDAR system for visual relative localization with application to leader-follower formations of multirotor UAVs. IEEE Robotics and Automation Letters, 2019; 4(3): 2637–2644.

[20] Park H, Choi I, Park S, Choi J. Leader-follower formation control using infrared camera with reflective tag. In: 2013 10th International Conference on Ubiquitous Robots and Ambient Intelligence, Jeju, Korea: IEEE, 2013; pp.321–324.

[21] Fang F, Qian K, Zhou B, Ma X. Real-time RGB-D based people detection and tracking system for mobile robots. In: 2017 IEEE International Conference on Mechatronics and Automation (ICMA), Takamatsu, Japan: IEEE, 2017; pp.1937–1941. doi: 10.1109/ICMA.2017.8016114.

[22] Xiang C, Mao J. Research on target detection method based on HSV fusion Gaussian mixture model. In: 2019 3rd International Conference on Electronic Information Technology and Computer Engineering (EITCE), Xiamen, China: IEEE, 2019; pp.327–331. doi: 10.1109/EITCE47263.2019.9094782.

[23] Janousek J, Marcon P, Pokorny J, Mikulka J. Detection and tracking of moving UAVs. In: 2019 PhotonIcs & Electromagnetics Research Symposium - Spring (PIERS-Spring), Rome: IEEE, 2019; pp.2759–2763. doi: 10.1109/PIERS-Spring46901.2019.9017351.

[24] Henriques J F, Caseiro R, Martins P, Batista J. High-speed tracking with kernelized correlation filters. IEEE Transactions on Pattern Analysis and Machine Intelligence, 2015; 37(3): 583–596.

[25] Li Q, Liu L, Ma X, Chen S, Yun H, Tang S. Development of multitarget acquisition, pointing, and tracking system for airborne laser communication. IEEE Transactions on Industrial Informatics, 2019; 15(3): 1720–1729.

[26] Luo Y, Ye G, Wu Y, Guo J, Liang J, Yang Y. An adaptive Kalman filter for UAV attitude estimation. In: 2019 IEEE 2nd International Conference on Electronic Technology (ICET), Chengdu: IEEE, 2019; pp.258–262. doi: 10.1109/ELTECH.2019.8839496.

[27] Lee D H, Lee S S, Kang H H, Ahn C K. Camera position estimation for UAVs using SolvePnP with Kalman filter. In: 2018 1st IEEE International Conference on Hot Information-Centric Networking (HotICN), Shenzhen: IEEE, 2018; pp.250–251. doi: 10.1109/HOTICN.2018.8606037.

网络首发时间：2023-11-22 11:17:52
网络首发地址：https://link.cnki.net/urlid/11.1964.S.20231121.1431.006

直播稻播前不同土壤火焰温度条件下杂草种子发芽率试验

周志艳[1,2]，李鑫[1,3]，黄俊浩[1,3]，杨得帅[1,4]，林键沁[1,3]，姜锐[1,5]

（1. 华南农业大学工程学院，广州 510642；2. 岭南现代农业科学与技术广东省实验室，广州 510642；3. 广东省农业人工智能重点实验室，广州 510642；4. 广东省农业航空应用工程技术研究中心，广州 510642；5. 华南农业大学南方农业机械与装备关键技术教育部重点实验室，广州 510642）

摘　要：杂草的有效控制是降低直播稻稳产风险的重要措施，播前土壤火焰处理是以非化学方法在进行播种前抑制杂草种子萌发的有效手段。为明确土壤火焰处理中温度场对杂草种子发芽率的影响规律，采用数值模拟方法对燃料分流部件中集管的结构参数进行了研究，数值模拟和验证试验结果表明，当集管内径 d 为 20 mm，气体输入流量为 1.0~3.5 m^3/h 时，最大流量偏差系数$\Delta\eta$ 在 3.0%以内，支管间气体流量分配较均匀。基于数值模拟结果设计了火焰燃烧装置，研究了 6 种输入流量（1.0 ~3.5 m^3/h）的液化石油气燃料对火焰高度和火焰温度分布的影响，以拖拉机行进速度、燃料输入流量和土壤深度作为试验因素，进行了全因素试验，采用稻田间常见的杂草种子研究了温度场对杂草种子发芽率的影响规律。试验结果表明，在常温常压工作环境下，火焰高度和火焰温度最高值均随着燃料输入流量的增大而增大；当拖拉机行进速度为 2.36 km/h，燃料输入流量为 2.5、3.0、3.5 m^3/h 时，土壤温度最高值可分别达到 92.83、116.58、156.83℃；相比未经火焰处理的对照组，当土壤温度达到 92.83℃时，在 α=0.05 的显著性水平下，千金子、异型莎草种子的发芽率显著降低，但马唐、鳢肠种子的发芽率受影响不显著，当土壤温度达到 116.58℃和 156.83℃时，4 种杂草种子的发芽率均显著降低；当土壤温度达到 156.83℃时，马唐、鳢肠、千金子和异型莎草 4 种杂草种子的发芽率分别降低了 94.82%、87.81%、86.54%和 84.05%。田间试验结果表明，土壤火焰处理对稗草、马唐、鳢肠和异型莎草有显著的抑制萌发作用，其相对除草率 $Y\geq$80.00%。

关键词：水稻直播；土壤消杀；燃烧特性；温度场；种子发芽率

中图分类号：S224.9　　**文献标志码：**A

Experiment on Weed Seed Germination Rate in Soil under Different Flame Temperature Conditions before Sowing of Direct-Seeded Rice

ZHOU Zhiyan[1,2] LI Xin[1,3] HUANG Junhao[1,3] YANG Deshuai[1,4] LIN Jianqin[1,3] JIANG Rui[1,5]

(1. College of Engineering, South China Agricultural University，Guangzhou 510642, China 2. Guangdong Laboratory for Lingnan Modern Agriculture, Guangzhou 510642, China 3. Guangdong Provincial Key Laboratory of Agricultural Artificial Intelligence, Guangzhou 510642, China 4. Guangdong Engineering Research Center for Agricultural Aviation Application, Guangzhou 510642, China 5. Key Laboratory of Key Technology on Agricultural Machine and Equipment, South China Agricultural University, Ministry of Education, Guangzhou 510642, China)

收稿日期：2023-09-18 修回日期：2023-10-30

基金项目：岭南现代农业实验室科研项目（NT2021009）、广州市重点研发计划项目（202206010149）、广东省科技计划项目（2021B1212040009）和江西省井冈山农高区省级科技专项（20222−051252−02）

作者简介：周志艳（1972—），男，教授，博士，主要从事农业航空应用技术研究，E-mail：zyzhou@scau.edu.cn

通讯作者：姜锐（1993—），男，副教授，博士，主要从事智能农业装备技术研究，E-mail：ruiojiang@scau.edu.cn

Abstract: Effective weed control is an important measure to reduce the risk of stable yields in direct seeded rice, and pre-sowing soil flame treatment is an effective means of suppressing weed seed germination prior to sowing by non-chemical methods. In order to clarify the law of the influence of the temperature field on the germination rate of weed seeds in soil flame treatment, the structural parameters of the header pipe in the fuel diversion component were investigated using numerical simulation. The results of the numerical simulation and validation test showed that when the inner diameter of the header pipe d was 20 mm and the gas input flow rates were 1.0~3.5 m^3/h, the maximum flow deviation rates $\Delta\eta$ were within 3.0%, more uniform gas flow distribution between outlet branches. Based on the numerical simulation results, a flame combustion device was designed to study the effects of six types of LPG fuels with input flow rates (1.0~3.5 m^3/h) on the flame height and the flame temperature distribution, and a full-factorial test was carried out by using the tractor traveling speed, fuel input flow rate, and soil depth as test factors, and the effect of temperature field on the germination pattern of weed seeds was studied using common weed seeds among rice fields. The test results showed that the flame height and the maximum value of flame temperature both increase with the increase of fuel input flow rates under normal temperature and pressure operating environment; when the tractor traveled at a speed of 2.36 km/h and the fuel input flow rates were 2.5, 3.0, 3.5 m^3/h, the soil temperature could reach 92.83, 116.58 ,156.83℃, respectively; compared to the un-flamed treatment control group, when the soil temperature reached 92.83℃, the germination rate of seeds of *Leptochloa chinensis (L.) Nees* and *Cyperus difformis* were significantly reduced at the significance level of $\alpha=0.05$, but the germination rate of seeds of *Digitaria sanguinalis* and *Eclipta prostrata* were not significantly affected, and the germination rate of seeds of the four weeds were significantly reduced when the soil temperature reached 116.58 and 156.83℃. When the soil temperature reached 156.83℃, the germination of seeds of four weed species *Digitaria sanguinalis*, *Eclipta prostrata*, *Leptochloa chinensis (L.) Nees* and *Cyperus difformis* decreased by 94.82%, 87.81%, 86.54% and 84.05%. The results of the field test showed that the soil flame treatments have significant germination inhibiting effects on *Echinochloa crusgalli*, *Digitaria sanguinalis*, *Eclipta prostrata*, and *Cyperus difformis*. their relative weed control rates $Y \geqslant 80.00\%$.

Key words: direct seeding of rice; soil abatement; combustion characteristics; temperature field; seed germination rate

0 引 言

水稻直播技术作为一种轻简、高效、可持续发展的栽培技术，能够有效缓解我国农村劳动力短缺问题[1-3]。水稻田间杂草种类繁多，生长迅速，危害严重[4]。尤其在直播稻田中存在水稻与杂草同步生长的现象，而水稻的养分竞争能力弱于杂草，促使杂草大量生长，杂草问题已成为阻碍水稻直播技术推广的重要因素[5-6]。杂草的有效控制是降低直播稻稳产风险的重要措施，在播种前抑制杂草种子的萌发是控制草害的有效手段[7]。随着化肥农药减量增效工作的持续推进，使用非化学方法对稻田杂草种子进行处理的需求越来越迫切[8]。

欧美国家使用火焰处理方法对土壤中的病原孢子、虫卵和田间杂草等进行处理，燃烧装置采用拖拉机牵引，常用燃料为丙烷或液化石油气[9-11]，燃烧方式主要采用燃烧强度大、热释放率高的扩散射流火焰[12]，并通过设置燃烧器限制火焰的燃烧范围和射流方向，以形成下喷火焰对土壤进行火焰处理，达到以非化学方法对土壤进行消杀处理的目的[13]。

近年来，已有学者对土壤火焰处理方法进行了系列研究。MILOS 等[14]通过测量燃烧器在不同燃料输入剂量和分布位置下所产生的火焰温度，在综合考虑火焰温度及其作用范围后，确定火焰消杀装置中燃烧器的最佳布置为平行布置；NICOLO 等[15]研制了一种以生物质为燃料的火焰消杀装置，其相比产生同等热值的液化石油气燃料，减少了 72%的燃料成本和118%的二氧化碳排放，但该装置结构复杂，造价高昂，预加热时间长，整体工作效率较低；GUO 等[16]通过田间试验，对比了两种自制的火焰消杀装置对田

间的害虫和杂草的作用效果；MAO 等[17]使用火焰消杀装置开展了土壤处理试验研究，该装置在行进过程中先将土壤压碎并带到燃烧室内，在 2~3 s 内将土壤温度加热至 50~70℃，但是受工作效率的影响，该装置进行土壤处理的成本较高。

综上所述，目前田间土壤火焰处理相关的研究主要集中于装置设计和田间试验，而火焰温度场及其对杂草种子发芽率的影响规律不明确。为明确土壤火焰处理中温度场对杂草种子发芽率的影响规律，本文采用数值模拟方法分析燃料分流部件中集管内径对各支管间燃料流体分配均匀性的影响规律，然后再基于数值模拟结果设计相应的火焰燃烧装置，通过测量火焰高度分布、火焰温度分布和土壤温度变化情况，探讨该装置进行土壤火焰处理中温度场对杂草种子发芽率的影响规律，最后进行田间试验验证土壤火焰处理的作业效果，以期用最低燃烧成本取得较好的旱直播稻田杂草种子萌发抑制效果。

1　燃料分流部件的数值模拟与验证试验

1.1　燃料分流部件设计

燃料分流部件结构示意图如图 1 所示，本文研究的燃料分流部件采用并联管组设计，其原理是将从集管输入的燃料分配至与集管相连的多个支管，以满足作业行宽的要求。燃料入口处的集管以径向方式安装，设置有 4 个支管，支管沿燃料入口处的集管等距对称分布。

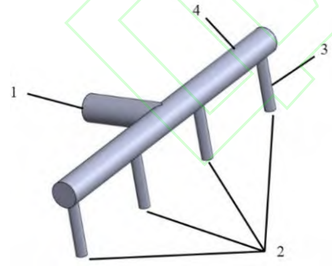

图 1　燃料分流部件结构示意图

Fig. 1　Structure diagram of the fuel diverter component

1. 燃料入口　2. 燃料出口　3. 支管　4. 集管

各支管间燃料流量分配的均匀性是影响火焰热效率的关键。根据 Tong 等[18]的研究，并联管组中集管与支管的内径比直接影响各支管间燃料流量分配的均匀性。本文采用控制变量法，通过数值模拟方法对不同参数的集管内径进行研究，集管内径 d 选取为 5、10、15、20、25、30 mm，燃料分流部件其他结构尺寸参数如表 1 所示。

表 1　燃料分流部件结构尺寸

Tab. 1　Structural dimensions of fuel diverter Components　mm

参数	数值
入口集管长度	100
集管总幅宽	370
支管内径	2
支管长度	50
支管间距	120

1.2　几何模型和边界条件

使用 Solidworks 创建了燃料分流部件三维模型。在 Ansys 2022 R2 Workbench 中选择 Fluid Flow (Fluent)分析系统。整体网格尺寸设置为 0.5 mm，对支管出口处进行局部加密，其网格尺寸为 0.05 mm，采用三角形网格。在流体域中创建的网格节点为 15~100 万个。

在 Fluent 模块中，将气态的液化石油气（主要成分为 C_3H_8 和 C_4H_{10}）设置为传输介质，将入口边界设为速度入口（velocity inlet），出口边界设为压力出口（pressure outlet），其余边界选择为壁面（wall）。流体输入流量设为 2.0 m³/h，出口边界条件设为 1 个标准大气压，采用空气作为流体介质，湍流模型选取 k-ε 湍流模型，近壁面的流动模拟采用标准壁面函数。求解采用 SIMPLEC 算法和二阶迎风格式计算，设置收敛精度为 10^{-4}[19]。

燃料分流部件的出口流量分配均匀性评价指标用每根支管的流量分布不均匀系数 η_i 和最大流量偏差系数 $\Delta\eta$ 来表示[20]。流量分布不均匀系数 η_i 计算公式为：

$$n_i = \frac{nQ_i}{\sum_{i=1}^{n} Q_i} \tag{1}$$

式中 Q_i——第 i 根支管的体积流量，m³/h

n——支管个数

最大流量偏差系数计算公式为：

$$\Delta\eta = (\eta_{\max} - \eta_{\min}) \times 100\% \tag{2}$$

式中 $\eta_{\max}$——并联管组中支管的最大流量分布均匀系数

$\eta_{\min}$——并联管组中支管的最小流量分布不均匀系数

1.3　数值模拟结果与分析

通过数值模拟仿真得到的不同集管内径下各支管入口处速度云图，如图 2 所示。从速度云图可以看出，流体速度沿集管轴线呈两侧对称分布；当集管内径为 5~15 mm 时，集管中流体速度分布趋于平缓，

流体速度的最大值减小，原因在于集管内流体速度减小，流体通过集管内的沿程阻力减小，由支管分流和汇流引起的集管内静压分布变化的作用减小，支管两端的压差减小，各支管间流体速度分配的均匀性提高。此外，当集管内径为 20~30 mm 时，各支管间流体速度分布较均衡，流体速度的最大值趋于稳定，各支管间流体速度分配的均匀性较好。

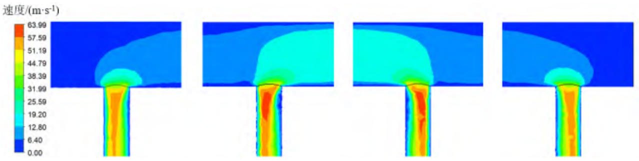

（a）5mm

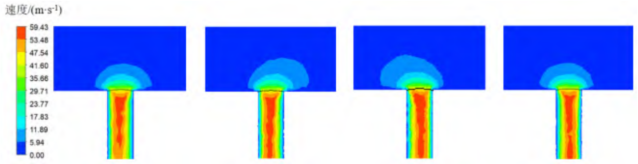

（b）10 mm

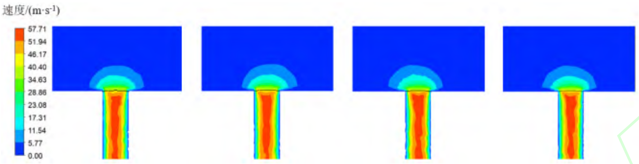

（c）15 mm

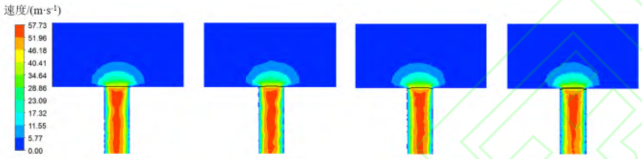

（d）20 mm

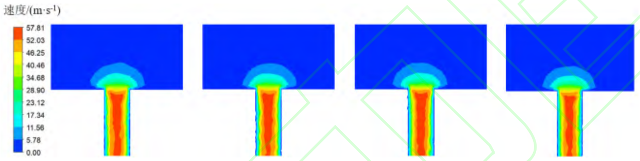

（e）25 mm

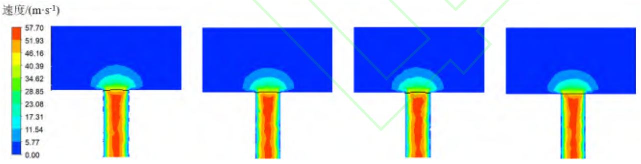

（f）30 mm

图 2 不同集管内径下各支管入口处速度云图

Fig. 2 Velocity magnitude contour at the inlet of each branch with different inner diameters of header pipe’s pipes

根据最大流量偏差系数Δη 随着集管内径 d 的数值变化规律，得出图 3。由图 3 可知，随着集管内径 d 增大，最大流量偏差系数Δη 减小，各支管间流量分配均匀性越好，该趋势与杨程等[20]观察到的结果较为一致。当集管内径为 5 mm 和 10 mm 时，最大流量偏差系数Δη 分别为 5.31%和 3.26%；当集管内径为 15~30 mm 时，最大流量偏差系数Δη 均在 3.0%以内，此时燃料分流部件流量分配的均匀性较好。考虑到燃料分流部件的整体尺寸、质量和成本，采用集管外径 25 mm、内径 20 mm 为实际尺寸。为防止支管在田间作业过程中折断，选取支管外径为 10 mm。

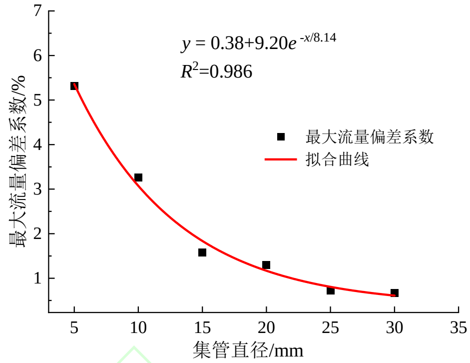

图 3 集管直径变化与最大流量偏差系数的关系曲线

Fig. 3 Relationship curve between maximum flow deviation rate and header pipe’s diameters

1.4 验证试验

在前文设计的基础上，加工了一种燃料分流部件。为验证数值模拟结果的准确性，进行气体流量分配均匀性验证试验，将数值模拟结果与验证试验结果对比。由于气态的液化石油气具有易燃易爆的特点，在使用中有安全隐患，因此本文采用空气作为验证试验的介质，并在数值模拟中对比相同工况下气态液化石油气和空气之间最大流量偏差系数的差值。验证试验所选取的气体输入流量范围为 1.0~3.5 m^3/h，试验在常温常压下的室内环境中进行。图 4 为现场试验图，采用空气压缩机（Outstanding 公司生产的型号为 800W–30L，输出流量范围 0~60L/min）为燃料分流部件提供试验所需的气体流量，通过调节流量计（南京顺来达测控设备有限公司生产的 SLD–LBZ 型玻璃转子流量计，精度为 2.5 级）上的流量阀门以达到试验所需的流量，读取进出口各流量计的量程，计算最大流量偏差系数。

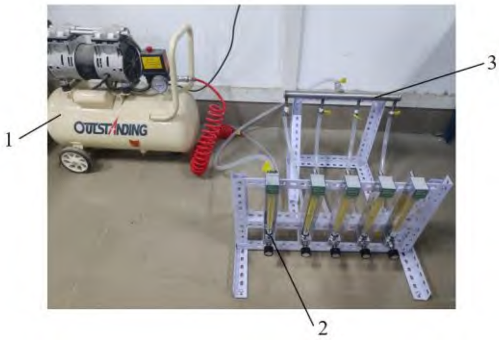

图 4 气体流量分配均匀性验证试验

Fig. 4 Gas flow distribution uniformity verification test

1. 空气压缩机 2. 流量计 3. 燃料分流部件

模拟结果与验证试验结果对比如图 5 所示，F_{af}、F_l 和 F_{as} 分别代表以介质为空气的数值模拟结果、以介质为液化石油气的仿真结果和以介质为空气的试验结果。从图 5 可以看出，当集管内径为 20 mm，气体输入流量为 1.0 ~3.5 m^3/h 时，以空气和液化石油气为介质的数值模拟结果和以空气为介质的试验结果得出的最大流量偏差系数均在 3.0%以内，此时的燃料分流部件流量分配均匀性较好。模拟结果与试验结果之间有一定误差，这主要是因为在数值模拟的过程中忽略了管道、密封等机械损失和容积损失等。

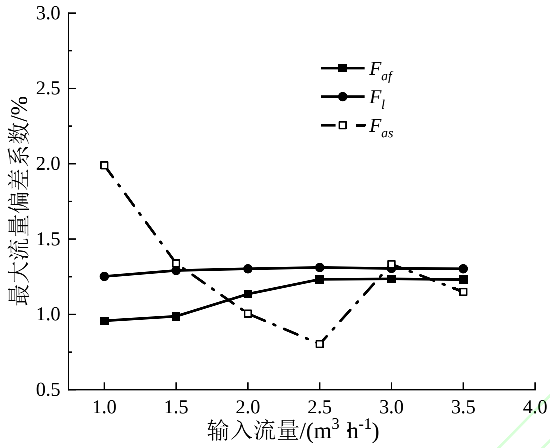

图 5 数值模拟结果与试验结果对比

Fig. 5 Comparison of numerical simulation results with experimental results

2 火焰温度场变化特性试验

2.1 单因素火焰燃烧试验

2.1.1 试验材料与测量仪器

试验设计了一种火焰燃烧装置，主要包括火焰燃烧部件和远程控制系统。火焰燃烧部件主要由燃料分流部件、燃烧器和导热板组成，其结构如图 6 所示。为限制火焰流动方向以保证火焰的热效率，将导热板尺寸 L_1×L_2 设置为 500 mm×300 mm，并将导热板固接在支管上，将 L_3 设置为 200 mm。此外，在导热板设置穿线孔便于控制线远程控制。

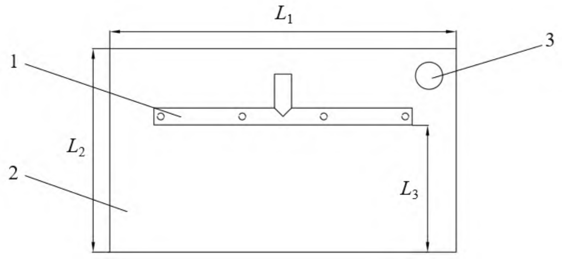

（a）俯视图

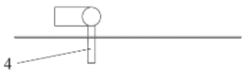

（b）侧视图

图 6 火焰燃烧部件结构示意图

Fig. 6 Structure diagrams of flame burning component

1. 集管 2. 导热板 3. 穿线孔 4. 出口支管

目前田间火焰处理方法通常采用燃烧器约束火焰的宽度和射流方向，燃烧器的形状主要有圆柱型、扇型和方型等。本文以一种能够产生均匀火焰的圆柱型燃烧器为试验对象，该燃烧器外径为 60 mm，壁厚为 1 mm，高度为 100 mm，其剖面图如图 7a 所示。燃烧器气孔沿圆周中心阵列分布，共 8 个，直径为 6 mm，如图 7b 所示。燃烧器编号如图 7c 所示，正面视角与燃料入口方向相反，设置从左到右依此为 1~4 号。火焰燃烧部件各部分材质均采用 304 号不锈钢。

远程控制系统通过按钮控制电动气阀和脉冲点火器的开关。将电动气阀设置于液化石油气罐出口处，用于控制燃料的流出。脉冲点火器具有正负两端，一端连接机架，将燃烧器本身成为负极，另一端连接陶瓷点火针使其成为阳极，使陶瓷点火针在燃烧器内部形成电火花，点燃燃料。远程控制系统由 12 V 电池供电。

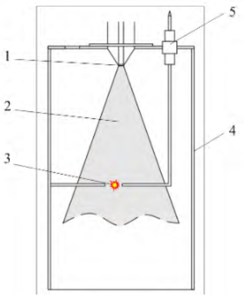

（a）剖面图

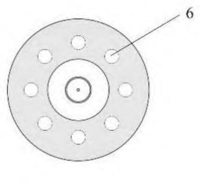

（b）俯视图

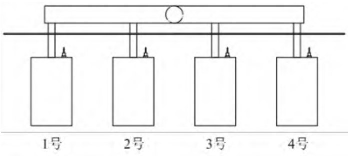

（c）燃烧器编号

图 7 燃烧器结构示意图

Fig. 7 Structure diagrams of burner

1. 支管 2. 气体燃料 3. 电火花 4. 燃烧器外壳 5. 点火针 6. 气孔

燃料输入流量的计量采用南京顺来达测控设备有限公司生产的 SLD-MFC 型质量流量计，量程为 0.15~6.0 m^3/h，精度 1.0 级。红外热成像仪采用美国 FLIR 公司生产的 T1050sc 型非制冷式红外探测器，测量温度范围-40~2000℃，精度±2℃，分辨率 1024 像素×768 像素。视频录制设定辐射率为 0.96，反射温度为 25℃，速率为 30 帧/s，用于拍摄记录火焰中轴线温度分布。高清数码摄像机采用小蚁运动相机进行拍摄，视频录制分辨率为 1920 像素×1080 像素，速率为 25 帧/s，用于拍摄记录火焰高度分布。

2. 1. 2　试验设计

试验以液化石油气为燃料，其流量输入数值依次设置为 1.0~3.5 m^3/h，共 6 个水平。液化石油气的特性和试验操作条件如表 2 所示。

表 2 液化石油气的特性以及试验操作条件

Tab. 2 Characteristics of liquefied petroleum gas and test operating conditions

参数	数值
组成	C_3H_8、C_4H_{10}
密度/($kg\cdot m^{-3}$)	2.35
运动粘度/($m\ s\cdot kg^{-1}$)	7.59×10^{-6}
热值/($MJ\cdot m^{-3}$)	92.1-121.4
环境温度/K	293
环境压力/MPa	0.1
燃料输入流量/($m^3\cdot h^{-1}$)	1.0、1.5、2.0、2.5、3.0、3.5

试验开始前，将火焰燃烧装置固定在距地面高度 1 m 处，设置火焰射流方向竖直指向地面，红外热成像仪和高清数码摄像机通过三脚架水平固定在火焰燃烧装置正面位置，使拍摄范围始终保持一致。在高清数码摄像机拍摄可见光图像时，使用标尺定标，记录标尺所对应的像素个数并计算出每一个像素对应的长度。为便于在图像处理时能准确将火焰与背景进行阈值分割，使用黑色背景布突出火焰的形态特征。为避免风速、光照等环境因素对试验的影响，将试验设置在室内进行，如图 8 所示。视频录制在质量流量计示数稳定后进行，每组试验采用时间不少 40 s。每组试验结束后，待测量仪器及火焰燃烧部件充分冷却至室温（20℃）后，再继续试验。

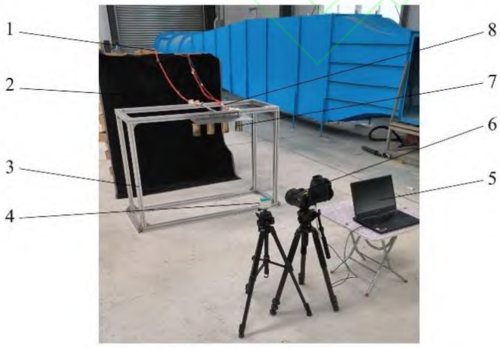

图 8 台架试验布置图

Fig. 8 Bench test

1. 燃料输送管 2. 黑色背景布 3. 铝型材台架 4. 高清数码摄像机 5. 计算机 6. 红外热成像仪 7. 火焰燃烧部件 8. 高压脉冲点火控制线

2. 1. 3　图像处理方法

本文利用图像二值化技术批量处理可见光火焰图像，其原理为：将图像转化为二维矩阵像素点，采用 OTSU 算法（最大类间方差法）对图像阈值进行动态选择。将图像的像素分为火焰部分（像素值为 255）和非火焰部分（像素值为 0），确定竖直方向上像素值为 255 的边界点，最后根据像素点数量计算火焰高度 H[21]。

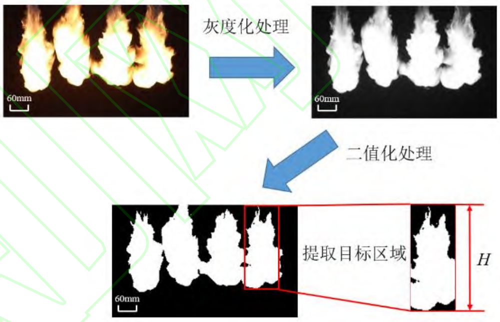

图 9 可见光火焰图像处理过程

Fig. 9 Visible flame image processing

火焰高度 H 被定义为边界点在竖直方向上所间隔的最大的像素点数量，根据提前准备好的像素点和实际尺寸进行换算。可见光火焰图像处理过程如图 9 所示，使用视频处理软件 Premiere 5.5 对原始视频进行处理，在每组试验随机选取连续的 5s，即 125 幅火焰图像作为试验样张[22]。红外热成像仪拍摄记录下热红外图像后，采用 FLIR Research Studio 工具软件从热红外图像中提取各燃烧器火焰射流方向上中轴线的平均温度 T，并在转换成 csv 格式后进行数据处理[23]。每个燃料输入流量选取连续的 30 幅火焰图片作为样本，确定火焰温度分布。

2. 2 不同深度土壤温度变化规律试验

2022 年 11 月在华南农业大学岑村校内农场进行土壤温度变化规律试验研究。试验地的土壤类型为黏土，土壤平均含水率为 16.52%，选择平整的地块作为试验区。为了保证火焰的稳定性和减少外界因素对装置作业效果的影响，试验在自然风风速 2 级以下、天气晴朗的情况下进行。试验现场如图 10a 所示，试验时将火焰燃烧装置挂载到雷沃 M540 型拖拉机上，采用 K 型热电偶（东莞市立林电热制品有限公司，测量范

围 0~600℃，精度为±1℃）测量土壤温度，采用 MAX6675 温度检测模块（美国 MAXIM 公司，精度为±0.25℃）读取温度数值。为了更准确地分析土壤温度变化，将热电偶的热端竖直朝向火焰燃烧区域，将冷端埋入土壤深处。通过调节热电偶热端与土壤表面之间的高度 L_b 来模拟土壤深度的变化，热电偶放置示意图如图 10b 所示。吴竞伦等[24]的研究表明，0~1.0 cm 的土壤深度是稗草、异型莎草、千金子和鳢肠 4 种杂草种子的主要出苗深度，因此本试验将设置在 0~1.0 cm 的土壤深度下进行。试验设计如下：

（1）为确定土壤温度变化规律试验中各参数组合所能达到的土壤温度最高值，以土壤温度为试验指标，以拖拉机行进速度（2.75、2.36 km/h）、燃料输入流量（2.5、3.0、3.5 m^3/h）和土壤深度（0、0.5、1.0 cm）为自变量进行全因素试验，各因素和水平见表 3。

（2）试验共设置有 18 个试验区，每个试验区的尺寸为 0.5 m×0.5 m，设置燃烧器出口距地高度 200 mm，设置热电偶间距 L_t 为 200 mm。试验时设置温度检测模块每 0.2 s 采集一次温度数据，并将温度数据存储到计算机中。

（a）土壤温度变化试验现场图

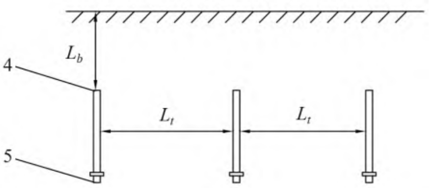

（b）热电偶在土壤中的布置示意图

图 10 土壤温度变化试验图

Fig. 10 Experimental plot of soil temperature change

1. 信息采集系统 2. 土壤火焰处理区域 3. 燃料供应系统及远程控制系统 4. 热电偶热端 5. 热电偶冷端

表 3 不同深度土壤温度变化试验参数

Tab. 3 Experimental parameters of soil temperature variation at different depths

处理组编号	拖拉机行进速度 $/(\mathrm{km\cdot h^{-1}})$	燃料输入流量 $/(\mathrm{m^3\cdot h^{-1}})$	土壤深度/cm
1	2.36	3.5	0
2	2.36	3.0	0
3	2.36	2.5	0
4	2.36	3.5	0.5
5	2.36	3.0	0.5
6	2.36	2.5	0.5
7	2.36	3.5	1.0
8	2.36	3.0	1.0
9	2.36	2.5	1.0
10	2.75	3.5	0
11	2.75	3.0	0
12	2.75	2.5	0
13	2.75	3.5	0.5
14	2.75	3.0	0.5
15	2.75	2.5	0.5
16	2.75	3.5	1.0
17	2.75	3.0	1.0
18	2.75	2.5	1.0

2.3 结果与分析

2.3.1 火焰高度的变化规律

不同燃料输入流量下火焰高度变化示意图如图 11 所示，火焰高度随燃料输入流量的增大而增大，并且火焰的上下往复振荡加剧，火焰高度的波动范围扩大。燃料输入流量从 1.0 m^3/h 增至 3.5 m^3/h 时，火焰高度的增幅超过 230%。在燃料输入流量为 1.0~2.5 m^3/h 时，火焰高度值的最大差值小于 5%，1 号~4 号燃烧器对应的火焰高度差别较小，此时各燃烧器间火焰高度分布较均匀。当燃料输入流量为 3.0 m^3/h 时，从 1 号至 4 号燃烧器对应的火焰高度依此为 317.99、361.43、379.18、333.68 mm；当燃料输入流量为 3.5 m^3/h 时，从 1 号~4 号燃烧器对应的火焰高度依此为 409.30、436.44、418.17、384.19 mm。这表明当燃料输入流量为 3.0~3.5 m^3/h 时，火焰高度继续增大，且火焰高度出现“中间高两边低”的现象。

对于多个扩散射流火焰的相互作用而言，输入流量增大，在相同时间内燃料喷射的距离增大，火焰高度相应增大,这与 LIU 等[25]的研究结果较为一致。而当多个火源靠近时，相互竞争有限的氧气，导致中间燃烧器（2 号和 3 号）的燃料需要扩散至距燃烧器出口更远的位置才可与氧气接触并发生燃烧，因此中间（2 号和 3 号）燃烧器的火焰高度比两边（1 号和 4 号）燃烧器的火焰高度更大。

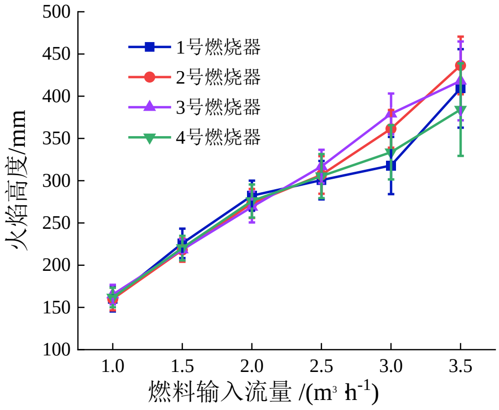

图 11 不同燃料输入流量下火焰高度变化

Fig. 11 Flame height with different fuel input flow rates

2. 3. 2 火焰温度的分布规律

不同燃料输入流量下火焰温度分布如图 12 所示。由图 12 可知，火焰温度分布的曲线呈现单驼峰形状，在燃烧器出口处，温度较低，随着燃烧器出口距离的增大，温度先增大后快速减小。这是因为处于湍流状态下的燃料在发生放热反应前发生裂解，因而主要的放热反应并不在燃烧器出口处进行，而是在距离出口一定高度处进行。然后，火焰对外界进行热辐射并不断卷吸周围冷空气，致使火焰温度逐渐减小。

随着燃料输入流量的增大，对应的火焰温度最大值逐渐增大，温度最高点逐渐远离燃烧器出口；火焰温度最高点位于燃烧器出口位置约 1/2~2/3 火焰高度之间，整体处于火焰高度中线偏下的位置。在田间火焰处理过程中，燃烧器与土壤表面的距离一般不低于 200 mm，若燃烧器出口距地高度过小则可能导致碰撞和损坏[26]。为保证火焰温度最高点能够贴合土壤表面，以提高加热效率，因此要求燃烧器出口处距火焰温度最高点处的高度 H_t 和燃烧器出口处距地高度 H_f 之间的关系满足 $H_t \geqslant H_f \geqslant 200$ mm，并以此为限制条件，可选取燃料输入流量为 2.5、3.0、3.5 m^3/h 共 3 个水平。在 3 个水平下，各燃烧器对应的火焰温度分布主要为中间高两边低，即火焰温度最高点出现在中间两个燃烧器的火焰中。3 个水平下，中间燃烧器的火焰温度最高值 T_m 分别为 293.33、319.38、366.44℃，两边燃烧器火焰温度最高值 T_n 分别为 249.63、245.73、271.33℃，相同条件下 T_m 与 T_n 的之间差值呈逐渐增大的趋势。这是由于在燃料输入流量增大的过程中，中间燃烧器对应的火焰燃烧更加剧烈，卷吸了更多空气，使得中间火焰的火力更集中，温度更高。综上所述，在燃烧器出口距地高度为 200 mm 时，燃料输入流量选择 2.5~3.5 m^3/h 较合适。

2. 3. 3 不同深度土壤温度的变化规律

不同试验参数下土壤温度随时间变化规律如图

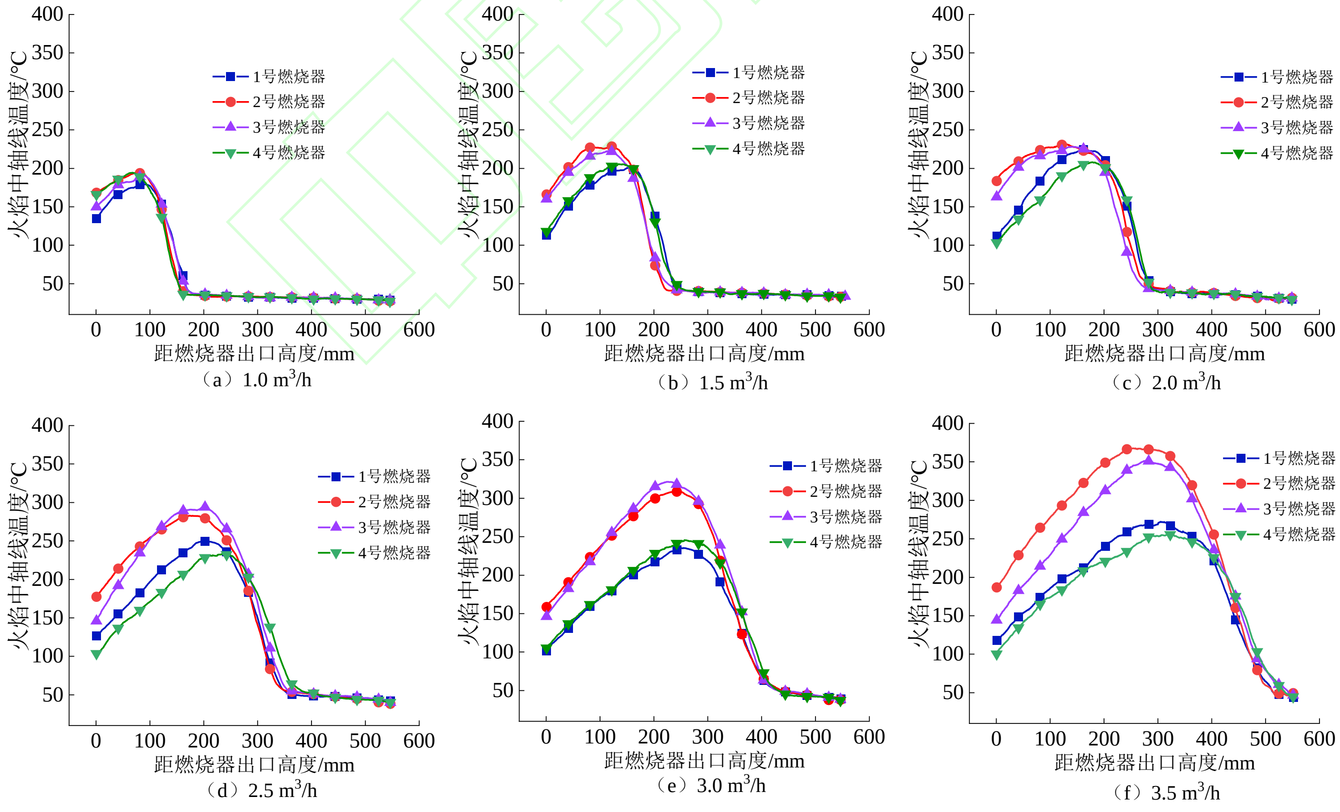

（a）1.0 m^3/h （b）1.5 m^3/h （c）2.0 m^3/h

（d）2.5 m^3/h （e）3.0 m^3/h （f）3.5 m^3/h

图 12 不同燃料输入流量下火焰温度分布

Fig. 12 Flame temperature distribution at different fuel input flow rates

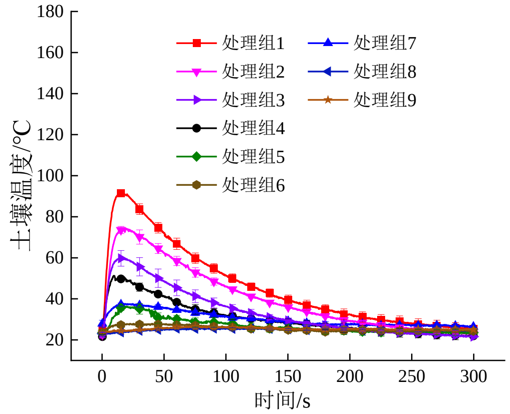

（a）拖拉机行进速度为 2.75 km/h 时

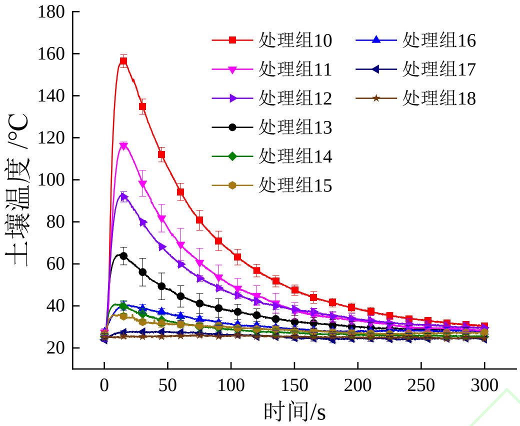

（b）拖拉机行进速度为 2.36 km/h 时

图 13 不同试验参数下土壤温度随时间变化

Fig. 13 Soil temperature values with time under different experimental parameters

13 所示。随着时间的推移，土壤温度变化表现为先快速增大、后缓慢减小的趋势，这是由于火焰释放的大量热量在经过土壤表面时，可使土壤温度在短时间内快速增大，火焰远离后，土壤不断与周围环境进行热交换，土壤温度缓慢减小。在相同燃料输入流量下，土壤温度最高值随着土壤深度的增大而减小，这是由于随着土壤深度增大，更多的土壤能够吸收热量，削弱了火焰对一定深度内土壤的影响。在相同土壤深度下，拖拉机行进速度 2.36 km/h 对应的温度最高值比行进速度 2.75 km/h 的大，可以看出，土壤深度和拖拉机行进速度一定时，土壤温度随着燃料输入流量的增大而增大，这是由于火焰温度随着燃料输入流量增大而增大，导致处理后的土壤在单位时间内所受的热量增大，其温度也相应增大。

根据现有研究，绝大多数杂草种子的致死温度在 80℃以上[27, 28]，结合土壤温度变化规律试验研究结果可以看出，处理组 1、10、11、12 的土壤温度最高值可分别达到 91.67、92.83、116.58、156.83℃，土壤温度最高值均高于 80℃，此时土壤深度均为 0 cm，能够满足土壤火焰处理的温度要求。而当土壤深度在 0.5 cm 以下时，土壤温度最高值均低于 80℃，不能满足土壤火焰处理的温度要求，这可能是因为土壤的导热系数较大，有限的火焰热量不能对土壤表面以下的土壤进行有效的加热处理，而土壤表面处能够直接接触火焰，因此能对其进行较为有效的加热处理。由于处理组 1 和处理组 10 的土壤温度最高值仅相差 1.16℃，数值较为接近，为方便后续试验，选择处理组 10、11 和 12 作为后续的试验参数。

3 温度场对杂草种子发芽率的影响

3.1 试验方法

选择稻田中常见的杂草：马唐、鳢肠、千金子和异型莎草作为研究对象。2022 年 8 月份在华南农业大学增城试验教学基地的稻田收集群落中常见杂草种子，每个品种的种子均来自不少于 30 株大小相近的个体。将收集的种子风干并分拣以去除小枝、叶或花序，每个品种选取 1000 粒籽粒均匀、饱满的种子。将采集好的杂草种子存放在-5℃低温环境中保存 4 个月后进行试验。试验设计如下：

(1) 对杂草种子品种和燃料输入流量进行全因素试验，杂草种子包括马唐、鳢肠、千金子和异型莎草，共 4 个品种；根据前文优选的试验参数，设置为未经火焰处理组、处理 10、11 和 12 共 4 个水平。

(2) 设置燃烧器出口距土壤表面高度为 200 mm。每组试验均在尺寸为 0.5 m×0.5 m 的土壤表面均匀撒 250 粒对应的杂草种子，在火焰处理后回收杂草种子，使用蒸馏水洗净，放置在自然环境中风干。

(3) 每组试验随机选取 50 粒风干后的种子，放入玻璃培养皿并使用培养箱培养（QHX-250 型常州金坛良友仪器有限公司），重复 4 次。试验时将培养箱的温度设置为 30℃，并将光照模式设置为“12 h 有光和 12 h 无光交替”模式。

3.2 评价指标

以杂草种子发芽后 14d 内的发芽特性为试验指标，以种子露出幼苗为标志，每天检查种子的出苗情况，记录后将幼苗及时拔除。计算公式为[29]：

$$G_p = \sum G_t / N \times 100\% \tag{3}$$

$$G_e = \sum G_5 / N \times 100\% \tag{4}$$

$$G_i = \sum G_t / D_t \tag{5}$$

$$T = \sum (G_t \times D_t) / N \tag{6}$$

式中　G_p——发芽率，%

N——供试种子数

G_e——发芽势，%

G_i——发芽指数

T——平均发芽时间，d

G_t——第 t 天发芽种子数

D_t——第 t 天发芽天数，d

杂草种子的平均发芽时间越长，越有利于水稻吸收养分；杂草种子的发芽指数、发芽势和发芽率越小，说明杂草种子的活性越差，越有利于水稻的生长。

表 4 不同燃料输入流量处理下杂草种子发芽特性变化

Tab. 4 Weed seed germination characteristics with different fuel input flow treatments

种子品种	处理组	平均发芽时间/d	发芽指数	发芽势/%	发芽率/%
马唐	未经火焰处理	4.57±0.37	21.23±1.82	20.00±1.47	29.00±1.66
	10	3.19±0.22	19.50±1.56	20.50±0.95	23.00±1.32
	11	3.48±0.34	10.45±0.71	9.50±1.18	12.50±1.11
	12	3.00±0.57	1.08±0.21	1.50±0.25	1.50±0.25
鳢肠	未经火焰处理	3.88±0.58	15.32±1.13	15.00±0.65	20.50±2.09
	10	4.43±0.56	9.48±1.59	9.00±0.87	14.00±1.63
	11	4.69±0.84	5.58±0.97	4.50±0.75	8.00±1.35
	12	8.29±1.50	0.66±0.15	0.00±0.00	2.50±0.48
千金子	未经火焰处理	2.88±0.26	25.24±3.75	23.00±2.96	26.00±3.08
	10	4.24±0.26	7.87±1.03	9.50±1.55	12.50±1.31
	11	2.94±0.63	8.10±1.10	6.50±0.85	8.00±1.22
	12	5.71±1.22	1.67±0.40	2.00±0.58	3.50±0.75
异型莎草	未经火焰处理	6.51±0.36	55.91±2.87	30.00±0.00	81.50±2.17
	10	6.74±0.53	27.56±0.63	18.50±2.29	59.50±2.56
	11	7.42±1.71	6.61±1.00	5.00±0.96	18.00±3.34
	12	8.08±0.97	3.99±0.26	1.50±0.25	13.00±1.32

3.3 结果与分析

不同燃料输入流量对应的杂草种子发芽特性如表 4 所示。从表 4 可以看出，处理组 10 中马唐种子、鳢肠种子的发芽指数和发芽率与未处理组没有显著差异，其余处理组中杂草种子的发芽指数和发芽率对比未处理组均有显著差异，且随着土壤温度的增加而逐渐减小。处理组 10 中马唐种子的发芽势与未处理组没有显著差异，其余处理组中杂草种子的发芽势对比未处理组均有显著差异，且随着土壤温度的增加而逐渐减小。这说明当土壤温度达到 92.83℃以上时，已经超过了鳢肠种子、千金子种子和异型莎草种子的安全温度，种子活力大幅降低。而马唐种子则需要在土壤温度达到 116.58℃以上时才能显著降低其种子活力。

此外，在处理组 10 中，马唐、鳢肠、千金子和异型莎草种子的发芽率相比未处理组分别减小了 20.69%、31.71%、51.92%和 27.00%。在处理组 11 中，马唐、鳢肠、千金子和异型莎草种子的发芽率相比未处理组分别减小了 56.90%、60.98%、69.23%和 77.91%。在处理组 12 中，马唐、鳢肠、千金子和异型莎草种子的发芽率相比未处理组分别减小了 94.82%、87.81%、86.54%和 84.05%。

随着土壤温度的增加，杂草种子的发芽率逐渐减小。相比未处理组，92.83℃的土壤温度可以使千金子种子和异型莎草种子的发芽率显著减小，但不足以使马唐种子和鳢肠种子的发芽率显著减小，当土壤温度达到 116.58℃和 156.83℃时，4 种杂草种子的发芽率均显著减小，这表明马唐种子和鳢肠种子耐热性较好，可能需要提高土壤温度或延长土壤温度处于较高温度的时间，以达到较好的消杀效果。

4　田间试验

为进一步验证火焰消杀装置对土壤中杂草种子的处理效果，检验其田间作业性能，于 2023 年 7 月在广东省河源市柳城镇下坝村农业科学试验基地开展土壤火焰处理田间试验。田间试验时，以主要存在的杂草稗草、马唐、鳢肠和异型莎草等为处理对象，配套动力为雷沃 M1204–B 型拖拉机，土壤含水率为 21.58%。试验中，燃料输入流量设置为 3.5 m^3/h，作业速度为 2.2 km/h，燃烧器距地高度为 200 mm，在旋耕前、后分别进行一次土壤火焰处理，旋耕前土壤火焰处理效果如图 14a 所示，旋耕后土壤火焰处理过程如图 14b 所示。

土壤火焰处理后，在处理区域随机选取 4 个 500

mm×500 mm 的采样点，调查杂草在第 42 天的对照组发芽数量 Z_1 和对照组发芽数量 Z_2，结果如表 5 所示，并计算相对除草率 Y，计算公式为：

$$Y=\frac{Z_1-Z_2}{Z_1}\times 100\% \qquad (7)$$

式中 Z_1——对照组发芽数量，株

Z_2——处理组发芽数量，株

（a）旋耕前火焰热力消杀处理效果图

（b）旋耕后火焰热力消杀处理过程

图 14 田间火焰热力消杀试验

Fig. 14 Field Flame Thermal Abatement Test

表 5 田间试验各种类杂草发芽率

Tab. 5 Germination rates of various weed types in field test

杂草种类	对照组发芽数量 Z_1	处理组发芽数量 Z_2	相对除草率 Y/%
稗草	6	1	83.33
马唐	13	2	84.62
鳢肠	5	1	80.00
异型莎草	11	0	100.00

田间试验结果表明，在土壤火焰处理后第 42 天，相比对照组，土壤火焰处理组对稗草、马唐、异型莎草和鳢肠有显著的抑制萌发作用，相对除草率 $Y \geqslant 80.00\%$。

5 结论

(1) 燃料分流部件中集管内径对各支管间燃料流量分配的均匀性有重要影响。通过数值模拟和验证试验得出，当集管内径 d 为 20 mm，气体输入流量为 1.0 ~3.5 m^3/h 时，最大流量偏差系数 $\Delta\eta$ 在 3.0%以内，支管间流体流量分配较均匀。

(2) 火焰高度和火焰温度最高值均随着燃料输入流量的增大而增大。土壤温度变化规律试验结果表明，当拖拉机前进速度为 2.36 km/h，燃料输入流量为 2.5、3.0、3.5 m^3/h，燃烧器出口距地高度为 200 mm 时，土壤温度最高值可分别达到 92.83、116.58、156.83℃。

(3) 4种杂草种子的平均发芽时间、发芽指数、发芽势和发芽率等特性指标随着土壤温度的增大而逐渐减小。相比未经火焰处理的对照组，当土壤温度达到92.83℃时，在 $\alpha=0.05$ 的显著性水平下，火焰处理千金子、异型莎草种子的发芽率显著降低，但对马唐、鳢肠种子的发芽率影响不显著，当土壤温度达到116.58℃和156.83℃时，4种杂草种子的发芽率均显著降低，当土壤温度达到156.83℃时，马唐、鳢肠、千金子和异型莎草4种杂草种子的发芽率分别降低了94.82%、87.81%、86.54%和84.05%。

(4) 从土壤温度变化规律试验看出，土壤火焰处理主要适用于水稻旱直播种植，对较干旱土壤表面的加热效果较好，对土壤内部的加热效果受土壤导热系数和土壤含水量等因素的影响不明显。因此，如果需要对土壤内部的杂草种子进行火焰处理，可以先进行旋耕处理，将杂草种子带到土壤表面，再进行土壤火焰处理。另外，田间试验表明，土壤火焰处理对稗草、马唐、鳢肠和异型莎草有显著的抑制萌发作用，其相对除草率 $Y \geqslant 80.00\%$。

参 考 文 献

1 罗锡文，王在满，曾山，等. 水稻机械化直播技术研究进展[J]. 华南农业大学学报, 2019, 40(5): 1-13.
LUO Xiwen, WANG Zaiman, ZENG Shan, et al. Recent advances in mechanized direct seeding technology for rice[J]. Journal of South China Agricultural University,2019,40(5):1 - 13. (in Chinese)

2 罗锡文，廖娟，胡炼，等. 提高农业机械化水平促进农业可持续发展[J]. 农业工程学报, 2016, 32(1): 1-11.
LUO Xiwen, LIAO Juan, HU Lian, et al. Improving agricultural mechanization level to promote agricultural sustainable development[J]. Transactions of the CSAE,2016,32(1):1 – 11. (in Chinese)

3 臧英，罗锡文，周志艳. 南方水稻种植和收获机械化的发展策略[J]. 农业机械学报, 2008(1): 60-63.

ZANG Ying, LUO Xiwen, ZHOU Zhiyan. Development strategy on rice planting and harvesting mechanization in South China[J]. Transactions of The Chinese Society for Agricultural Machinery, 2008(1):60 – 63. (in Chinese)

4 张斌，董立尧. 水稻田杂草群落演化原因及趋势浅析[J]. 贵州农业科学, 2009, 37(2): 58-60.

ZHANG Bin, DONG Liyao. Preliminary analysis on reason and trend of weed community evolution in paddy field[J]. Guizhou Agricultural Sciences, 2009,37(2):58 – 60. (in Chinese)

5 张耗，余超，陈可伟，等. 直播方式对水稻生理性状和产量的影响及其成本分析[J]. 农业工程学报, 2017, 33(13): 58-64.

ZHANG Hao, YU Chao, CHEN Kewei, et al. Effect of direct-seeding methods on physiological characteristics and grain yield of rice and its cost analysis[J]. Transactions of the CSAE,2017,33(13):58 – 64. (in Chinese)

6 张夕林，张谷丰，孙雪梅，等. 直播稻田杂草发生特点及其综合治理[J]. 南京农业大学学报, 2000(1): 117-118.

ZHANG Xilin, ZHANG Gufeng, SUN Xuemei, et al. Characteristics and comprehensive control of weeds in direct seeding paddy fields[J]. Journal of Nanjing Agricultural University,2000(1):117-118. (in Chinese)

7 王卫，谢小立，谢永宏. 稻田土壤种子库研究进展[J]. 生态环境学报, 2010, 19(11): 2758-2763.

WANG Wei, XIE Xiaoli, XIE Yonghong. Progress in the researches of seed bank in rice paddy fields[J]. Ecology and Environmental Sciences, 2010,19(11):2758 – 2763. (in Chinese)

8 丛晓男，单菁菁. 化肥农药减量与农用地土壤污染治理研究[J]. 江淮论坛, 2019(2): 17-23.

CONG Xiaonan, SHAN Jingjing. Research on input of chemical fertilizers and pesticides and soil pollution control of agricultural land[J]. Jiang-Huai Tribune, 2019(2):17 – 23. (in Chinese)

9 ASCARD J. Effects of flame weeding on weed species at different developmental stages[J]. Weed research, 1995, 35(5): 397-411.

10 SIVESIND E C, LEBLANC M L, CLOUTIER D C, et al. Impact of selective flame weeding on onion yield, pungency, flavonoid concentration, and weeds[J]. Crop Protection, 2012, 39: 45-51.

11 RAHKONEN J, PIETIKAINEN J, JOKELA H. The effects of flame weeding on soil microbial biomass[J]. Biological Agriculture & Horticulture, 1999, 16(4): 363-368.

12 ULLOA S M, DATTA A, MALIDZA G, et al. Yield and yield components of soybean [Glycine max (L.) Merr.] are influenced by the timing of broadcast flaming[J]. Field Crops Research, 2010, 119(2-3): 348-354.

13 STEPANOVIC S, DATTA A, NELISON B, et al. The effectiveness of flame weeding and cultivation on weed control, yield and yield components of organic soybean as influenced by manure application[J]. Renewable agriculture and food systems, 2016, 31(4): 288-299.

14 RAJKOVIC M, MALIDZA G, STEPANOVIC S, et al. Influence of burner position on temperature distribution in soybean flaming[J]. Agronomy, 2020, 10(3): 391.

15 MORSELLI N, PUGLIA M, PEDRAZZI S, et al. Energy, environmental and feasibility evaluation of tractor-mounted biomass gasifier for flame weeding[J]. Sustainable Energy Technologies and Assessments, 2022, 50: 101823.

16 GUO Wenlei, LI Feng, WU Dandan, et al. Effectiveness of flame for preplant pest management in leaf vegetable fields[J]. Hort Technology, 2019, 29(6): 788-794.

17 MAO Liangang, WANG Qiuxia, YAN Dongdong, et al. Flame soil disinfestation: a novel, promising, non-chemical method to control soilborne nematodes, fungal and bacterial pathogens in China[J]. Crop Protection, 2016, 83: 90-94.

18 TONG J C K, SPARROW E M, ABRAHAM J P. Geometric strategies for attainment of identical outflows through all of the exit ports of a distribution manifold in a manifold system[J]. Applied Thermal Engineering, 2009, 29(17-18): 3552-3560.

19 孙文峰，王进，常晋恺，等. 喷雾机预混装置动态流场分析与参数优化[J]. 农业机械学报, 2023, 54(4): 83-95.

SUN Wenfeng, WANG Jin, CHANG Jinkai, et al. Dynamic flow field analysis and parameter optimization of premixing divice of spray[J]. Transactions of the Chinese Society for Agricultural Machinery, 2023, 54(4): 83-95.（in Chinese）

20 杨程，刘宏昭，原大宁. 并联管组流体特性分析及均流模型设计[J]. 太阳能学报, 2015, 36(7): 1573-1578.

YANG Cheng, LIU Hongzhao, YUAN Daning. Fluid characteristic analysis and flow sharing model design of parallel pipe group[J]. Acta Energiae Solaris Sinica, 2015,36(7):1573 – 1578. (in Chinese)

21　杨断利，张然，陈辉，等. 蛋鸡羽毛覆盖度计算及其与体温关系研究[J]. 农业机械学报, 2022, 53(10): 242-251.
YANG Duanli, ZHANG Ran, CHEN Hui, et al. Calculation of feather coverage and relationship between coverage and body temperature in laying hens[J]. Transactions of the Chinese Society for Agricultural Machinery, 2022, 53(10): 242-251.（in Chinese）

22　张玉涛，林国铖，史学强，等. 横向声波扰动下的乙醇燃烧火焰结构和振荡特性[J]. 工程科学学报, 2022, 44(8): 1453-1461.
ZHANG Yutao, LIN Guocheng, SHI Xueqiang, et al. Flame structure and oscillation characteristics of ethanol combustion under transverse acoustic disturbance[J]. Chinese Journal of Engineering, 2022,44(8):1453 – 1461. (in Chinese)

23　刘晓文，曾雪婷，李涛，等. 基于改进YOLO v7的生猪群体体温自动检测方法[J]. 农业机械学报, 2023: 1-11.
LIU Xiaowen, ZENG Xueting, LI Tao, et al. Automatic detection method of body temperature in herd of pigs based on improved YOLO v7[J]. Transactions of the Chinese Society for Agricultural Machinery, 2023: 1-11.（in Chinese）

24　吴竞仑，李永丰，张志勇，等. 土层深度对稻田杂草种子出苗及生长的影响[J]. 江苏农业学报, 2003(3): 170-173.
WU Jinglun, LI Yongfeng, ZHANG Zhiyong, et al. Effect of difference soil depths on emergence of weed seeding and its growth in rice Field[J]. Jiangsu Journal of Agricultural Sciences, 2003(3): 170 – 173.（in Chinese）

25　LIU Changchun, LIU Xinle, GE Hong, et al. On the influence of distance between two jets on flickering diffusion flames[J]. Combustion and Flame, 2019, 201: 23-30.

26　ULLOA S M, DATTA A, KNEZEVIC S Z. Growth stage impacts tolerance of winter wheat (Triticum aestivum L.) to broadcast flaming[J]. Crop Protection, 2010, 29(10): 1130-1135.

27　陈树人，栗移新，潘雷. 热除草技术现状和展望[J]. 安徽农业科学, 2007(33): 10695-10697.
CHEN Shuren, LI Yixin, PAN Lei. Review and Prospect of Thermal Weed Control Technologies[J]. Journal of Anhui Agricultural Sciences,2007(33):10695 – 10697. (in Chinese)

28　许永福. 刺罩式土壤蒸汽除草消毒装置设计及试验[D]. 西北农林科技大学, 2020.
XU Yongfu. Design and experiment of spike-hood soil steam weeding and disinfection device[D]. Yangling: Northwest A&F University, 2020. (in Chinese)

29　杨洪伟，张丽颖，纪建伟，等. 低场核磁共振分析聚乙二醇对萌发期水稻种子水分吸收的影响[J]. 农业工程学报, 2018, 34(17): 276-283.
YANG Hongwei, ZHANG Liying, JI Jianwei, et al. Effect of establishment and application of prediction model of soil water in walunt orchard based on unmanned aerial vehicle thermal infrared imagery[J]. Transactions of the CSAE, 2018,34(17):276 - 283. (in Chinese)

Computers and Electronics in Agriculture 229 (2025) 109760

Contents lists available at ScienceDirect

Computers and Electronics in Agriculture

journal homepage: www.elsevier.com/locate/compag

Original papers

Pomelo-Net: A lightweight semantic segmentation model for key elements segmentation in honey pomelo orchard for automated navigation

Xianlu Guan [a,b], Huan Wan [a,b], Zixuan He [f,*], Zibo Liu [a,c], Rui Jiang [a,b,c,d,e,*], Yuanzhen Ou [a,c], Yuli Chen [a,c], Huaning Gu [a], Zhiyan Zhou [a,b,c,d,e,g,*]

[a] *College of Engineering, South China Agricultural University and Heyuan Branch of Guangdong Laboratory for Lingnan Modern Agriculture , Guangzhou 510642, China*
[b] *Guangdong Provincial Key Laboratory of Agricultural Artificial Intelligence (GDKL-AAI), Guangzhou 510642, China*
[c] *Guangdong Engineering Research Center for Agricultural Aviation Application (ERCAAA), Guangzhou 510642, China*
[d] *Key Laboratory of Key Technology On Agricultural Machine and Equipment (South China Agricultural University), Ministry of Education, Guangzhou 510642, China*
[e] *State Key Laboratory of Agricultural Equipment Technology, Guangzhou 510642, China*
[f] *Center for Precision and Automated Agricultural Systems, Washington State University, Prosser, WA 99350, United States*
[g] *Centre for Pesticide Application and Safety, the University of Queensland, Gatton QLD 4343, Australia*

ARTICLE INFO

Keywords:
Honey pomelo orchard
Pomelo-Net
Key elements segmentation
Lightweight
Agricultural robotics

ABSTRACT

Accurately segmenting key elements in honey pomelo orchards is vital for the development of intelligent agricultural robotics in these orchards. In this study, a new model for key elements segmentation (such as roadways, orchard ways, pomelo trees, obstacles, and persons) in honey pomelo orchards, Pomelo-Net, was introduced, in order to conduct autonomous navigation and precise operations of the agricultural robotics working in this area. This study proposes that the Pomelo-Net mainly consists of an encoder and a decoder. Key features from orchard images were efficiently captured by Pomelo-Net using a lightweight, efficient channel attention-Mobilenet V2 (EMNet) feature extraction network in its encoder. To perceive target information across various receptive fields within the orchard, the depthwise separable atrous spatial pyramid pooling (DSASPP) structure was employed by Pomelo-Net. Additionally, the efficient channel attention (ECA) mechanism within Pomelo-Net's deep feature extraction network filtered out irrelevant features from orchard images, enhancing feature utilization without reducing channel numbers. To improve decoding speed and reduce computational load, efficient depthwise separable convolution (DSC) modules were integrated into Pomelo-Net's decoder. Finally, for the loss function of the proposed model, the robust combination of dice loss (DL) and focal loss (FL) functions was utilized in order to address the imbalance between target information pixels and orchard background pixels. The experimental results indicated that Pomelo-Net achieved a mean intersection over union (MIOU) of 89.3% and a mean pixel accuracy (MPA) of 95.1% on the test set for roadways, orchard ways, pomelo trees, obstacles, and persons in "Jinsha" pomelo orchards. Robustness tests demonstrated that satisfactory perception results were delivered by Pomelo-Net under various lighting conditions and motion blur, with MIOU and MPA both exceeding 84.7 % and 90.9 %, respectively. Compared to state-of-the-art models (such as U-Net, PSPNet, Segformer, and HRNet), high accuracy, a lightweight design, robustness, and fast inference were offered by Pomelo-Net, making it highly promising for the development of intelligent pomelo orchard agricultural robotics.

1. Introduction

Pomelo, esteemed for its flavor, aroma, texture, and nutritional richness, stands as a significant economic crop in the region of southeast China (Pei et al., 2022). Specifically, the honey pomelo cultivated in the Jinggang mountains region of Ji'an City, Jiangxi Province, China, is renowned for its sweetness and exceptional nutritional profile, boasting elevated levels of vitamin C, calcium, and magnesium compared to other pomelo varieties. Recently, there has been a notable surge in interest towards the intelligent management of honey pomelo orchards. To realize intelligent orchard management, it is essential to develop intelligent agricultural machinery specifically designed for pomelo orchards.

---

* Corresponding authors at: College of Engineering, South China Agricultural University, Guangzhou 510642, China.
E-mail addresses: zixuan.he2@wsu.edu (Z. He), ruiojiang@scau.edu.cn (R. Jiang), zyzhou@scau.edu (Z. Zhou).

https://doi.org/10.1016/j.compag.2024.109760
Received 23 June 2024; Received in revised form 24 November 2024; Accepted 1 December 2024

These machines or robotics should facilitate advanced plant protection operations as well as other tasks like trenching and fertilization. Orchestrating as a pivotal technology for these intelligent systems, the methods for segmenting key elements play a crucial role in empowering agricultural machineries to dynamically perceive and comprehend the orchard surroundings. This capability facilitates autonomous navigation, precise path planning, and adept obstacle avoidance. Hence, developing a method for segmenting key elements specifically suited for pomelo orchards is imperative.

Traditional computer vision methods are renowned for their stability in controlled environments, interpretability, and low computational costs (Kaushalya Madhavi et al., 2022), making them extensively employed in orchard environment perception. Previous research has demonstrated the efficacy of computer vision in aiding smart robots deployed in diverse orchard settings, including apple orchards (Zhang et al., 2017) and orange groves (Chen et al., 2018), showcasing commendable performance, particularly in obstacle detection within greenhouse environments (Nissimov et al., 2015). Moreover, studies have successfully utilized computer vision techniques to distinguish between trees, non-tree objects, and tree trunks within orchards (Shalal et al., 2015; Lyu et al., 2018). However, recent investigations suggest that while low-cost computer vision methods offer promise, they encounter challenges in accurately detecting and precisely locating various objects within complex orchard environments (Anagnostis et al., 2021; Li et al., 2021).

In recent years, the rapid advancement of deep learning methods has gained significant attention for orchard applications (da Silva et al., 2022; Taner et al., 2024). Object detection algorithms like Faster R-CNN, YOLOv3, YOLOv4, YOLOv5, and YOLOv7 (Huang et al., 2023) have been used to detect orchard traffic signs (Gao et al., 2023), banana clusters (Fu et al., 2022), and tree trunks (Su et al., 2022), providing bounding boxes with positional and dimensional data. This information aids orchard vehicle navigation (Zhou et al., 2022; Jiang et al., 2022) and, combined with distance measurement techniques, helps estimate object distances (Huang et al., 2023). Despite their success, studies have pointed out that these methods still have limitations in accurately capturing the three-dimensional shapes and boundary details of objects (Kang et al., 2019; Hou et al., 2022).

Consequently, pixel-level precise semantic segmentation methods have begun to emerge in orchard information perception. Sun et al. (2022) and Anagnostis et al. (2021) proposed utilizing semantic segmentation networks to segment orchard images acquired via drones, demonstrating that accurately delineating fruit trees facilitates precise orchard path planning (Sun et al., 2022; Anagnostis et al., 2021). However, detection approaches based on drone-captured images are constrained in real-time perception of orchard environments. To address the demand for real-time orchard environment perception in intelligent operation of robots and vehicles, some studies have leveraged semantic segmentation networks for on-the-fly detection of pathways, obstacles, fruit trees, and individuals in orchards (Shang et al., 2021; Yang et al., 2022; Zhang et al., 2024). Findings suggest that vehicle-mounted image sensors coupled with refined semantic segmentation methods offer greater benefits for vehicle navigation and environment perception compared to object detection methods (Wen et al., 2023).

Classic semantic segmentation models include U-Net (Ronneberger et al., 2015), PSPNet (Zhao et al., 2017), HRNet (Wang et al., 2020), Segformer (Xie et al., 2021), and DeepLabV3+ (Chen et al., 2018). U-Net achieves excellent segmentation performance through multi-resolution feature concatenation. HRNet improves prediction accuracy by running parallel multi-resolution branches and cascading their features. However, Tian et al. (2024) found that U-Net and HRNet have large parameter sizes and high computational costs, making them unsuitable for real-time perception. Tian et al. (2024) also pointed out that the lightweight PSPNet relies on multi-resolution pooling layers, while DeepLabV3 + uses multi-layer atrous convolution with different dilation rates, resulting in better feature extraction compared to PSPNet. Segformer is lightweight and computationally efficient, making it suitable for real-time applications, but it tends to confuse foreground and background in complex scenarios (Wen et al., 2023), limiting its effectiveness in orchard environment perception. Multiple studies have shown that DeepLabV3 + encodes rich contextual information and restores object boundaries through a simple and efficient decoder, capturing multi-scale information in orchard images and fully utilizing pixel spatial correlations (Chen et al., 2022; Wu et al., 2021). Therefore, DeepLabV3 + demonstrates better potential for orchard environment perception tasks compared to U-Net, PSPNet, HRNet, and Segformer.

The key elements to be detected in honey pomelo orchards include roadways, orchard ways, obstacles, pomelo trees, and persons. However, the complex lighting conditions and noise interference in natural pomelo orchards pose significant challenges to environment perception methods. Additionally, practical applications must consider the computational cost and recognition rate of perception methods. Some researchs indicates that the original DeepLabv3+, due to its high computational complexity, is not well-suited for real-time perception tasks. Therefore, there is a need to improve its efficiency to better fit orchard scenarios and enhance its detection capabilities (Su et al., 2021; Zhang et al., 2022; Lv et al., 2022).

To address the current research gaps in key elements segmentation in honey pomelo orchards and enable automated navigation, this study aims to propose a method based on the DeepLabv3 + semantic segmentation algorithm to support the development of intelligent agricultural machinery. To this end, the specific objectives were to (1) to gather authentic environmental images of honey pomelo orchards for constructing a dataset on orchard environment information, (2) to improve DeepLabv3 + and propose a model suitable for key elements detection in honey pomelo orchards, and (3) to test the robustness of the orchard environment perception model.

2. Materials and methods

2.1. Sample collection and preprocessing

From November 23 to December 1, 2023, images were collected from the Jinggang honey pomelo demonstration orchard in the Agricultural Science and Technology Park of Ji’an City, Jiangxi Province, China. The variety of honey pomelo grown in the orchard is “Jinsha” pomelo. The ZED 2i stereo camera was used as the image acquisition device, mounted on an operational vehicle as shown in Fig. 1a, at a height of approximately 1.2 m above the ground. To ensure a high-quality dataset, the image acquisition process was not restricted by weather or lighting conditions. Furthermore, to expedite model training and detection speed, the 2208 × 1242 pixels images captured by the ZED 2i were transferred to 576 × 324 pixels. We initially selected 673 images of pomelo orchard and augmented them into a comprehensive dataset of 3365 images of the pomelo orchard. This augmentation was achieved using techniques such as rotation, translation, flipping, noise addition, and brightness adjustment. The resulting dataset was then divided into a training set (2355 images), a validation set (337 images), and a test set (673 images) in a 7:1:2 ratio. The study focused on segmenting major objects in the pomelo orchard such as roadways, orchard ways, pomelo trees, obstacles (streetlight poles, signposts), and persons. The Labelme software (Fig. 1b) was used to annotate these objects in the pomelo orchard dataset images for training the environmental perception model. The resulting labeled images are shown in Fig. 1c.

2.2. Pomelo-Net network structure

To quickly and accurately detect environmental information in the pomelo orchard, this study proposed an improved deep learning model Pomelo-Net network based on the DeepLabV3 + architecture. As shown in Fig. 2, the Pomelo-Net network consisted of an encoder and a decoder. In the encoder part, a lightweight efficient channel attention-MobileNet

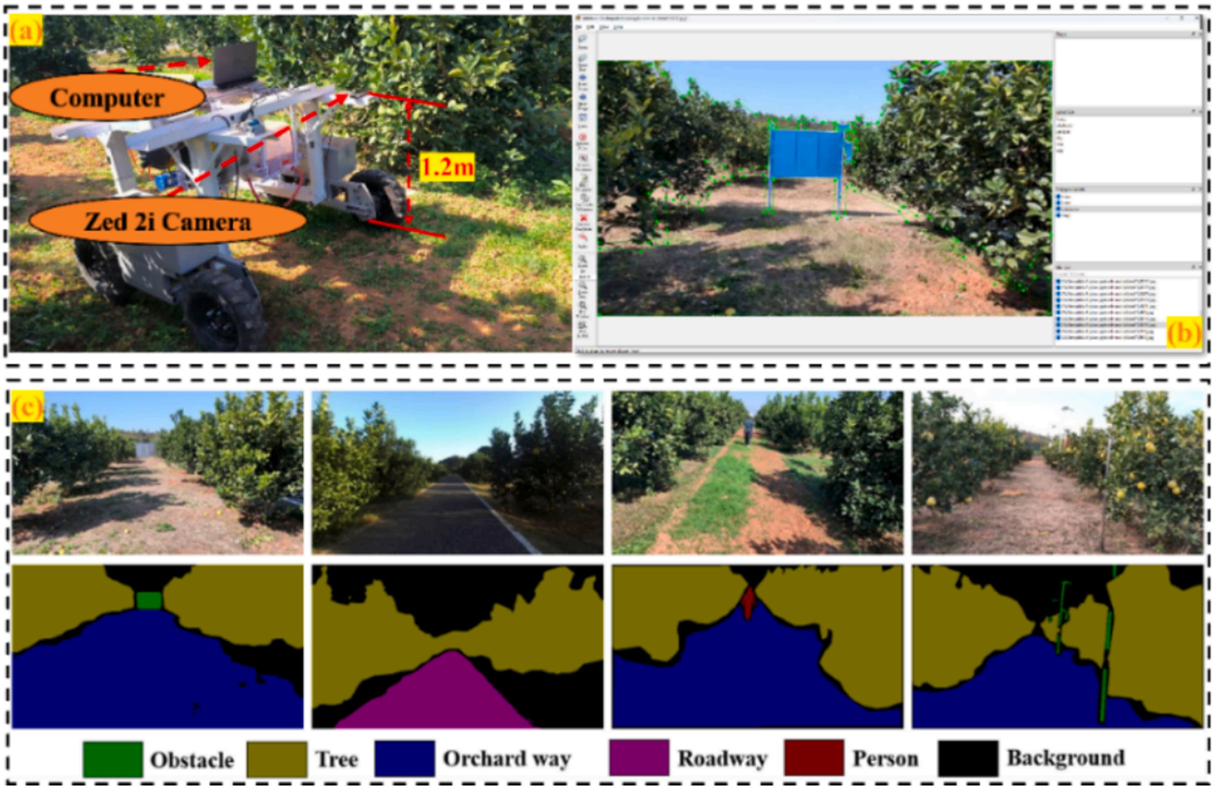

Fig. 1. Image collection site (a), image annotation (b), and labeled images (c).

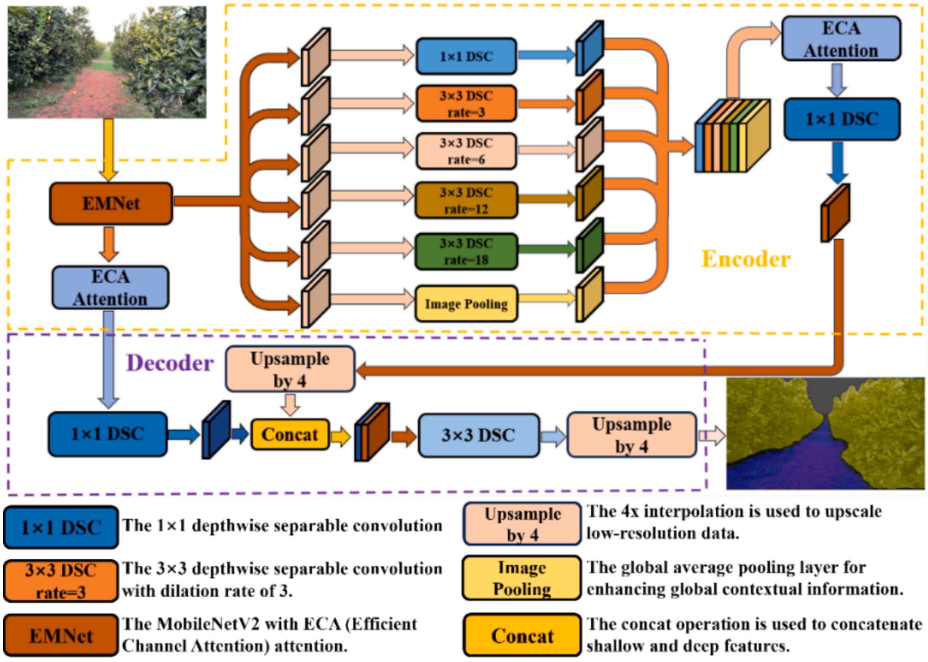

Fig. 2. The Pomelo-Net network structure for environmental information detection in honey pomelo orchards.

V2 (EMNet) feature extraction network was used to swiftly and accurately extract key features from pomelo orchard images. The depthwise separable atrous spatial pyramid pooling (DSASPP) structure was employed to perceive target information at different receptive fields in the pomelo orchard, enhancing Pomelo-Net's feature extraction capabilities. Additionally, lightweight efficient channel attention (ECA) modules were introduced at the output of EMNet and at the end of the encoder in Pomelo-Net, respectively, to filter out useless features in orchard images in both shallow and deep networks, further improving feature utilization.

In the decoder part, to reduce the model's computational load and increase detection speed, the study employed an efficient depthwise separable convolution (DSC) module. A 1 × 1 DSC module was utilized to accelerate the channel dimension reduction for low-level features. At the end of the decoder, the 3 × 3 DSC module was used to quickly refine features and perform upsampling, restoring the image to its original resolution and achieving clearer perception results. Furthermore, addressing the imbalance between target information pixels and orchard background pixels, the combination of dice loss (DL) and focal loss (FL) functions was utilized as the loss function of Pomelo-Net, ensuring robust performance.

2.3. Efficient channel attention-MobileNet V2 (EMNet)

The DeepLabV3 + network utilized Xception as its backbone. Despite its robust feature extraction capabilities, the intricate architecture and numerous parameters contributed to reduced detection speeds (Liu et al., 2024). To expediently and accurately extract features within the intricate environment of a pomelo orchard, this study proposed augmenting the inverted residual modules of MobileNet V2 by integrating the ECA mechanism, thus creating EMNet. This lightweight EMNet was subsequently deployed as the feature extraction network for Pomelo-Net.

Specifically, the improved inverted residual modules in the EMNet feature extraction network consisted of two types, as illustrated in Fig. 3. The module depicted in Fig. 3a initially employed a 1 × 1 convolution to augment the input dimensionality, facilitating comprehensive information extraction. It subsequently conducted feature extraction using a 3 × 3 depthwise convolution, selectively filtering out irrelevant features through the attention mechanism. Following this, a 1 × 1 convolution was employed to reduce dimensionality, ensuring efficient high-dimensional feature extraction. Finally, the input and output of the 1 × 1 convolution were aggregated. The alternate improved inverted residual module, depicted in Fig. 3b, utilized a 3 × 3 depthwise convolution with a stride of 2 for feature extraction subsequent to the 1 × 1 convolution. This was succeeded by the attention mechanism and a subsequent 1 × 1 convolution for pivotal feature extraction and dimensionality reduction. These enhancements enabled the EMNet feature extraction network to significantly alleviate computational burden while upholding feature extraction efficiency, thereby bolstering the network's detection speed.

2.3.1. Efficient channel attention (ECA) module

To suppress irrelevant features and enhance focus on key features in pomelo orchard images, this study introduced the ECA module (Fig. 4).

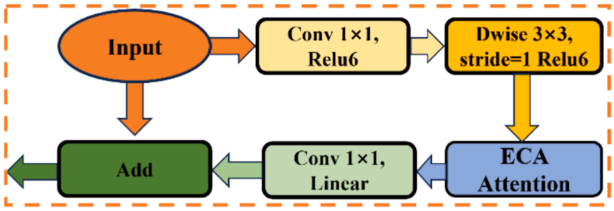

(a) Inverted residual structure when stride is 1

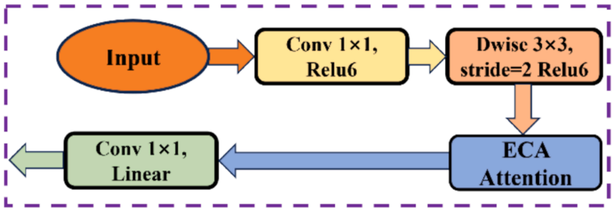

(b) Inverted residual structure when stride is 2

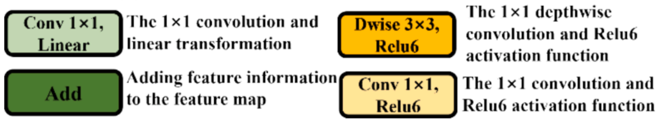

Fig. 3. Improved inverted residual structures in EMNet.

The ECA module uses global average pooling (GAP) to average feature values of each channel, followed by a 1D convolution with K kernels, producing a 1 × 1 × C feature map. This map is combined with the original feature map to emphasize important orchard information and reduce noise. The formula for calculating the convolution kernel K is formulated as follows:

$$K = \left|\frac{\log_2(c)}{\theta} + \frac{b}{\theta}\right| \tag{1}$$

In the formula, K represents the odd number closest to the formula value; θ and b are constants used to adjust the ratio between the number of channels and the size of the convolution kernel, with values of 2 and 1, respectively; c is the number of channels.

2.4. Depthwise separable atrous spatial pyramid pooling (DSASPP) structure

In the intricate landscapes of pomelo orchards, a wide range of scales was observed, presenting a rich array of semantic details across various levels. To enhance the network's efficiency and its capacity to discern this multi-scale information, the DSASPP architecture was introduced as a replacement for the conventional atrous spatial pyramid pooling (ASPP). Its aim was to encapsulate multi-scale semantic insights within orchard images effectively. As illustrated in Fig. 5, DSASPP ensures consistent receptive fields across branches and heightened perception speed by integrating atrous rates into the depthwise segment of depthwise separable convolutions, forming depthwise separable atrous convolutions. These modifications enhanced each branch of the ASPP structure. Additionally, to further amplify the model's capability to extract multi-scale information, DSASPP incorporated an extra branch containing a depthwise separable atrous convolution with an atrous rate of 3. This branch was specifically designed to capture minute features within orchard images, thereby improving the model's proficiency in gathering semantic data across diverse scales within the images.

2.4.1. Depthwise separable convolution (DSC) module

In traditional convolution (Fig. 6a), the convolution kernel is multiplied element-wise with each position of the input feature map, and the results are summed to generate the output feature map. However, traditional convolution has a large number of parameters and high computational costs, leading to low detection efficiency, especially in complex pomelo orchard scenes. To speed up model detection, this study introduced DSC modules (Fig. 6b) in the proposed Pomelo-Net network. The DSC module decomposes traditional convolution into two steps: depthwise convolution and pointwise convolution. Depthwise convolutions process each input channel independently, while pointwise convolutions (using 1x1 kernels) integrate information across channels. This reduces computational cost and enables efficient perception of pomelo orchard scenes.

2.5. Loss function of Pomelo-Net

This study found a significant imbalance between background pixels and perceived information pixels in pomelo orchard images. To address this issue, a new loss function design strategy was adopted, combining the dice loss (DL) function and the focal loss (FL) function as the loss function. The DL function measures the similarity between the predicted results and the ground truth labels, while the FL function effectively handles the problems caused by imbalanced samples. Through this combination, we can more effectively reduce the imbalance between perceived information pixels and orchard background pixels, thereby improving the model's performance and robustness. Additionally, the FL function guides the optimization learning of the DL function, focusing on difficult-to-classify samples and increasing attention to key pixels. Therefore, the design of DL, FL, and the final loss function φ

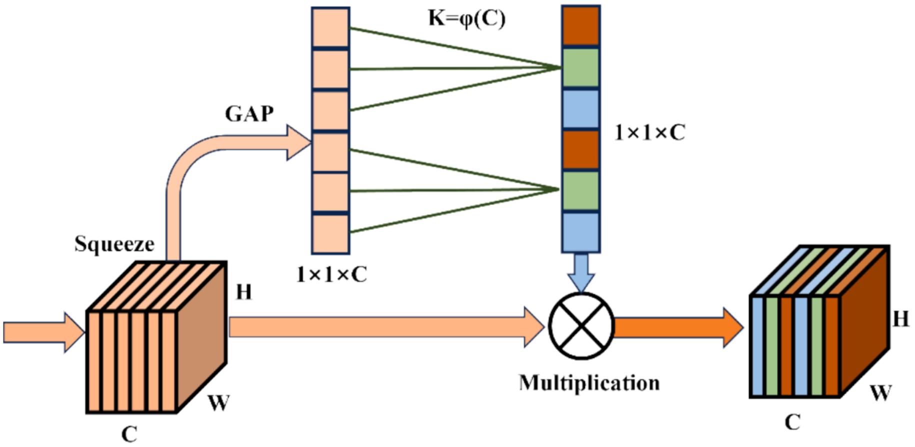

Fig. 4. ECA module. H × W × C represents the height (H), width (W), and number of channels (C) of the feature map. The Squeeze operation involves performing global average pooling on each channel, resulting in a 1 × 1 × C vector. The Multiplication operation involves element-wise multiplication of the calculated attention weights with the input feature map, resulting in the weighted feature map.

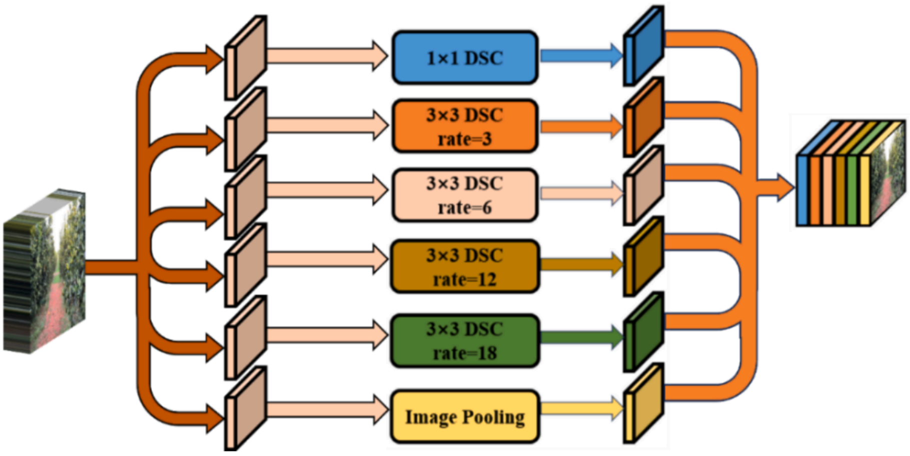

Fig. 5. DSASPP structure. DSC represents the depthwise separable convolution module. Rate represents to atrous rates applied to the depthwise segment of depthwise separable convolutions. Image pooling represents to global average pooling operation.

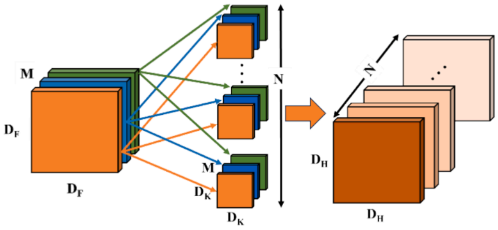

(a) Traditional convolution

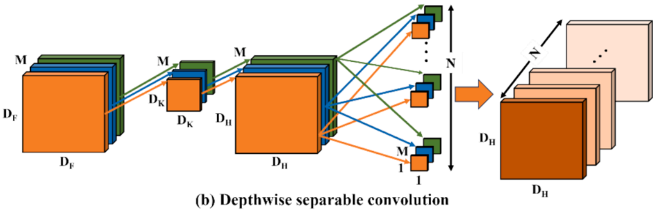

(b) Depthwise separable convolution

Fig. 6. The comparison of traditional convolution and depthwise separable convolution. D_F is the input feature size, M is the number of input channels, D_H be the output feature size, N be the number of output channels, and D_K be the kernel size.

comprehensively addresses the issue of sample imbalance, enhancing the model's perception and generalization abilities in the pomelo orchard scene. The DL, FL, and final loss functions φ are formulated as follows:

$$DL = 1 - \frac{2 \times g_{truth} \cap g_{pred} + \varepsilon}{g_{truth} + g_{pred} + \varepsilon} \tag{2}$$

$$FL = -(1 - g_{truth})^{\gamma} \ln g_{pred} \tag{3}$$

$$\varphi = \overline{DL} + \overline{FL} \tag{4}$$

In the formula, g_{truth} and g_{pred} represent the sets of label pixel values and predicted pixel values, respectively; ε represents the smoothing coefficient of DL, γ represents the modulation coefficient of FL, and $\overline{DL}$ and $\overline{FL}$ respectively represent the averages of the DL set and the FL set.

2.6. Experimental environment and model evaluation

The experimental computer used in this study was equipped with Windows 10 Professional, an NVIDIA Quadro RTX 5000 graphics processor, and an Intel(R) Xeon(R) Gold 6240 processor. The Python 3.8 environment leveraged CUDA 10.2 to enhance model speed. After training the model, its performance was validated using a test set. The evaluation metrics used in this study included pixel accuracy (PA), mean pixel accuracy (MPA), mean intersection over union (MIOU), number of parameters (Params), floating point operations (FLOPs), frame per second (FPS), and model volume. The formulas for these metrics are as follows:

$$\mathrm{PA} = \frac{\sum_{i=0}^{k} P_{ii}}{\sum_{i=0}^{k}\sum_{j=0}^{k} P_{ij}} \tag{5}$$

$$\mathrm{MPA} = \frac{1}{k+1}\sum_{i=0}^{k}\frac{P_{ii}}{\sum_{j=0}^{k} P_{ij}} \tag{6}$$

$$\mathrm{MIOU} = \frac{1}{k+1}\sum_{i=0}^{k}\frac{P_{ii}}{\sum_{j=0}^{k} P_{ij} + \sum_{j=0}^{k} P_{ji} - P_{ii}} \tag{7}$$

Where P_{ii} is the total number of pixels belonging to class i and predicted as class i, P_{ij} is the total number of pixels belonging to class i and predicted as class j, and P_{ji} is the total number of pixels belonging to class j but predicted as class i. $k+1$ is the number of classes.

3. Results and Discussion

3.1. Training process analysis

The training process curve of the Pomelo-Net model is shown in Fig. 7. It can be observed that the MIOU of Pomelo-Net quickly rose to 70 % after the start of training and began to converge rapidly around 40 epochs, eventually reaching approximately 89 % after multiple iterations. Additionally, the loss value of Pomelo-Net also rapidly decreased after the start of training, beginning to converge around 0.25 and eventually converging to below 0.18 after 500 epochs of model training. These results indicated that the training process of Pomelo-Net was stable, and there was no evidence of overfitting or underfitting.

3.2. Ablation experiment

The study conducted the ablation experiment on the test set to validate the impact of various improvement methods on the orchard perception model, Pomelo-Net. The results, as presented in Table 1, show that DeepLabV3 + achieved a modest MIOU of 80.8 % and MPA of 84 % on the test set. By replacing Xception with EMNet as the backbone of DeepLabV3 + and incorporating DF + FL Loss, DSASPP, and the ECA module, Pomelo-Net demonstrated significant performance improvements. Its MIOU increased to 85.3 %, 86.2 %, 88.4 %, and 89.3 %, while the MPA rose to 88.2 %, 90.8 %, 93.8 %, and 95.1 %, respectively. Pomelo-Net exhibited an 8.5 % improvement in MIOU and an 11.1 % improvement in MPA compared to DeepLabV3 + .These improvements stem from key innovations tailored for pomelo orchard segmentation. EMNet, a lightweight backbone, reduces computational cost while maintaining strong feature extraction for complex orchard scenes. DF + FL Loss mitigates pixel imbalance, enhancing segmentation in densely packed or ambiguous regions like tree trunks and foliage. DSASPP enables multi-scale feature extraction, handling the size and spatial variability of orchard elements. The ECA module refines feature selection, improving overall segmentation accuracy. Together, these enhancements make Pomelo-Net more effective at segmenting diverse and cluttered orchard environments.

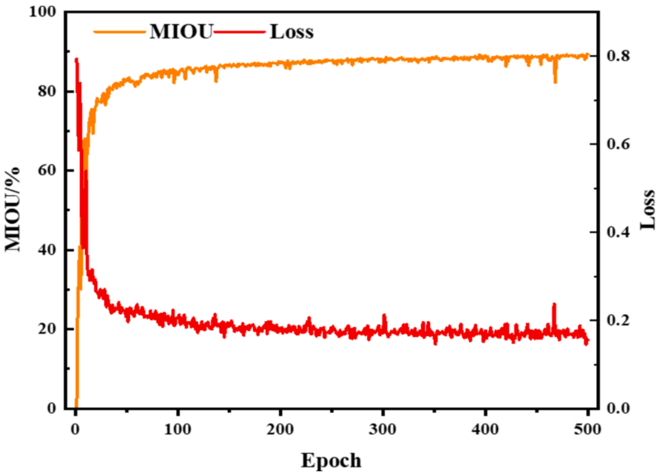

Fig. 7. Training process of Pomelo-Net.

Furthermore, Pomelo-Net's parameters, FLOPs, and model volume were reduced by 94.8 %, 94.3 %, and 94.6 %, respectively, compared to DeepLabV3+, while achieving a detection speed of 32 FPS. These advancements are primarily attributed to the introduction of EMNet and DSASPP. Specifically, by replacing Xception with EMNet, proposed in this study, the parameters of DeepLabV3 + were reduced by 89.4 %. This is due to EMNet's incorporation of inverted residual, which effectively reduce computational complexity by employing narrower channels in intermediate layers. And, the inclusion of DSASPP, which replaced the original ASPP of DeepLabV3+, further reduced DeepLabV3+'s parameters by 51.7 %, thanks to its lightweight design utilizing depthwise separable convolutions. Overall, these innovations, as validated by the ablation experiments, significantly enhance Pomelo-Net's performance, demonstrating its commendable efficiency and segmentation accuracy relative to other models on the test set.

3.3. Model robustness experiment

3.3.1. Detection of orchard scenes under different lighting conditions

As a passive sensor, the ZED 2i camera is influenced by lighting variations stemming from the orientation of the sun and prevailing weather conditions. To assess the Pomelo-Net model's capability in discerning orchard environments across diverse lighting conditions, this study curated data encompassing three distinct scenarios in sunny weather between 9:00 a.m. and 5:00p.m.: front lighting (when the camera's field of view is oriented towards the sun), back lighting (when the camera's field of view is oriented away from the sun), and side lighting (when the camera's field of view is positioned to the side of the sun). Additionally, scenes captured under cloudy weather conditions were included to evaluate Pomelo-Net's performance.

Upon inspecting the RGB images in Fig. 8, it's evident that the orchard ways are typically shrouded in tree shadows (Fig. 8a, b, and c) during sunny weather, contrasting with their appearance in cloudy conditions (Fig. 8d). The varying camera angles result in noticeable color discrepancies among the trees across different images (Fig. 8a and c). Furthermore, when the camera's field of view is facing towards the sun, it leads to overexposure of the image background, thus complicating the discernment of foreground details (Fig. 8c). This presents a significant challenge to the robustness and generalization capacity of the orchard environment perception model.

From the detection results in Fig. 8, it can be observed that U-Net (Ronneberger et al., 2015), PSPNet (Zhao et al., 2017), Segformer (Xie et al., 2021), and HRNet (Wang et al., 2020) share a common issue of failing to detect or misclassifying distant small signs (Fig. 8d), indicating their poor ability to detect small objects under varying lighting conditions. Additionally, PSPNet tends to miss detecting persons (Fig. 8a) and misclassifies shadowed ground as roadway (Fig. 8c), while Segformer often misclassifies persons as ground (Fig. 8a), suggesting that their discriminative ability is limited under different lighting conditions. In contrast, Pomelo-Net demonstrates better recognition capabilities across varying lighting conditions. The quantitative analysis results in Table 2 further confirm Pomelo-Net's advantages. As shown in Table 2, compared to U-Net, PSPNet, Segformer, and HRNet, Pomelo-Net's MIOU values were increased by 2.3 %, 5.1 %, 3.6 %, and 2.7 %, respectively,

Table 1
Ablation experiment results. The √ represents adding the corresponding module.

Model	EMNet	DF + FL Loss	DSASPP	ECA module	MIOU/%	MPA/%	Params/M	FLOPs/G	Volume/MB	Speed/FPS[a]
DeepLabV3+[b]					80.8	84	54.7	175.1	209	17.9
E-DeepLabV3+	√				85.3	88.2	5.8	18.9	22.9	26.9
EL-DeepLabV3+	√	√			86.2	90.8	5.8	18.9	22.9	26.9
ELD-DeepLabV3+	√	√	√		88.4	93.8	2.8	4.2	11.2	33.1
Pomelo-Net	√	√	√	√	**89.3**	**95.1**	**2.8**	**9.9**	**11.2**	**32**

[a] Processing speed might be varied under different computational environment. [b]DeepLabV3 + at this stage uses Xception as its backbone.

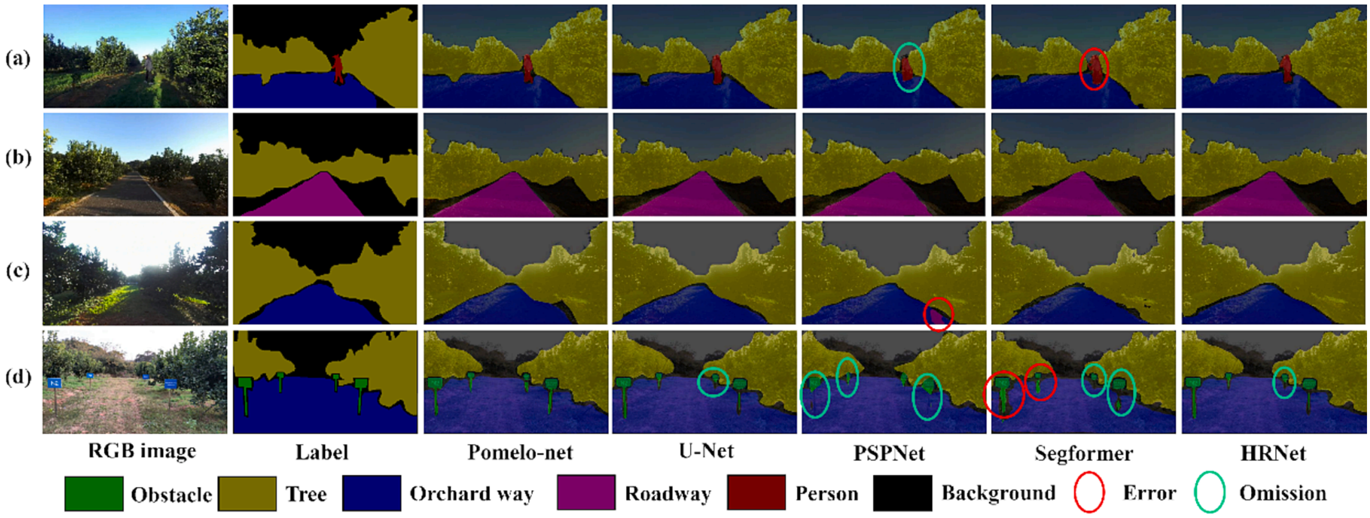

Fig. 8. Examples of the model detecting different lighting scenarios. (a) Camera field of view oriented away from the sun; (b) Camera field of view positioned to the side of the sun; (c) Camera field of view oriented towards the sun; (d) Cloudy weather during filming.

Table 2
Results of the model detecting various lighting scenarios.

Model	Number of test images	MIOU/%	MPA/%	Params/M	FLOPs/G	Volume/MB	Speed/FPS
Pomelo-Net	**424**	**89.8**	**95.2**	**2.87**	**9.93**	**11.2**	**32**
U-Net	424	87.5	93.7	24	159	94.9	27
PSPNet	424	84.7	90.3	2.37	2.20	9.3	23.2
Segformer	424	86.2	93.9	3.72	4.88	14.2	17.2
HRNet	424	87.1	92.5	9.64	13.49	37.5	20.5

and the MPA values were increased by 1.5 %, 4.9 %, 1.3 %, and 2.7 %, respectively. Moreover, while maintaining a lightweight volume, Pomelo-Net achieved a detection speed of 32 FPS. This indicates that Pomelo-Net exhibits good robustness and generalization ability when facing different lighting scenarios.

3.3.2. Detection of orchard images with motion blur

Camera shake can often result in image blur and the loss of certain features in the target area, impacting the model's ability to accurately perceive the scene. This study found that in the high-quality and structured honey pomelo orchard, roads are mostly roadways (Fig. 9a) and relatively flat orchard ways (Fig. 9b), but there are still sections with slopes prone to vehicle bumps due to hilly terrain (Fig. 9c). The complex orchard terrain necessitates verifying Pomelo-Net's ability to detect orchard images with motion blur.

Following the methodology in the reference literature (Lu et al., 2023; Kapuriya et al., 2024), this study proposes using the Laplacian of Gaussian operator to evaluate the degree of motion blur in images. Generally, a smaller variance of the Laplacian response indicates a lack of sharp edges in the image. Based on the variance of the Laplacian response in our dataset, the degree of image blur is categorized as mild blur (variance of Laplace response $>$ 200), moderate blur (150 $\leq$ variance of Laplace response $\leq$ 200), and high blur (variance of Laplace response $<$ 150). In addition, manual annotation was used to mark regions where motion blur caused edge blurring in the images. Specifically, these blurred edge regions were carefully annotated by professionals through strict observation and expert guidance, based on visible blur and the loss of object contours. This ensures an individualized analysis of each image, avoiding the limitations of a single algorithm.

It can be observed that as the degree of blur increases, the edges of the pomelo trees and person (marked by pink circles in Fig. 9b) become blurred, and the contours of obstacles also become difficult to distinguish (marked by pink circles in Fig. 9c). However, based on the detection results (marked by yellow circles in Fig. 9b and 9c), Pomelo-Net is still able to effectively distinguish the contours of various objects in images with different levels of blur. According to the detection results (Table 3), Pomelo-Net performs well when detecting images with mild blur, with PA for each perceived element exceeding 91.3 %, and MIOU and MPA reaching 90.2 % and 95.4 %, respectively. Pomelo-Net achieved MIOU of 86.2 % and 84.7 %, and MPA of 93.2 % and 90.9 % when detecting images with moderate blur and high blur, respectively. These results indicate that Pomelo-Net exhibits good detection capability for orchard images with motion blur.

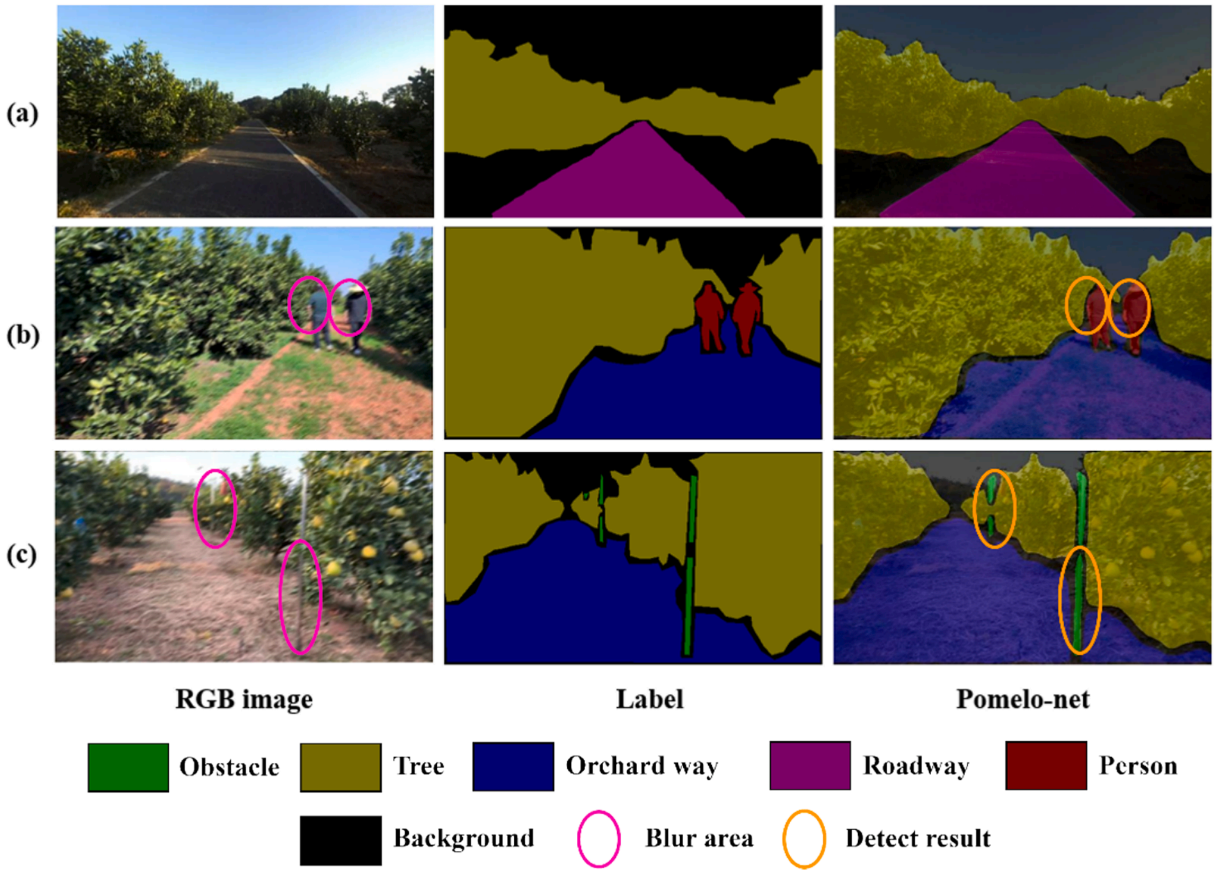

Fig. 9. Examples of Pomelo-Net detecting blurred pomelo orchard images due to motion. (a) Mild blur;(b) Moderate blur; (c) High blur.

Table 3
Results of Pomelo-Net detecting blurred pomelo orchard images due to motion.

Image status	Number of test images	PA/%						MIOU/%	MPA/%
		Obstacle	Tree	Orchard way	Roadway	Person	Background		
Mild blur	102	91.5	97.1	96.8	98.2	97.7	91.3	90.2	95.4
Moderate blur	85	84.7	95.3	92.6	97.7	95.1	94.2	86.2	93.2
High blur	62	71.6	96.3	95.4	96.8	93.9	91.5	84.7	90.9

To further verify Pomelo-Net's detection capabilities on images with varying degrees of motion blur and rigorously evaluate its accuracy across different object categories, this study selected images from the RUGD dataset (Wigness et al., 2019) with mild blur (variance of Laplace response > 200), moderate blur ($150 \leq$ variance of Laplace response ≤ 200), and high blur (variance of Laplace response < 150) to test Pomelo-Net. The example detection images and results are shown in Fig. 10 and Table 4, respectively.

As shown in Fig. 10a, Pomelo-Net performs well on images with mild blur, easily distinguishing grass, water, tree, sky, bush, rock-bed, and gravel, achieving a MIOU of 62.9 % and an MPA of 74.4 % (Table 4). For images with moderate blur (Fig. 10b), Pomelo-Net performs well in distinguishing grass, tree, table, and fence, but the model misclassifies the container due to blurred pixel edges (as indicated by the red circle in Fig. 10b). However, it still achieves a MIOU of 53.7 % and an MPA of 60.6 % (Table 4). As shown in Fig. 10c, for images with high blur, Pomelo-Net can still effectively distinguish grass, gravel, tree, mulch, and bush. However, due to fast vehicle movement, the boundaries between different objects in the captured images became extremely blurred, causing potential confusion in the contact areas between gravel and grass (marked by the red circle in Fig. 10c). Especially when the background and foreground colors are similar, some small objects in highly blurred images are difficult to discern even with the naked eye. For instance, when mulch is the background, small patches of grass and logs are hard to recognize, leading to missed detections (marked by the green circle in Fig. 10c). This results in a decrease in the model's MIOU and MPA in Table 4, dropping to 48.7 % and 54.2 %, respectively. Overall, Pomelo-Net shows good detection capabilities for various elements in images with different degrees of motion blur.

3.4. *Validation on the RUGD dataset*

This study further validated Pomelo-Net's versatility on the RUGD dataset and compared its results with models from previous studies on the same dataset. The RUGD dataset comprises 4759 training images and 1964 testing images captured by cameras mounted on mobile robot platforms. It covers 24 categories, including vehicles, buildings, sky, grass, and eight terrain types, making it suitable for evaluating algorithms' generalization capability and robustness across diverse real-world scenarios. The examples of Pomelo-Net's detection on the RUGD dataset is shown in Fig. 11.

The results, as shown in Table 5, demonstrated the outstanding performance of the proposed Pomelo-Net model on the RUGD dataset, achieving a MIOU of 60.15 % on the testing set. In comparison, the

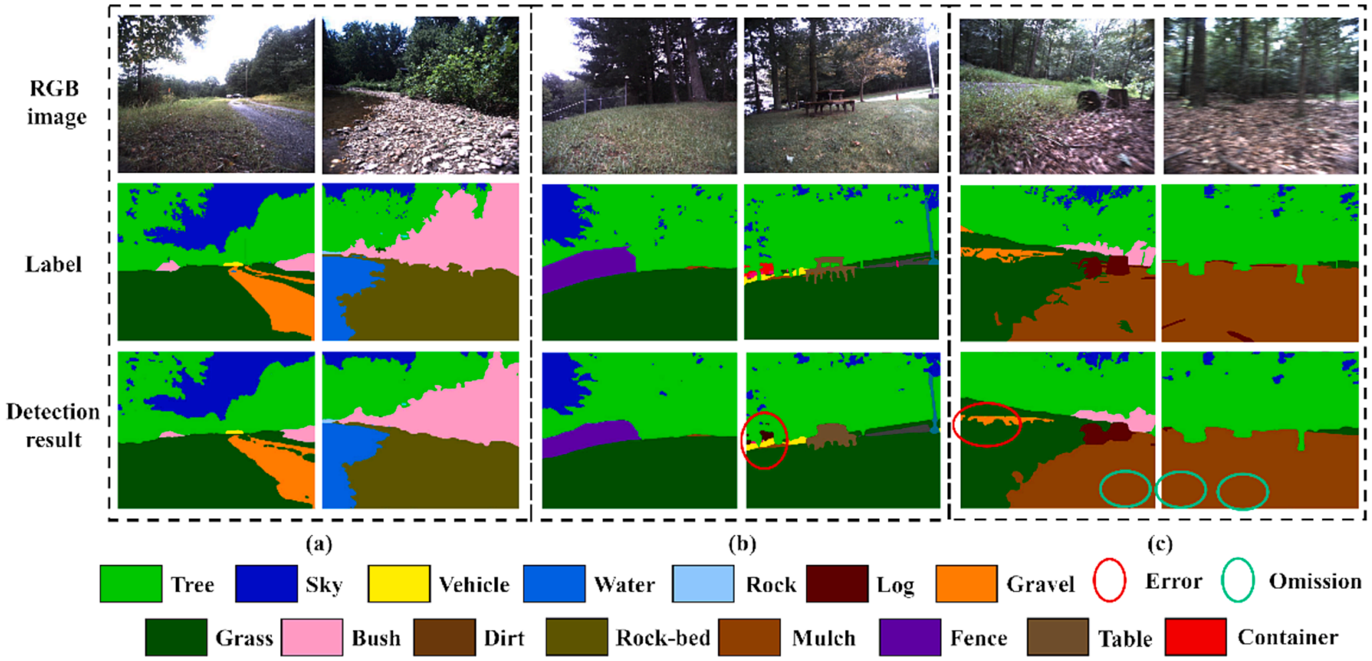

Fig. 10. Examples of Pomelo-Net detecting motion blurred images in RUGD dataset. (a) Mild blur; (b) Moderate blur; (c) High blur.

Table 4
The results of Pomelo-Net detecting motion blurred images in RUGD dataset.

Image status	Number of test images	MIOU/%	MPA/%
Mild blur	860	62.9	74.4
Moderate blur	512	53.7	60.6
High blur	278	48.7	54.2

Pomelo-Net model outperformed Memory-based SS, TrSeg, Deeplabv3, and ConvNext by 22.44 %, 26.24 %, 27.34 %, and 10.98 %, respectively. Although the proposed Pomelo-Net model increased FLOPs by 5.34 G and 4.66 G compared to DDRNet and FRPNet, its MIOU improved by 13.29 % and 5.05 %, respectively. Furthermore, the Params was reduced by 2.82 M and 6.87 M, respectively. These comparative results highlighted that Pomelo-Net not only excelled in segmentation accuracy and

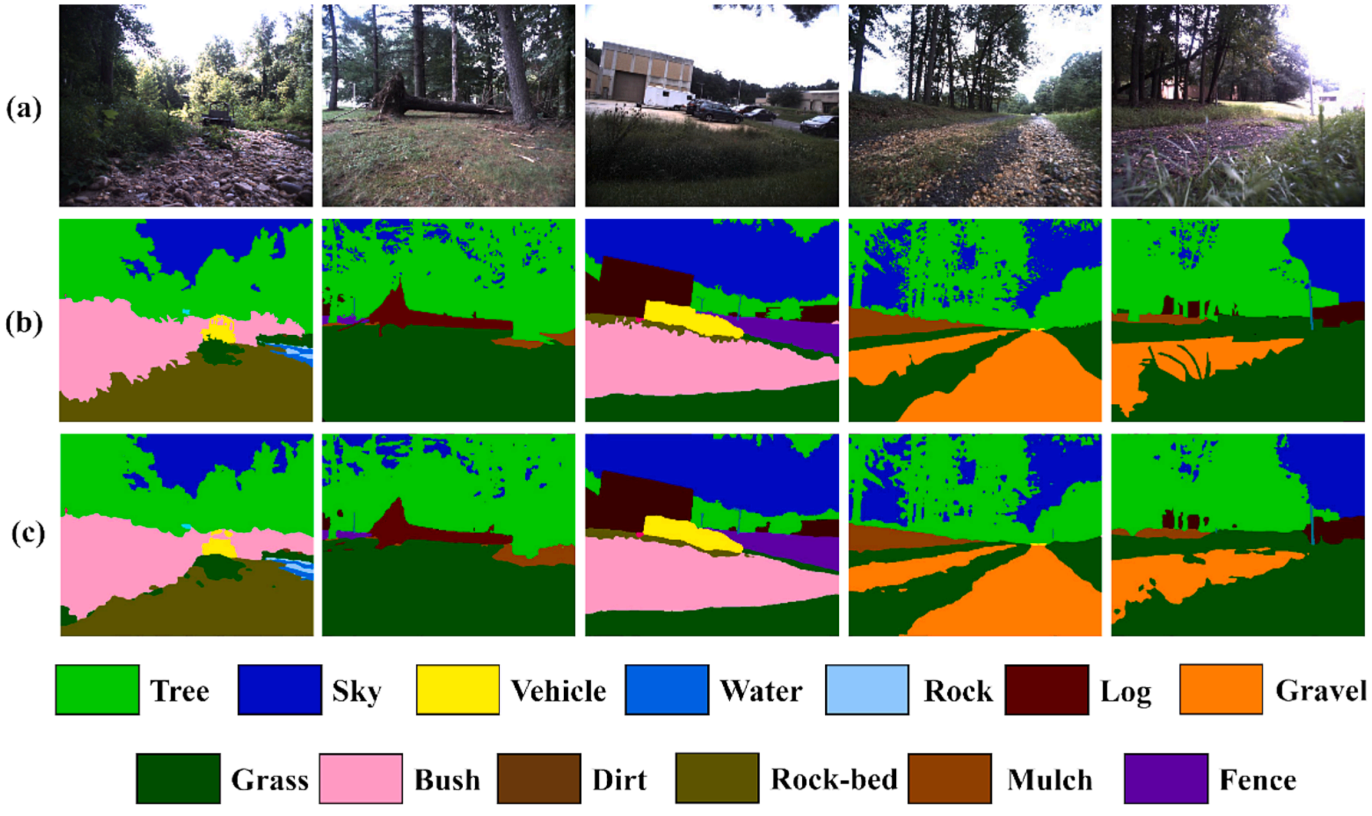

Fig. 11. Examples of Pomelo-Net's detection on the RUGD dataset. (a) RGB image; (b) Label image; (c) Detection result.

Table 5
Comparison with other studies on the RUGD dataset.

Existing study	Model	MIOU/%	FLOPs/G	Params/M
(Jin et al., 2021)	Memory-based SS	37.71	243.21	42.13
(Jin et al., 2021)	TrSeg	33.91	419	74
(Chen et al., 2017)	Deeplabv3	32.81	439	66
(Liu et al., 2022)	ConvNext	49.17	80.44	87.99
(Hong et al., 2021)	DDRNet	46.86	4.59	5.69
(Yang et al., 2024)	FRPNet	55.10	5.27	9.74
Ours	**Pomelo-Net**	**60.15**	**9.93**	**2.87**

efficiency, accurately distinguishing between different categories, but also adeptly handled boundary and confusion issues among similar categories.

3.5. Comparison with other orchard environment perception methods

This study investigates and compares recent methods for orchard environment perception, as shown in Table 6. The results indicate that the Pomelo-Net model proposed in this study outperforms the deep residual U-Net proposed by Shang et al. (2021) for peach orchard environment perception by 3.35 % in terms of MIOU. Additionally, Pomelo-Net exhibits comparable performance to SADNet, proposed by Sun et al. (2022), with improvements of 1.02 % and 1.49 % in MIOU and MPA, respectively, while reducing the Params by 71.7 %. Furthermore, when compared to MsFF-Segformer developed by Wen et al. (2023) for perceiving complex orchard scenes, Pomelo-Net shows a significant advantage with a 2.78 % improvement in MIOU and an 80.9 % reduction in Params. Moreover, Pomelo-Net demonstrates robust detection performance under complex lighting conditions and severe motion blur, making it particularly suitable for environmental perception in hilly and mountainous pomelo orchards. These findings underscore Pomelo-Net's significant advantages over existing orchard perception methods, highlighting its effectiveness and efficiency in such challenging environments.

3.6. Limitations and future work

The absence of effective methods for honey pomelo orchard environment perception significantly hampered the advancement of agricultural machinery intelligence. The Pomelo-Net orchard perception model proposed in this study showcased commendable perceptual capabilities tailored for high-quality structured honey pomelo orchards, exhibiting robustness against complex lighting conditions and motion blur. This robustness stood to benefit the evolution of intelligent agricultural robotics within honey pomelo orchards. Pomelo-Net also demonstrated promising performance on edge computing devices, achieving detection speeds surpassing 39 FPS on the NVIDIA Jetson AGX Orin platform via the TensorRT framework.

Nevertheless, certain limitations persisted. Firstly, the orchard image dataset utilized in this study was sourced from high-quality demonstration orchards. To enhance the generalization capabilities of the models, it is imperative to augment the dataset with additional data from non-structured pomelo orchards in the future. Additionally, expanding the dataset to include pomelo orchards at various growth stages is warranted. Secondly, relying solely on image sensors to perceive the intricate environments of pomelo orchards remains constrained. Future investigations could explore integrating cameras with lidar sensors. Furthermore, the findings of this research could be extrapolated to environmental perception tasks across diverse orchard types.

4. Conclusion

This study aimed to develop a method for key elements segmentation in honey pomelo orchard to enable automated navigation. To achieve this, an orchard image dataset was collected from honey pomelo orchards, and the Pomelo-Net orchard environment perception model was proposed based on an improved Deeplabv3 + architecture. The results demonstrated that the Pomelo-Net model could accurately segment roadways, orchard ways, pomelo trees, obstacles, and persons in honey pomelo orchard, achieving an MIOU of 89.3 % and an MPA of 95.1 %, with a segmentation speed of up to 32 FPS and a model Params of only 2.87 M. Pomelo-Net also exhibited high robustness in perceiving complex orchard environments, achieving an MIOU of over 84.7 % and an MPA of over 90.9 % on orchard images under different lighting conditions and motion blur. The Pomelo-Net model proposed in this study outperformed other deep learning models for orchard segmentation in terms of lightweight attributes, segmentation speed, and model size. It is anticipated that technical support will be available for path planning, autonomous obstacle avoidance, and precise operations of intelligent agricultural robotics at the honey pomelo orchard.

Table 6
Performance comparison with existing orchard environment perception methods.

Existing study	Types of orchards	Method	MIOU/ %	MPA/ %	Params/ M
Shang et al. (2021)	Peach	Deep residual U-Net	85.95	n/a	n/a
Sun et al. (2022)	n/a	SADNet	88.28	93.61	10.16
Wen et al. (2023)	Plums, pears, and kiwis	MsFF-segformer	86.52	94.05	15.1
Ours	**Honey pomelo**	**Pomelo-Net**	**89.3**	**95.1**	**2.87**

CRediT authorship contribution statement

Xianlu Guan: Writing – original draft, Software, Methodology, Formal analysis, Data curation, Conceptualization. **Huan Wan:** Software, Data curation. **Zixuan He:** Writing – review & editing, Formal analysis. **Zibo Liu:** Data curation. **Rui Jiang:** Validation, Data curation. **Yuanzhen Ou:** Resources, Methodology, Investigation. **Yuli Chen:** Resources. **Huaning Gu:** Validation. **Zhiyan Zhou:** Writing – review & editing, Supervision, Project administration, Methodology, Funding acquisition, Conceptualization.

Declaration of competing interest

The authors declare that they have no known competing financial interests or personal relationships that could have appeared to influence the work reported in this paper.

Acknowledgement

This work was supported by the National Key R&D Program of China (2022YFD2001501); in part by Science and Technology Plan of Jian City of China (20222-20-051256-01 and 20211-055316), Science and Technology Plan of Guangdong Province of China (2023B10564002), Innovative Research Team of Agricultural and Rural Big Data in Guangdong Province of China (2019KJ138), and China Scholarship Council (202308440394). The authors would like to thank the reviewers and editors for their constructive comments.

Data availability

Data will be made available on request.

References

Anagnostis, A., Tagarakis, A.C., Kateris, D., Moysiadis, V., Sørensen, C.G., Pearson, S., Bochtis, D., 2021. Orchard mapping with deep learning semantic segmentation. Sensors 21 (11), 3813. https://doi.org/10.3390/s21113813.

Chen, M., Jin, C., Ni, Y., Xu, J., Yang, T., 2022. Online detection system for wheat machine harvesting impurity rate based on DeepLabV3+. Sensors 22 (19), 7627. https://doi.org/10.3390/s22197627.

Chen, L.C., Papandreou, G., Kokkinos, I., Murphy, K., Yuille, A.L., 2017. Deeplab: Semantic image segmentation with deep convolutional nets, atrous convolution, and fully connected crfs. IEEE Trans. Pattern Anal. Mach. Intell. 40 (4), 834–848. https://ieeexplore.ieee.org/document/7913730.

Chen, X.Y., Wang, S.A., Zhang, B.Q., Luo, L., 2018b. Multi-feature fusion tree trunk detection and orchard mobile robot localization using camera/ultrasonic sensors. Comput. Electron. Agric. 147, 91–108. https://doi.org/10.1016/j.compag.2018.02.009.

Chen, L.C., Zhu, Y., Papandreou, G., Schroff, F., Adam, H., 2018a. Encoder-decoder with atrous separable convolution for semantic image segmentation. In: In Proceedings of the European Conference on Computer Vision (ECCV), pp. 801–818.

da Silva, D.Q., dos Santos, F.N., Filipe, V., Sousa, A.J., Oliveira, P.M., 2022. Edge AI-based tree trunk detection for forestry monitoring robotics. Robotics 11 (6), 136. https://doi.org/10.3390/robotics11060136.

Fu, L.H., Wu, F.Y., Zou, X.J., Jiang, Y.L., Lin, J.Q., Yang, Z., Duan, J.L., 2022. Fast detection of banana bunches and stalks in the natural environment based on deep learning. Comput. Electron. Agric. 194, 106800. https://doi.org/10.1016/j.compag.2022.106800.

Gao, Y., Tian, G.Z., Gu, B.X., Zhao, J.W., Liu, Q., Qiu, C., Xue, J.L., 2023. A Study on the Rapid Detection of Steering Markers in Orchard Management Robots Based on Improved YOLOv7. Electronics 12 (17), 3614. https://doi.org/10.3390/electronics12173614.

Hong, Y.D., Pan, H.H., Sun, W.C., Jia, Y.S., 2021. Deep dual-resolution networks for real-time and accurate semantic segmentation of road scenes. arXiv preprint arXiv:2101.06085. https://doi.org/10.48550/arXiv.2101.06085.

Hou, C.J., Zhang, X.D., Tang, Y., Zhuang, J.J., Tan, Z.P., Huang, H.S., Chen, W.L., Wei, S., He, Y., Luo, S.M., 2022. Detection and localization of citrus fruit based on improved You Only Look Once v5s and binocular vision in the orchard. Front. Plant Sci. 13, 972445. https://doi.org/10.3389/fpls.2022.972445.

Huang, P.C., Huang, P.K., Wang, Z.H., Wu, X., Liu, J., Zhu, L.X., 2023. Deep-Learning-Based Trunk Perception with Depth Estimation and DWA for Robust Navigation of Robotics in Orchards. Agronomy 13 (4), 1084. https://doi.org/10.3390/agronomy13041084.

Jiang, A.L., Noguchi, R., Ahamed, T., 2022. Tree trunk recognition in orchard autonomous operations under different light conditions using a thermal camera and faster R-CNN. Sensors 22 (5), 2065. https://doi.org/10.3390/s22052065.

Kang, H.W., Chen, C., 2019. Visual perception and modelling in unstructured orchard for apple harvesting robots. arXiv preprint arXiv:1912.12555. https://doi.org/10.48550/arXiv.1912.12555.

Kapuriya, B.R., Pradhan, D., Sharma, R., 2024. Detection of local motion blurred/non-blurred regions in an image. Multimed. Tools Appl. 83 (15), 43705–43725. https://doi.org/10.1007/s11042-023-17340-3.

Kaushalya Madhavi, B.G., Bhujel, A., Kim, N.E., Kim, H.T., 2022. Measurement of Overlapping Leaf Area of Ice Plants Using Digital Image Processing Technique. Agriculture 12 (9), 1321. https://doi.org/10.3390/agriculture12091321.

Li, Y., Li, M., Qi, J.T., Zhou, D.Y., Zou, Z.F., Liu, K., 2021. Detection of typical obstacles in orchards based on deep convolutional neural network. Comput. Electron. Agric. 181, 105932. https://doi.org/10.1016/j.compag.2020.105932.

Liu, H., Li, K., Ma, L.Y., Meng, Z.J., 2024. Headland Identification and Ranging Method for Autonomous Agricultural Machines. Agriculture 14 (2), 243. https://doi.org/10.3390/agriculture14020243.

Liu, Z., Mao, H.Z., Wu, C.Y., Feichtenhofer, C., Darrell, T., Xie, S.N., 2022. A convnet for the, 2020s. arXiv e-prints.

Lu, J.Q., Chen, P.F., Yu, C.R., Lan, Y.B., Yu, L.H., Yang, R.F., Niu, H.Y., Chang, H.H., Yuan, J.J., Wang, L., 2023. Lightweight green citrus fruit detection method for practical environmental applications. Comput. Electron. Agric. 215, 108205. https://doi.org/10.1016/j.compag.2023.108205.

Lv, S.N., Meng, L.S., Edwing, D., Xue, S.H., Geng, X.P., Yan, X.H., 2022. High-performance segmentation for flood mapping of hisea-1 sar remote sensing images. Remote Sens. (basel) 14 (21), 5504. https://doi.org/10.3390/rs14215504.

Lyu, H.K., Park, C.H., Han, D.H., Kwak, S.W., Choi, B., 2018. Orchard free space and center line estimation using Naive Bayesian classifier for unmanned ground self-driving vehicle. Symmetry 10 (9), 355. https://doi.org/10.3390/sym10090355.

Nissimov, S., Goldberger, J., Alchanatis, V., 2015. Obstacle detection in a greenhouse environment using the Kinect sensor. Comput. Electron. Agric. 113, 104–115. https://doi.org/10.1016/j.compag.2015.02.001.

Pei, Y., He, C.X., Liu, H.L., Shen, G.P., Feng, J.H., 2022. Compositional analysis of four kinds of citrus fruits with an NMR-based method for understanding nutritional value and rational utilization: From pericarp to juice. Molecules 27 (8), 2579. https://doi.org/10.3390/molecules27082579.

Ronneberger, O., Fischer, P., Brox, T.- U.-N., 2015. Convolutional networks for biomedical image segmentation. In Medical image computing and computer-assisted intervention–MICCAI. In: Proceedings, Part III, 18. Springer International Publishing, pp. 234–241.

Shalal, N., Low, T., McCarthy, C., Hancock, N., 2015. Orchard mapping and mobile robot localisation using on-board camera and laser scanner data fusion - Part A: Tree detection. Comput. Electron. Agric. 119, 254–266. https://doi.org/10.1016/j.compag.2015.09.025.

Shang, G.G., Liu, G., Zhu, P., Han, J.Y., Jiang, K., 2021. A Deep Residual U-Type Network for Semantic Segmentation of Orchard Environments. Appl. Sci. 11 (1), 322. https://doi.org/10.3390/app11010322.

Su, H.C., Peng, Y.H., Xu, C., Feng, A., Liu, T., 2021. Using improved DeepLabv3+ network integrated with normalized difference water index to extract water bodies in Sentinel-2A urban remote sensing images. J. Appl. Remote Sens. 15 (1), 018504. https://doi.org/10.1117/1.JRS.15.018504.

Su, F., Zhao, Y., Shi, Y.X., Zhao, D., Wang, G.H., Yan, Y.F., Zu, L.L., Chang, S.Y., 2022. Tree trunk and obstacle detection in apple orchard based on improved YOLOv5s model. Agronomy 12 (10), 2427. https://doi.org/10.3390/agronomy12102427.

Sun, Q.L., Zhang, R.R., Chen, L.P., Zhang, L.H., Zhang, H.M., Zhao, C.J., 2022. Semantic segmentation and path planning for orchards based on UAV images. Comput. Electron. Agric. 200, 107222. https://doi.org/10.1016/j.compag.2022.107222.

Taner, A., Mengstu, M.T., Selvi, K.Ç., Duran, H., Gür, İ., Ungureanu, N., 2024. Apple Varieties Classification Using Deep Features and Machine Learning. Agriculture 14 (2), 252. https://doi.org/10.3390/agriculture14020252.

Tian, Y., Zhang, K., Hu, X., Lu, Y., 2024. Crop type recognition of VGI road-side images via hierarchy structure based on semantic segmentation model Deeplabv3+. Displays 81, 102574. https://doi.org/10.1016/j.displa.2023.102574.

Wang, J.D., Sun, K., Cheng, T.H., Jiang, B.R., Deng, C.R., Zhao, Y., Liu, D., Mu, Y.D., Tan, M.K., Wang, X.G., Liu, W.Y., Xiao, B., 2020. Deep high-resolution representation learning for visual recognition. IEEE Trans. Pattern Anal. Mach. Intell. 43 (10), 3349–3364. https://doi.org/10.48550/arXiv.1908.07919.

Wen, Y., Xue, J.L., Sun, H., Song, Y., Lv, P.F., Liu, S.H., Chu, Y.Y., Zhang, T.Y., 2023. High-precision target ranging in complex orchard scenes by utilizing semantic segmentation results and binocular vision. Comput. Electron. Agric. 215, 108440. https://doi.org/10.1016/j.compag.2023.108440.

Wigness, M., Eum, S., Rogers, J.G., Han, D., Kwon, H., 2019. In: A Rugd Dataset for Autonomous Navigation and Visual Perception in Unstructured Outdoor Environments. IEEE, pp. 5000–5007.

Wu, Z., Yang, R., Gao, F., Wang, W., Fu, L., Li, R., 2021. Segmentation of abnormal leaves of hydroponic lettuce based on DeepLabV3+ for robotic sorting. Comput. Electron. Agric. 190, 106443. https://doi.org/10.1016/j.compag.2021.106443.

Xie, E.Z., Wang, W.H., Yu, Z.D., Anandkumar, A., Alvarez, J.M., Luo, P., 2021. SegFormer: Simple and efficient design for semantic segmentation with transformers. Adv. Neural Inf. Proces. Syst. 34, 12077–12090. https://doi.org/10.48550/arXiv.2105.15203.

Yang, Z., Ouyang, L., Zhang, Z.G., Duan, J.L., Yu, J.X., Wang, H., 2022. Visual navigation path extraction of orchard hard pavement based on scanning method and neural network. Comput. Electron. Agric. 197, 106964. https://doi.org/10.1016/j.compag.2022.106964.

Yang, B., Yang, S., Wang, P., Wang, H., Jiang, J.M., Ni, R.R., Yang, C.C., 2024. FRPNet: An improved Faster-ResNet with PASPP for real-time semantic segmentation in the unstructured field scene. Comput. Electron. Agric. 217, 108623. https://doi.org/10.1016/j.compag.2024.108623.

Zhang, C.Q., Chen, X.D., Ji, S.Y., 2022. Semantic image segmentation for sea ice parameters recognition using deep convolutional neural networks. Int. J. Appl. Earth Obs. Geoinf. 112, 102885. https://doi.org/10.1016/j.jag.2022.102885.

Zhang, L., Li, M., Zhu, X.H., Chen, Y.D., Huang, J.Q., Wang, Z.W., Hu, T., Wang, Z.R., Fang, K., 2024. Navigation path recognition between rows of fruit trees based on semantic segmentation. Comput. Electron. Agric. 216, 108511. https://doi.org/10.1016/j.compag.2023.108511.

Zhang, J.F., Yang, B., Geng, N., Huang, L.W., 2017. An obstacle detection system based on monocular vision for apple orchard robot. Int. J. Rob. Autom. 32 (6). https://doi.org/10.2316/Journal.206.2017.6.206-5036.

Zhao, H.S., Shi, J.P., Qi, X.J., Wang, X.G., Jia, J.Y., 2017. Pyramid scene parsing network. In: In Proceedings of the IEEE Conference on Computer Vision and Pattern Recognition, pp. 2881–2890.

Zhou, J.J., Geng, S.Y., Qiu, Q., Shao, Y., Zhang, M., 2022. A deep-learning extraction method for orchard visual navigation lines. Agriculture 12 (10), 1650. https://doi.org/10.3390/agriculture12101650.

drones

MDPI

Article

Quantity Monitor Based on Differential Weighing Sensors for Storage Tank of Agricultural UAV

Junhao Huang [1,2,3,4], Weizhuo He [1,2,3,4], Deshuai Yang [1,2,3,4], Jianqin Lin [1,2,3,4], Yuanzhen Ou [1,2,3,4], Rui Jiang [1,2,3,4,†] and Zhiyan Zhou [1,2,3,4,*,†]

[1] Guangdong Laboratory for Lingnan Modern Agriculture, College of Engineering, South China Agricultural University, Guangzhou 510642, China; boulet@stu.scau.edu.cn (J.H.); 15813301373@stu.scau.edu.cn (W.H.); dsyang@stu.scau.edu.cn (D.Y.); 602015148@stu.scau.edu.cn (J.L.); yuanzhenou@stu.scau.edu.cn (Y.O.); ruiojiang@scau.edu.cn (R.J.)
[2] Guangdong Provincial Key Laboratory of Agricultural Artificial Intelligence (GDKL-AAI), Guangzhou 510642, China
[3] Guangdong Engineering Research Center for Agricultural Aviation Application (ERCAAA), Guangzhou 510642, China
[4] Key Laboratory of Key Technology on Agricultural Machine and Equipment, South China Agricultural University, Ministry of Education, Guangzhou 510642, China
* Correspondence: zyzhou@scau.edu.cn; Tel.: +86-135-6002-6139
† These authors contributed equally to this work.

Abstract: Nowadays, unmanned aerial vehicles (UAVs) play a pivotal role in agricultural production. In scenarios involving the release of particulate materials, the precision of quantity monitors for the storage tank of UAVs directly impacts its operational accuracy. Therefore, this paper introduces a novel noise-mitigation design for agricultural UAVs' quantity monitors, utilizing differential weighing sensors. The design effectively addresses three primary noise sources: sensor-intrinsic noise, vibration noise, and weight-loading uncertainty. Additionally, two comprehensive data processing methods are proposed for noise reduction: the first combines the Butterworth low-pass filter, the Kalman filter, and the moving average filter (BKM), while the second integrates the Least Mean Squares (LMS) adaptive filter, the Kalman filter, and the moving average filter (LKM). Rigorous data processing has been conducted, and the monitor's performance has been assessed in three UAV typical states: static, hovering, and flighting. Specifically, compared to the BKM, the LKM's maximum relative error ranges between 1.24% and 2.74%, with an average relative error of 0.31%~0.58% when the UAV was in a hovering state. In flight mode, the LKM's maximum relative error varies from 1.68% to 10.06%, while the average relative error ranges between 0.74% and 2.54%. Furthermore, LKM can effectively suppress noise interference near 75 Hz and 150 Hz. The results reveal that the LKM technology demonstrated superior adaptability to noise and effectively mitigates its impact in the quantity monitoring for storage tank of agricultural UAVs.

Keywords: unmanned aerial vehicle (UAV); noise filtering; Butterworth low-pass filter; least mean squares (LMS) adaptive filter; quantity monitoring

check for updates

Citation: Huang, J.; He, W.; Yang, D.; Lin, J.; Ou, Y.; Jiang, R.; Zhou, Z. Quantity Monitor Based on Differential Weighing Sensors for Storage Tank of Agricultural UAV. *Drones* **2024**, *8*, 92. https://doi.org/10.3390/drones8030092

Academic Editor: Pablo Rodríguez-Gonzálvez

Received: 5 January 2024
Revised: 7 February 2024
Accepted: 2 March 2024
Published: 7 March 2024

1. Introduction

In recent years, unmanned aerial vehicles (UAVs) have developed significantly in agricultural production, including application such as scenarios spraying pesticides and herbicides, spreading fertilizers, seeding, and farmland monitoring, etc. [1,2]. Whether the UAV continues to work needs to be determined by judging whether there is still material in the storage tank. The controller unit carried by the UAV needs to determine whether the amount of material currently released is accurate using the mass flow rate. Therefore, it is essential to accurately monitor the allowance and the mass flow rate of the storage tank for the operation accuracy of the UAV in the process of releasing particulate materials [3].

In the existing scientific research, according to the different principles, the monitoring quantity and mass flow rate can be divided into four methods. The first method is the photoelectric method. In the study of this method, Swisher et al. designed an optical sensor for measuring fertilizer flow based on the laser light source. The sensor consisted of 32 photoelectric tubes. The instantaneous flow rate of the fertilizer was obtained according to the shielding strength of particles to light [4]. Grift et al. previously examined the correlation between the output pulse width of the near-infrared photodetector and the fertilizer flow rate. They verified the sensor's detection accuracy at various densities and flow rates. Previously, under high density conditions, they measured the flow rate of spherical granular fertilizer with a diameter of 4.45 mm, achieving a detection error of 3% [5]. Based on the principle of the photovoltaic effect, D. Youchun et al., in 2019, designed a seed flow monitoring device using a thin-surface laser emission module and a silicon photocell, carried out a field sowing test. The test showed that the monitoring accuracy of the device for rape seeds was not less than 98.6%, and the monitoring accuracy of wheat seeds was not less than 95.8% [6]. In a similar context, W. Zaiman et al. used a surface source photoelectric sensor to monitor rice seeds and established a mathematical model between seed number and pulse width, which provided a reference for seed monitoring of precision hill direct seeding of rice [7]. X. Chunji et al. proposed a seeding parameter monitoring method based on a laser sensor and carried out a dust-resistant simulation test, which proved that the laser sensor had stronger dust penetration resistance than the infrared sensor. The monitoring accuracy of the designed monitoring method for double-overlapped seeds can reach 95.4% [8].

The second method is the impact method; the Advanced Farming System of CASE IH Company, Grain-Trak System of the Micro-Trak Company, and Teris System of the Deutz-Fahr Company were all grain-flow monitoring systems based on this method [9]. X. Yingjun et al. previously introduced a digital adaptive interference cancellation method to address the issue of grain flow sensors being susceptible to vibration noise. This method effectively filters out most of the vibration noise, thereby enhancing the sensor's monitoring accuracy [10]. W. Jinwu et al. designed a rice hole direct seeding monitoring system based on the principle of the piezoelectric impact method, which had an effective monitoring accuracy of 97.67%, and the sound and light alarm can be carried out when replaying or missing seedings [11]. W. Shuai used adaptive complementary ensemble empirical mode decomposition wavelet threshold denoising algorithm to denoise the signal of impulse sunflower seed flow sensor. According to the characteristics of sensor voltage signal, the adaptive decomposition is realized. The signal was decomposed into IMF components from high frequency to low frequency. After denoising the high frequency IMF components with low signal-to-noise ratio, the voltage signal which can be used to establish the yield model was obtained [12].

The third method is the capacitance method whose principle is that the capacitance changes with the mass of the plate medium, and the calibration method was used to construct the relationship model between the capacitance value and the seeding rate, so as to realize the monitoring of seed sowing rate. Z. Liming et al. designed a set of seed sowing rate monitoring device this method [13]. C. Jianguo et al. designed a wheat seed number detection system based on a capacitance sensor, established a relationship model between the capacitance value and wheat seed number, and realized seed-number monitoring with a monitoring error of about 2% [14]. Z. Mingyan et al. designed a quantity monitor for a fertilizer storage tank and constructed a relationship model between the fertilizer height and capacitance value based on the capacitance method, which realized the monitoring of fertilizer height [15]. Based on the capacitance method, T. Yanan et al. designed a fertilizer tank level sensor, which realized the effect of on-line monitoring of the fertilizer tank level [16].

The final method is the weighing method. With the rapid development of precision agriculture, weighing sensors have been increasingly used in precision seeding, grain yield monitoring, and quantity monitoring. AI-Jalil et al. designed a weighing sensor device with adjustable height and width, which was suitable for a variety of agricultural machinery equipment and can realize the weighing of a storage tank [17]. An example of this is the work developed, in 2001, by Van Bergeijk et al., in which a dynamic weighing system for fertilizer applicators was projected. The system included a main weighing sensor and a reference weighing sensor. The reference weighing sensor was used to compensate for the vibration and other signals, which can realize automatic calibration and real-time dynamic weighing [3]. Using a similar approach, Koichi et al. designed a grain yield sensor composed of a ring weighing sensor and an impact plate to realize the real-time estimation of the grain yield [18]. In terms of harvest yield measurements, X. Zhang et al. proposed a method for measuring yield of the harvester based on the weighing method. Short-time wavelet filtering and other methods were used to process flow data in real time. The error of bench test was less than 2%, and the accuracy was good [19]. In terms of fertilization, W. Liguo et al. used the weighing principle to feed back the fertilizer flow information and adjusted the amount of fertilizer in real time according to the speed of the fertilizer applicator to realize the variable fertilizer distribution and fertilization operation, and the fertilization accuracy reached more than 95% [20]. In terms of sowing, L. Haitao et al. designed a seeding rate monitoring system for ground fertilizer applicator based on the weighing sensor. The filtering combination of low-pass filtering + mean filtering + moving average filtering was used to eliminate the mechanical vibration noise. Field experiments showed that the maximum relative error of the monitoring system was 4.88%, and the average relative error was 2.62% [21].

According to the above research, the following results can be obtained; firstly, the monitoring sensor based on the photoelectric method has the advantages of being simple and efficient and having convenient installation. By using the instantaneous flow of the material, the allowance of the material in the storage tank can be calculated. However, it requires a complex calibration process for different materials, and its monitoring accuracy is easily affected by dust. Therefore, it is not suitable for use in a working environment with high dust content. Secondly, the sensors based on the impact method need to construct the relationship model between the flow and impulse. The operation was cumbersome, and the monitoring accuracy was easily affected by the vibration noise. Thirdly, the monitoring device using the capacitance method also needed to calibrate different materials. In addition, the capacitance value was easily affected by environmental factors such as temperature, humidity, and mechanical vibration. It was usually necessary to add a shielding shell around the capacitance plate to reduce the interference of the external environment. And finally, the weighing sensor can directly obtain the allowance of the material and monitor the mass flow. However, in the actual operation process, the body of the agricultural machinery shakes obviously, which easily causes vibration interference of the weighing sensor, resulting in unstable weight data. It is necessary to filter the vibration and noise of the weighing sensor. Therefore, this paper proposed a detection method of the differential weighing sensors with a combination of a measurement sensor and noise sensor to explore the effects of various filtering methods and select a better method.

2. Materials and Methods

2.1. Design of Test Device and Weighing System

2.1.1. Test Device and Circuit Design

The UAV's communication link used in the test included a seeding controller, flight controller, remote controller, UAV ground station, voltage signal conversion module, weighing sensors, and the UAV itself, which is shown in Figure 1. The voltage signal conversion module converts the analog signal of the sensor into a digital signal. It communicates with the seeding controller through USART, the seeding controller communicates with the flight control through USART, and the ground station communicates with the flight control through the Mobile SDK interface. Before the operation, the route was planned, and the seeding parameters were set in the UAV ground station. The ground station uploaded the route and parameters to the flight controller and seeding controller through the Mobile SDK interface. During the operation, the UAV was seeded according to the set parameters. During the sowing process, the real-time weight of the storage tank displayed on the ground station [22,23].

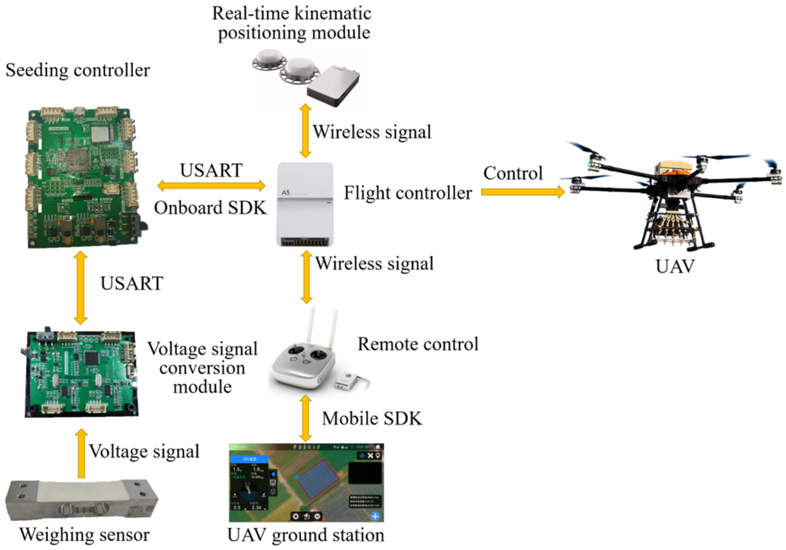

Figure 1. The UAV shot seeding device for test.

The experimental setup used a two-cantilever-beam weighing sensor (Yongkang Jushi Weighing Instrument Co., Ltd., Yongkang, China) monitoring storage tank, and its technical information as shown in Table 1. Generally, an analog-to-digital conversion circuit was used to convert the analog signal into a digital signal, and the single-chip microcomputer read the digital signal. This paper designed an analog-to-digital conversion circuit board using the AD7190 (Analog Devices, Inc., Wilmington, MA, USA), whose technical information is shown in Table 2. The REF3025 voltage reference chip (Texas Instruments, Dallas, TX, USA) was used to provide a precise 2.5 V reference voltage.

Table 1. The technical information of the weighing sensor used in the test.

Range (kg)	Energizing Voltage (V)	Sensitivity (mV/V)	Temperature Range (°C)	Number of Input and Output	Output Signal Type
0~20	2.5~12	2	−20~60	2 and 2	analog

Table 2. The technical information of AD7190.

Number of A/D Converters	Bits	Temperature Range (°C)	Number of Input & Output	Input Signal Type	Output Signal Type
1	24.0	−40~105	2 and 4	analog	digital

2.1.2. Data Processing Scheme

For the noise in the signal, common filtering methods include high-pass filtering, low-pass filtering, band-pass filtering, notch filtering, etc. Such filtering methods need to measure the frequency band of the noise in advance to reduce the noise, and it is difficult to apply to scenes containing a large amount of random noise. The adaptive filter has been widely used in audio processing, power ripple processing, and image processing because of its small amount of calculation, no prior data, good real-time performance, and automatic adjustment of filter coefficients.

In order to reduce the interference of the UAV vibration noise weighing sensor, this paper designed two filtering schemes based on the Least Mean Squares (LMS) adaptive filter and conventional low-pass filter, respectively. The filtering effects of the two schemes were compared through experiments to pick up the suitable filtering scheme of the weighing sensor and provide reliable data for the UAV. The output frequency (filtering frequency) of the data was 250 Hz, and the data processing flow first converts the voltage signal of the weighing sensor into the original weight data, then performs data preprocessing, and finally performs data smoothing. Data processing was a pretreatment with a Butterworth low-pass filter named scheme 1 and with an LMS adaptive filter named scheme 2, as shown in Figure 2. Kalman filtering and moving average filtering were carried out to further reduce the noise in the data and improve the smoothness of the data.

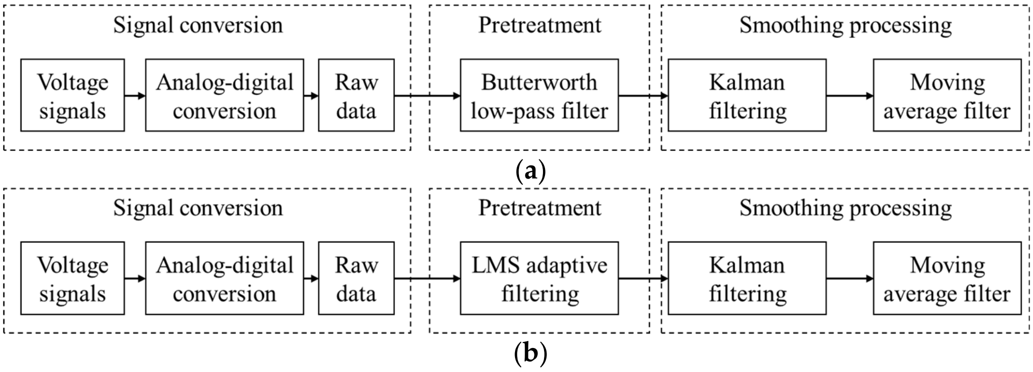

Figure 2. Two data processing schemes: (**a**) scheme 1 with Butterworth low-pass filter and (**b**) scheme 2 with LMS adaptive filter.

2.1.3. Differential Weighing Sensors Installation

The installation method of the weighing sensor is shown in Figure 3. Two weighing sensors (No. 1 and No. 2) were used as the main sensors, which were fixed on both sides of the crossbeam of the frame and were used to directly weigh the storage tank. A third weighing sensor (No. 3) was used as a noise monitoring sensor, which was connected to the bottom of the frame beam through a copper column, and the force end of the sensor was fixed to a 500 g counterweight block. When the data processing scheme 1 was adopted, only the data of two main sensors were used; when the data processing scheme 2 was adopted, the data of the two main sensors were used as the reference signal of the LMS adaptive filter, and the data of the noise monitoring sensor were used as the input signal.

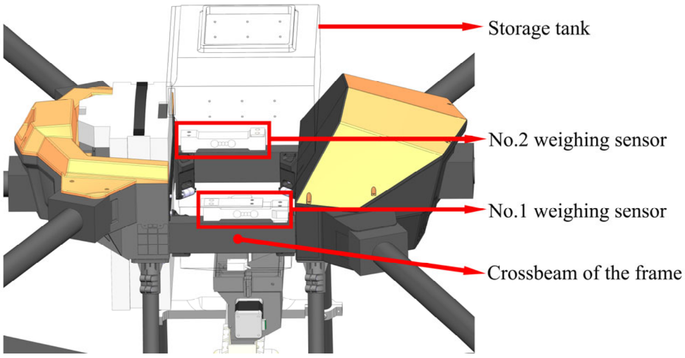

(**a**)

Figure 3. *Cont.*

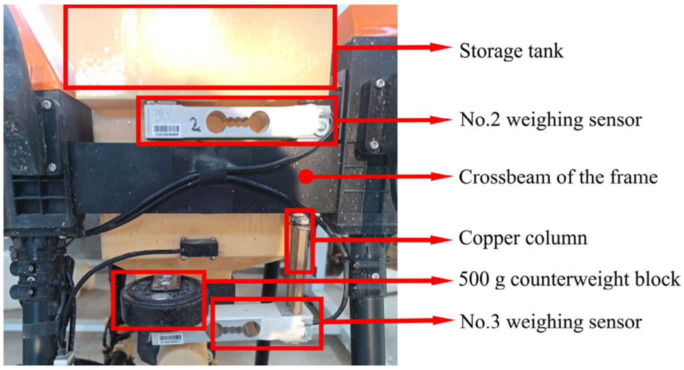

(**b**)

Figure 3. The installation method of differential weighing sensors: (**a**) the installation of the main sensors and (**b**) the installation of the noise monitoring sensor.

2.1.4. Filtering Requirements

The filtering requirements were generally considered from two aspects: convergence speed and convergence accuracy, which sometimes contradict each other, that is, increasing the convergence speed (reducing the convergence time) will lead to a convergence accuracy, and reducing the convergence speed (increasing the convergence time) can improve the convergence accuracy. The specific filtering requirements are as follows:

(1) The weight data mentioned in this paper were mainly used to monitor the storage tank and indicate that there was no material left in the storage tank. The quantity monitor is installed on the UAV and connected to the controller of the UAV. During the operation of the UAV, when the quantity monitor detects that there is nothing remaining in the storage tank, it sent an instruction to the UAV's controller to suspend the operation of the UAV and remind the operator so that the operator can control the UAV to return to the feeding point to add materials, avoiding having the empty storage tank continuing to operate, resulting in missed application. The maximum acceptable error of missed application of the device for the test was 1 m. According to the maximum 3 m/s operating speed of the prototype, the maximum acceptable delay time of the filtered data was 333 ms, that is, the convergence time should be less than 333 ms.

(2) When the weighing data were used for the judgment of the shortage warning, if the data fluctuation range is large, the accuracy of the shortage warning will be affected. Therefore, the higher the convergence accuracy is, the better. The average relative error of the weighing data during the UAV flight should be less than 3%.

2.2. Data Preprocessing Based on Butterworth Low-Pass Filter

The main feature of the Butterworth filter is that the frequency response curve in its passband has the maximum flatness. The higher the order of the filter, the better the passband characteristics and flatness [24]. The Butterworth low-pass filter can be used to reduce the high-frequency vibration noise in the data. The normalized transfer formula of the n-order Butterworth low-pass filter is as follows [25]:

$$H(s) = \frac{1}{a_0 + a_1 s + a_2 s^2 + a_3 s^3 + \cdots + a_n s^n}, \tag{1}$$

where a_0, a_1, a_2, a_3, and a_n represent polynomial coefficients; n represents the order of the filter. Although increasing the order of the filter can improve the filtering effect, the delay of the filtered data increases, and the amount of calculation becomes larger. Considering both the delay and computational complexity, a second-order Butterworth low-pass filter is selected to preprocess the data, and its normalized transfer formula is as follows:

$$H(s) = \frac{1}{s^2 + 1.414s + 1} \tag{2}$$

Let $P = \tan(\frac{\pi f_d}{f_s})$, the above transfer formula is discretized by bilinear transformation, and s can be transformed into

$$s = \frac{\frac{1 - z^{-1}}{1 + z^{-1}}}{P}, \tag{3}$$

where f_d represents cut-off frequency, and f_s represents sampling frequency. Replacing (3) in (2)

$$H(z) = \frac{Y(z)}{X(z)} = \frac{P^2 + 2P^2 z^{-1} + P^2 z^{-2}}{(1 + 1.414P + P^2) + (2P^2 - 2)z^{-1} + (1 - 1.414P + P^2)z^{-2}}, \tag{4}$$

$$Y(z) = b_0 X(z) + b_1 X(z-1) + b_2 X(z-2) - a_1 Y(z-1) - a_2 Y(z-2), \tag{5}$$

$$b_0 = b_2 = \frac{P^2}{1 + 1.414P + P^2}, \tag{6}$$

$$b_1 = \frac{2P^2}{1 + 1.414P + P^2}, \tag{7}$$

$$a_1 = \frac{2P^2 - 2}{1 + 1.414P + P^2}, \tag{8}$$

$$a_2 = \frac{1 - 1.414P + P^2}{1 + 1.414P + P^2}, \tag{9}$$

where b_0, b_1, a_1, and a_2 represent coefficients of the filter, and the expression in (5) is the final second-order Butterworth low-pass filter data update formula.

By inputting a step signal to the system, the convergence speed of Butterworth low-pass filter is observed to confirm the cut-off frequency and filter coefficient of the filter. The method was to place 10 kg weight on the storage tank. After the weight data are stable, 5 kg of the weight was reduced in an instant, the data change is observed, and the data are recorded before and after filtering at a sampling frequency of 250 Hz when collecting the data.

2.3. Data Preprocessing Based on LMS Adaptive Filtering

The filter mainly included two parts, namely the Finite Impulse Response (FIR) filter and the coefficient update algorithm. The output signal is generated after the input signal passes through the FIR filter, and the error was calculated after the output signal was compared with the desired signal. The coefficient update algorithm adjusted the coefficients of the FIR filter according to the output signal and the error, so that the error gradually became smaller, and then, the adaptive parameter adjustment and filtering were performed.

The main adjustable parameters of the LMS adaptive filtering algorithm were the order k and step factor m. The larger the order, the larger the filter cache, the more data available for the filter reference, but the larger the single calculation; the larger the step size factor, the faster the tracking and convergence speed of the algorithm, but the lower the convergence accuracy. The iterative formula of the LMS adaptive filtering algorithm is [26]

$$\begin{cases} y(n) = b(1)x(n) + b(2)x(n-1) + b(3)x(n-2) + \cdots + b(k)x(n-k+1) \\ e(n) = d(n) - y(n) \\ b(k) = b(k-1) + 2me(n)x(n-k+1) \end{cases}, \tag{10}$$

where $e(n)$ is the error at time n; $d(n)$ is the desired signal at time n; $x(n)$ is the input signal at time n; $y(n)$ is the output signal at time n; and $b(k)$ is the k-order filter cache.

The input signal of the LSM adaptive filter is the data of the noise monitoring sensor, the expected signal is the data of the two main sensors, and the output signal is the filtered data. The data of the main sensor will become smaller and smaller due to the continuous reduction of seed weight during UAV working, and the data can be regarded as a signal source containing noise. The weight of the weight block fixed by the noise monitoring sensor is unchanged, but due to the interference of noise, the data will fluctuate continuously, and the data can be regarded as the noise source. After inputting the data of the main sensor and the noise monitoring sensor into the LMS adaptive filter, the coefficient update algorithm constantly adjusts the coefficients of the FIR filter, gradually eliminates the noise of the main sensor data, and makes the output signal gradually approach the real signal source to realize the data filtering.

The step size factor is the main parameter that affects the convergence speed of the LMS adaptive filter. To determine the size of the step size factor, the order of the filter was fixed to 100. By changing the size of the step size factor, the delay time of the data was observed to analyze the convergence speed. The experimental design is as follows:

(1) The step size factor was set to 10 levels, ranging from 0.01 to 0.1, and each 0.01 was a level;
(2) By inputting the step signal into the system, the convergence speed of the filtering algorithm was observed: 10 kg of weight was placed on the storage tank, and 5 kg of weight was reduced in an instant after the weight data were stable, and the data corresponding to different step-size factors were recorded at a sampling frequency of 250 Hz.

2.4. Data Smoothing

2.4.1. Kalman Filtering

As an optimal estimation algorithm [27], the Kalman filter algorithm can filter the observation data with noise. In this paper, the linear Kalman filter algorithm was used to further smooth the data. The algorithm mainly includes two parts: prediction and update. The formula is as follows [28]:

$$\hat{x}_k^- = \hat{x}_{k-1}^- + u_k, \tag{11}$$

$$P_k^- = P_{K-1} + Q, \tag{12}$$

$$K_k = \frac{P_k^-}{P_k^- + R}, \tag{13}$$

$$\hat{x}_k = \hat{x}_k^- + K_k(y_k - \hat{x}_k^-), \tag{14}$$

$$P_k = (I - K_k)P_k^-, \tag{15}$$

In the above formulas, (11) and (12) are the prediction equations of the algorithm, and (13)–(15) are the update equations of the algorithm. Where $\hat{x}_k$ represents the predicted state at time k; y_k represents the observation at time k; u_k represents the control effect of the outside world on the system at time k; P_k represents the covariance matrix at time k; Q represents the prediction noise matrix; R represents the measurement noise matrix; K_k represents the Kalman gain at time k; I represents the unit matrix; and $\hat{x}_k^-$ and $\hat{P}_k^-$ represent the corresponding prior variables. When the algorithm is executed, the prior estimation of the state variables is first performed, and the prior covariance is calculated. Then, the Kalman gain is calculated, and finally, the data estimation and covariance update are performed.

When adjusting the parameters of the algorithm, the prediction noise covariance Q and the observation noise covariance R are mainly adjusted. When the Q increases, the dynamic response becomes faster, that is, the convergence speed is accelerated, but the convergence accuracy is reduced. As R increases, the dynamic response becomes slower, that is, the convergence speed becomes slower, but the convergence accuracy is improved. According to the experience of Q and R tuning parameters, there is a final R value of 1.2 and a Q value of 0.1.

2.4.2. Moving Average Filter

In the actual operation process, the frame of the UAV is prone to random vibration, which causes random noise interference to the weight data. Therefore, it is necessary to further smooth the data. The moving average filtering algorithm has the characteristics of simplicity and small computation and can effectively eliminate the random noise in the data and improve the smoothness of the data. The formula is as follows:

$$y(n) = \frac{1}{L}[x(n) + \sum_{t=n-L+1}^{n} y(t)], \tag{16}$$

where $y(n)$ represents the data after moving average at time n; $x(n)$ represents the input data at time n; and L represents the window size of moving average filtering. The window size L determines the filtering effect of the algorithm. When the algorithm is executed, the moving average is calculated after waiting for L data. In theory, the data lags L data. The larger the value of L, the better the filtering effect, but the longer the data delay time.

In this paper, the convergence time of the expected filtering data is less than 333 ms. After the Kalman filter (in Section 2.4.1) is added, the convergence time of the two data processing schemes is 260 ms and 280 ms, respectively. Therefore, after the moving average filtering is added in this section, the convergence time can be extended by 73 ms and 53 ms, respectively. The weight data output frequency of this subject is set to 250 Hz (the filtering period is 4 ms), and the window size should be less than 18.25 and 13.25, respectively, so the window size was 18 and 13, respectively.

2.4.3. Static Filtering Effect

The control system designed in this project had the function of seeding quantity calibration, and the weight data needed to be obtained during calibration. The accuracy requirement of the calibration process for the weight data was a deviation of less than 2 g. The static filtering data were analyzed, the data of 10 s were collected, and the accuracy of the data was evaluated by the average deviation. The average deviation calculation method is as follows:

$$E = \frac{\sum_{n=1}^{n} |e_n - e_t|}{n}, \tag{17}$$

where E represents the average deviation of the sample (g); e_n represents nth filter data (g); and e_t represents reference weight (g).

2.5. Data Processing Comparison Test

2.5.1. When the UAV Is Hovering

In the hovering state of the UAV, which means that the UAV is stationary in the air, maintaining a certain height and position, the filtering effects of the two data processing schemes were tested, and the design is as follows:

(1) The test was carried out in sunny conditions with a natural wind speed of less than 3 m/s, and the temperature was between 20 and 28 degrees Celsius. The test site was the open space of the wind tunnel laboratory of South China Agricultural University, Guangzhou, China.

(2) Before the test, the weight of the storage tank was peeled, and the actual load of the UAV storage tank was changed by adding a 5 kg weight to the storage tank. Five levels of 5, 10, 15, 20, and 25 kg (25 kg is the maximum load) were set up for a total of 5 groups of tests.

(3) The hovering height of the UAV was set to 1.5 m. At the same time, two filtering schemes were used to filter the original data in real time, and the update rate (output rate) of the filter was 250 Hz. The data were recorded after the UAV hovered stably, and the data recording time was 30 s, that is, 7500 data points were collected.

The actual weight of 5 bags of heavy objects was recorded before the test. The weight was used as the reference weight in the data analysis. The filtered data were compared with the reference weight, and the data were analyzed from the aspects of maximum deviation, maximum relative error, average relative error, and FFT spectrum. The calculation method of the relative error is as follows:

$$\delta_i = \frac{|X_i - X_t|}{X_t} \times 100\% \tag{18}$$

where δ_i represents the relative error of the i th filtered data (kg); X_t represents reference weight (kg). The smaller the relative error, the better the filtering effect. The FFT spectrum can reflect the distribution of noise and the size of noise. The smaller the amplitude corresponding to a certain frequency, the smaller the noise in the data corresponding to that frequency.

Six kinds of filter data were recorded during the experiment. To facilitate chart reading and data analysis, the code shown in Table 3 was used to replace each filter processing.

Table 3. Methods of different filtering processing.

Filter Processing	Code
Butterworth low-pass filter	Treatment 1
LMS adaptive filter	Treatment 2
Butterworth low-pass filter + Kalman filter	Treatment 3
LMS adaptive filter + Kalman filter	Treatment 4
Butterworth low-pass filter + Kalman filter + moving average filter (BKM)	Treatment 5
LMS adaptive filter + Kalman filter + moving average filter (LKM)	Treatment 6

2.5.2. When the UAV Is Flying

In the actual operation process, the UAV was not only in the hovering state, but also in the switching route state and the flight state. However, the UAV was in the flight state most of the time, so the weight data in the flight state were more important. In this test, the corresponding weight data were analyzed when the prototype was in flight, but its actuator was not working. The specific experimental design is as follows:

(1) The test weather conditions and test sites were the same as those in Section 2.5.1.

(2) We planned the route at the ground station to make the prototype fly along the route. The working height was set at 1.5 m, and the working speed was set at three levels of 1, 2, and 3 m/s, respectively. The weight of the storage tank was set to 5 levels, which were 5, 10, 15, 20, and 25 kg (25 kg was the maximum load), and a total of 15 groups of tests were carried out.

(3) At the same time, two filtering schemes were used to filter the weight data in real time, and the update rate (output rate) of the filter was 250 Hz. The data were recorded during the flight of the prototype, and the data recording time was 15 s, that is, 3750 data points were collected.

2.6. UAV Seeding Field Test

To further verify the practical application effect of the treatments, three field tests of rice seeding were carried out in the Mark Village, Dongchong Town, Nansha, Guangzhou, China, the Dagang Village, Zhucun Town, Zengcheng, Guangzhou, China, and the Zengcheng Teaching and Research Base of South China Agricultural University, Guangzhou, China. During the test period, the wind speed was less than 3 m/s, and the temperature was between 22 and 30 degrees Celsius. The test sites and planting features are shown in Figure 4 and Table 4.


(**a**) (**b**) (c)

Figure 4. The test sites: (**a**) Mark Village, Dongchong Town, Nansha, Guangzhou, China, (**b**) Dagang Village, Zhucun Town, Zengcheng, Guangzhou, China, and (**c**) Zengcheng Teaching and Research Base of South China Agricultural University, Guangzhou, China.

Table 4. UAV seeding field test scheme.

Test Name	Location	Area (hm^2)	Seeding Rate (kg/hm^2)	Row Spacing (m)	Height (m)	Speed (m/s)
Test 1	Mark Village, Dongchong Town, Nansha, Guangzhou, China	0.4453	90	0.25	1.5	2.0
Test 2	Dagang Village, Zhucun Town, Zengcheng, Guangzhou, China	0.1906	150	0.25	1.5	2.0
Test 3	Zengcheng Teaching and Research Base of South China Agricultural University, Guangzhou, China	0.1047	150	0.25	1.5	2.3

In seeding, it was difficult to obtain reliable reference data because the quantity of the storage tank was becoming smaller and smaller. Therefore, the stability of the monitor for the storage tank mainly performed FFT analysis on the data and observed the noise changes before and after filtering to analyze the stability of the monitor for the storage tank.

The weight data of test 1, test 2, and test 3 were recorded and collected at a frequency of 250 Hz when seeding. After the tests, the weight data of three consecutive routes were selected from each test for comparison and analysis.

3. Results

3.1. Determination of Cut-Off Frequency and Filtering Coefficient

Before determining the cut-off frequency, the data needed to be analyzed by Fast Fourier Transform (FFT) to obtain the noise frequency band in the data. When the load of the UAV was about 5 kg, the weight data of the UAV in static was collected, hovering and flight states, and the data acquisition frequency was 250 Hz. The three sets of data were compared and analyzed by FFT using MATLAB® software (R2022a 9.12.0.1884302). The results are shown in Figure 5. The weight data fluctuated less in the stationary state, while the data fluctuated greatly in the hovering and flight states, and the data stability in flight was worse than that in hovering. It can be seen from the FFT spectrum that the noise frequency bands during hovering and flight were widely distributed, and obvious noise interference was generated near the frequencies of 75 and 150 Hz.

Because the noise frequency band was widely distributed and the noise caused great interference to the data, to retain useful low-frequency data, the cut-off frequency was selected at 30 Hz. The stability of the filter was preliminarily verified by using the Filter Designer in MATLAB® software. The response type was selected as 'Lowpass', the design method was selected as 'IIR-Butterworth', the order was selected as '2', the sampling frequency was selected as '250 Hz', and the cutoff frequency was selected as '30 Hz'. Figure 5 shows that the amplitude–frequency response curve of the filter is a non-oscillatory curve, which met the stability requirements.

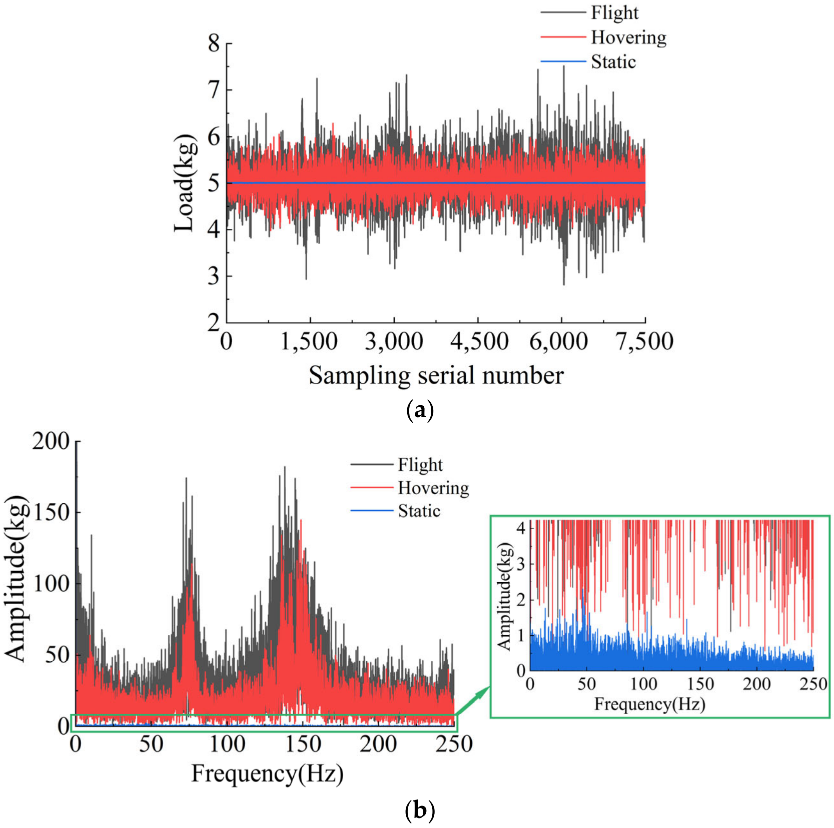

Figure 5. (**a**) Data comparison and (**b**) FFT spectrum of UAV in different states.

Using the Filter Designer, the coefficients of the second-order Butterworth low-pass filter are generated. The results were $b_0 = 0.0913$, $b_1 = 0.1826$, $b_2 = 0.0913$, $a_1 = -0.9824$, and $a_2 = 0.3477$.

We input a step signal into the system, and the results are shown in Figure 6.

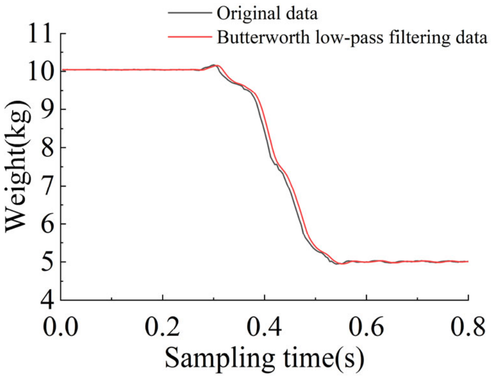

Figure 6. Butterworth low-pass filtering data.

The Butterworth low-pass filtering data lagged behind the original data by about 16 ms, and the convergence time was about 200 ms. The results met the requirement that the convergence time was less than 333 ms. In actual sowing, the instantaneous reduction in the weight of the storage tank by 5 kg was almost non-existent, so the convergence time of the designed Butterworth low-pass filtering algorithm was less than 200 ms.

3.2. Determination of Step Size Factor

For the determination test of the step factor, the weight change is shown in Figure 7. It can be seen from the figure that as the step size factor increased, the convergence speed of the data accelerated. The step size factor started from 0.06, and the growth rate of convergence gradually decreased. Further analysis of the delay time is shown in Table 5. The convergence time corresponding to the step size factors of 0.06, 0.07, 0.08, 0.09, and 0.10 were 294, 255, 222, 216, and 212 ms, respectively, which were within the acceptable convergence time range (less than 333 ms). Since the convergence speed of the step size factor did not change significantly after 0.08, and increasing the step size factor may reduce the convergence accuracy, it was more appropriate to select 0.08 as the step size factor.

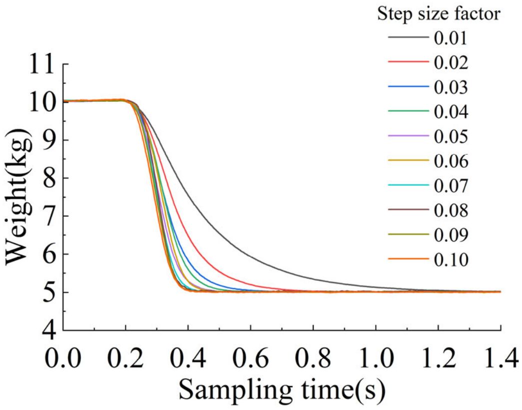

Figure 7. Weight variation in different step size factors.

Table 5. The delay time corresponding to different step size factors.

Step size factor	0.01	0.02	0.03	0.04	0.05	0.06	0.07	0.08	0.09	0.10
Delay time (ms)	1112	720	496	426	343	294	255	222	216	212

3.3. Result of Data Smoothing

3.3.1. Result of Kalman Filtering

By inputting a step signal into the system, the convergence speed of the filtering algorithm was observed. As shown in Figure 8, the data convergence time processed by 'Butterworth low-pass filtering + Kalman filtering' was about 260 ms, and the data convergence time processed by 'LMS self-adaptive filtering + Kalman filtering' was about 280 ms. The convergence time met the requirements.

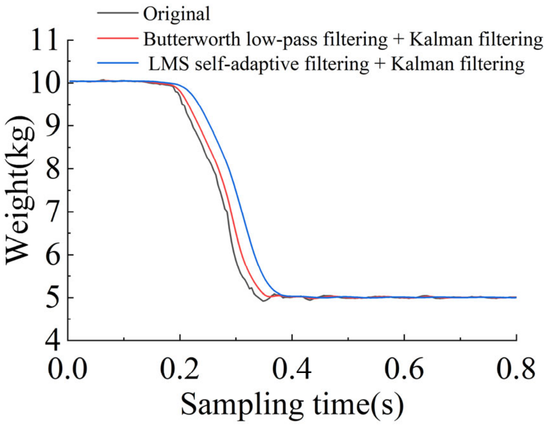

Figure 8. Data comparison after adding Kalman filter.

3.3.2. Result of Moving Average Filter

By inputting a step signal into the system, the convergence speed of the filtering algorithm was observed. The results are shown in Figure 9. The data convergence time processed by BKM was about 318 ms. The data convergence time processed by LKM was about 329 ms, and the convergence time was less than 333 ms, which met the demand. Because this experiment tested the convergence speed of the filtering algorithm by inputting the limit of the step signal (instantaneous reduction of 5 kg), and in the actual UAVs' working, the system input was not a step signal but generally a skew signal, the filtering algorithm convergence speed will be faster, and the convergence time will be shorter.

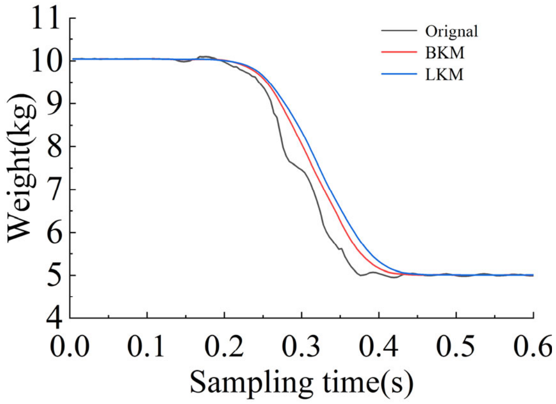

Figure 9. Increase in the data comparison after moving average filtering.

3.3.3. Result of Static Filtering Effect

The experimental results are shown in Figure 10 and Table 6. The average deviation of the data processed by BKM was 1.41 g. The average deviation of the data processed by LKM was 1.47 g, and the average deviation of the original data was 4.79 g. The two data processing schemes had a better filtering effect in the static state, which can meet the accuracy requirements of sowing quantity calibration.

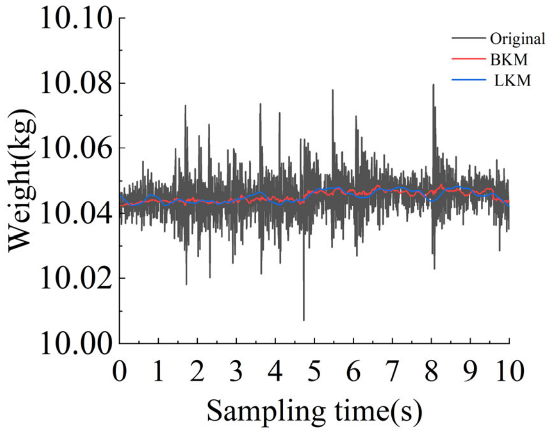

Figure 10. Static filtering data comparison.

Table 6. The average deviation of data in static state.

Filter Processing	Average Deviation (g)
Original	4.79
BKM	1.41
LMS	1.47

3.4. Data Processing Comparison Result When the UAV Was Hovering

After different filtering processing under different loads, the data pair is shown in Figure 11. It can be seen from the figure that under the five load levels, the original weight data without filtering fluctuates greatly. This is due to the vibration of the frame when the UAV was hovering. In addition, the UAV was not kept at the same height, and the UAV continued to move up and down at the target height. The vibration generated by the frame was transmitted to the storage tank, which ultimately caused the measurement result of the weighing sensor to be unstable.

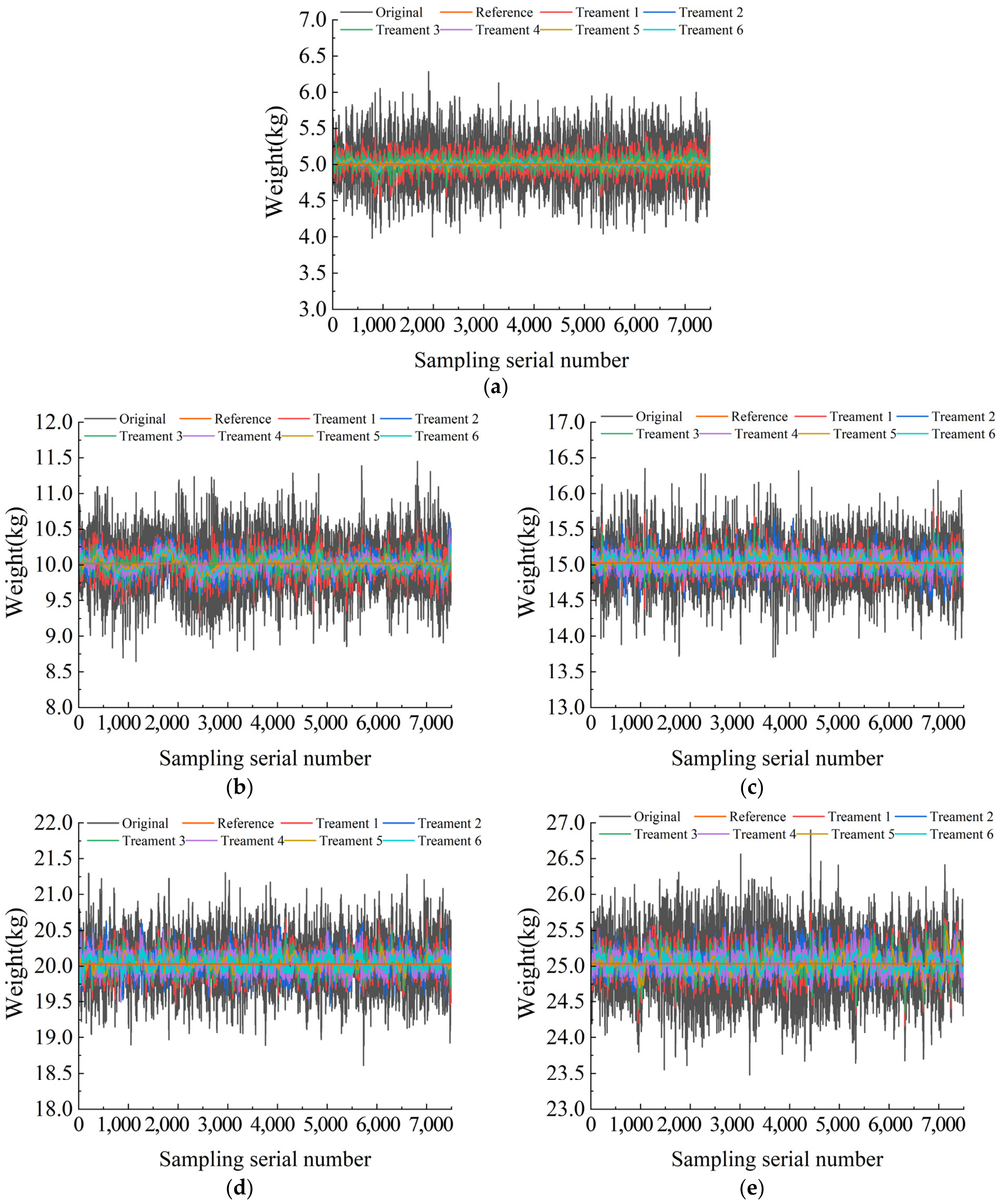

(**a**)

(**b**) (**c**)

(**d**) (**e**)

Figure 11. Comparison of processing data under different loads: (**a**) 5 kg, (**b**) 10 kg, (**c**) 15 kg, (**d**) 20 kg, and (**e**) 25 kg.

The data are further analyzed to calculate the maximum deviation, the maximum relative error, and the average relative error. The results are shown in Table 7. When the UAV was loaded with 5, 10, 15, 20 and 25 kg, respectively, the maximum deviations of the original data were 1.574, 1.690, 1.380, 1.522, and 1.872 kg, respectively, indicating that the unfiltered data had a large deviation and was difficult to use directly. After Treatment 5 and 6, the maximum deviation of the original data was less than 0.5 kg.

Table 7. Maximum relative error, average relative error, and standard deviation.

Load (kg)	Filter Processing	Maximum Deviation (kg)	Maximal Relation Error (%)	Mean Relative Deviation (%)
5	Original data	1.574	31.48	4.80
	Treatment 1	0.779	15.58	1.84
	Treatment 2	0.138	2.76	0.66
	Treatment 3	0.513	10.26	1.24
	Treatment 4	0.125	2.50	0.62
	Treatment 5	0.146	2.92	0.66
	Treatment 6	0.108	2.16	0.58
10	Original data	1.690	16.90	2.61
	Treatment 1	0.753	7.53	1.26
	Treatment 2	0.603	6.03	1.00
	Treatment 3	0.562	5.62	0.82
	Treatment 4	0.491	4.91	0.70
	Treatment 5	0.246	2.46	0.57
	Treatment 6	0.274	2.21	0.49
15	Original data	1.380	9.20	1.55
	Treatment 1	0.784	5.23	0.77
	Treatment 2	0.641	4.27	0.69
	Treatment 3	0.500	3.33	0.55
	Treatment 4	0.409	2.73	0.53
	Treatment 5	0.275	1.83	0.38
	Treatment 6	0.172	1.15	0.47
20	Original data	1.522	7.61	1.39
	Treatment 1	0.755	3.78	0.64
	Treatment 2	0.608	3.04	0.59
	Treatment 3	0.546	2.73	0.48
	Treatment 4	0.587	2.94	0.49
	Treatment 5	0.251	1.26	0.34
	Treatment 6	0.232	1.16	0.33
25	Original data	1.872	7.49	1.18
	Treatment 1	0.866	3.46	0.60
	Treatment 2	0.576	2.30	0.42
	Treatment 3	0.672	2.69	0.47
	Treatment 4	0.587	2.35	0.34
	Treatment 5	0.464	1.86	0.36
	Treatment 6	0.310	1.24	0.31

The filtered data of Treatment 5 and Treatment 6 are further analyzed, and the FFT spectrum diagram is drawn as shown in Figure 12.

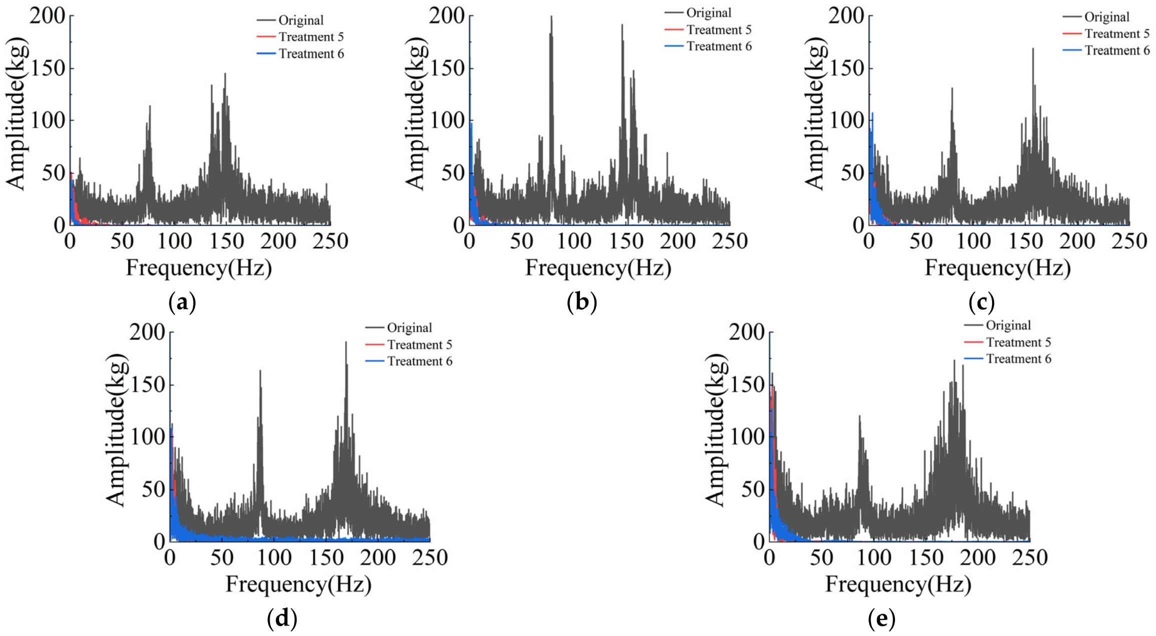

(**a**) (**b**) (**c**) (**d**) (**e**)

Figure 12. FFT spectrum of each processing data under different loads: (**a**) 5 kg, (**b**) 10 kg, (**c**) 15 kg, (**d**) 20 kg, and (**e**) 25 kg.

3.5. Data Processing Comparison Result When the UAV Was Flighting

Section 3.4 has analyzed each processing, indicating that the filtering effect of Treatment 5 and Treatment 6 was better. Therefore, when analyzing the weight data of flight, this section focuses on comparing the data of Treatment 5 and Treatment 6. The filtered data waveform is shown in Figure 13.

Further analyzing the above data, the statistical maximum deviation, maximum relative error, and average relative error are shown in Table 8.

Table 8. Corresponding results of different loads and different operating speeds.

Evaluating Indicator	**Filter Processing**	**Speed (m/s)**	**Load (kg)**				
			5	**10**	**15**	**20**	**25**
Maximum deviation (kg)	Original data	1	1.995	2.924	2.201	2.669	2.427
		2	2.316	2.584	2.417	2.587	2.552
		3	2.654	3.136	2.547	3.103	3.666
	Treatment 5	1	0.642	0.943	0.763	0.901	1.064
		2	0.515	1.088	1.448	0.895	1.503
		3	0.621	1.173	1.799	1.329	2.031
	Treatment 6	1	0.381	0.391	0.306	0.396	0.420
		2	0.425	0.392	0.368	0.546	0.817
		3	0.503	0.484	0.427	0.654	0.888
Maximal relation error (%)	Original data	1	39.90	29.24	14.67	13.35	9.71
		2	46.32	25.84	16.11	12.94	10.21
		3	53.08	31.36	16.98	15.52	14.66
	Treatment 5	1	12.84	9.43	5.09	4.51	4.26
		2	10.30	10.88	9.65	4.48	6.01
		3	12.42	11.73	11.99	6.65	8.12
	Treatment 6	1	7.62	3.91	2.04	1.98	1.68
		2	8.50	3.92	2.45	2.73	3.27
		3	10.06	4.84	2.85	3.27	3.55

Table 8. *Cont.*

Evaluating Indicator	Filter Processing	Speed (m/s)	Load (kg)				
			5	10	15	20	25
Mean relative deviation (%)	Original data	1	6.94	4.35	2.77	2.34	1.67
		2	7.30	5.37	3.65	2.54	2.23
		3	7.90	5.39	3.71	2.77	2.62
	Treatment 5	1	1.64	1.11	0.75	0.72	0.82
		2	2.40	1.87	1.85	1.31	1.61
		3	2.86	2.21	2.02	1.55	1.96
	Treatment 6	1	1.38	1.13	0.74	0.78	0.76
		2	2.32	1.43	1.09	0.97	1.13
		3	2.54	1.79	1.10	0.92	1.37

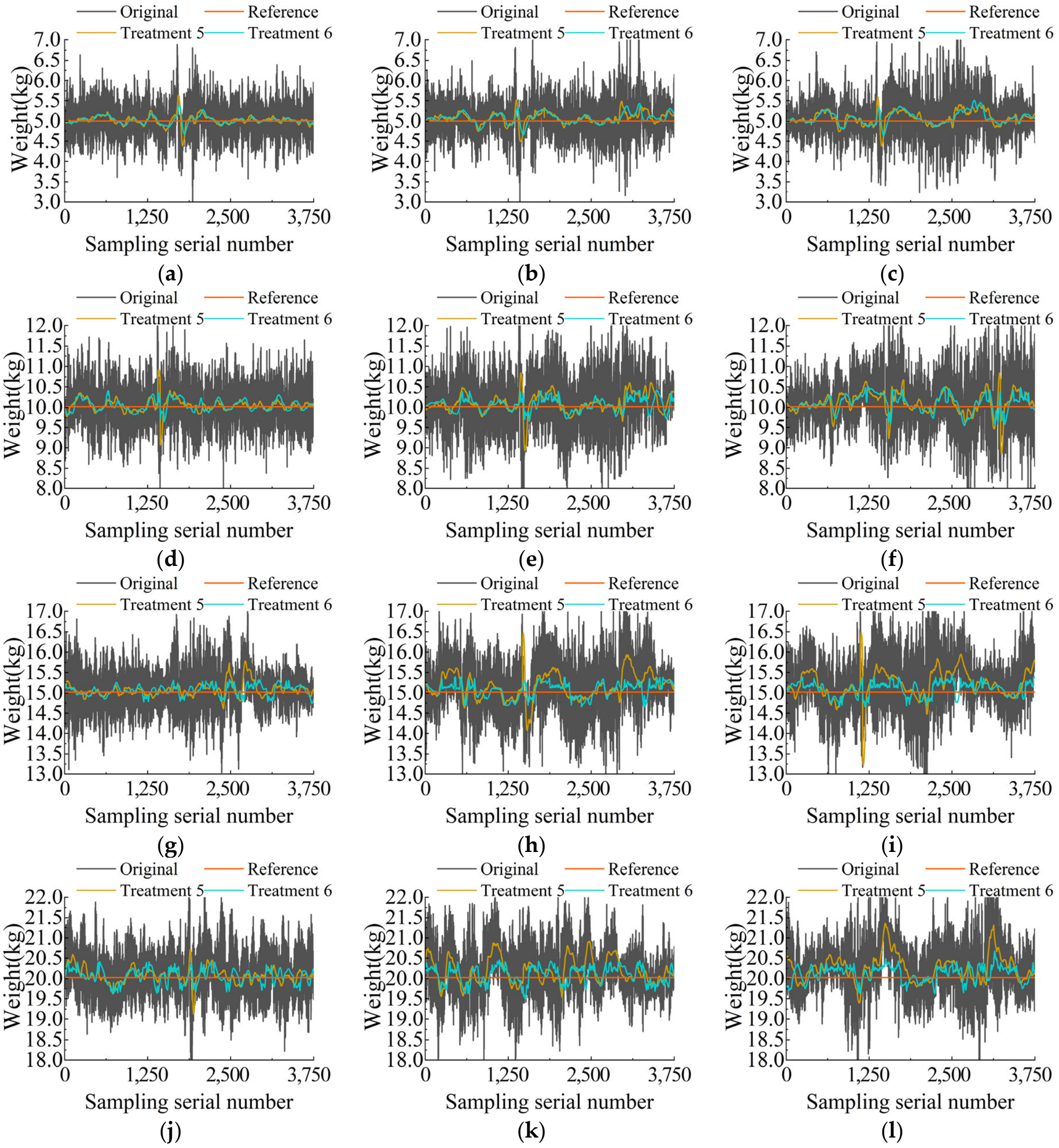

Figure 13. *Cont.*

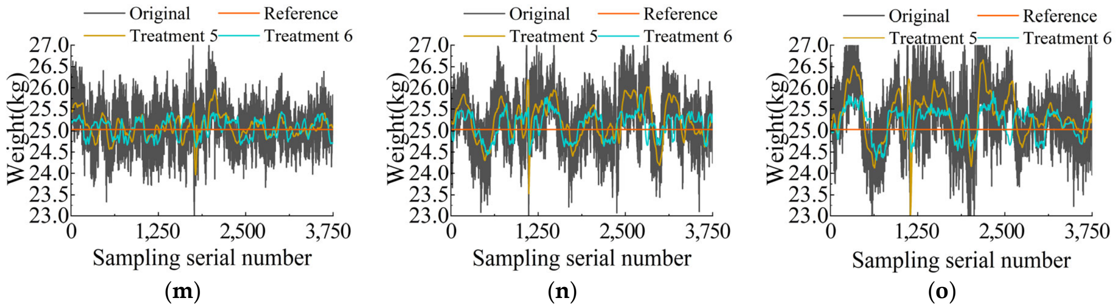

Figure 13. Data comparison under different loads and different flight speeds: (**a**–**c**) 5 kg (1~3 m/s), (**d**–**f**) 10 kg (1~3 m/s), (**g**–**i**) 15 kg (1~3 m/s), (**j**–**l**) 20 kg (1~3 m/s), and (**m**–**o**) 25 kg (1~3 m/s).

3.6. Result of Field Tests

The data of field tests and result of the FFT analysis are shown in Figure 14.

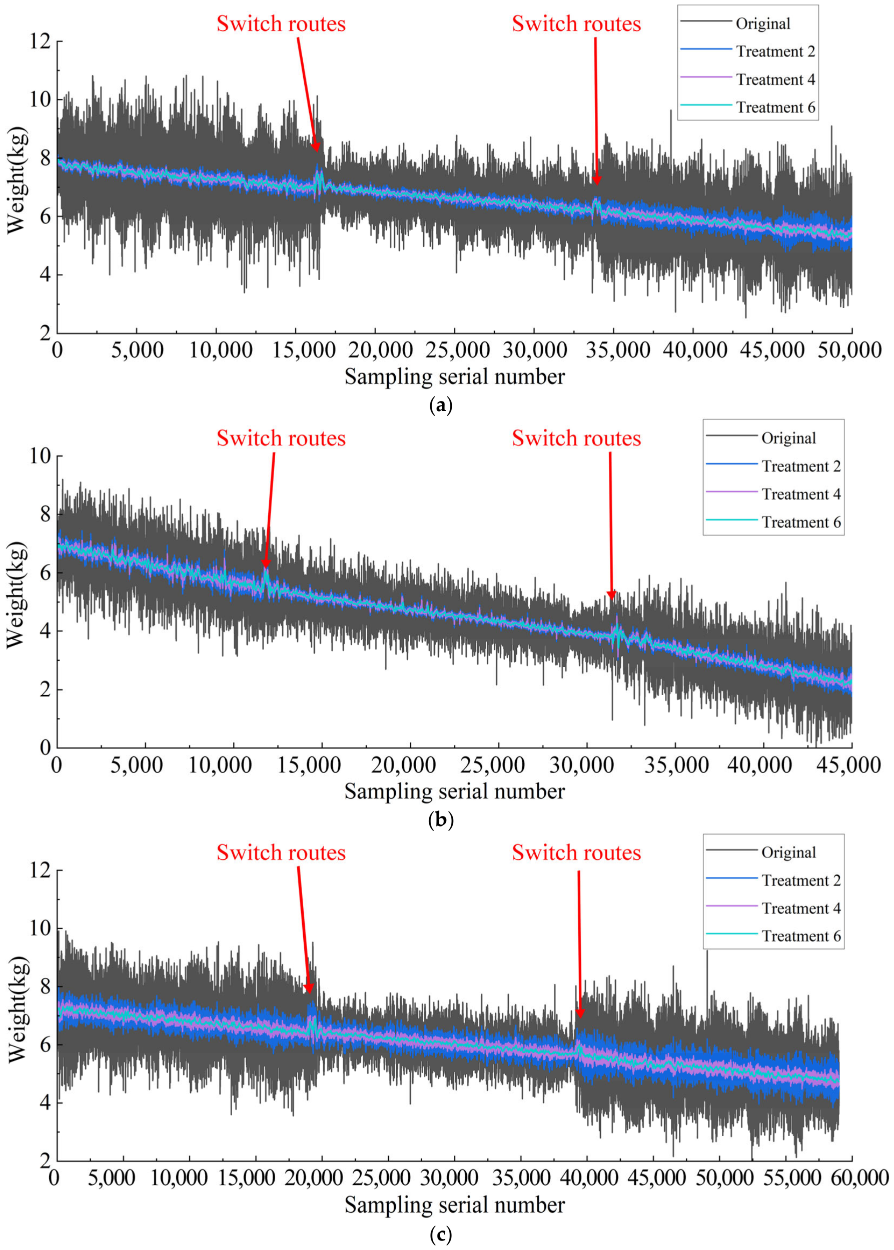

Figure 14. *Cont.*

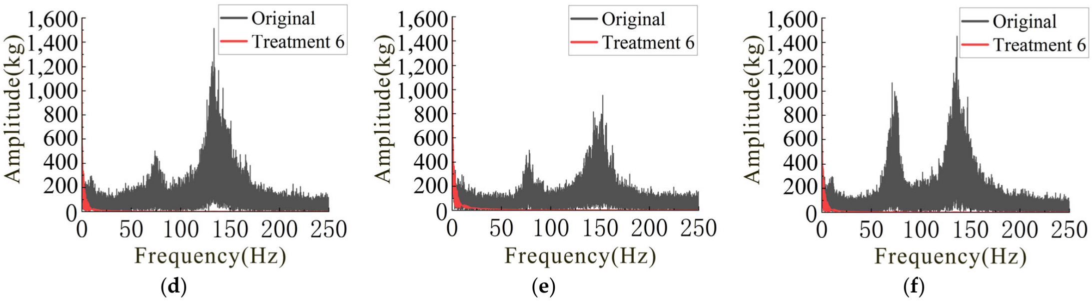

Figure 14. Data of field tests: (**a**) test 1, (**b**) test 2, and (**c**) test 3; and results of FFT analysis: (**d**) test 1, (**e**) test 2, and (**f**) test 3.

4. Discussion

4.1. Analysis of UAV Hovering Test

It can be seen from Figure 11 that the unfiltered original weight data fluctuate greatly at five load levels. This is due to the vibration of the frame when the UAV was hovering. In addition, the UAV was not kept at the same height, and the UAV continued to move up and down at the target height. The vibration generated by the frame was transmitted to the storage tank, which ultimately caused the measurement result of the weighing sensor to be unstable.

After processing 1 and processing 2, the amplitude of data fluctuation was significantly reduced. Under the load of 5, 10, and 15 kg, the data fluctuation amplitude of treatment 2 was less than that of treatment 1, while under the load of 20 and 25 kg, the data fluctuation amplitude of treatment 1 and treatment 2 was similar, which proves that the filtering effect of treatment 2 was better than that of treatment 1, and the adaptability of treatment 2 was stronger. The reason for this phenomenon may be that under different loads, the vibration of the frame was irregular, and the generated vibration noise was random. Processing 1 set a fixed cut-off frequency, which made it difficult to effectively eliminate random noise. Processing 2 continuously adjusted the coefficient of the filter during execution and had an adaptive adjustment ability, which can better filter out random noise.

After the original data were processed by processing 3 and processing 4, respectively, the amplitude of data fluctuation was further reduced, and the filtering effect was better than that of processing 1 and processing 2, respectively, indicating that the Kalman filter algorithm can effectively reduce the noise and further eliminate the random noise. After the original data were processed by processing 5 and 6, respectively, the amplitude of data fluctuation was further reduced, and the filtering effect was better than that of processing 3 and 4, respectively, which shows that the moving average filtering had a better noise reduction ability and can improve the smoothness of the data.

Table 7 shows that there was a large deviation in the unfiltered data, which was difficult to use directly. After processing 5 and 6, the maximum deviation of the original data was less than 0.5 kg, but under the same load, the maximum deviation of processing 6 was smaller. With the increase in load, the maximum deviation of treatment 5 and treatment 6 became larger, which indicated that the larger the load, the larger the noise generated by the UAV frame and the larger the deviation. From the perspective of maximum relative error, the maximum relative error of the original data after processing 5 was 1.26~2.94%, while the maximum relative error after processing 6 was 1.24~2.74%, indicating that under the same load, the maximum relative error of processing 6 was smaller, so the filtering effect of processing 6 was better. From the perspective of average relative error, the average relative error of the original data was within 1.18~4.80%, the average relative error of treatment 5 was within 0.34~0.66%, and the average relative error of treatment 6 was within 0.31~0.58%, indicating that treatment 5 and treatment 6 had a better filtering effect and met the filtering requirements.

It can be seen from Figure 12 that a large amount of noise was mixed in the original data. Near the frequencies of 75 and 150 Hz, the fluctuation range of the original data was large, and the noise interference to the data was more serious. After processing 5 and 6, the amplitude corresponding to the same frequency was reduced by about 100 orders of magnitude, and the noise was well suppressed.

4.2. Analysis of UAV Flighting Test

It can be seen from Figure 13, under the same load, with the increase in working speed, the fluctuation range of data became larger. This is because the greater the speed, the greater the vibration amplitude of the frame, and the greater the noise. At the same operating speed, with the increase in load, the fluctuation range of data became larger, indicating that the noise increases with the increase in load. By comparing the data waveforms of processing 5 and processing 6, it can be seen that the data waveform of processing 5 fluctuates less when the load was 5 and 10 kg, but the fluctuation became larger when the load was 15, 20, and 25 kg, while the data of processing 6 fluctuate slightly near the reference data, which shows that processing 6 encounters larger vibration and noise, better stability, stronger adaptability, and better filtering effect.

In Table 8, the maximum deviation range of the original data was 1.995~3.666 kg. Overall, the deviation is larger than the original data of the hovering test in Section 3.4, indicating that the vibration noise of the UAV during flight was larger than that during hovering. With the increase in load and working speed, the maximum deviation of treatment 5 and treatment 6 gradually becomes larger. When the load was 25 kg, the deviation increases obviously. Currently, the maximum deviation of treatment 5 was in the range of 1.064~2.031 kg, and the maximum deviation of treatment 6 is in the range of 0.420~0.888 kg. In contrast, treatment 6 had a better noise suppression ability.

From the perspective of relative error, the maximum relative error of treatment 5 was 4.26~12.84%, and the average relative error was 0.72~2.86%. The maximum relative error of treatment 6 was 1.68~10.06%, and the average relative error was 0.74~2.54%, which all met the filtering requirements. Under the same conditions, the maximum relative error and average relative error of treatment 6 were smaller than those of treatment 5, which shows that treatment 6 has a better noise suppression ability and smoother data filtering data.

4.3. Analysis of Field Test

Figure 14 shows that the original data are seriously disturbed by the vibration and noise of the UAV, and the data fluctuate in a large range. After processing 2 (LMS adaptive filtering), the stability of the data is greatly improved. After the original data were processed by processing 4 (LMS adaptive filtering + Kalman filtering), the fluctuation range of the data was reduced again, and the noise was further filtered out. After the original data were processed by processing 6 (LKM), the data were smoother, the stability was better, and the noise was effectively suppressed. The data fluctuation range of test 3 was larger than that of test 1 and test 2, because the working speed of test 3 was faster than that of test 1 and test 2. The faster the working speed, the greater the vibration noise and the more unstable the data.

Further analysis shows that when the UAV switches the route, the data had a large fluctuation. The possible reason was that during the switching route, the gravity acceleration of the UAV changed drastically, and the UAV switched continuously in the two states of overweight and weightlessness, resulting in the continuous shaking of the storage tank and the large-scale fluctuation of the data.

The FFT analysis in Figure 14 shows that the frequency band of noise was widely distributed before filtering, and the noise interference was more serious near the frequency of 75 Hz and 150 Hz. After filtering, the amplitude corresponding to the same frequency was reduced by about 1000 orders of magnitude, and the noise near 75 Hz and 150 Hz was effectively suppressed.

4.4. A Comparison with Existing Research

Obtaining the allowance in the storage tank is very important for various devices in agricultural production and is a key factor in improving the working accuracy of the devices [29,30]. In the existing research, the filtering processing of weighing data is often limited to the use of a single filter. This paper innovatively proposes a new processing scheme, that is, multiple filters optimized for different noise types are continuously applied. In order to verify the effectiveness of this scheme, this paper compares several groups of experiments and finds a better filter combination to further improve the accuracy and effect of data processing. Through this continuous filtering method, it can filter out all kinds of noise interference more comprehensively, so as to obtain more accurate and reliable weighing data.

The final filtering scheme adopts the LMS adaptive filtering scheme with fixed step size factor, but the fixed step size factor is difficult to balance with the steady-state error and convergence speed. In order to further improve the filtering effect, the variable-step-size LMS adaptive filtering algorithm can be used in subsequent research [31]. In addition, compared with existing schemes, a noise monitoring sensor is added to the final determined storage tank allowance monitoring scheme, which means an increase in cost and an increase in installation difficulty. Other schemes can also be tried to further improve the stability and reliability of seed box allowance monitoring data [32].

5. Conclusions

In this paper, aiming to evaluate the influence of UAV's vibration noise in the accurate quantity weighing of the storage tank, a differential sensor and supporting two filtering methods with strong adaptability were provided to filter out the noise. The quantitative evaluation was summarized as follows:

(1) The analog-to-digital conversion circuit for reading the weighing sensor signal was designed, and two data processing schemes were proposed, which are Butterworth low-pass filter + Kalman filter + moving average filter (BKM) and LMS adaptive filter + Kalman filter + moving average filter (LKM).

(2) The UAV hovering test was carried out, and two data processing schemes were compared. The results show that for different loads, the scheme of LKM can effectively suppress noise. The maximum relative error of the filtered data is 1.24~2.74%, and the average relative error is 0.31~0.58%.

(3) The results of the UAV flight test show that for different loads and different flight speeds, the LKM has a better noise suppression ability and better filtering effect than the BKM. The maximum relative error of the filtered data is 1.68~10.06%, and the average relative error is 0.74~2.54%.

Author Contributions: Writing—original draft preparation, J.H.; methodology and validation, W.H.; investigation, D.Y.; data curation, J.L.; visualization, Y.O.; writing—review and editing, R.J.; conceptualization, Z.Z. All authors have read and agreed to the published version of the manuscript.

Funding: This work was supported by the Laboratory of Lingnan Modern Agriculture Project (NT2021009); the Project of key R&D program of Guangzhou of China (202206010149), in part by Science and Technology Plan of Jian City of China (20211-055316 and [2020]83), Science and Technology Plan of Jian City of China (2022-051252-02), Science and Technology Plan of Guangdong Province of China (2023B10564002 and 2021B1212040009), Innovative Research Team of Agricultural and Rural Big Data in Guangdong Province of China (2019KJ138), and China Scholarship Council (202308440394).

Data Availability Statement: Data are contained within the article.

Conflicts of Interest: The authors declare no conflicts of interest.

References

1. Kim, J.; Kim, S.; Ju, C.; Son, H.I. Unmanned Aerial Vehicles in Agriculture: A Review of Perspective of Platform, Control, and Applications. *IEEE Access* **2019**, *7*, 105100–105115. [CrossRef]
2. Rejeb, A.; Abdollahi, A.; Rejeb, K.; Treiblmaier, H. Drones in agriculture: A review and bibliometric analysis. *Comput. Electron. Agric.* **2022**, *198*, 107017. [CrossRef]
3. van Bergeijk, J.; Goense, D.; van Willigenburg, L.G.; Speelman, L. PA—Precision Agriculture. *J. Agric. Eng. Res.* **2001**, *80*, 25–35. [CrossRef]
4. Swisher, D.W.; Borgelt, S.C.; Sudduth, K.A. Optical sensor for granular fertilizer flow rate measurement. *Trans. ASAE* **2002**, *45*, 881–888. [CrossRef]
5. Grift, T.E.; Walker, J.T.; Hofstee, J.W. Mass flow measurement of granular materials in aerial application. Part 2: Experimental model validation. *Trans. ASAE* **2001**, *44*, 27–34. [CrossRef]
6. Ding, Y.; Wang, K.; Du, C.; Liu, X.; Chen, L.; Liu, W. Development of monitoring device for medium and small size seed flow based on thin surface laser- silicon photocell. *Trans. Chin. Soc. Agric. Eng.* **2019**, *35*, 12–20. [CrossRef]
7. Wang, Z.; Pei, J.; He, J.; Zhang, M.; Yang, W.; Luo, X. Development of the sowing rate monitoring system for precision rice hill-drop drilling machine. *Trans. Chin. Soc. Agric. Eng.* **2020**, *36*, 9–16. [CrossRef]
8. Xie, C.; Zhang, D.; Yang, L.; Cui, T.; He, X.; Du, Z. Seeding parameter monitoring method based on laser sensors. *Trans. Chin. Soc. Agric. Eng.* **2021**, *37*, 140–146. (In Chinese)
9. Wang, S.; Yu, Z.; Zhang, W.; Yang, L.; Zhang, Z.; Ao, R. Review of recent advances in online yield monitoring for grain combine harvester. *Trans. Chin. Soc. Agric. Eng.* **2021**, *37*, 58–70. [CrossRef]
10. Xiong, Y.; Zhou, J.; Wei, W.; Shen, M.; Zhang, B. Design and experiment of grain mass flow sensor based on embedded system. *Trans. Chin. Soc. Agric. Eng.* **2018**, *34*, 39–46. [CrossRef]
11. Wang, J.; Zhang, Z.; Wang, F.; Jiang, Y.; Zhou, W. Design and Experiment of Monitoring System for Rice Hill-direct-seeding Based on Piezoelectric Impact Method. *Trans. Chin. Soc. Agric. Mach.* **2019**, *50*, 74–84, 99. [CrossRef]
12. Wang, S. Study on Design and Key Technology for Sunflower Combine Harvester Online Yield Monitor System Based on Pneumatic Conveying Structure. Ph.D. Thesis, Inner Mongolia Agricultural University, Hohhot, China, 2022. (In Chinese)
13. Zhou, L.; Ma, M.; Yuan, Y.; Zhang, J.; Dong, X.; Wei, C. Design and test of fertilizer mass monitoring system based on capacitance method. *Trans. Chin. Soc. Agric. Eng.* **2017**, *33*, 44–51. [CrossRef]
14. Chen, J.; Li, Y.; Qin, C.; Liu, C. Design and Experiment of Precision Detecting System for Wheat-planter Seeding Quantity. *Trans. Chin. Soc. Agric. Mach.* **2019**, *50*, 66–74. [CrossRef]
15. Zhao, M.; Wang, X.; Qi, Z.; Tian, Y. Design and Test of Material Level Detection Sensor for Fertilizer Box Based on Capacitance Method. *J. Agric. Mech. Res.* **2019**, *41*, 151–155. [CrossRef]
16. Tian, Y.; Qi, Z.; Wang, X.; Zhao, M. Design and Experiment of Material Level Sensor for Fertilizer Tank Based on Single Chip Microcomputer. *J. Agric. Mech. Res.* **2020**, *42*, 105–110. [CrossRef]
17. Al-Jalil, H.F.; Khdair, A.; Mukahal, W. Design and performance of an adjustable three-point hitch dynamometer. *Soil Till Res* **2001**, *62*, 153–156. [CrossRef]
18. Shoji, K.; Itoh, H.; Kawamura, T. A Mini- grain Yield Sensor Compensating for the Drift of its Own Output. *Eng. Agric. Environ. Food* **2009**, *2*, 44–48. [CrossRef]
19. Zhang, X.C.; Hu, X.; Zhang, A.G.; Zhang, Y.; Yuan, Y. Method of measuring grain-flow of combine harvester based on weighing. *Trans. Chin. Soc. Agric. Eng.* **2010**, *26*, 125–129.
20. Wei, L.; Zhang, X.; Yuan, Y.; Liu, Y.; Li, Z. Design and experiment of 2F-6-BP1 variable rate assorted fertilizer applicator. *Trans. Chin. Soc. Agric. Eng.* **2012**, *28*, 14–18. [CrossRef]
21. Liu, H.; Ding, Y.; Yu, H.; Jin, M.; Jiang, Y.; Fu, X. Signal processing method and performance tests on weighting-sensor-based measuring system of output quantity for a seeding and fertilizing applicator. *IFAC-PapersOnLine* **2018**, *51*, 536–540. [CrossRef]
22. He, W.; Liu, W.; Jiang, R.; Gu, Q.; Huang, J.; Zou, S.; Xu, X.; Zhou, Z. Control system design and experiments of UAV shot seeding device for rice. *Trans. Chin. Soc. Agric. Eng.* **2022**, *38*, 51–61. (In Chinese)
23. Liu, W.; Zhou, Z.; Xu, X.; Gu, Q.; Zou, S.; He, W.; Luo, X.; Huang, J.; Lin, J.; Jiang, R. Evaluation method of rowing performance and its optimization for UAV-based shot seeding device on rice sowing. *Comput. Electron. Agric.* **2023**, *207*, 107718. [CrossRef]
24. Liu, Y. A Thesis Submitted in Partial Fulfillment of the Requirements For the Degree of Master of Engineering. Master's Thesis, Huazhong University of Science and Technology, Wuhan, China, 2016. (In Chinese)
25. Li, Z.S. The Design of Butterworth Lowpass Filter Based on MATLAB. *Inf. Technol.* **2003**, *27*, 49–50. [CrossRef]
26. Gao, Y.; Xie, S. A Variable Step Size LMS Adaptive Filtering Algorithm and Its Analysis. *Acta Electron. Sin.* **2001**, *8*, 1094–1097. (In Chinese)
27. Kalman, R.E. A New Approach to Linear Filtering and Prediction Problems. *J. Fluids Eng.* **1960**, *82*, 35–45. [CrossRef]
28. Peng, D. Pseudo-linear Kalman Filter in Passive Target Tracking. *Softw. Guide* **2009**, *8*, 32–34.
29. Arianti, N.D.; Muslih, M.; Sitorus, A.; Bulan, R. Oscillation effect dataset on the measurement accuracy of load-cell sensor applied to the weigh basket. *Data Brief* **2021**, *38*, 107453. [CrossRef]
30. Ji, C. Study on Weighing Device for Seeding Amount of Tray in Rice Seedling Production Line. Master's Thesis, South China Agricultural University, Guangzhou, China, 2020. (In Chinese)

31. Gao, Y.; Zhao, H.; Zhu, Y.; Lou, J. The q-gradient LMS spline adaptive filtering algorithm and its variable step-size variant. *Inf. Sci.* **2024**, *658*, 119983. [CrossRef]
32. Liu, H. Design of the Weighting-principle-based Application Rate Measuring–Controlling System and Study of the Signal Processing Method. Master's Thesis, Nanjing Agricultural University, Nanjing, China, 2019. (In Chinese)

agronomy

Article

A UAV-Borne Six-Vessel Negative-Pressure Enrichment Device with Filters Designed to Collect Infectious Fungal Spores in Rice Fields

Xiaoyan Guo [1,2,3], Yuanzhen Ou [1,2,3], Konghong Deng [1,2,3], Xiaolong Fan [1,2,3], Rui Jiang [1,2,3,*] and Zhiyan Zhou [1,2,3,4,*]

[1] Guangdong Laboratory for Lingnan Modern Agriculture, College of Engineering, South China Agricultural University, Guangzhou 510642, China; guoxiaoyan@scau.edu.cn (X.G.); yuanzhenou@scau.edu.cn (Y.O.); 15813301373@stu.scau.edu.cn (K.D.); 20223142002@scau.edu.cn (X.F.)
[2] Guangdong Provincial Key Laboratory of Agricultural Artificial Intelligence (GDKL-AAI), Guangzhou 510642, China
[3] Guangdong Engineering Research Center for Agricultural Aviation Application (ERCAAA), Guangzhou 510642, China
[4] Key Laboratory of Key Technology on Agricultural Machine and Equipment, South China Agricultural University, Ministry of Education, Guangzhou 510642, China
* Correspondence: ruiojiang@scau.edu.cn (R.J.); zyzhou@scau.edu.cn (Z.Z.); Tel.: +86-20-3867975 (Z.Z.)

check for updates

Citation: Guo, X.; Ou, Y.; Deng, K.; Fan, X.; Jiang, R.; Zhou, Z. A UAV-Borne Six-Vessel Negative -Pressure Enrichment Device with Filters Designed to Collect Infectious Fungal Spores in Rice Fields. *Agronomy* **2024**, *14*, 716. https://doi.org/10.3390/agronomy14040716

Academic Editor: Luís Manuel Navas Gracia

Received: 23 January 2024
Revised: 20 March 2024
Accepted: 22 March 2024
Published: 29 March 2024

Correction Statement: This article has been republished with a minor change. The change does not affect the scientific content of the article and further details are available within the backmatter of the website version of this article.

Abstract: Fungal spores that cause infectious fungal diseases in rice are mainly transmitted through air. The existing fixed, portable or vehicle-mounted fungal spore collection devices used for rice infectious diseases have several disadvantages, such as low efficiency, large volume, low precision and incomplete information. In this study, a mobile fungal spore collection device is designed, consisting of six filters called "Capture-A", which can collect spores and other airborne particles onto a filter located on a rotating disc of six filters that can be rotated to a position allowing for the capture of six individual samples. They are captured one at a time and designed and validated by capturing spores above the rice field, and the parameters of the key components of the collector are optimized through fluid simulation and verification experiments. The parameter combination of the "Capturer-A" in the best working state is as follows: sampling vessel filter screen with aperture size of 0.150 mm, bent air duct with inner diameter of 20 mm, negative pressure fan with 1500 Pa and spore sampling of cylindrical shape. In the field test, the self-developed "Capturer-A" was compared with the existing "YFBZ3" (mobile spore collection device made by Yunfei Co., Ltd., Zhengzhou, China). The two devices were experimented on at 15 sampling points in three diseased rice fields, and the samples were examined and counted under a microscope in the laboratory. It was found that the spores of rice blast disease and rice flax spot disease of rice were contained in the samples; the number of samples collected by a single sampling vessel of "Capturer-A" was about twice that of the device "YFBZ3"in the test.

Keywords: diseases of rice; fungal spores; sampling; UAV

1. Introduction

More than 50 kinds of rice fungal diseases, 6 kinds of bacterial diseases, 11 kinds of viral and mycoplasmosis, and 4 kinds of nematode diseases have been found in China [1–3]. The common diseases mainly include rice blast, sheath blight, white leaf blight, flax spot, rice stalk, rice grain smut and bad seedling [4–6]. The infection of rice by airborne spores is an important factor causing rice infection [5,7–9]. The determination of spores in the air is an indispensable part in the analysis of the degree of disease occurrence, early warning and prevention [10–13]. To monitor the process of airborne sporogenesis, it is necessary to have an effective collection device to monitor the temporal and spatial dynamics of pathogens [11,12,14,15].

The collection technology of rice fungal spores is the basis of pathogen identification and monitoring, as well as the premise of disease control [16,17]. The traditional devices for acquiring microorganisms such as rice infectious fungal spores are large and heavy, as shown in Table 1 [18,19]. The efficiency of the existing mobile spore collection device is low, and only one sample can be collected at a time, which cannot meet the requirements of efficient and intelligent modern agriculture [20,21]. In view of the problems of the existing spore capture instruments, the work efficiency and application range of the spore capture instrument need to be improved [22,23].

Table 1. Specifications of existing spore collection devices used in China.

Brand/Country	Model	Mode of Use	Sample Carrier	L × W × H (mm)	Weight (kg)
Yunfei/China	YFBZ3	Portable	Slide	250 × 250 × 300	8
Yunfei/China	YFBZ2	Vehicular	Slide	300 × 200 × 300	12
Yunfei/China	YFBZ1	Stationary	Slide	760 × 760 × 1850	35
Tianhe/China	TH-BZ01	Stationary	Slide	650 × 650 × 1500	30
Oukeqi/China	OK-BZ1	Portable	Slide	450 × 280 × 100	--
Oukeqi/China	OK-BZ2	Vehicular	Slide	250 × 300 × 760	--
Oukeqi/China	OK-BZ10	Stationary	Slide	450 × 280 × 1000	--
Wanxiang/China	WX-BZ3	Stationary	Slide	420 × 308 × 787	--
Bangyou/China	BY-BZ3	Portable	Slide	280 × 280 × 450	--
Aiwo/China	AW-BZ2	Vehicular	Slide	250 × 300 × 760	--
Aiwo/China	AW-BZ1	Portable	Slide	240 × 240 × 360	--
Burkard/England	HIRST	Portable	Transparent plastic (mylar)	600 × 700 × 800	16
Burkard/England	Spore watch	Bracket type	Transparent plastic (mylar)	240 × 100 × 550	3.5
Burkard/England	B-350	Bracket type	Liquid or Eppendorf bottle	1250 × 870 × 770	24
Burkard/England	SRVST	Bracket type	Container	570 × 650 × 650	--

There are several potential aspects that can be considered:

(1) Lighter weight and smaller sizes need to be adopted to make the spore collection device smaller and more lightweight [24–27].

(2) The existing fixed spore capture equipment can obtain spores in glass slides, Eisenhoff bottles, scotch tape or bottle containers (as shown in Table 1), and the design of sample carriers also has room for research [28,29].

(3) We improve the work efficiency of mobile spore collection device by enhancing the ability of a single device that supports multiple sample collection tasks [21,30].

(4) Integrating with contemporary UAV technology, the development of versatile mobile spore collection devices broadens the utility of spore capture devices [31–33].

In order to improve the collection effectiveness of rice infectious fungal spores, and explore a rice infectious fungal spores collection device suitable to be mounted on UAV, this study proposes a design scheme of a mobile rice infectious fungal spore collection device named "Capturer-A", which uses air flow to collect biological particles, such as spores, onto filters. In this study, the features of key components of the developed device were simulated, and the key parameters affected were analyzed and optimized.

2. Working Principle and Structure Design of Spore Collection Device

To collect the rice fungal spores more efficiently, a UAV-borne mobile collecting device named "Capturer-A" was designed according to the characteristics of spores [19]. "Capturer-A" is mainly composed of air intake, sample collection vessel cover, sample collection vessel shell, fan and turntable shell, motor and microprocessor shell, sample collection filter vessel, spore sample filter vessel-positioning turntable, angle-positioning motor, bent air duct, negative-pressure fan, air outlet, microprocessor, motor and battery, etc., as shown in Figure 1.

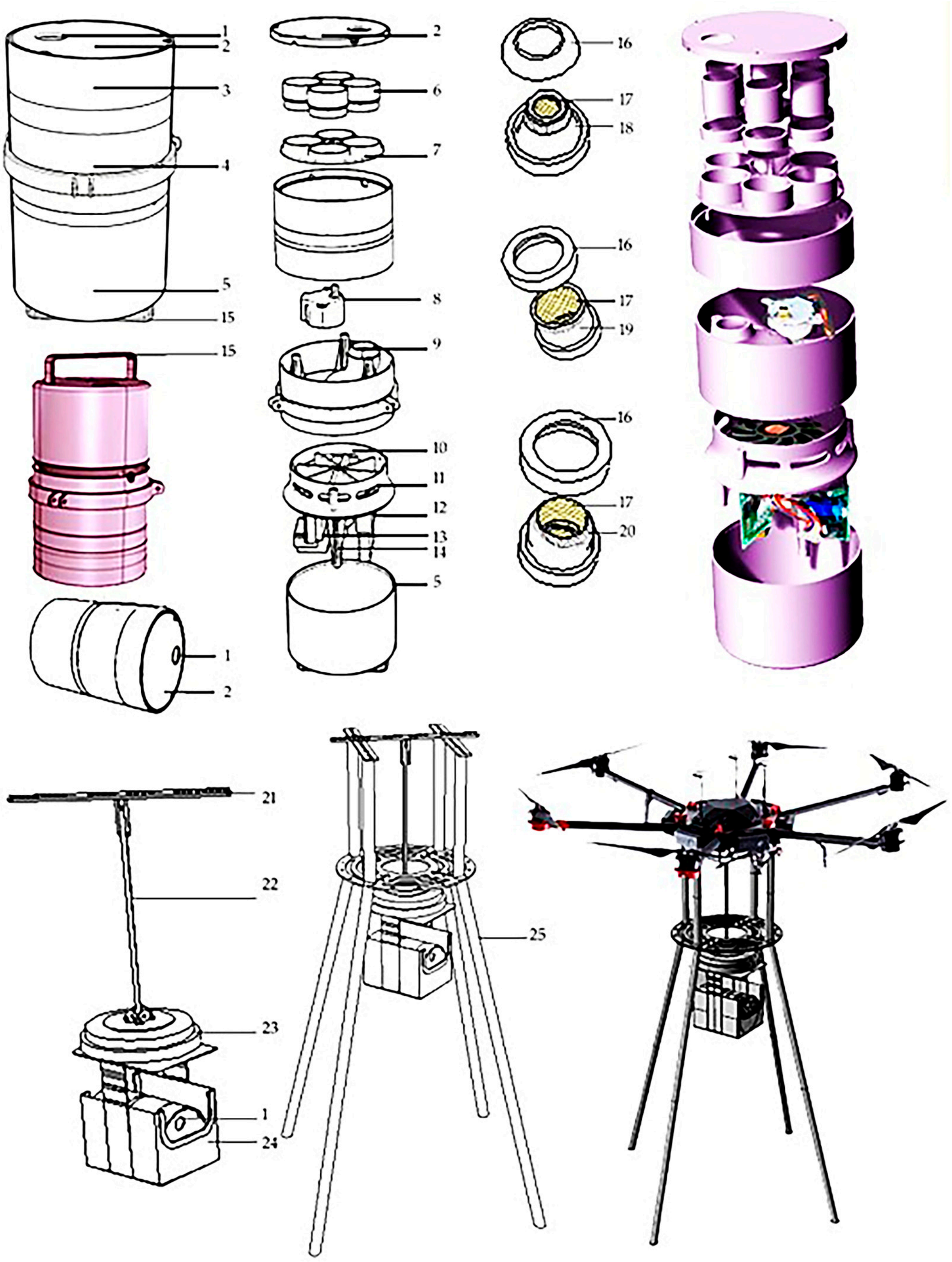

Figure 1. Structure diagram of the fungal spore collection device. Note: 1. air intake; 2. sample collection cover; 3. sample collection shell; 4. fan and turntable shell; 5. motor and microprocessor shell; 6. spore collection; 7. spore sample filter-positioning turntable; 8. angle-positioning motor; 9. bent air duct; 10. negative-pressure fan; 11. air outlet; 12. microprocessor; 13. motor; 14. battery; 15. lifting handle; 16. screen-fixing cover; 17. sample screen; 18. truncated cone sampling; 19. cylindrical sampling; 20. hemisphere-shaped sampling; 21. aluminum alloy beam; 22. electric telescopic rod; 23. electric turntable; 24. waterproof frame; 25. aluminum alloy bracket.

The negative-pressure fan rotates to form negative pressure in the capture bin, and the air containing spores outside is inhaled by the air intake, through the air duct and the filter vessel, and the spores and other microbial particles will be attached to the filter of the filter vessel, so as to complete the capture of spores. After completing the sample collection, the filter vessel is rinsed with pure water in the laboratory; then, the fungal spores can be further observed and analyzed.

The workflow of the field experiment of the UAV-borne mobile rice fungal spore collection device is as follows:

(1) The rice fungal spore collection device starts to work at a fixed position in the field. The device uses suction to sample airborne particles such as spores in the air into the first filter vessel through a negative-pressure fan.

(2) When the fungal spore collection device is transferred to the second collection point, the filter flow vessels changed to the second air filter for the collection of fungal spores.

(3) When the working process needs to enter the next collection point, it is necessary to switch the sample collection filter through the remote control or timer for sample collection.

3. Design and Simulation of Key Components of the Fungal Spore Collection Device

Since the sample collection efficiency may be affected by several main factors, this study analyzed different simulation results of the "Capturer-A", assessing the following effects: inner diameter of bent air duct, wind pressure, sample filter vessel shape and aperture size of sampling vessel filter screen. Microbial particles in paddy fields include inorganic particles, organic particles and a small number of mixed particles, which usually exist in the form of dust in the crown of rice, with a diameter of about 0.001 µm to 10 µm. The simulation process is described below.

3.1. Simulation of Inner Diameter of Bent Air Duct

Since the key step of collecting spores in the "Capturer-A" is that the air containing spores is sucked by negative-pressure wind into the sampling vessels with filter nets through the bent air duct, the diameter of the bent air duct has a certain influence on the collection efficiency of "Capturer-A". Due to the limited overall size of "Capturer-A", the space to accommodate the bent air duct is limited, and the shape of the bent air duct will change slightly due to the size change, which has a certain impact on its spore-catching ability. ANSYS 23 (ANSYS Inc., Canonsburg, PA, USA) was used to simulate the inner diameter of the bent air duct in "Capturer-A". By establishing a simplified model to compare and simulate the bent air duct with different diameters, the flow field changes of "Capturer-A" during operation were analyzed, and the optimal inner diameter of the bent air duct was determined.

The velocity cloud of the flow simulation situation with the inner diameter of the bent air duct of 15 mm is shown in Figure 2a. It can be found that the maximum velocity is mainly concentrated at the waist of the bend and the exit, and the velocity begins to increase from the waist. Changes in the mass flow at the outlet monitored during the simulation calculation are shown in Figure 3. It can be seen that the minimum flow at the outlet is 4.633 L/min. This value is maintained when the calculation conditions are stable.

A simulation of the flow field with an inner diameter of 20 mm of the bent air duct is shown in Figure 2b. It can be seen from the cloud image that the flow field pressure increases from the entrance, and the flow speed is mainly concentrated at the exit. When other conditions remain unchanged, it can be found that the maximum velocity is the smallest compared with that of 15 mm, but through the outlet flow ratio, it is found that the outlet mass flow of 20 mm with an inner diameter is about 13.693 L/min, and the outlet mass result of the bent air duct with an inner diameter of 20 mm is greater.

A simulation of the flow field with the bent air duct with an inner diameter of 25 mm is shown in Figure 2c. It can be seen from the cloud image that the flow field pressure increases from the entrance, and the flow speed is mainly concentrated at the exit. If other conditions remain constant, compared with bent air ducts with an inner diameter of 25 mm and 20 mm, it can be found that the corresponding bent air duct with an inner diameter of 25 mm whose maximum velocity is less than 20 mm has the same velocity as a diameter of 20 mm. However, through the outlet flow ratio, it is found that the outlet mass flow of the bent air duct with an inner diameter of 25 mm is about 13.216 L/min, and the result of the bent air duct with an inner diameter of 25 mm is very close to the outlet mass of the bent air duct with an inner diameter of 20 mm.

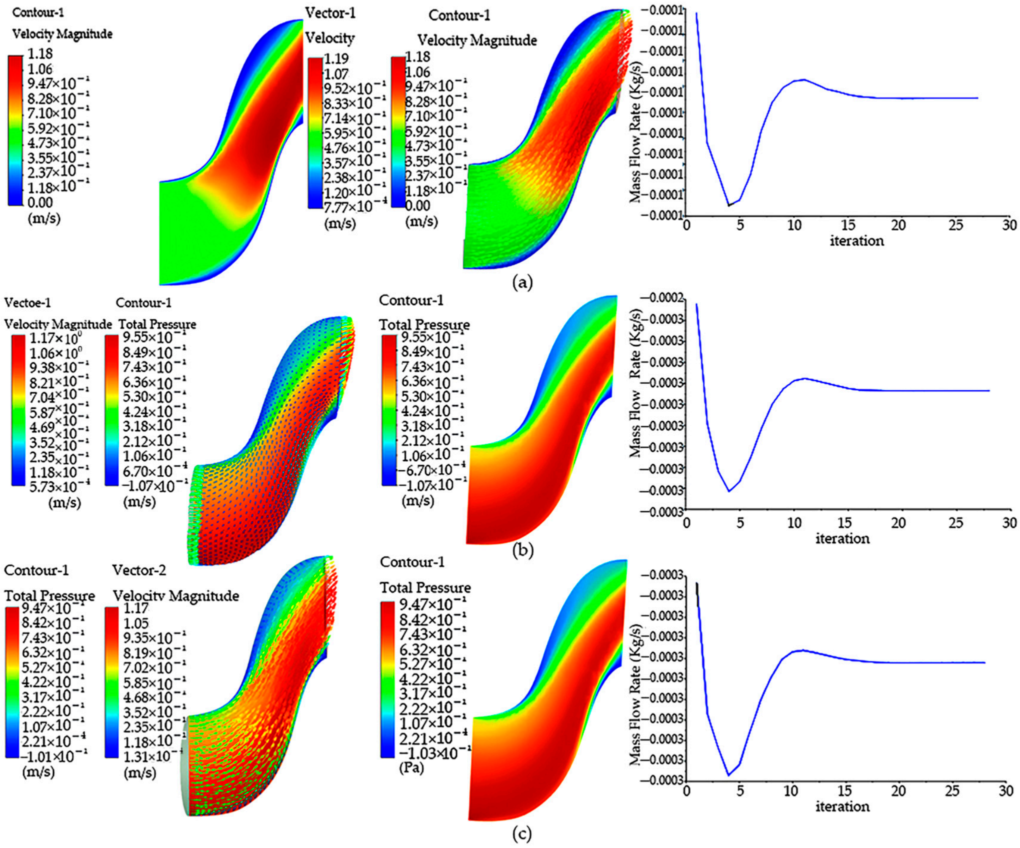

Figure 2. Compare and simulate the bent air duct of different diameters: (**a**) velocity cloud image, pressure cloud image and outlet mass flow image of bent air duct of 15 mm; (**b**) velocity cloud image, pressure cloud image and outlet mass flow image of bent air duct of 20 mm diameters; (**c**) velocity cloud image, pressure cloud image and outlet mass flow image of bent air duct of 25 mm diameters.

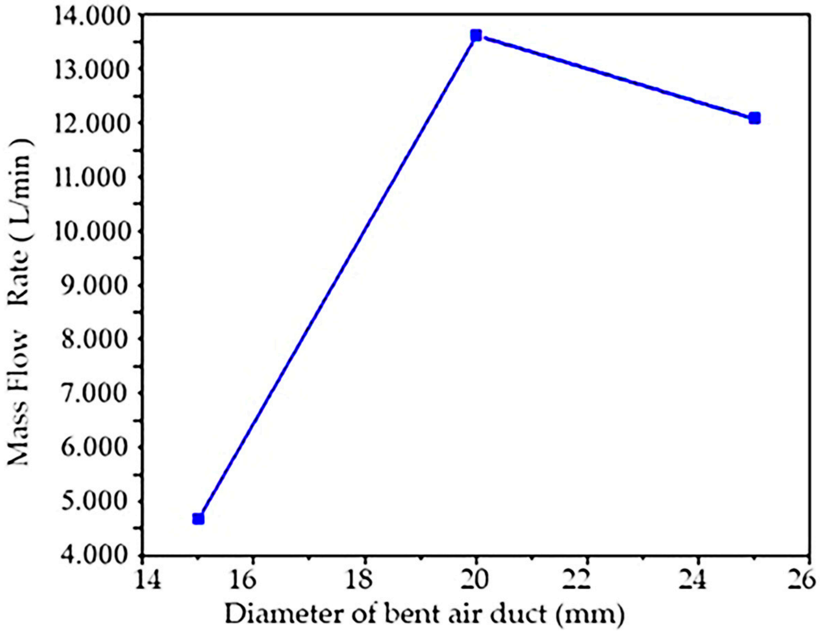

Figure 3. Numerical simulation of the influence of diameter variable on air flow rate.

In order to compare the air flow state under different diameters more accurately, other variables can be kept consistent through numerical simulation, as shown in Figure 3. Only the influence of diameter variables on the air flow rate was simulated and studied, while other variables remained unchanged. Three kinds of bent air ducts with different inner diameters were designed, and the influence of diameter on air flow was analyzed through the mass ratio of the outlet.

From Figure 3, it can be seen that the suction mass flow of the bent air duct with an inner diameter of 20 mm and 25 mm is much higher than that of 15 mm, and the outlet mass flow of the bent air duct with an inner diameter of 20 mm and 25 mm is very similar; the outlet mass flow of the bent air duct with an inner diameter of 20 mm is slightly higher than the outlet mass flow of the bent air duct with an inner diameter of 25 mm, so an inner diameter of 20 mm was selected as the optimal diameter.

3.2. Simulation Analysis of the Wind Speed of Fungal Spore Collection Device

In order to verify the influence of the parameters of the negative-pressure fan on the spore sample collection effect of the equipment, the sampling effect of the negative-pressure fan working under different wind pressures was simulated and analyzed in this study. ANSYS 23 (ANSYS Inc., Canonsburg, Pennsylvania, America) was used to simulate the air flow during the negative fan of the "Capturer-A" operation, pressure distribution cloud diagram and the velocity distribution cloud diagram (Figure 3). Since the above simulation results show that the bent air duct with a diameter of 20 mm is the most efficient, in order to ensure the compatibility of "Capturer-A", the interior diameter of the sampling vessel is consistent with the diversion duct with an inner diameter of 20 mm.

In order to simulate accurately and conveniently, a simplified model of the "Capturer-A" was built in Workbench in advance. The simplified model only retains important components, such as negative-pressure fan, air duct and sample collection filter vessel. The performance of the whole device can be evaluated through simulation analysis of the simplified model.

In this simulation, a turbulent model was adopted for simulation. In this model, the turbulent kinetic energy k and turbulent dissipation rate ε are defined as:

$$k = \frac{\overline{U_i' U_l'}}{2} \tag{1}$$

$$\varepsilon = \frac{u}{\rho} \overline{\left(\frac{\partial u_l'}{\partial \chi_k}\right)\left(\frac{\partial u_l'}{\partial x_k}\right)} \tag{2}$$

The turbulent viscosity can be expressed as a function of k and ε, namely:

$$u_t = \rho c_u \frac{k^2}{\varepsilon} \tag{3}$$

C_μ is the empirical constant, where the transport equation for k and $\boldsymbol{\varepsilon}$ is:

$$\frac{\partial(p_k)}{\partial t} + \frac{\partial(\rho k u_i)}{\partial x_i} = \frac{\partial}{\partial x_j}\left[\left(u + \frac{u_\varepsilon}{\delta_\varepsilon}\right)\frac{\partial \varepsilon}{\partial x_i}\right] + G_k - \rho_\varepsilon \tag{4}$$

$$\frac{\partial(\rho_k)}{\partial_t} + \frac{\partial(\rho_k u_i)}{\partial x_j} = \frac{\partial}{\partial x'}\left[\left(u + \frac{u_i}{\delta \varepsilon}\right)\frac{\partial_\varepsilon}{\partial x_i}\right] + \frac{c_{i\varepsilon}\varepsilon}{k} G_k - \rho C_{2\varepsilon}\rho\frac{\varepsilon}{k} \tag{5}$$

$$G_k = u_t\left(\frac{\partial u_i}{\partial x_j} + \frac{\partial u_j}{\partial x_i}\right)\frac{\partial u_i}{\partial x_j} \tag{6}$$

where $C_{1\varepsilon}$ = 1.44, $C_{2\varepsilon}$ = 1.92, C_μ = 0.09, δ_k = 1.0, δ_ε = 1.3.

The standard model is a complete turbulence model, which is mainly used to solve the turbulence core region. For the solution of the region near the wall where turbulence is not fully developed, the wall function method needs to be adopted:

$$\frac{\overline{u}C_u^{0.25}k_p^{U\cdot 5}}{\tau w/\rho} = \frac{1}{k}ln\left(E\frac{\rho C_u^{0.25}k_\rho^{0.5}y}{u}\right) \tag{7}$$

$$\overline{U} = U - \frac{1}{2}v\frac{d\rho}{dx}\left[\frac{y_\vartheta}{\rho k_\rho^{1.5}}ln\left(\frac{y}{y_v}\right) + \frac{y \cdot y_v}{\rho k_p^{15}} + \frac{y_v^2}{u}\right] \tag{8}$$

$$y_v = \frac{uy_v^*}{k_u^{0.25}k_\rho^{0.5}} \tag{9}$$

The change in wind pressure, temperature and humidity will affect the density of air. When the temperature is 20 °C, the absolute pressure is 760 mmHg, and this state is generally 1.293 kg. In this study, due to the high humidity of the air collected in the rice field and the possibility of a small amount of dust in the rice cluster, the air density ρ = 1.295 kg/m^3. If the wind pressure of the negative-pressure fan is represented by N, the wind speed of the negative-pressure fan is represented by V, the rotation speed of the negative-pressure fan is represented by Y and the fan blade length is represented by J; then, the wind speed is converted to wind pressure by the following formula:

$$N = \frac{1}{2}pkV^2 \tag{10}$$

The formula of rotation speed of the negative-pressure fan is:

$$Y = \frac{60V}{\pi J} \tag{11}$$

By fitting the relationship data between velocity and pressure difference, the fitting graph shown in Figure 4 is obtained. Because the microbial particles suspended in the air move in a Boolean manner in a small area in the absence of wind, when the negative-pressure fan of the device does not work, there is also a small air flow inside the device in the absence of wind. When the negative-pressure fan of the equipment is working, the microbial particles suspended in the air will move in a large range when there is wind action.

Through the setting of boundary conditions, the simulation results of the model were analyzed when the negative fan was not working, as shown in Figure 5. According to the cloud image analysis obtained through the simulation results in the figure, when the negative-pressure fan of the spore collection device does not rotate, the flow rate in the suction movement channel can pass through the bent air channel, and the maximum flow rate appears near the lower exit. The entire static suction motion obstructs the fluid in the device channel, causing it to flow around the phenomenon, and the velocity behind the movement is very small. In the case that the front negative-pressure fan does not rotate, the fluid can only pass through one inlet, and the device cannot complete the spore collection work.

The analysis of model simulation results during fan rotation is shown in Figure 5. As can be seen from the pressure cloud map, the maximum pressure is mainly concentrated in the front of the moving negative-pressure fan, and there is no large pressure on the back. Combining the flow velocity cloud image and the pressure cloud image, it can be seen that this is mainly due to the lack of rotation in the front disk, so this non-uniformity appears. Through the above simulation of the non-rotating negative-pressure fan, it is found that the flow field before and after the fan is not uniform. Now, the fixed disc of the six filter slots in front of the movement rotates, and the negative-pressure fan rotates at a speed of 5000 revolutions per minute; that is, when the wind speed is 2.62 m/s, cloud image data can be obtained. There is no large speed distribution phenomenon at the top of the movement of the spore collection device, only a small part of local movement. There is no obvious large jet phenomenon in the bent duct, and the speed becomes smaller. At the same time, in order to obtain the data change diagram, a straight line is drawn at the movement position of the negative-pressure fan, and the simple model of "Capturer-A" is observed by the speed and pressure changes on the straight line. Through the data monitoring chart, it can be found that the maximum peak speed appears at both ends of the fixed turntable of the filter vessel. In the cloud image, the flow rate corresponds to the maximum position, and there is symmetry.

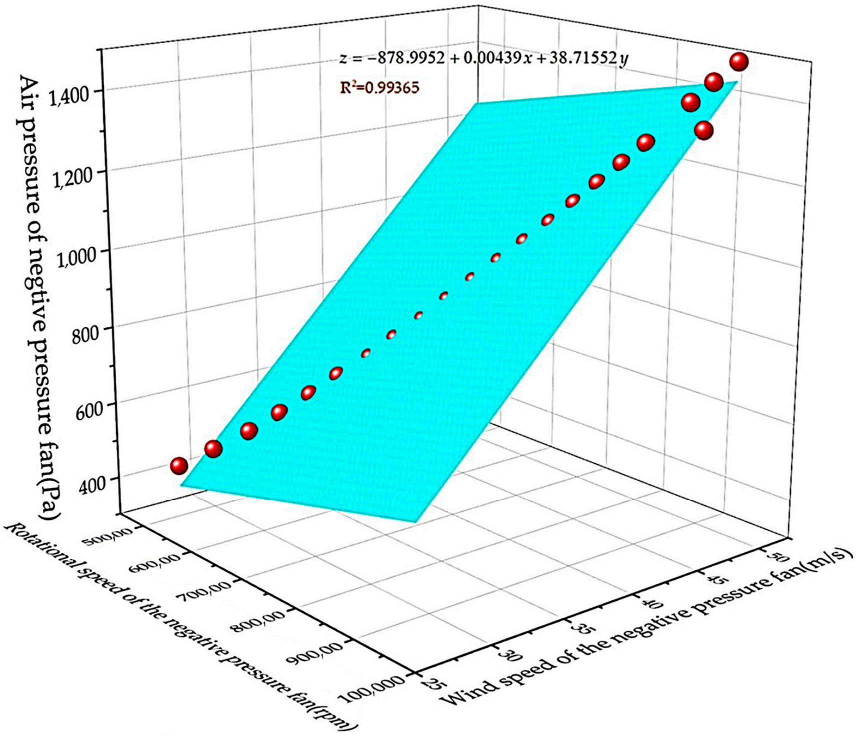

Figure 4. Fitting graph of speed of negative-pressure fan and wind pressure.

From the results, when the negative-pressure fan works, the internal pressure of the device is negative, and the bent air duct of the on-site spore-trapping device will produce negative pressure, so that the outside air is forced into the bent air duct, and the surrounding air is absorbed into the bent air duct, so as to achieve the effect of inhaling spores. From the cloud image, it can be seen that the speed and pressure are relatively high only at a short distance in front of the tube outlet, indicating that if the tube outlet of the device is far from the spores, it may not be able to create air flow delivering spores or guide the spores into the tube. In order to solve this problem, the speed of the fan can be increased, and the attraction range of the outlet of the bent air duct can be expanded.

It can be seen from the results that when the negative-pressure fan of the spore collection device rotates, the bent air duct of the rice fungus spore-sampling device will produce negative pressure, so that the outside air will be forced into the bent air duct, so as to achieve the effect of inhaling spores. From the velocity cloud map, it can be seen that the gas pressure in the bent air duct line reaches 450–1500 Pa, which is enough to adsorb spores in the bent air duct line. However, it can be seen from the cloud image that the speed and pressure of the bent air duct entrance are relatively high only at a short distance in front of the bent air duct entrance, which indicates that if the bent air duct entrance of the device is far from the spores, it may not be possible to guide the spores into it. In order to solve this problem, the speed of the fan can be increased, and the attraction range of the bent air duct hole can be expanded.

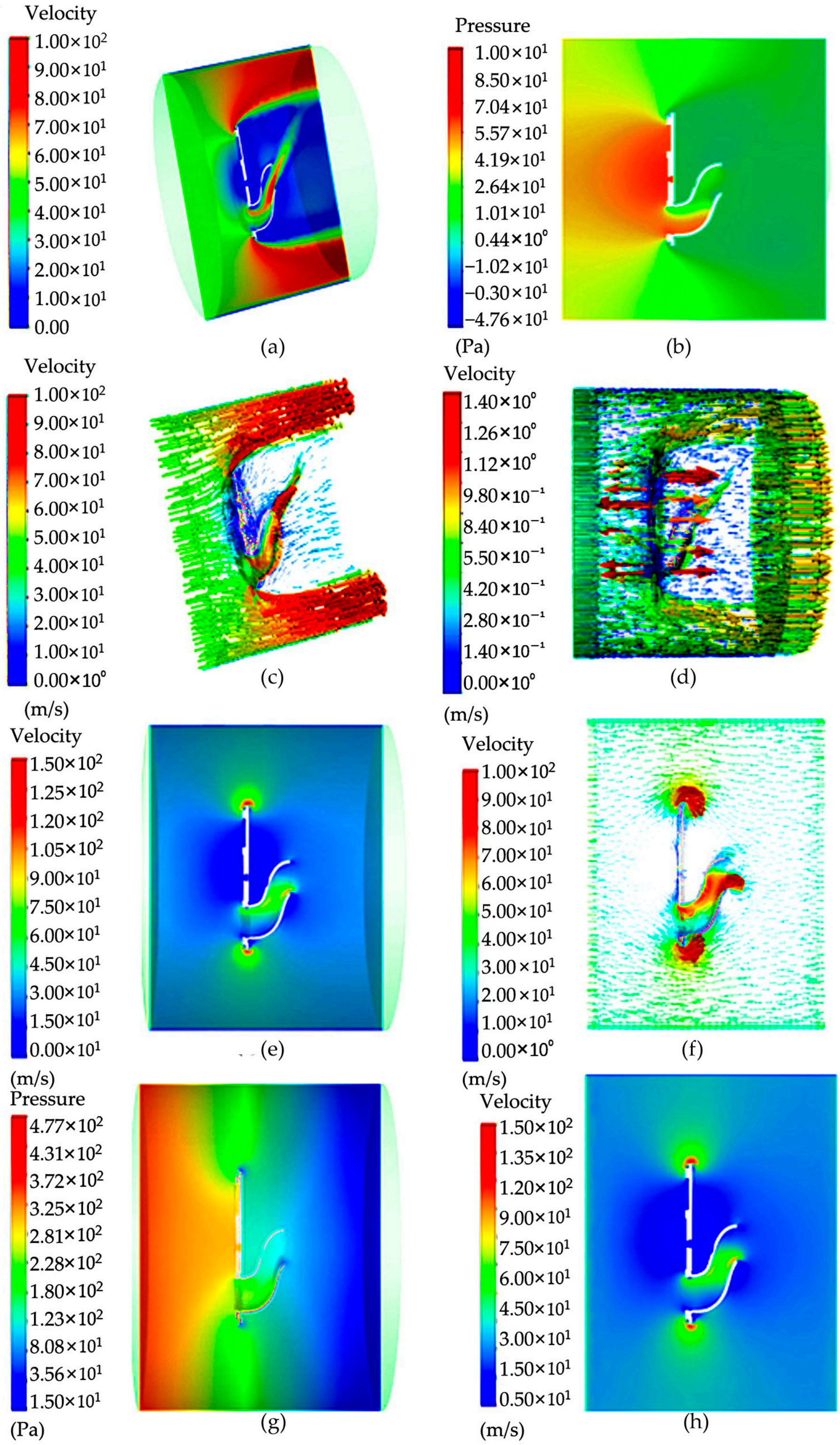

Figure 5. Pressure and velocity distribution cloud diagram: (**a**) velocity cloud image inside the "Capturer-A" before the negative-pressure fan starts; (**b**) pressure image inside the "Capturer-A" when the negative-pressure fan starts; (**c**) velocity vector image inside the "Capturer-A" when the negative-pressure fan starts; (**d**) velocity cloud image inside the "Capturer-A" when the negative-pressure fan starts; (**e**) velocity cloud image inside the "Capturer-A" after the negative-pressure fan starts; (**f**) vector velocity image inside the "Capturer-A" after the negative-pressure fan starts; (**g**) pressure cloud image; (**h**) cross-section pressure image inside the "Capturer-A" after the negative-pressure fan starts.

3.3. Simulation of Sample Filter Vessel Shape

In order to verify the influence of the shapes of the sampling vessels on the spore sample collection effect of "Capturer-A", this study simulated the working state and working effect of different shapes of sampling vessels. According to the actual filter model settings, the geometric model is established by Workbench (ANSYS Inc., Canonsburg, PA, USA). Since the above simulation results show that the bent air duct with a diameter of 20 mm is the most efficient, in order to ensure the compatibility of "Capturer-A", the interior diameter of the sampling vessel is consistent with the diversion duct with an inner diameter of 20 mm. The exterior diameter of the sampling vessel cylinder is 22 mm, and the interior diameter sampling vessel cylinder is 20 mm. The truncated cone sampling collection vessels with filter nets were installed in an inverted way; the top exterior diameter was 22 mm, the top interior diameter was 20 mm, the bottom exterior diameter was 18 mm and the bottom interior diameter was 16 mm. The model consists of three parts: inlet fluid region, porous media region and outlet fluid region.

For meshing of the above model, Fluent meshing is used as the meshing tool, and the mesh is a polyhedral mesh. In practice, the problem of porous media is often encountered, such as filter containers, filters, soil, air, etc., which is characterized by a large number of geometric pores. This problem is usually simplified in fluid simulation calculation, and the porous region is simplified to the fluid region with increased resistance source, thus avoiding the trouble of establishing porous geometry. The air sample in this study also belongs to porous media, and the simplified method usually provides a velocity-dependent momentum source in the porous region, which is expressed as:

$$S_i = -\left(\sum_j^3 D_{ij} u v_j \cdot \Sigma_j^3 = jC_{ij}\frac{1}{2}p|v|v_j\right) \tag{12}$$

S_i is the source term of the momentum equation in the *i* (*x*, *y*, *z*) direction; *V* is the speed value; *D* and *C* are the specified matrices. In the formula, the first term on the right is the viscosity loss term, and the second term is the inertia loss term.

For uniform porous media, it can be rewritten as:

$$s_i = -\left(\frac{u}{\alpha}v_i + c_2\frac{1}{2}|v|v_i\right) \tag{13}$$

α is permeability; C_2 is the inertial drag coefficient. The matrix *D* is $1/\alpha$. The momentum acts on the fluid to create a pressure gradient,

$$\Delta\rho = S_i \tag{14}$$

Δn is the thickness of the porous media domain. If the above two formulas are connected, they can be uniformly expressed as the following formula:

$$\Delta p = av^2 + b \cdot v \tag{15}$$

From the flow field velocity cloud in Figure 6, it can be seen that because the sample filter vessel of the circular table is inverted on the rotary table, the inlet is large, and the outlet radius is small, so it can be seen that in the sample filter vessel of the circular table shape, the existence of porous media will cause the velocity distribution in this hierarchical gradient, and there is a velocity difference. From the flow rate area product flow formula, it can be seen that the outlet diameter becomes smaller and the velocity increases, so even if there is a porous medium obstruction, the air in the roundtable shape of the filter net still has the maximum speed at the outlet. Figure 6a is a velocity distribution cloud map of the porous media model on different sections corresponding to the circular platform, and it can be seen that the maximum velocity reaches 300 m/s.

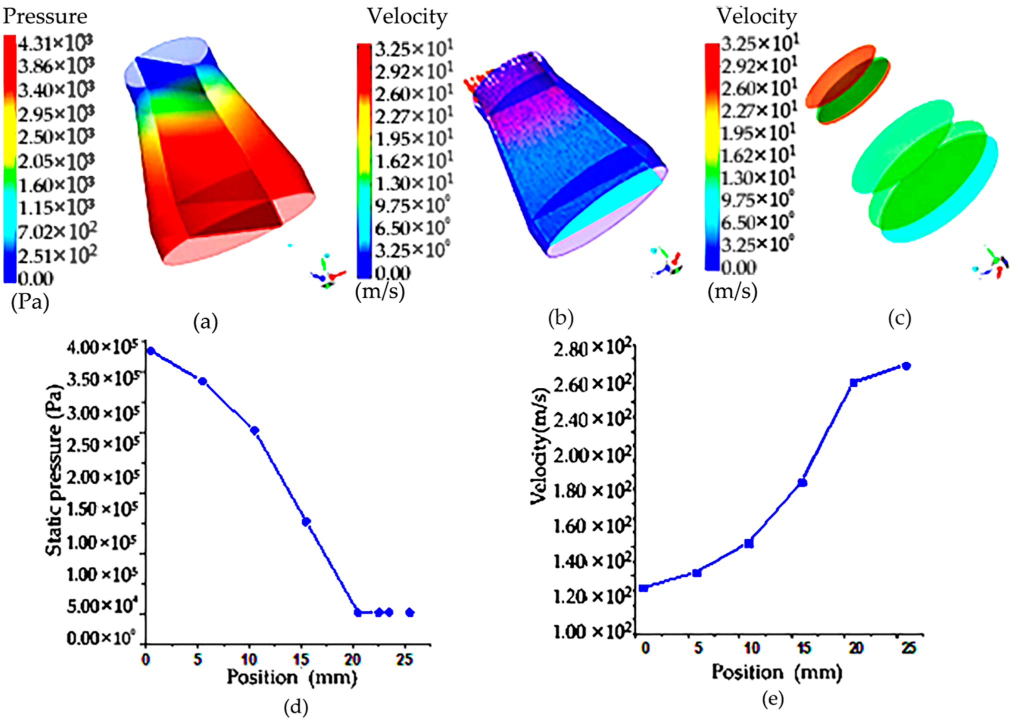

Figure 6. Pressure cloud diagram and cloud image of upstream field and velocity at different sections of the truncated cone sampling vessel with filter net: (**a**) pressure cloud image of truncated cone sampling vessel with a filter net; (**b**) velocity cloud image of truncated cone sampling vessel with a filter net; (**c**) velocity cloud image of flow field on different sections of truncated cone sampling with a filter net; (**d**) pressure distribution on the symmetric line of truncated cone sampling vessel with a filter net; (**e**) velocity distribution on the symmetric line of truncated cone sampling vessel with a filter net.

According to the pressure distribution cloud map in the circular platform porous media model, the existence of porous areas makes the pressure drop obvious. The maximum pressure at the entrance is 400,000 Pa, the pressure in the middle is 240,000 Pa and the pressure drop is 160,000 Pa. As can be seen from the velocity and pressure distribution diagram on the symmetric line in Figure 6b, the velocity on the symmetric line gradually increases with the position change, but the pressure decreases along the symmetric line. To sum up, it can be seen that because of the shape of the filter net, the outlet flow rate is large, and the influence of the porous area on it is not very large. Compared with the cylindrical shape, the porous area is not dominant, and the cylindrical shape of the filter net is dominant.

The following is the simulation analysis of the cylindrical filter net. Because the section size and radius of the entrance and exit of the cylinder are the same, the pressure distribution cloud map shows that the existence of porous areas makes the pressure drop obvious. The maximum pressure at the entrance is 30,000 Pa, and the pressure drop at the middle is 18,000 Pa. However, due to the existence of porous regions, the pressure drop of the flow is larger than that of the flow without porous media, and there is a well-defined pressure change, as shown in Figure 7a below. Compared with the circular shape, it can be seen that the pressure drop generated by the porous region of the cylindrical-shape filter is smaller than that of the circular-shape filter under the same boundary conditions. As shown in Figure 7b, the velocity and pressure distribution diagram on the symmetric line shows that the velocity on the symmetric line gradually decreases with the change in position, which is mainly due to the existence of the porous region in the middle, which obstructs the flow and makes the velocity smaller. The pressure on the symmetric line is in the form of a piece wise function, and the outlet pressure increases due to the obstruction of the porous region.

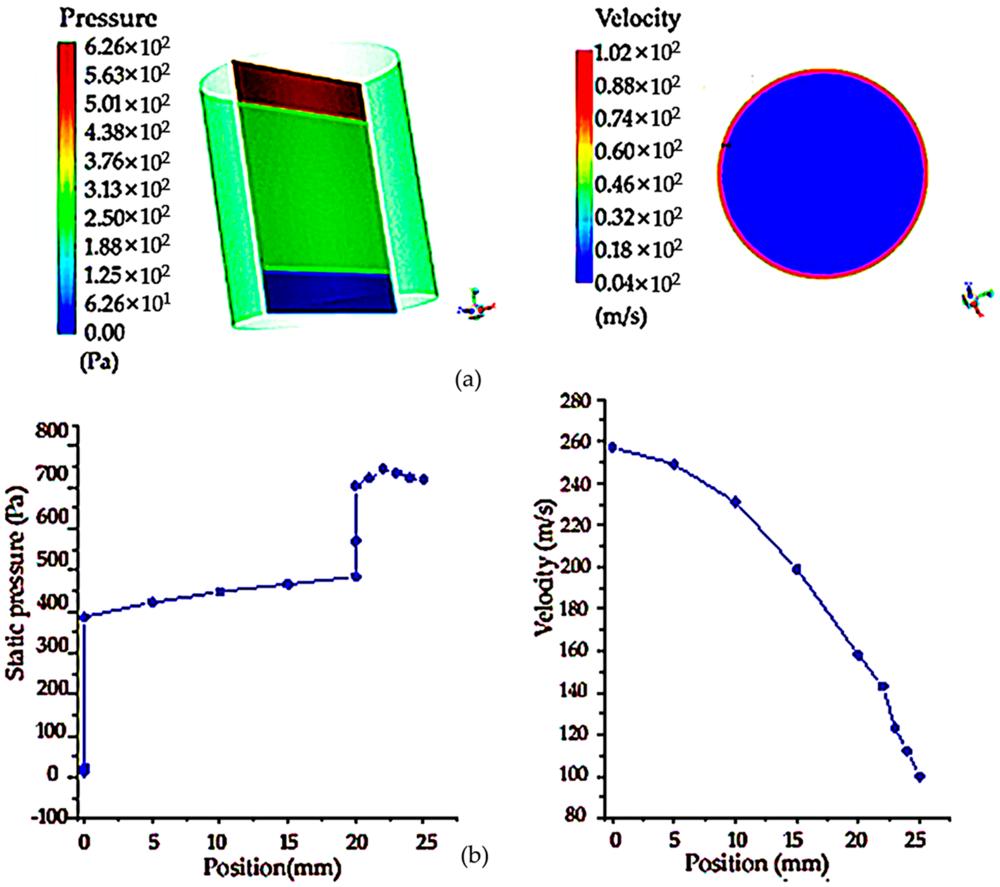

Figure 7. Pressure cloud image and flow field cloud image of cylindrical shaped sampling vessel with filter net and velocity and pressure distribution on the symmetry line of the cylindrical section: (**a**) pressure cloud diagram and velocity cloud image of upstream field velocity at different sections of cylinder sampling vessel with filter net; (**b**) pressure and velocity distribution on the symmetry line of the diagram of cylindrical sampling vessel with filter net.

The following is the simulation analysis of the hemispherical sampling vessel with a filter net. It can be seen from the pressure distribution cloud map that the existence of porous regions makes the pressure drop obvious. However, due to the presence of porous regions, the flow has a greater pressure drop than the flow of a medium without pores, and there is a significant pressure change, as shown in Figure 8a below. Compared with the hemisphere-shaped sampling vessel with a filter net, it can be seen that under the same boundary conditions, the pressure drop generated by the porous region of the cylindrical filter is smaller than that of the hemisphere-shaped sampling vessel with a filter net.

In order to accurately reflect the changes in the flow field in the hemisphere, we make a symmetrical line and observe the changes in velocity and pressure on the line. Figure 8b below shows the velocity pressure distribution on a symmetric line. It can be seen that the velocity on the symmetric line gradually decreases with the change in position, mainly due to the existence of porous regions in the middle, which hinders the flow and makes the velocity smaller. The pressure on the symmetric line is in the form of a piecewise function, and the outlet pressure is reduced due to the obstruction of the porous area, which was found to be different from the cylindrical-shaped sampling vessel with filter net.

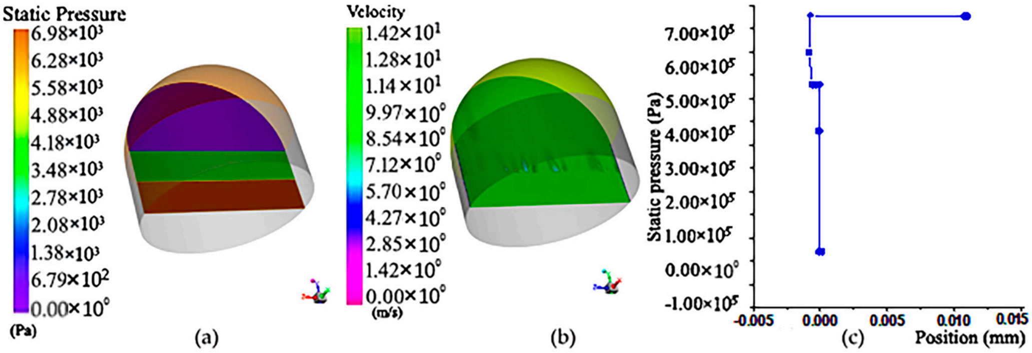

(a) Cloud image of flow field of hemispherical filter box;
(b) Velocity image of flow field of hemispherical filter box;
(c) Velocity and pressure distribution on the systemmetrical line of the hemispherical shape filter tank.

Figure 8. Pressure cloud diagram and cloud image of upstream field velocity at different sections and velocity and pressure distribution diagram of symmetry line of section of hemisphere-shaped sampling vessel with filter net: (**a**) pressure cloud diagram of hemisphere-shaped sampling vessel with filter net; (**b**) cloud image of upstream field velocity at different sections of hemisphere-shaped sampling vessel with filter net; (**c**) velocity and pressure distribution diagram of symmetry line of section of hemisphere-shaped sampling vessel with filter net.

3.4. Simulation of Aperture Size of Sampling Filter Screen

In order to verify the effect of the aperture size of the sampling filter screen on spore sample collection of "Capturer-A", the working state and working effect of filter nets with different aperture sizes of sampling filter screens installed in the sampling vessels were simulated and analyzed.

Since the above simulation results show that the bent air duct with a diameter of 20 mm is the most efficient, in order to ensure the compatibility of "Capturer-A", the interior diameter of the sampling vessel is consistent with the diversion duct with an inner diameter of 20 mm. According to the model setting of the actual filter net, a geometric model was established in Workbench (ANSYS Inc., Canonsburg, PA, USA), as shown in Figure 9. The cylinder has an outer diameter of 22 mm and an inner diameter of 20 mm. The circular table is installed in a reverse way, and the top is the same as the cylindrical sampling vessel with an outer diameter of 22 mm and an inner diameter of 20 mm. The bottom has an 18 mm outside diameter and 16 mm inside diameter. The model consists of three parts: inlet fluid region, porous media region and outlet fluid region.

The monitoring data of microparticle mass flow at the outlet of the truncated cone sampling collection vessel with a filter net in the simulation process are shown in Figure 9b. The three groups of working conditions when the aperture sizes of the sampling filter screen of filter nets are 0.180 mm, 0.150 mm or 0.0750 mm are installed in the sampling vessels. It can be seen from the monitoring chart that the mass flow at the outlet fluctuates mainly due to the existence of porous media and finally reaches stability. It was found that the fluctuation in the sampling vessel when installing the filter net with an aperture size of 0.180 mm was gentle, and the obstruction was relatively large.

Three different aperture sizes of sampling filter screens in the cylindrical sampling vessel with a filter net were simulated and compared, and it can be seen from the monitoring chart that the mass flow at the outlet between them fluctuates mainly due to the existence of porous media and finally reaches stability, as shown in Figure 9c. Compared with the three different aperture sizes of sampling filter screens, it is found that the fluctuation is still flat, and the fluctuation in the sampling vessel when installing the filter net with an aperture size of 0.150 mm was gentle and the obstruction was relatively large.

For the comparative monitoring of the three aperture sizes of sampling filter screens in the hemisphere-shaped sampling vessel with a filter net, it can be seen from the monitoring chart that the mass flow at the outlet between them fluctuates mainly due to the existence of porous media and finally reaches stability, as shown in Figure 9d. Compared with the three different aperture sizes of sampling filter screens, it is found that the fluctuation was flat, and the fluctuation in the collection vessel when installing the filter net with an aperture size of 0.0750 mm was gentle and the obstruction was relatively large.

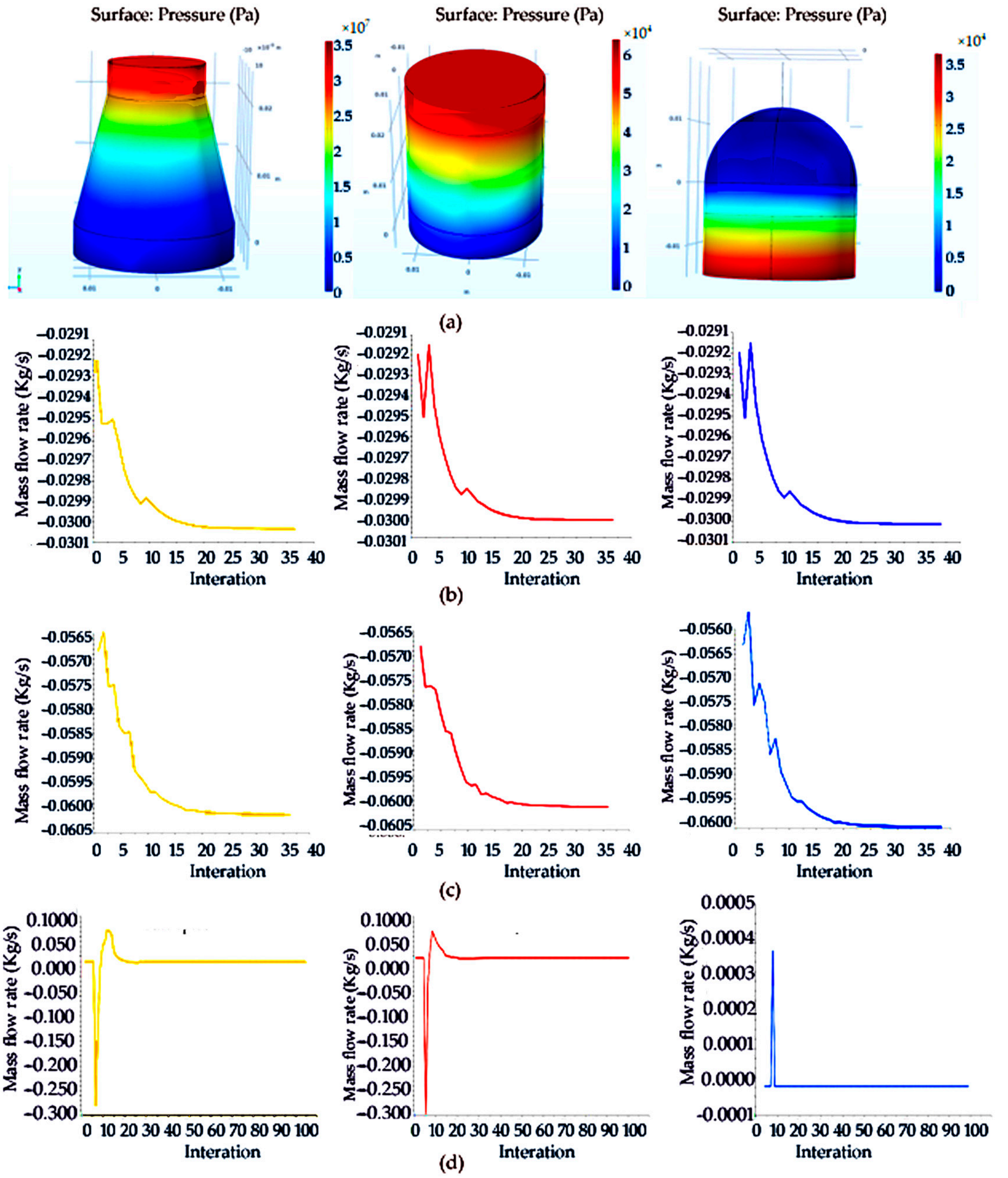

Figure 9. Model of three different shapes of sample collection vessels with filter net and analysis of microparticle mass flow: (**a**) model of truncated cone, cylindrical, hemisphere-shaped sampling collection vessel with filter net; (**b**) analysis of microparticle mass flow of truncated cone-, cylindrical-, hemisphere-shaped sampling filter screen with aperture size of 0.180 mm; (**c**) analysis of microparticle mass flow of truncated cone-, cylindrical-, hemisphere-shaped sampling filter screen with aperture size of 0.150 mm; (**d**) analysis of microparticle mass flow of truncated cone-, cylindrical-, hemisphere-shaped sampling filter screen with aperture size of 0.0750 mm.

This simulation mainly compares the sample collection capability of filter nets with different aperture sizes, so it is mainly through the porous media of the filter net to distinguish and simulate the filtration capacity of filter nets with different aperture sizes. Through the pressure distribution of the model of truncated cone-, cylindrical- and hemisphere-shaped sampling vessels with filter screens in the simulation of porous media, it can be found that the pressure distribution under the cylindrical filter is the largest, which is distributed in a step to the outlet.

3.5. Summary Findings of the Simulations

According to the above simulation results, if “Capturer-A” is equipped with an aperture sampling vessel filter screen of 0.150 mm, bent air duct with an inner diameter of 20 mm, negative-pressure fan of 1500 Pa and cylindrical spore-sampling vessel, “Capturer-A” can complete the spore sample collection more efficiently.

4. Verification Test of Prototype

In order to verify the effectiveness of “Capturer-A” in collecting spores, a prototype was designed and field test conducted with reference to the model parameters and simulation results above (as shown in Figure 10). The size and weight parameters of the prototype are shown in Table 2. The prototype test was used to verify the effect of several important parameters on the collection of microbial particles such as spores, and the validity of the parameters of simulation analysis was verified.

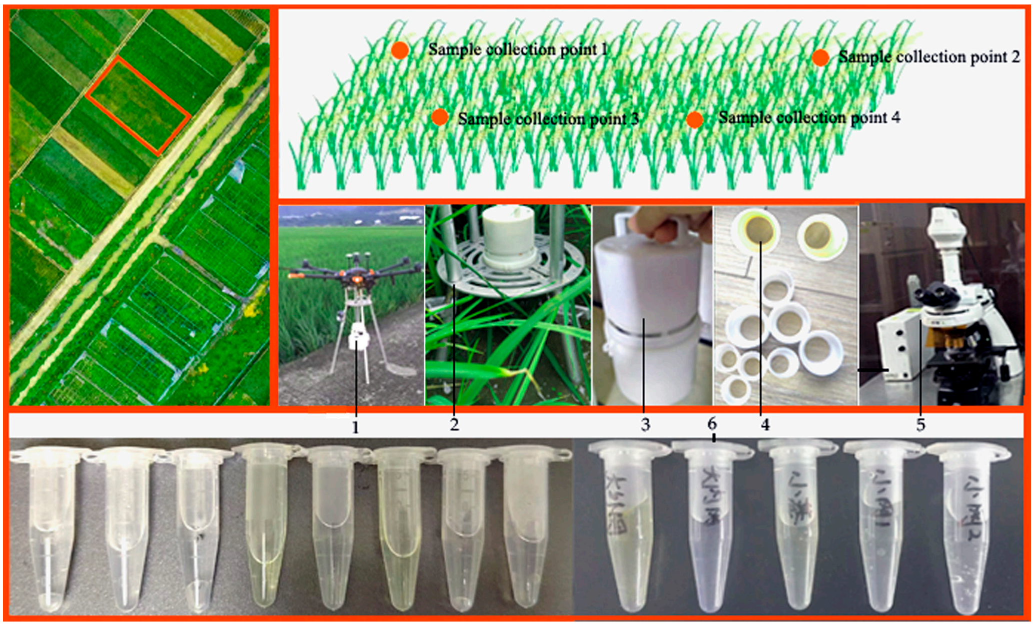

Figure 10. Verification test of prototype. Note: 1. pre-flight status of the drone carrying Capturer-A; 2. status of Capturer-A when it is installed on an aluminum alloy bracket; 3. portable prototype; 4. sample collection filter; 5. microscope; 6. sample diluent.

Table 2. Size and weight parameters of “Capturer-A”.

Parameters	Length (mm)	Width (mm)	Height (mm)	Weight (kg)
Values	90	90	150	0.47

4.1. Test Method

4.1.1. Test Methods for Prototype

The rice fungus spore collection device “Capture-A” was used to sample the suspected diseased paddy field. First of all, the collection points were planned, so that “Capture-A” could operate at several collection points within a certain distance from the rice crown cluster for a certain period of time. “Capture-A” has six sampling vessels with filter nets, each sampling vessel works for a certain period of time and the collected samples are tested and counted under a microscope to analyze the microbial information contained in the samples. During the validation test of the equipment, diseased rice fields of different growth stages were selected for the experiment.

4.1.2. Counting of Rice Disease Spore Information in Laboratory

(1) Put the sample into water, shake it in a conical bottle to disperse the conidia, then filter and rinse with multi-layer gauze, making sure that the filter residue does not contain spores, and dilute to 100 mL [16,34–36].

(2) Take one drop of dilute liquid, drop it on the calculation grid of the blood cell counting board, then gently press the cap from side to side, so that the cap is completely close to the counting board, and there are no bubbles in the liquid; use filter paper to absorb the excess suspended spore liquid, and let it sit for a few minutes until the spores settle [12,37].

(3) Observe the sample with a microscope. Since the spores in the dilution are in different spatial positions on the hemocytometer and can only be seen at different focal lengths, the micro-spiral must be mobilized one by one when counting, so as not to miss it. Spores are usually located on the lines of a large grid and should be counted on both sides and discarded on the other side to reduce errors. Each sample is observed and counted no less than two times, and its average value is taken [22,35].

4.2. Analysis of Experimental Results

4.2.1. Influence of Negative-Pressure Fan Power of the "Capture-A" on Sample Collection Effect

In order to ensure the reliability of the test data, under the same other conditions, "Capturer-A" equipped with negative-pressure fans of different wind pressures (450 Pa, 800 Pa, 1500 Pa) was used to sample the four sampling points of eight different rice fields affected by rice blast, and the sampling time was 5 min (as shown in Figure 10). Collected samples were counted under a laboratory microscope to obtain the number of disease spores in each sample. It can be seen from the figure that the fan power is positively correlated with the number of spores collected (as shown in Figure 11).

4.2.2. Comparative Test of Equipment Installation of Different Parameter Components

In order to optimize the fungal spore collection device parameters, a comparative test of equipment installation of different parameter component orthogonal experiments are carried out in this study. The test scheme and test results are as follows:

Four factors (aperture size of filter net, size of sampling vessel, shape of sampling vessel and air pressure of negative-pressure fan) that have an impact on the results were selected, and three levels were determined for each factor. The L9 (34) orthogonal test was used to determine the optimal formulation process based on the results as an index. Orthogonal test factors and level design are shown in Table 3.

The self-developed rice fungal spore collection device named "Capturer-A" was used to assemble different components in a rice field with suspected disease. In the same area of the paddy field, the device maintain a certain distance from the rice crown cluster and runs for the same period of time through a negative-pressure fan against each spore sample collection filter vessel at the inlet of the device. The rice fungus spore collection device is equipped with sample collection vessels of different sizes, sample collection vessels of different shapes, filter nets of different aperture sizes and different wind pressure brought by different negative fans with different pressures. The collected samples are monitored and counted in the laboratory and then analyzed using orthogonal tests. Several parameters affecting the device are set as factors and levels in the orthogonal test. Specific test factors and levels are shown in Table 3.

According to the range analysis of the orthogonal test, the most suitable combination is A3B2C1D3. The device can meet the requirements of rice disease information collection when the pressure of the negative-pressure fan is 450 Pa to 1500 Pa. If the aperture size of the sampling filter screen is 0.150 mm, sampling vessel size is 20 mm, sampling vessel shape is cylindrical and the pressure of the negative-pressure fan is 1500 Pa, the sampling effect is the best.

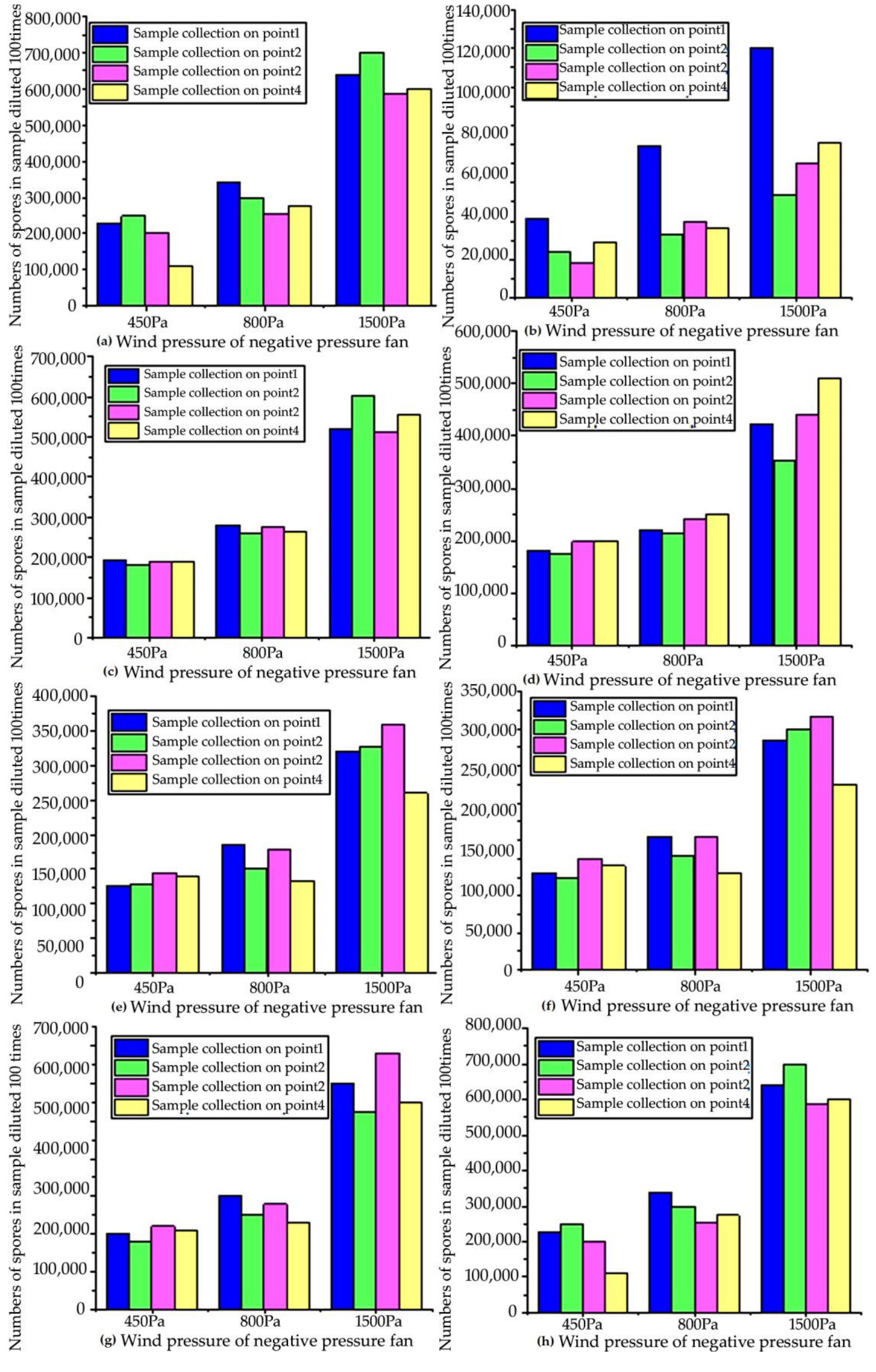

Figure 11. Comparison of numbers of samples collected by negative-pressure fans with different wind pressures in the prototype test: (**a**) number of spores collected by "Capturer-A" at 4 sampling sites in the first blast rice field; (**b**) number of spores collected by "Capturer-A" at 4 sampling sites in the second blast rice field; (**c**) number of spores collected by "Capturer-A" at 4 sampling sites in the third blast rice field; (**d**) number of spores collected by "Capturer-A" at 4 sampling sites in the fourth blast rice field; (**e**) number of spores collected by "Capturer-A" at 4 sampling sites in the fifth blast rice field; (**f**) number of spores collected by "Capturer-A" at 4 sampling sites in the sixth blast rice field; (**g**) number of spores collected by "Capturer-A" at 4 sampling sites in the seventh blast rice field; (**h**) number of spores collected by "Capturer-A" at 4 sampling sites in the eighth blast rice field.

Table 3. Orthogonal experimental factors and levels.

Factor Name/Serial Number	Aperture Size of Filter Net (mm) A	Diameter of Bent Air Duct (mm) B	Shape of Sampling Vessel C	Wind Pressure (Pa) D
1	0.180	15	Cylinder	450
2	0.150	20	Circular	800
3	0.0750	25	Platform	1500

In orthogonal test analysis, *ki* is the sum of the *i* level test index values in the corresponding factors, *ki* represents the mean value of the *i* level test index values in the corresponding factors and the r value represents the difference between the maximum and minimum values of *ki* in the fixed factors. The larger the *r* value is, the greater the influence of different levels of the factor settings on the evaluation indicators. Therefore, it shows that the greater the influence of this factor on the evaluation index, and vice versa, the smaller the influence of this factor on the experimental results. Through orthogonal analysis of the results, the results of four columns of tests A, B, C and D in Table 4 show that the change in test results caused by the change in parameters of A is the largest, and the change in test results caused by the change in parameters of B is followed by C and then D. It can be seen from the range (*r*-value) analysis in Table 4 that the influence degree of the four factors on the results is successively A > B > C > D (the aperture size of the sampling vessel filter net > an inner diameter of bent air duct > the shape of the sampling vessel > the wind pressure of the negative-pressure fan), with the maximum result as the optimization objective. From the size analysis of *k1*, *k2* and *k3*, the optimal condition of the result is A3B2C1D3. The experiment was carried out according to the L9 (34) orthogonal design table, and the results are shown in Table 4.

Table 4. Orthogonal experimental results.

Serial Number of Experiments	A	B	C	D	Results ($\times 10^7$)
1	1	1	1	1	1.26
2	1	2	2	2	9.2
3	1	3	3	3	16
4	2	1	2	3	30.4
5	2	2	3	1	39.2
6	2	3	1	2	48
7	3	1	3	2	812
8	3	2	1	3	1000
9	3	3	2	1	906
K_1	26.46	843.66	1049.26	946.46	
K_2	117.60	1048.40	945.60	869.20	
K_3	2718.00	970.00	867.20	1046.40	
k_1	8.82	281.22	349.75	315.49	
k_2	39.20	349.47	315.20	289.73	
k_3	906.00	323.33	289.07	348.80	
r	897.18	68.25	60.69	59.07	
Primary and secondary order of factors	A > B > C > D				
Optimal combination	$A_3B_2C_1D_3$				

The data were processed by the R language data processing program (Lucent Technologies Co., LTD., Hangzhou, China). The results of ANOVA for a single factor showed that factor A had a significant impact on the results ($p < 0.01$), while factors B, C and D had no statistically significant impacts on the results ($p > 0.05$).

The analysis of variance is used to test the actual situation of the influence of various factors on the results. The larger the sum of squares of deviation for the factor, the greater the difference between the test results and the greater the influence of the factor on the test results. $p < 0.01$ indicates a very significant effect, and $p < 0.05$ indicates a significant effect (as shown in Table 5).

Table 5. Variance analysis of situation of the influence of various factors on the results.

Source of Variation	Sum of Squares	Degree of Freedom	Mean Square	Value of F	Value of *p*	Significance
A	1,557,197.137	2	778,598.568	295.939	0.003	**
B	7114.091	2	3557.046	1.352	0.425	
C	5559.755	2	2779.878	1.057	0.486	
D	5261.883	2	2630.942	1.000	0.500	
Error e	5261.883	2	2630.942			

Note: ** indicates very significant ($p < 0.01$) effect.

The sum of squares of deviation for each factor and error is calculated, and then the degree of freedom, mean square and F-value are obtained; the F-test is then carried out. The specific calculation process is as follows:

$$\overline{y} = \frac{1}{n}\sum_{i=1}^{n} y_i \tag{16}$$

$$Q = \Sigma_{i=1}^{n} y_i^2 \tag{17}$$

$$P = \frac{1}{n}\left(\sum_{i=1}^{n} y_i\right) = \frac{T^2}{n} \tag{18}$$

$$SS_T = \sum_{i=1}^{n}(y_i - \overline{y})^2 = \sum_{i=1}^{n} y_i^2 - \frac{1}{n}\left(\sum_{i=1}^{n} y_i\right)^2 = Q - P \tag{19}$$

$$SS_A = \frac{\gamma}{n}\sum_{i=}^{\gamma} l^2_{(k_i \overline{-y})=}\frac{n}{r}\left(\sum_{i=1}^{r} k_i^2\right) - \frac{T^2}{n} = \frac{n}{r}\left(\sum_{i=1}^{r} k_i^2\right) - P \tag{20}$$

SS_T refers to the sum of squares of the total deviation, which is used to reflect the total difference change in data during the test. The sum of squares of deviation reflects the degree of influence of various factors on the experimental results. The larger the sum of squares of deviation is, the greater the influence of selected factors on the test results.

The sum of squares of deviation of each factor reflects the degree of influence of each factor on the test results. The larger the sum of squares of deviation of the factor, the greater the difference between the test results when the factor is taken to different levels, and the greater the influence of the factor on the test results. The sum of squares of deviations for each factor is calculated as follows:

$$T = \sum_{i=1}^{n} y_i \tag{21}$$

SS_B, SS_C and SS_D were processed in the same way. The variance results of each factor on the results are shown in Table 6. It can be seen from Table 6 that the aperture size of the spore sampling filter net has a very significant impact on the results ($p < 0.01$), while the shape of the sampling vessel, the air pressure of the negative-pressure fan and the size of the sampling vessel have no significant impacts on the results ($p > 0.05$). The order of influence of the four factors is as follows: number of filter meshes > size of sampling vessel > shape of sampling vessel > air pressure of negative-pressure fan. Considering the influence of the four factors on the results, the optimal combination is A3B2C1D3; that is, when the aperture size of the filter net is 0.150 mm, the diameter of the sampling vessel is 20 mm, the shape of the sampling vessel is cylindrical and the air pressure of the negative-pressure fan is 1500 Pa, the maximum result is obtained.

Table 6. Validation test of orthogonal test result.

Process Condition	Test 1	Test 2	Test 3	Mean Value	Standard Error	Relative Standard Deviation/%
$A_3B_2C_1D_3$	909	900	892	900.33	8.5	0.85

In order to verify the reliability of the L9 (34) orthogonal test results, three parallel tests were carried out under the conditions of the aperture size with a filter net of 0.0750 mm, sampling vessel with diameter of 20 mm, the shape of the sampling vessel of cylinder and air pressure of negative-pressure fan of 1500 Pa. The verification results are shown in Table 6, and the obtained results are 900.33 ± 8.5. The results were higher than those of the single factor test and orthogonal test group, indicating that the optimal condition (A3B2C1D3) obtained the by L9 (34) orthogonal test was stable and reasonable.

4.3. Comparison Test between Self-Developed Device and Existing Market Device

In order to verify the sampling effect of "Capturer-A", the sampling effect of "Capturer-A" and "YFBZ3" are compared and tested. The two devices were placed at the same sampling point in the same plot, at the same time. In order to avoid mutual influence, the two devices were 2 m apart. The "Capturer-A" (aperture sizes of filter net of sampling with 0.150 mm, bent air duct with an inner diameter of 20 mm, negative-pressure fan with 1500 Pa, sampling of cylindrical shape) and the mobile spore collection device of "YFBZ3" (YunFei Co., Ltd., Zhengzhou, China) were used to carry out five-point sampling on rice fields suspected of diseases. The two devices were simultaneously placed on the ridge of the same sampling point in the same plot, and the distance between the two devices and the rice was 250 mm. Analyzing the microbial information contained in the sample, a test process field diagram and results are shown in Figure 12.

According to the test data, there was a certain difference in the number of spore samples collected by A and B at the same sampling point in the same period of time. The two devices were operated at fifteen points for 1 min, 3 min, 5 min and 10 min, respectively.

Through paired T-test analysis in the R language data processing program (Lucent Technologies Co., LTD., Hangzhou, China), it was found that there were significant differences between "Capturer-A" and "YFBZ3" in 1 min, 3 min, 5 min and 10 min collection at field A ($p < 0.05$), and the value collected by "Capturer-A" was significantly higher than that by "YFBZ3" (as shown in Table 7).

Table 7. Paired *t* test analysis table of "Capturer-A" and "YFBZ3".

Serial of Sampling Field	Sampling Time (Min)	Mean Value ± SD of the "Capturer-A"	Mean Value ± SD of the "YFBZ3"	Value of T	Value of *p*	Significance
A	1	1871 ± 742.2	749.6 ± 279	5.100	0.007	**
A	3	5142 ± 2271	1922 ± 647.4	4.122	0.015	*
A	5	8431.6 ± 3280.4	3378 ± 1297.9	4.848	0.008	**
A	10	17,600 ± 7542.9	6784 ± 2474.3	4.506	0.011	*
B	1	1537.4 ± 493.3	780 ± 252.3	5.598	0.005	**
B	3	3948 ± 1190.7	3384 ± 1672.9	0.979	0.383	
B	5	6944 ± 2230.3	3190 ± 779.7	5.067	0.007	**
B	10	14,120 ± 4326.9	6748 ± 1633.9	5.621	0.005	**
C	1	1608 ± 343.6	930 ± 364.1	5.279	0.006	**
C	3	4316 ± 963.3	2682 ± 1186.1	4.850	0.008	**
C	5	6544 ± 2114.4	3130 ± 1378	5.059	0.007	**
C	10	11,774 ± 2847.4	7534 ± 3120.8	5.552	0.005	**

Note: ** indicates very significant ($p < 0.01$) effect, * indicates significant ($p < 0.05$) effect.

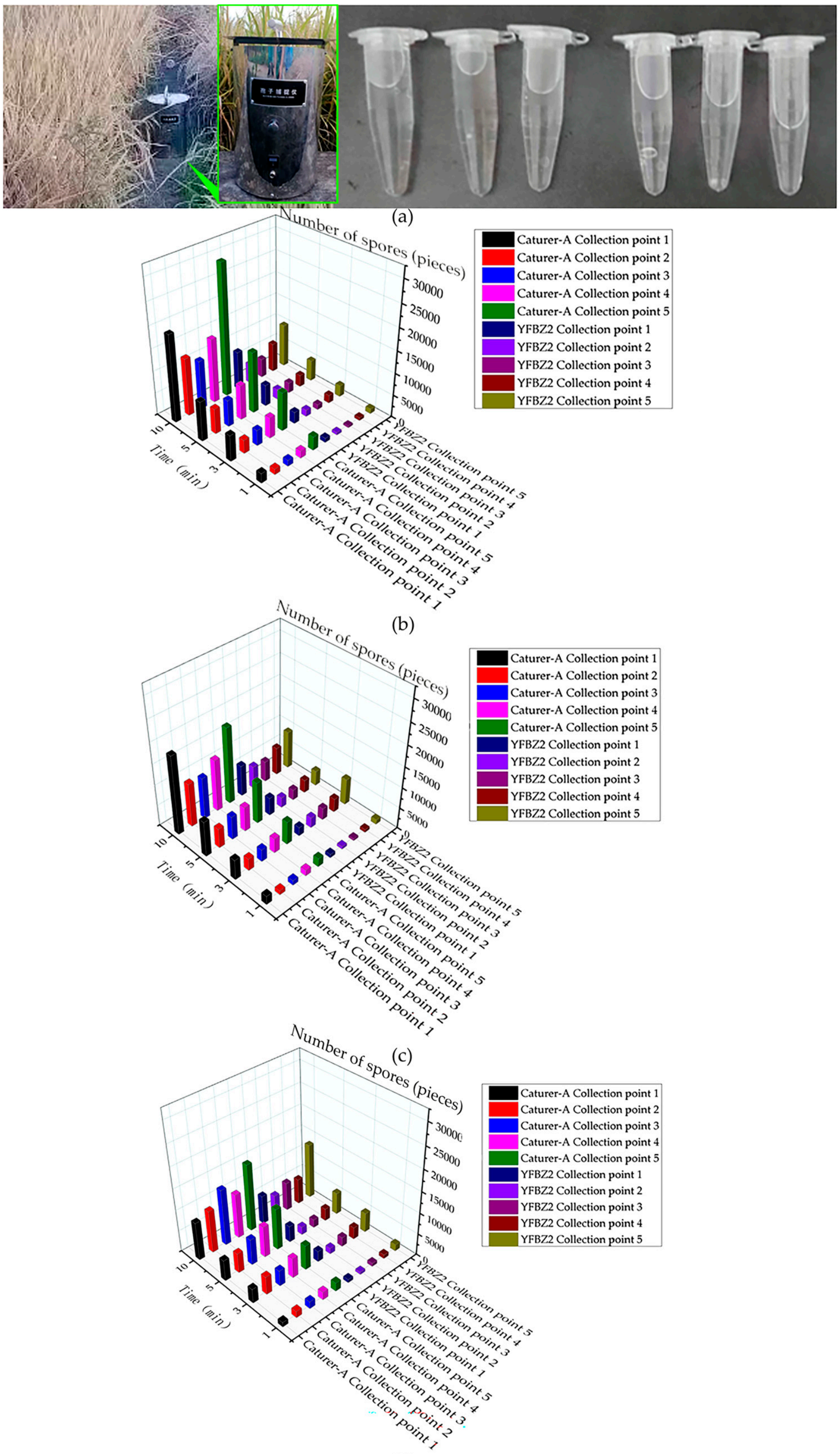

Figure 12. Test comparison of spore catching ability between self-developed device and portable spore trap (YFBZ3): (**a**) comparison of the "Capturer-A" and the mobile spore collection (YFBZ3) and sample diluent from a single test; (**b**) the number of spores collected by the "Capturer-A" and mobile spore collection device (YFBZ3) working in field A for 1 min, 3 min, 5 min, 10 min; (**c**) the number of spores collected by the "Capturer-A" and mobile spore collection device (YFBZ3) working in field B for 1 min, 3 min, 5 min, 10 min; (**d**) the number of spores collected by the" Capturer-A" and mobile spore collection (YFBZ3) working in field C for 1 min, 3 min, 5 min, 10 min.

At 1 min, 5 min and 10 min collection at field B, there were significant differences between "Capturer-A" and "YFBZ3" ($p < 0.05$), and the value of "Capturer-A" was significantly higher than that of "YFBZ3". There was no significant difference between "Capturer-A" and "YFBZ3" at 3 min ($p > 0.05$).

It was found that there were significant differences between "Capturer-A" and "YFBZ3" at 1 min, 3 min, 5 min and 10 min collection at field C ($p < 0.05$), and the value collected by "Capturer-A" was significantly higher than that by "YFBZ3".

The comprehensive analysis shows that no matter on field A, field B or field C, the acquisition time is 1 min, 3 min, 5 min and 10 min, and the value collected by "Capturer-A" is higher than that collected by "YFBZ3".

5. Conclusions and Prospects

5.1. Main Conclusions

This study mainly studied the rapid detection of spores of rice infectious fungal diseases in scattered, numerous and geographically remote plots, and it solved the shortcomings of the existing spore detection methods, such as high cost, low intelligence and long detection cycle. After the prototype development and field test, the conclusions were as follows:

(1) A rice fungal spore collection device is developed, which is suitable for mobile field operation. The mobile spore collection device is small and easy to carry, and it can be carried by hand, vehicle or UAV. In operation, the system can complete the collection of fungal spores from multiple sample collection points at one time, realize the collection of spores from multiple points in the monitoring plot and comprehensively monitor the disease situation of the field. The mobile spore collection device has the advantages of reasonable structure, safety and lightweight, convenient operation, small size, overall mass less than 2 kg and can be mounted on the UAV.

(2) A rice fungal spore collection device is designed. The microcomputer controls the stepper motor to rotate the fixed plate of the sampling vessel for collecting spores by writing a program, so that the sampling vessel on the fixed plate of the sampling vessel can rotate to the working position within a set time and start collecting spores. After the collection task of a collection point is completed, the stepper motor can be controlled by a programmed microcomputer to make the next sampling vessel reach the working position, and so on, so that the collection task of multiple collection points can be continuous. The prototype produced in this study was equipped with six sampling vessels to achieve the efficient collection of fungal disease spores.

(3) After the simulation and test analysis of the components of the mobile rice infectious fungal disease collection device, it was found that the aperture size of the sampling vessel filter net, the inner diameter of bent air duct, the shape of the sampling vessel, the wind pressure of the negative-pressure fan and other parameters were basically selected. The scheme is as follows: when the device adopts 450 Pa, 800 Pa or 1500 Pa negative-pressure fans, the sampling filter vessel shape adopts a cylinder, truncated cone or hemisphere form, and the aperture sizes of the sampling spore filter net are 0.180 mm, 0.150 mm, 0.0750 mm, bent air duct with an inner diameter of 15 mm, 20 mm and 25 mm, "Capturer-A" can meet the functional requirements of rice infectious fungal spore collection. The parameter combination of "Capturer-A" in the best working state is as follows: the aperture size of the sampling filter net with 0.150 mm, the inner diameter of the bent air duct is 20 mm, the shape of the sampling vessel of cylinder and the wind pressure of the negative-pressure fan is 1500 Pa. In the field test, the self-developed "Capturer-A" (inner diameter of bent air duct of 20 mm, the shape of the sampling vessel of cylinder and the aperture size of the sampling spore filter is 0.150 mm, the wind pressure of the negative-pressure fan 450 Pa) was compared with the existing "YFBZ3" (mobile spore collection device made by Yunfei Co., Ltd., Zhengzhou, China) fungal spore collection device in the market. Samples were collected from 15 sampling points in three suspected diseased rice fields. The two devices were operated at fifteen collection points for 1 min, 3 min, 5 min and 10 min. The samples

were examined and counted under a microscope in the laboratory, and it was found that the spores of rice blast disease and rice flax spot disease of rice were contained in the samples. It was found that under the same conditions, “Capturer A” was about twice that of the existing spore collection device “YFBZ3” (mobile spore collection device made by Yunfei Co., Ltd., Zhengzhou, China).

(4) The field test of the prototype showed that the device could effectively collect spore information on rice crown bush disease when working within a certain distance from the crown bush. If the spore collection work needs to be expanded, the parameters of the device should be adjusted to meet the functional requirements.

5.2. Prospects

In this study, the rapid collection of rice fungal spores and microorganisms in rice crown and rapid image collection of rice crop phenotypic information were studied. Some research achievements and new technical progress were made. Due to the limitation of personal ability and research time, there are still many problems in this project that need further research and exploration:

(1) The prototype test in this study only verified the working effect of the prototype with a certain range of parameters in the rice crown cluster and did not verify the working effect of the prototype in a larger range. The prototype produced in this study was equipped with 4–6 sampling vessels; more sampling vessels can be installed in order to achieve the efficient collection of fungal disease spores. The performance of ”Capturer-A” needs to be further optimized in future work.

(2) The self-developed rice fungal spore collection device needs to conduct follow-up monitoring, data statistics and processing of samples through a microscope in the laboratory after collecting information, and the intelligence level is not high. It is hoped that an integrated spore information monitoring function can be added in follow-up work.

(3) The hardware structure of “Capturer-A” needs to be further optimized. Since water resistance needs to be considered in the work of rice crown clusters, it is necessary to add shells and metal brackets when installing on mobile devices such as drones, and the volume and weight will further increase. The further research direction of this topic is to further optimize the structure and make the whole system more convenient.

Author Contributions: Methodology, X.G.; software, X.G., Y.O. and K.D.; validation, X.G.; formal analysis, Y.O.; investigation, X.G.; resources, X.G. and X.F.; data curation, X.G. and X.F.; writing—original draft preparation, Y.O. and K.D.; writing—review and editing, R.J.; visualization, X.G.; supervision, R.J. and Z.Z.; project administration, Z.Z. All authors have read and agreed to the published version of the manuscript.

Funding: This work was supported by the National Key R&D Program of China (2022YFD2001501) and the Laboratory of Lingnan Modern Agriculture Project (NT2021009); in part by Science and Technology Plan of Jian City of China (20211-055316 and 2022-051252-02), Science and Technology Plan of Guangdong Province of China (2023B10564002 and 2021B1212040009), Innovative Research Team of Agricultural and Rural Big Data in Guangdong Province of China (2019KJ138), and China Scholarship Council (202308440394).

Data Availability Statement: The authors confirm that the data supporting the findings of this study are available within the article.

Conflicts of Interest: The funders had no role in the design of the study; in the collection, analyses, or interpretation of data; in the writing of the manuscript; or in the decision to publish the results.

References

1. Hibino, H. Biology and epidemiology of rice viruses. *Annu. Rev. Phytopathol.* **1996**, *34*, 249–256. [CrossRef] [PubMed]
2. Azizi, M.; Lau, H. Advanced diagnostic approaches developed for the global menace of rice diseases: A review. *Can. J. Plant Pathol.* **2022**, *44*, 627–651. [CrossRef]
3. Callaway, E. Devastating wheat fungus appears in Asia for first time. *Nature* **2016**, *532*, 421–422. [CrossRef] [PubMed]

4. Kim GwanWon, K.G. An analysis on spatial spillover effects of rice pest and disease damages under climate change. *J. Rural. Dev.* **2018**, *41*, 51–81.
5. Zhang, H.L. *Study on the Germination and Pathogenicity of Small Conidium of Blast Fungus*; Northwest A&F University: Beijing, China, 2017.
6. Sesma, A.; Osbourn, A.E. The rice leaf blast pathogen undergoes developmental processes typical of root-infecting fungi. *Nature* **2004**, *431*, 582–586. [CrossRef] [PubMed]
7. Oh, J.Y.; Jee, S.N.; Nam, Y.; Lee, H.; Ryoo, M.I.; Kim, K.D. Populations of Fungi and Bacteria Associated with Samples of Stored Rice in Korea. *Mycobiology* **2007**, *35*, 36–44. [CrossRef] [PubMed]
8. Mousanejad, S.; Alizadeh, A.; Safaie, N. Effect of Weather Factors on Spore Population Dynamics of Rice Blast Fungus in Guilan Province. *J. Plant Prot. Res.* **2009**, *49*, 319–329. [CrossRef]
9. Ordynets, A.; Keßler, S.; Langer, E. Geometric morphometric analysis of spore shapes improves identification of fungi. *PLoS ONE* **2021**, *16*, e0250477. [CrossRef] [PubMed]
10. Traore, M.D. Abiotic transmission of Rice yellow mottle virus through soil and contact between plants. *Pak. J. Biol. Sci.* **2008**, *11*, 900–904. [CrossRef]
11. Robertson, L.; Brandys, R. A multi-laboratory comparative study of spore trap analyses. *Mycologia* **2011**, *103*, 226–231. [CrossRef]
12. Gómez-Noguez, F.; Pérez-García, B.; Mendoza-Ruiz, A.; Orozco-Segovia, A. A Pluviometric Fern Spore, Fungal Spore, and Pollen Trap. *Bioone. Am. Fern J.* **2014**, *104*, 1–6. [CrossRef]
13. Suzuki, H. The falling of Piricularia oryzae-spore by rain. *Annu. Rep. Soc. Plant Prot.* **1965**, *16*, 135–139.
14. Valent, B.; Chumley, F.G. Molecular genetic analysis of rice blast fungus, Magnaporth grisea. *Annu. Rev. Phytopathol.* **1991**, *29*, 443–467. [CrossRef]
15. Leal, P.L.; Carvalho, T.S.; Siqueira, J.O.; Moreira, F. Assessment of the occurrence and richness of arbuscular mycorrhizal fungal spores by direct analysis of field samples and trap culture—A comparative study. *An. Da Acad. Bras. De Ciências* **2018**, *2*, 2–19. [CrossRef] [PubMed]
16. Pityn, P.J.; Anderson, J. Air sampling of mold spores by slit impactors: Yield comparison. *J. Environ. Sci. Health* **2013**, *11*, 22–34. [CrossRef] [PubMed]
17. Huang, C.M.; Liao, D.J.; Wu, H.S.; Shen, W.C.; Chung, C.L. Cyclone-based spore trapping, quantitative real-time polymerase chain reaction and high-resolution melting analysis for monitoring airborne inoculum of Magnaporthe oryzae. *Ann. Appl. Biol.* **2016**, *169*, 75–90. [CrossRef]
18. Huang, J.; Pan, W.; Ni, W. Application of Spore Capture Technology to Guide green disease control in wheat. *Shanghai Agric. Sci. Technol.* **2016**, *2*, 119–120.
19. Berruyer, R.; Poussier, S.; Mosquera, G. Quantification of the invasion of rice leaves by Magnaporthe grisea using a direct extraction method and Q-PCR. *Phytopathology* **2005**, *95*, S9–S10.
20. Qi, L.; Ma, X.; Liang, B. Research status of rice blast surveillance and prediction methods and establishment of epidemic risk assessment system. *Chin. Agric. Sci. Bull.* **2011**, *27*, 213–216.
21. Wang, C. *Development of Pulse Cloud Intelligent Spore Catcher and Remote Monitoring of Wheat Rust Disease*; Shandong Agricultural University: Jinan, China, 2018.
22. Xia, X. *Research on Microscopic Image Acquisition and Processing System of Field Plant Fungi Spores*; Agricultural University of Hebei: Shijiazhuang, China, 2015.
23. Lei, Y. *Hyperspectral Detection of Wheat Stripe Rust and Monitoring Method of Summer Spore in Air*; Northwest A&F University: Xi'an, China, 2019.
24. Reddy, P.S.K.; Nagaraju, C. Weight optimization and finite element analysis of composite automotive drive shaft for maximum stiffness. *Mater. Today* **2017**, *4*, 2390–2396. [CrossRef]
25. Li, Y.; Xu, Z.; Zhang, L. Lightweight design of soybean harvesting locomotive frame. *J. Chongqing Univ.* **2019**, *42*, 14–21.
26. Zhang, N. Lightweight design of high-speed rice transplanter frame. *Trans. Chin. Soc. Agric. Eng.* **2012**, *28*, 55–59.
27. Font-Llagunes, J.M.; Lugrís, U.; Clos, D.; Alonso, F.J.; Cuadrado, J. Design, Control, and Pilot Study of a Lightweight and Modular Robotic Exoskeleton for Walking Assistance After Spinal Cord Injury. *J. Mech. Robot. Trans. ASME* **2020**, *12*, 031008. [CrossRef]
28. Duan, X.; Cao, X.; Zhou, Y. Application of a fixed-volume spore trap in the Study of Plant disease Epidemiology. In Proceedings of the 2008 Annual Conference of the Chinese Society for Plant Pathology, Guangzhou, China, 21–24 July 2008.
29. Bao, Y.; Li, H.; Luo, P. Technology Development and Development of Network Remote Control of pathogen spore capture System. In Proceedings of the 2010 International Agricultural Engineering Congress, Shanghai, China, 17–21 September 2010.
30. Cao, X.; Zhou, Y.; Duan, X. Dynamic monitoring of conidia concentration of wheat Powderomyces in air. In Proceedings of the Chinese Society for Plant Pathology, Changsha, China, 15–18 August 2010.
31. Wu, Y. *Design of Agricultural Monitoring System Based on Rotary-Wing UAV*; China Jiliang University: Hangzhou, China, 2018.
32. Ding, L.; Liu, G. Positioning analysis and error correction of DJI M600 UAV equipped with D-RTK GNSS. *Geospat. Inf.* **2020**, *18*, 16–20.
33. Wang, P. Review of key technologies for remote sensing information acquisition based on micro-UAV. *Chin. J. Agric. Eng.* **2014**, *30*, 1–12.
34. Greer, C.; Webster, R. Occurrence, Distribution, Epidemiology, Cultivar Reaction and Management of Rice Blast Disease in California. *Plant Dis.* **2001**, *85*, 1096–1102. [CrossRef] [PubMed]

35. Wiwattanapatapee, R.; Chumthong, A.; Pengnoo, A.; Kanjanamaneesathian, M. Preparation and evaluation of Bacillus megaterium alginate microcapsules for control of rice sheath blight disease. *World J. Microbiol. Biothechnol.* **2013**, *29*, 1487–1497. [CrossRef] [PubMed]
36. Karlsson, M.; Elfstrand, M.; Stenlid, J.; Olson, Å. A fungal cytochrome P450 is expressed during the interaction between the fungal pathogen Heterobasidion annosum sensu lato and conifer trees. *J. DNA Seq. Mapp.* **2008**, *19*, 455–469.
37. Li, J.; Zhang, T.; Liao, Y. Farmland Information sampling method and aircraft platform design. *J. Vib. Meas. Diagn.* **2013**, *3*, 465–481.

国家出版基金项目
NATIONAL PUBLICATION FOUNDATION

国家出版基金项目
“十四五”时期国家重点出版物出版专项规划项目

智慧农业关键技术集成与应用系列丛书

大田无人化智慧农场

Unmanned Smart Farm for Field Crops Production

罗锡文　胡　炼◎主编

中国农業大學出版社
China Agricultural University Press

内容简介

无人化智慧农场是智慧农业的主要实现方式，是一个多学科交叉的应用领域，涉及农业工程、车辆工程、控制工程、计算机科学与技术、机器人工程等，并融合了自动驾驶、机器视觉、深度学习、遥感信息和农机-农艺融合等前沿技术。

本书的作者为高校从事智慧农业方向的教师、科研人员和研究生，依托“无人化智慧农场”团队的教研与推广实践，全面详细地介绍了大田无人化智慧农场的技术体系，内容涵盖了从农场规划建设至运行维护所涉及的各个环节，重点阐述支撑农场高效生产的智能农机装备的相关理论与方法，特别是线控底盘、卫星定位、路径规划、导航控制、自动避障和多机协同等。本书适合作为现代农业研究人员和应用技术人员的参考资料，也可作为农业工程、智慧农业和车辆工程等相关专业研究生、本科生和专科生的学习资料。

图书在版编目(CIP)数据

大田无人化智慧农场/罗锡文，胡炼主编. --北京：中国农业大学出版社，2024.12.
ISBN 978-7-5655-3346-4

Ⅰ. S126

中国国家版本馆 CIP 数据核字第 2024JS6117 号

书　　名　大田无人化智慧农场
Datian Wurenhua Zhihui Nongchang
作　　者　罗锡文　胡　炼　主编

总 策 划　王笃利　丛晓红　张秀环
策划编辑　刘　聪　石　华
出版发行　中国农业大学出版社
社　　址　北京市海淀区圆明园西路 2 号
电　　话　发行部 010-62733489,1190
编辑部 010-62732617,2618
网　　址　http://www.caupress.cn
经　　销　新华书店
印　　刷　涿州市星河印刷有限公司
版　　次　2024 年 12 月第 1 版　　2024 年 12 月第 1 次印刷
规　　格　185 mm×260 mm　　16 开本　　23.5 印张　　509 千字
定　　价　128.00 元

责任编辑　刘　聪　石　华　蔡恩嘉
封面设计　中通世奥图文设计中心
邮政编码　100193
读者服务部 010-62732336
出　版　部 010-62733440
E-mail cbsszs@cau.edu.cn

图书如有质量问题本社发行部负责调换

编委会

目录

第 1 章　绪论 …… 1
　1.1　农业机械化发展阶段概述 …… 1
　　1.1.1　1.0 原始生产阶段 …… 1
　　1.1.2　2.0 传统生产阶段 …… 2
　　1.1.3　3.0 机械化生产阶段 …… 2
　　1.1.4　4.0 智慧化生产阶段 …… 3
　1.2　大田无人化智慧农场的发展需求 …… 3
　　1.2.1　可大幅提高农业生产的三率 …… 3
　　1.2.2　是解决“谁来种地”和“怎样种地”的有效途径 …… 4
　参考文献 …… 5
第 2 章　大田无人化智慧农场概述 …… 6
　2.1　大田无人化智慧农场的概念 …… 6
　2.2　大田无人化智慧农场的系统架构 …… 6
　2.3　大田无人化智慧农场的关键技术 …… 7
　　2.3.1　数字化感知 …… 7
　　2.3.2　智能化决策 …… 10
　　2.3.3　精准化作业 …… 11
　　2.3.4　智慧化管理 …… 14
　参考文献 …… 15
第 3 章　大田无人化智慧农场基础设施 …… 16
　3.1　大田无人化智慧农场整体规划 …… 16
　3.2　农场仓储设施建设 …… 16
　　3.2.1　农机机库 …… 16
　　3.2.2　粮仓与物料仓库 …… 17
　3.3　大田无人化智慧农场的农田建设 …… 17
　　3.3.1　规模化 …… 17
　　3.3.2　宜机化 …… 18
　　3.3.3　田间道路 …… 19

3.3.4 农田标准化改造模式 …… 20
3.4 田间智能设施建设 …… 21
3.4.1 灌排设施 …… 21
3.4.2 电力设施 …… 21
3.4.3 传感器设施 …… 21
3.5 农田建设案例 …… 21
参考文献 …… 22
第 4 章 大田作业农机构造基础 …… 23
4.1 大田作业农机概述 …… 23
4.2 农机转向系统 …… 23
4.2.1 前轮转向 …… 24
4.2.2 后轮转向 …… 26
4.2.3 四轮转向 …… 27
4.2.4 折腰转向 …… 27
4.2.5 差速转向 …… 29
4.3 农机动力与机具连接 …… 30
4.3.1 电控液压三点悬挂系统 …… 30
4.3.2 快速挂接结构 …… 32
4.3.3 PTO 动力输出 …… 34
4.3.4 液压输出阀组 …… 35
4.4 总线技术 …… 35
4.4.1 SAE J1939 …… 35
4.4.2 ISO 11783 …… 36
4.4.3 ISOBUS …… 36
4.5 底盘线控技术 …… 38
4.5.1 概念 …… 38
4.5.2 线控底盘中的典型技术 …… 39
参考文献 …… 42
第 5 章 数字化感知关键技术 …… 43
5.1 作业环境信息感知 …… 43
5.1.1 高精度地图 …… 43
5.1.2 水、温度、气象 …… 50
5.1.3 土壤 …… 52
5.1.4 水田硬底层感知 …… 52
5.2 作业对象信息感知 …… 69
5.2.1 作物长势 …… 69

5.2.2　病虫害 …… 72
5.2.3　处方图 …… 75
5.3　作业机械信息感知 …… 79
5.3.1　农机机械的性能参数 …… 79
5.3.2　传感器选用与测量方法 …… 79
5.3.3　数据处理方法 …… 80
5.3.4　三种典型农机的性能参数监测与数据处理 …… 80
参考文献 …… 81
第6章　农机无人驾驶路径规划关键技术 …… 84
6.1　运移路径规划 …… 84
6.1.1　基于路网的双向Dijkstra运移路径规划算法 …… 84
6.1.2　运移路径实例 …… 86
6.2　不同形状地块的作业路径规划 …… 88
6.2.1　轮廓形状的描述指标 …… 88
6.2.2　作业路径规划 …… 91
6.3　农机转弯路径规划方式 …… 95
6.3.1　弓形、半圆形、鱼尾形转弯算法 …… 97
6.3.2　“Ω”形和“M”形转弯算法 …… 100
6.3.3　螺旋式转弯算法 …… 102
6.4　全覆盖作业路径规划 …… 107
6.4.1　耕作环节路径规划 …… 108
6.4.2　种植环节路径规划 …… 108
6.4.3　管理环节路径规划 …… 109
6.4.4　收获环节路径规划 …… 109
6.4.5　开边/封圈路径规划 …… 109
6.4.6　多约束全覆盖路径规划 …… 111
6.5　避障路径规划 …… 113
6.5.1　直接构造法 …… 114
6.5.2　样条曲线 …… 116
6.6　智能路径规划算法 …… 117
6.6.1　智能全局路径规划 …… 117
6.6.2　智能局部路径规划 …… 123
参考文献 …… 125
第7章　农机无人驾驶控制关键技术 …… 126
7.1　定位技术 …… 126
7.1.1　全球卫星导航系统 …… 126

7.1.2 多传感器融合定位技术 …… 131
7.1.3 单天线 GNSS/INS 组合导航 …… 133
7.2 农机无人驾驶坐标系统 …… 157
7.2.1 参考坐标系建立 …… 157
7.2.2 坐标系转换 …… 158
7.3 导航控制技术 …… 159
7.3.1 农机运动的数学模型 …… 159
7.3.2 农机转向控制 …… 165
7.3.3 路径跟踪控制 …… 171
参考文献 …… 177
第 8 章 精准作业关键技术 …… 179
8.1 精准耕整 …… 179
8.1.1 耕深监测与自动控制 …… 179
8.1.2 动力自适应匹配 …… 183
8.1.3 精准平整 …… 185
8.2 精准种植 …… 194
8.2.1 水稻育秧播种(密植、钵苗、钵毯苗) …… 194
8.2.2 精量直播 …… 198
8.3 精准管理 …… 201
8.3.1 水管理 …… 201
8.3.2 肥管理 …… 210
8.3.3 药管理 …… 213
8.3.4 杂草管理 …… 216
8.4 精准收获 …… 222
8.4.1 精准对行 …… 222
8.4.2 喂入量估计 …… 225
8.4.3 自动卸粮 …… 229
8.4.4 智能测产 …… 234
参考文献 …… 236
第 9 章 协同作业关键技术 …… 239
9.1 主从协同作业关键技术 …… 239
9.1.1 等待模式 …… 239
9.1.2 跟随模式 …… 246
9.2 多机协同作业关键技术 …… 251
9.2.1 地面农机群体协同作业 …… 251
9.2.2 多机协同作业 …… 258

9.3 人机协同作业关键技术 …… 262
9.3.1 人机协同作业技术概述 …… 262
9.3.2 无人和人工驾驶农机协同作业区域的划分 …… 262
9.4 不同生产环节协同关键技术 …… 263
9.4.1 再生稻种收同轨协同作业 …… 264
9.4.2 甘蔗收获机对行收获 …… 265
参考文献 …… 268
第 10 章 智慧化管理关键技术 …… 270
10.1 信息传输 …… 270
10.1.1 物联网 …… 270
10.1.2 4G/5G …… 271
10.2 作物生长管理 …… 273
10.3 智能农机管理 …… 279
10.4 农场管理 …… 282
10.4.1 农事管理：全程精细化与智能化 …… 282
10.4.2 农资管理：精准化与绿色化 …… 286
10.4.3 经营管理：节本增效与可持续发展 …… 286
10.5 无人农机管控平台 …… 287
10.5.1 无人农机管控平台概述 …… 287
10.5.2 无人农机管控平台的架构设计 …… 288
10.5.3 相关案例 …… 289
参考文献 …… 293
第 11 章 大田无人化智慧农场安全技术 …… 294
11.1 大田无人化智慧农场安全概述 …… 294
11.2 大田无人化智慧农场安全技术 …… 295
11.2.1 避障路径规划 …… 295
11.2.2 主动感知 …… 296
11.2.3 车路协同 …… 302
11.2.4 碰撞接触 …… 304
11.2.5 急停避障 …… 306
11.2.6 信息安全 …… 312
11.3 安全系统设计 …… 318
11.3.1 安全系统功能设计 …… 318
11.3.2 安全功能冗余设计 …… 321
11.3.3 安全规范 …… 323
参考文献 …… 326

第 12 章　大田无人化智慧农场应用 ………………………………………… 327
12.1　英国哈珀・亚当斯大麦无人化智慧农场实践(Hands Free Hectare project) ………………………………………… 327
12.2　广东增城水稻无人化智慧农场………………………………………… 327
12.2.1　项目背景………………………………………… 327
12.2.2　无人化精准平整………………………………………… 329
12.2.3　建设成效………………………………………… 333
12.3　湖南大通湖再生稻无人化智慧农场………………………………………… 333
12.3.1　项目背景………………………………………… 333
12.3.2　无人化作业………………………………………… 334
12.3.3　建设成效………………………………………… 341
12.4　上海联适水稻无人化智慧农场………………………………………… 341
12.4.1　项目背景………………………………………… 341
12.4.2　无人化作业………………………………………… 342
12.4.3　建设成效………………………………………… 346
12.5　安徽中科智能感知无人化智慧农场………………………………………… 347
12.5.1　项目背景………………………………………… 347
12.5.2　无人化作业………………………………………… 347
12.5.3　建设成效………………………………………… 349
12.6　黑龙江七星大田无人化智慧农场………………………………………… 349
12.6.1　项目背景………………………………………… 349
12.6.2　无人化作业………………………………………… 350
12.6.3　建设成效………………………………………… 350
12.7　河北赵县小麦无人化智慧农场………………………………………… 351
12.7.1　项目背景………………………………………… 351
12.7.2　无人化作业………………………………………… 351
12.7.3　建设成效………………………………………… 353
第 13 章　发展与展望………………………………………… 354
13.1　发展机遇与挑战………………………………………… 354
13.1.1　发展机遇………………………………………… 354
13.1.2　面临挑战………………………………………… 355
13.2　发展趋势展望………………………………………… 356
13.2.1　关键技术创新发展………………………………………… 356
13.2.2　应用规模和场景不断拓展………………………………………… 357
13.2.3　产业体系逐步完善………………………………………… 357

证书号第7239004号

专利公告信息

发明专利证书

发 明 名 称：一种单目高分多光谱的成像系统及控制方法

专 利 权 人：华南农业大学

地　　　址：510530 广东省广州市天河区五山路483号

发　明　人：姜锐;欧媛珍;万欢;管宪鲁;林键沁;梁浩伟;周志艳;罗锡文

专　利　号：ZL 2024 1 0345985.5　　　授权公告号：CN 118050328 B

专利申请日：2024年03月26日　　　授权公告日：2024年07月30日

申请日时申请人：华南农业大学

申请日时发明人：姜锐;欧媛珍;万欢;管宪鲁;林键沁;梁浩伟;周志艳;罗锡文

国家知识产权局依照中华人民共和国专利法进行审查，决定授予专利权，并予以公告。

专利权自授权公告之日起生效。专利权有效性及专利权人变更等法律信息以专利登记簿记载为准。

局长

申长雨

申长雨

2024年07月30日

证书号第7214861号

专利公告信息

发明专利证书

发明名称：一种基于主动光源的植被指数快速采样系统与方法

专利权人：华南农业大学

地　　址：510530 广东省广州市天河区五山路483号

发明人：姜锐;欧媛珍;臧禹;邓孔洪;蔡国奥;李杰浩;周志艳;罗锡文

专利号：ZL 2024 1 0508713.2　　授权公告号：CN 118111954 B

专利申请日：2024年04月26日　　授权公告日：2024年07月19日

申请日时申请人：华南农业大学

申请日时发明人：姜锐;欧媛珍;臧禹;邓孔洪;蔡国奥;李杰浩;周志艳;罗锡文

国家知识产权局依照中华人民共和国专利法进行审查，决定授予专利权，并予以公告。

专利权自授权公告之日起生效。专利权有效性及专利权人变更等法律信息以专利登记簿记载为准。

局长
申长雨

申长雨

2024年07月19日

证书号第7090104号

专利公告信息

发明专利证书

发明名称：一种基于主动光源的植物叶片透射与反射纹理影像同步采集装置与方法

专利权人：华南农业大学

地址：510530 广东省广州市天河区五山路483号

发明人：姜锐;欧媛珍;万欢;管宪鲁;廖娟;黄健斌;周志艳;罗锡文

专利号：ZL 2024 1 0334281.8

授权公告号：CN 117929376 B

专利申请日：2024年03月22日

授权公告日：2024年06月11日

申请日时申请人：华南农业大学

申请日时发明人：姜锐;欧媛珍;万欢;管宪鲁;廖娟;黄健斌;周志艳;罗锡文

国家知识产权局依照中华人民共和国专利法进行审查，决定授予专利权，并予以公告。

专利权自授权公告之日起生效。专利权有效性及专利权人变更等法律信息以专利登记簿记载为准。

局长
申长雨

申长雨

2024年06月11日

证书号第7189311号

专利公告信息

发明专利证书

发 明 名 称：一种原位半地埋式田间农情信息采集装置与方法

专 利 权 人：华南农业大学

地　　　址：510642 广东省广州市天河区五山路483号

发　明　人：姜锐;欧媛珍;管宪鲁;邓孔洪;蔡国奥;林衍承;周志艳
罗锡文

专　利　号：ZL 2024 1 0451200.2　　　授权公告号：CN 118050053 B

专利申请日：2024年04月16日　　　授权公告日：2024年07月12日

申请日时申请人：华南农业大学

申请日时发明人：姜锐;欧媛珍;管宪鲁;邓孔洪;蔡国奥;林衍承;周志艳
罗锡文

国家知识产权局依照中华人民共和国专利法进行审查，决定授予专利权，并予以公告。

专利权自授权公告之日起生效。专利权有效性及专利权人变更等法律信息以专利登记簿记载为准。

局长
申长雨

申长雨

2024年07月12日

证书号第5951457号

发明专利证书

发 明 名 称：一种多路差分多模卫星导航定位方法及装置

发　　明　　人：周志艳;姜锐;徐岩;汪沛;臧英;罗锡文;孔令熙

专　　利　　号：ZL 2017 1 1248657.X

专利申请日：2017年12月01日

专 利 权 人：华南农业大学

地　　　　址：510630 广东省广州市天河区五山

授权公告日：2023年05月09日　　　　授权公告号：CN 107957587 B

国家知识产权局依照中华人民共和国专利法进行审查，决定授予专利权，颁发发明专利证书并在专利登记簿上予以登记。专利权自授权公告之日起生效。专利权期限为二十年，自申请日起算。

专利证书记载专利权登记时的法律状况。专利权的转移、质押、无效、终止、恢复和专利权人的姓名或名称、国籍、地址变更等事项记载在专利登记簿上。

局长
申长雨

申长雨

2023年05月09日

其他事项参见续页

证书号第5951698号

发明专利证书

发明名称：一种基于主动光源的植物长势监测系统及应用方法

发明人：周志艳;姜锐;李克亮;何子玄;罗锡文

专利号：ZL 2017 1 0245874.7

专利申请日：2017年04月14日

专利权人：华南农业大学

地址：510642 广东省广州市天河区五山路483号

授权公告日：2023年05月09日　　授权公告号：CN 107219224 B

国家知识产权局依照中华人民共和国专利法进行审查，决定授予专利权，颁发发明专利证书并在专利登记簿上予以登记。专利权自授权公告之日起生效。专利权期限为二十年，自申请日起算。

专利证书记载专利权登记时的法律状况。专利权的转移、质押、无效、终止、恢复和专利权人的姓名或名称、国籍、地址变更等事项记载在专利登记簿上。

局长
申长雨

申长雨

2023年05月09日

其他事项参见续页

证书号第4147053号

发明专利证书

发明名称：一种液量监测装置及监测方法

发　明　人：周志艳;姜锐;罗锡文;兰玉彬;何新刚;明锐;徐岩

专　利　号：ZL 2017 1 0476751.4

专利申请日：2017年06月21日

专利权人：华南农业大学

地　　　址：510642 广东省广州市天河区五山路483号

授权公告日：2020年12月11日　　　　授权公告号：CN 107421598 B

国家知识产权局依照中华人民共和国专利法进行审查，决定授予专利权，颁发发明专利证书并在专利登记簿上予以登记。专利权自授权公告之日起生效。专利权期限为二十年，自申请日起算。

专利证书记载专利权登记时的法律状况。专利权的转移、质押、无效、终止、恢复和专利权人的姓名或名称、国籍、地址变更等事项记载在专利登记簿上。

局长
申长雨

申长雨

2020年12月11日

其他事项参见续页

证书号第6160397号

发明专利证书

发明名称：一种无人飞机低空遥感数据自适应分片处理算法

发　明　人：周志艳;周子滨;姜锐;何思敏;黄俊浩;罗锡文

专　利　号：ZL 2023 1 0452690.3

专利申请日：2023年04月25日

专利权人：华南农业大学

地　　址：510000 广东省广州市天河区五山路483号

授权公告日：2023年07月21日　　　　授权公告号：CN 116192242 B

国家知识产权局依照中华人民共和国专利法进行审查，决定授予专利权，颁发发明专利证书并在专利登记簿上予以登记。专利权自授权公告之日起生效。专利权期限为二十年，自申请日起算。

专利证书记载专利权登记时的法律状况。专利权的转移、质押、无效、终止、恢复和专利权人的姓名或名称、国籍、地址变更等事项记载在专利登记簿上。

局长
申长雨

申长雨

2023年07月21日

其他事项参见续页

证书号第7234403号

专利公告信息

发明专利证书

发 明 名 称：一种栅格参数可自定义的处方图生成方法

专 利 权 人：华南农业大学

地　　　址：510640 广东省广州市天河区五山路483号

发　明　人：周志艳;何思敏;姜锐;欧媛珍;邓孔洪;罗锡文

专　利　号：ZL 2024 1 0467480.6　　授权公告号：CN 118114951 B

专利申请日：2024年04月18日　　授权公告日：2024年07月26日

申请日时申请人：华南农业大学

申请日时发明人：周志艳;何思敏;姜锐;欧媛珍;邓孔洪;罗锡文

国家知识产权局依照中华人民共和国专利法进行审查，决定授予专利权，并予以公告。

专利权自授权公告之日起生效。专利权有效性及专利权人变更等法律信息以专利登记簿记载为准。

局长

申长雨

申长雨

2024年07月26日

报告编号	220861
总 页 数	共 14 页 第 1 页

检验报告

产品名称：TSL-Scanner 无人机载多光谱遥感传感器

产品型号：CTXGPNX01

生产单位：广州五山农业服务有限责任公司

委托单位：华南农业大学

检验类别：委托检验

广东省质量监督无人机检验站（河源）

注　意　事　项

1　报告无“检验检测专用章”无效。

2　报告无主检、审核、批准人签字无效。

3　复制报告未重新加盖“检验检测专用章”无效。

4　未经本单位批准，不得复制（全文复制除外）报告。

5　报告涂改无效。

6　一般情况，本次检验仅对来样负责。

7　对检验报告若有异议，应于收到报告之日起十五日内向广东省质量监督无人机检验站（河源）提出，经确认，需要复检的，按照复检程序进行处理；未反馈意见的，视为同意检验结果，逾期不予受理。

8　“-”表示不作判定。

地　　址：广东省河源市高新技术开发区科技大道

邮政编码：517001

技术咨询：0762-3607121/0762-3609333

传　　真：0762-3603336

电子邮箱：ncctmail@126.com

广东省质量监督无人机检验站（河源）

检 验 报 告

报告编号：220861　　　　　　　　　　　　　　　　　　　　　共 14 页 第 3 页

样品名称	TSL-Scanner 无人机载多光谱遥感传感器	样品型号	CTXGPNX01
商　　标	/	生产单位	广州五山农业服务有限责任公司
委托单位	华南农业大学	检验类别	委托检验
客户地址	广东省广州市天河区五山路 483 号		
送样者	华南农业大学	到样日期	2022.8.21
样品数量	1 套	样品等级	合格品
检验依据	华南农业大学检测委托合同书合同附件《TSL-Scanner 多光谱遥感传感器检测方案》。		
检验结论	本次检验依据华南农业大学检测委托合同书合同附《TSL-Scanner 多光谱遥感传感器检测方案》为测试方法，未规定限值，数据仅供参考，不作判定。 所检项目检测数据详见本报告第 7 页至第 13 页。 签发日期：2022 年 10 月 8 日		
备注	相关项目未取得资质认定，仅作为科研、教学或内部质量控制之用。		

批准：贺财鹏　　　　审核：周泽仕　　　　编制：林俊

检验报告

样品描述：

被检样品为 CTXGPNX01 型 TSL-Scanner 无人机载多光谱遥感传感器。

TSL-Scanner 多光谱遥感传感器技术参数（参考值）

尺寸	80×56×53（长×宽×高，mm）	接口	GPS、DLS（光照传感器）、串口
供电	4～36VDC（典型 2W）	镜头	FOV：60°，焦距：6.0 mm
电子快门	1/10 - 1/29000 s	影像传感器	5 个 128×1 线阵 CCD 传感器
光谱波段（5 个）	#1 蓝（中心 494nm,带宽 20nm）	触发模式	内部信号触发
	#2 绿（中心 532nm,带宽 20nm）	拼图速率	≥20 公顷/分钟
	#3 红（中心 653nm,带宽 20nm）	配套云台	DJI X-PORT
	#4 红边（中心 745nm,带宽 20nm）	适配无人机机型	DJI M210 RTK、M300 系列等
	#5 近红外(中心 843nm,带宽 20nm)	输出数据格式	GeoTIFF
空间分辨率（GSD）	1.5m @100m 飞行高度	数据坐标系	WGS-84
帧 率	10 FPS	数据处理方式	本地端配套软件
工作环境温度	0°C至 40°C	支持文件系统	FAT32（32 GB）

重要描述：

1、检测任务于 2022 年 8 月 21 日（星期日）09:00AM - 14:00PM 在华南农业大学增城教学科研基地进行。

2、检测设备 ASD Field spec3 光谱仪(型号：FS3 350-2500、制造商：ASD)、标准反射板（型号：500×500 漫反射目标板、制造商：广州景颐光电科技有限公司）和 RedEdge-M 多光谱遥感传感器（型号：RedEdge-M、制造商：MicaSense）由华南农业大学提供。

3、经核查检测设备 ASD Field spec3 光谱仪、标准反射板和 RedEdge-M 多光谱遥感传感器均有校准，且设备均在有效期内，经核查设备合格。

4、辅助设备无人机（型号：DJI M210 RTK V2、制造商：深圳市大疆创新科技有限公司）由华南农业大学提供。

检验描述：

一、检测项目

序号	检测项目		样品编号
1	通道光谱波长测试	适用	1#
2	动态反射率测试	适用	1#
3	拼图速度测试	适用	1#
4	植被指数相关性测试	适用	1#

二、检验日期

2022 年 8 月 21 日

时间段	检测任务
09:00AM-10:00AM	通道光谱波长测试
11:00AM-13:00PM	动态反射率测试
10:00AM-11:00AM、13:00PM-14:00PM	拼图速度测试
10:00AM-11:00AM、13:00PM-14:00PM	植被指数相关性测试

三、检验环境

温度：27 ℃～29 ℃　　相对湿度：65%～74%　　风速：1.45m/s～1.73m/s

四、辅助设备描述

设备名称:　无人机

设备型号:　DJI M210 RTK V2

设备串号:　/

制 造 厂:　深圳市大疆创新科技有限公司

连接方式:　通过 DJI X-PORT 云台连接

样 品 照 片
 图 1 被检样品外观图（TSL-Scanner 多光谱遥感传感器）
 图 2 被检样品试验图

检 测 结 果

检测项目一：通道光谱波长测试

测试时间：检测当日 9:00AM-10:00AM。

测试方法：采用 ASD Field spec3 光谱仪对 TSL-Scanner 多光谱遥感传感器的各通道滤光片进行峰值波长测试，各个通道分别采集 10 次数据取平均。对比机型为 RedEdge-M 多光谱遥感传感器，波长数据以其数据手册为准。通道光谱波长测试在室外太阳光下使用标准反射板进行。

计算指标：计算两个传感器各波段峰值波长实际数据并列表对比。

表 1 TSL-Scanner 与 RedEdge-M 各波段峰值波长（nm）

对比机型	#1 波段	#2 波段	#3 波段	#4 波段	#5 波段
TSL-Scanner	494.1	532.0	653.0	745.5	843.0
RedEdge-M	475.0	560.0	668.0	717.0	840.0

检测项目二：动态反射率测试

测试时间：检测当日 11:00AM-13:00PM。

测试方法：准备 10 块不同反射率的标准反射板，在太阳光下使用 TSL-Scanner 多光谱遥感传感器对反射板进行反射率数据采集，实时输出反射率数据。采样时间段为 11:00AM-13:00PM，每隔 24 分钟进行 1 组数据采集，一共 5 组，每组 10 次重复。反射率数据采集时传感器镜头的视场角需完全包含在标准反射板内。ASD Field spec3 的反射率对比数据在室内使用卤素光源进行采集，一共 5 组，每组 10 次重复。

计算指标：按光谱通道（#1 蓝光、#2 绿光、#3 红光、#4 红边光和#5 近红外光）计算两个对比传感器（仪器）的动态反射率数据 *MAE*（平均绝对误差）和 *RMSE*（均方根误差）作为测试指标。

$$MAE = \frac{\sum_{i=1}^{n}\left|y_{i-}x_i\right|}{n} \qquad (1)$$

$$RMSE=\sqrt{\frac{\sum_{i=1}^{n}(y_i-x_i)^2+....+(y_n-x_n)^2}{n}} \qquad (2)$$

y_i 为 TSL-Scanner 测得的反射率数据平均值，x_i 为 ASD Field spec3 测得的反射率数据平均值。

表 2 TSL-Scanner 测得的动态反射率数据（#1 蓝光波段）

测试组号	起始测试时间	标准反射板反射率									
		2%	10%	20%	30%	40%	50%	60%	70%	80%	90%
1	11:00 AM	0.090	0.152	0.220	0.307	0.454	0.533	0.632	0.735	0.835	0.936
2	11:24 AM	0.036	0.154	0.201	0.335	0.427	0.534	0.635	0.735	0.836	0.937
3	11:48 AM	0.012	0.146	0.254	0.384	0.435	0.534	0.636	0.747	0.848	0.937
4	12:12 PM	0.093	0.127	0.226	0.387	0.483	0.529	0.634	0.736	0.835	0.937
5	12:36 PM	0.091	0.193	0.241	0.340	0.416	0.521	0.628	0.734	0.835	0.936
平均值		0.064	0.154	0.228	0.351	0.443	0.530	0.633	0.737	0.838	0.937

表 3 TSL-Scanner 测得的动态反射率数据（#2 绿光波段）

测试组号	起始测试时间	标准反射板反射率									
		2%	10%	20%	30%	40%	50%	60%	70%	80%	90%
1	11:00 AM	0.093	0.144	0.272	0.378	0.413	0.521	0.663	0.747	0.849	0.947
2	11:24 AM	0.027	0.141	0.238	0.309	0.451	0.542	0.649	0.767	0.839	0.952
3	11:48 AM	0.032	0.147	0.238	0.363	0.420	0.549	0.648	0.780	0.872	0.957
4	12:12 PM	0.098	0.116	0.297	0.352	0.440	0.547	0.684	0.717	0.870	0.961
5	12:36 PM	0.099	0.197	0.224	0.313	0.482	0.535	0.615	0.757	0.849	0.907
平均值		0.070	0.149	0.254	0.343	0.441	0.539	0.652	0.754	0.856	0.945

表 4 TSL-Scanner 测得的动态反射率数据（#3 红光波段）

测试组号	起始测试时间	标准反射板反射率									
		2%	10%	20%	30%	40%	50%	60%	70%	80%	90%
1	11:00 AM	0.012	0.143	0.259	0.392	0.435	0.590	0.615	0.711	0.829	0.961
2	11:24 AM	0.023	0.138	0.263	0.372	0.448	0.568	0.613	0.741	0.810	0.968
3	11:48 AM	0.046	0.127	0.214	0.335	0.494	0.584	0.677	0.719	0.821	0.942
4	12:12 PM	0.017	0.112	0.273	0.341	0.454	0.548	0.682	0.786	0.859	0.939
5	12:36 PM	0.014	0.105	0.224	0.314	0.483	0.532	0.667	0.736	0.845	0.925
平均值		0.022	0.125	0.247	0.351	0.463	0.564	0.651	0.739	0.833	0.947

表 5 TSL-Scanner 测得的动态反射率数据（#4 红边光波段）

测试组号	起始测试时间	标准反射板反射率									
		2%	10%	20%	30%	40%	50%	60%	70%	80%	90%
1	11:00 AM	0.012	0.143	0.222	0.392	0.435	0.590	0.615	0.711	0.829	0.961
2	11:24 AM	0.028	0.161	0.275	0.328	0.443	0.545	0.618	0.781	0.859	0.920
3	11:48 AM	0.026	0.143	0.288	0.382	0.447	0.515	0.669	0.727	0.828	0.922
4	12:12 PM	0.079	0.110	0.237	0.314	0.441	0.544	0.653	0.777	0.850	0.939
5	12:36 PM	0.098	0.186	0.258	0.382	0.455	0.591	0.692	0.780	0.848	0.987
平均值		0.049	0.149	0.256	0.360	0.444	0.557	0.649	0.755	0.843	0.946

表 6 TSL-Scanner 测得的动态反射率数据（#5 近红外光波段）

测试组号	起始测试时间	标准反射板反射率									
		2%	10%	20%	30%	40%	50%	60%	70%	80%	90%
1	11:00 AM	0.012	0.143	0.242	0.392	0.435	0.590	0.615	0.711	0.829	0.961
2	11:24 AM	0.098	0.143	0.209	0.347	0.475	0.587	0.620	0.724	0.805	0.937
3	11:48 AM	0.055	0.158	0.220	0.310	0.464	0.510	0.618	0.794	0.837	0.939
4	12:12 PM	0.015	0.151	0.230	0.383	0.409	0.565	0.620	0.713	0.868	0.941
5	12:36 PM	0.019	0.110	0.207	0.381	0.434	0.575	0.639	0.742	0.885	0.916
平均值		0.040	0.141	0.222	0.363	0.443	0.565	0.622	0.737	0.845	0.939

表 7 ASD Field spec3 测得的动态反射率数据（#1 蓝光波段）

测试组号	标准反射板反射率									
	2%	10%	20%	30%	40%	50%	60%	70%	80%	90%
1	0.045	0.130	0.260	0.348	0.448	0.579	0.675	0.745	0.882	0.964
2	0.045	0.131	0.260	0.347	0.448	0.580	0.676	0.752	0.881	0.965
3	0.045	0.130	0.260	0.347	0.448	0.580	0.676	0.752	0.881	0.966
4	0.045	0.130	0.260	0.347	0.448	0.580	0.676	0.750	0.881	0.965
5	0.045	0.130	0.260	0.348	0.448	0.580	0.677	0.748	0.880	0.965
6	0.045	0.130	0.260	0.349	0.448	0.580	0.679	0.749	0.880	0.966
7	0.045	0.130	0.260	0.349	0.448	0.580	0.679	0.744	0.880	0.966
8	0.046	0.130	0.260	0.350	0.447	0.581	0.680	0.743	0.879	0.966
9	0.045	0.131	0.261	0.350	0.446	0.581	0.680	0.752	0.877	0.966
10	0.045	0.130	0.260	0.350	0.445	0.580	0.679	0.752	0.874	0.968
平均值	0.045	0.130	0.260	0.349	0.447	0.580	0.678	0.749	0.880	0.966

表 8 ASD Field spec3 测得的动态反射率数据（#2 绿光波段）

测试组号	标准反射板反射率									
	2%	10%	20%	30%	40%	50%	60%	70%	80%	90%
1	0.045	0.124	0.254	0.342	0.443	0.572	0.669	0.747	0.875	0.960
2	0.044	0.124	0.255	0.342	0.443	0.572	0.669	0.746	0.874	0.961
3	0.044	0.124	0.255	0.342	0.443	0.572	0.669	0.745	0.874	0.961
4	0.044	0.124	0.255	0.343	0.443	0.572	0.670	0.743	0.874	0.961
5	0.044	0.124	0.255	0.344	0.443	0.572	0.671	0.745	0.873	0.961
6	0.044	0.124	0.255	0.344	0.443	0.572	0.672	0.738	0.873	0.961
7	0.044	0.124	0.255	0.345	0.442	0.572	0.672	0.738	0.872	0.961
8	0.044	0.124	0.255	0.345	0.441	0.572	0.672	0.746	0.870	0.962
9	0.045	0.124	0.255	0.345	0.440	0.573	0.672	0.747	0.867	0.964
10	0.044	0.124	0.254	0.343	0.443	0.571	0.667	0.774	0.875	0.959
平均值	0.044	0.124	0.255	0.344	0.442	0.572	0.670	0.747	0.873	0.961

表 9 ASD Field spec3 测得的动态反射率数据（#3 红光波段）

测试组号	标准反射板反射率									
	2%	10%	20%	30%	40%	50%	60%	70%	80%	90%
1	0.050	0.127	0.254	0.347	0.444	0.568	0.668	0.740	0.863	0.947
2	0.050	0.127	0.255	0.346	0.444	0.569	0.669	0.747	0.862	0.948
3	0.049	0.127	0.255	0.346	0.444	0.569	0.669	0.746	0.862	0.948
4	0.049	0.126	0.255	0.346	0.444	0.569	0.669	0.745	0.862	0.949
5	0.049	0.127	0.255	0.347	0.444	0.569	0.670	0.743	0.861	0.949
6	0.049	0.127	0.255	0.348	0.444	0.569	0.671	0.745	0.861	0.949
7	0.049	0.127	0.255	0.348	0.443	0.569	0.672	0.738	0.861	0.949
8	0.049	0.127	0.255	0.348	0.443	0.569	0.673	0.738	0.860	0.950
9	0.049	0.127	0.255	0.348	0.442	0.570	0.673	0.746	0.858	0.950
10	0.049	0.127	0.255	0.349	0.441	0.570	0.672	0.747	0.855	0.952
平均值	0.049	0.127	0.255	0.347	0.443	0.569	0.671	0.744	0.861	0.949

表 10 ASD Field spec3 测得的动态反射率数据（#4 红边光波段）

测试组号	标准反射板反射率									
	2%	10%	20%	30%	40%	50%	60%	70%	80%	90%
1	0.055	0.134	0.263	0.360	0.454	0.575	0.681	0.747	0.856	0.938
2	0.055	0.134	0.263	0.359	0.454	0.575	0.681	0.755	0.856	0.938
3	0.055	0.134	0.263	0.359	0.454	0.576	0.682	0.754	0.855	0.939
4	0.055	0.134	0.263	0.359	0.454	0.576	0.682	0.753	0.855	0.939
5	0.055	0.134	0.263	0.360	0.454	0.576	0.682	0.751	0.855	0.939
6	0.054	0.135	0.264	0.361	0.454	0.576	0.684	0.752	0.854	0.939
7	0.054	0.135	0.264	0.361	0.453	0.576	0.685	0.746	0.854	0.940
8	0.055	0.135	0.264	0.362	0.453	0.576	0.685	0.746	0.853	0.940
9	0.040	0.135	0.264	0.362	0.452	0.576	0.685	0.754	0.851	0.940
10	0.055	0.135	0.264	0.362	0.451	0.576	0.684	0.755	0.848	0.943
平均值	0.053	0.135	0.264	0.361	0.453	0.576	0.683	0.751	0.854	0.940

表 11 ASD Field spec3 测得的动态反射率数据（#5 近红外光波段）

测试组号	标准反射板反射率									
	2%	10%	20%	30%	40%	50%	60%	70%	80%	90%
1	0.050	0.125	0.250	0.349	0.440	0.562	0.672	0.736	0.840	0.927
2	0.050	0.125	0.251	0.348	0.440	0.563	0.672	0.744	0.840	0.927
3	0.050	0.125	0.251	0.349	0.440	0.563	0.673	0.743	0.840	0.928
4	0.050	0.125	0.251	0.349	0.440	0.563	0.673	0.742	0.839	0.928
5	0.050	0.125	0.251	0.350	0.440	0.563	0.674	0.740	0.839	0.928
6	0.050	0.126	0.251	0.351	0.440	0.563	0.675	0.741	0.838	0.928
7	0.050	0.126	0.251	0.351	0.440	0.564	0.676	0.735	0.839	0.928
8	0.050	0.126	0.251	0.351	0.439	0.564	0.676	0.735	0.838	0.929
9	0.050	0.126	0.251	0.352	0.438	0.564	0.676	0.744	0.836	0.929
10	0.050	0.126	0.251	0.352	0.438	0.564	0.675	0.744	0.833	0.931
平均值	0.050	0.126	0.251	0.350	0.440	0.563	0.674	0.740	0.838	0.928

表 12 TSL-Scanner 与 ASD Field spec3 的动态反射率数据差异对比

指标	光谱通道				
	#1 蓝光波段	#2 绿光波段	#3 红光波段	#4 红边光波段	#5 近红外光波段
平均绝对误差/*MAE*	0.026	0.015	0.012	0.013	0.015
均方根误差/*RMSE*	0.043	0.026	0.022	0.024	0.029

检测项目三：拼图速度测试

测试时间：检测当日 10:00AM-11:00AM，13:00PM-14:00PM。

测试方法：使用 RedEdge-M 多光谱遥感传感器与 TSL-Scanner 多光谱遥感传感器进行拼图速度对比测试，两款无人机遥感平台对同一地块进行遥感作业，试验在华南农业大学增城教学科研基地进行。RedEdge-M 传感器使用 DJI 悟 1 搭载飞行，飞行速度为 10 m/s，高度为 100 m，旁向重叠为 75%。TSL-Scanner 传感器使用 DJI M210 RTK 搭载飞行，飞行速度为 10 m/s，高度为 100 m。RedEdge-M 采用 PIX4D 进行图像拼接，TSL-Scanner 采用配套软件拼接。每次拼接完成后使用 QGIS 软件对实际遥测面积进行统计。对比试验重复 6 次，上午 3 次（试验序号 1-3），下午 3 次（试验序号 4-6）。拼图软件使用同一软硬件资源的计算机（CPU: Intel Core i7 12700K, RAM: 32 GB, 显卡 GTX1050Ti, 操作系统：Windows 10 64 Bit）进行处理。

计算指标：计算两个传感器单位时间内拼图速度（公顷/分钟）

$$S = \frac{AREA}{T}$$

式中：S 为拼接速度（公顷/分钟，ha/min），$AERA$ 为实际遥测面积（公顷/ha），T 为拼接耗费时间（分钟/min）。

表 13 TSL-Scanner 与 RedEdge-M 多光谱遥感传感器图像拼接速度（ha/min）

对比机型	参数	试验序号					
		1	2	3	4	5	6
RedEdge-M	面积/公顷（ha）	44.441	44.995	43.592	44.033	44.432	43.205
	处理耗时（min）	47.783	40.183	28.633	35.017	32.550	36.733
	拼接速度（ha/min）	0.931	1.119	1.519	1.259	1.366	1.177
TSL-Scanner	面积/公顷（ha）	38.084	38.582	39.021	39.121	39.249	39.380
	处理耗时（min）	1.010	1.013	1.043	1.030	1.040	1.017
	拼接速度（ha/min）	37.707	38.087	37.412	37.982	37.739	38.722

检测项目四：植被指数相关性测试

测试时间：检测当日 10:00AM-11:00AM，13:00PM-14:00PM。

测试方法：将 RedEdge-M 多光谱遥感传感器与 TSL-Scanner 多光谱遥感传感器进行植被指数对比测试，试验采用检测项目三中获取的遥感数据，每个传感器有 6 组遥感影像（对应试验序号 1-6），对每组遥感影像随机提取 10 个地物（包括裸地、植被、路面）进行植被指数对比，包括有 NDVI、SAVI 和 EVI。

计算指标：计算两个传感器三个植被指数数据的决定系数 R^2 作为测试指标。

表 14 植被指数集

指数	公式	备注
NDVI	$\frac{\text{NIR-R}}{\text{NIR+R}}$	#1=B、#3=R、#5=NIR
SAVI	$1.5\times\frac{NIR-R}{NIR+R+0.5}$	
EVI	$\frac{2.5\times(\text{NIR-R})}{\text{NIR}+6\times\text{R}-7.5\times\text{B}+1}$	

表 15 TSL-Scanner 与 RedEdge-M 多光谱遥感传感器植被指数相关性分析

试验序号	植被指数	相关性（决定系数） R^2
1	NDVI	0.820
	SAVI	0.879
	EVI	0.751
2	NDVI	0.862
	SAVI	0.933
	EVI	0.817
3	NDVI	0.936
	SAVI	0.966
	EVI	0.921
4	NDVI	0.783
	SAVI	0.898
	EVI	0.840
5	NDVI	0.813
	SAVI	0.911
	EVI	0.801
6	NDVI	0.860
	SAVI	0.923
	EVI	0.955

检验仪器设备清单

序号	设备名称	型号、规格	设备编号	本次使用
1	风速计	AVM-07	E0295	√
2	计时器	SEWAN	E0117-7	√
3	ASD Field spec3 光谱仪*	FS3 350-2500	/	√
4	标准反射板*	500×500 漫反射目标板	/	√
5	RedEdge-M 多光谱遥感传感器*	RedEdge-M	/	√

注：1.“√”为本次试验使用仪器、设备，空白表示本次试验未使用的仪器、设备。

2.所有仪器设备均在有效期内。

3.设备名称中带“*”号的检测仪器设备由华南农业大学提供。

————————————

此为报告最后一页

广东省发展改革委

发布者：科学研究院 发布时间：2025-07-04 浏览次数： 36

序号	平台名称	成立时间	批准部门	所在学院
1	广东省人兽共患病防控制剂工程实验室	2010. 12	广东省发改委	兽医学院
2	大田作物种植智能化装备广东省工程研究中心	2024. 07	广东省发改委	工程学院

广东省工程研究中心

组建方案

中心名称： 大田作物智能化种植装备广东省工程研究中心

承担单位： 华南农业大学、华南农业大学黄埔创新研究院

联系地址： 广州市天河区五山路483号

邮政编码： 510642

负 责 人： 罗锡文

联 系 人： 王在满

联系电话： 13642730710

电子邮箱： wangzaiman@scau.edu.cn

填报时间： 2023年11月18日

广东省工程研究中心申报数据表

（高等院校和科研院所填报）

申报的省工程研究中心或依托单位（盖章） 填表时间： 2023 年 11 月 18 日

省工程研究中心名称	广东省大田作物智能化种植装备工程研究中心		
所属战略性新兴产业	高端装备制造产业—智能装备制造产业		
建设总投资	600万元	建设期	2023年11月-2026年12月
运行模式	☑法人实体 □非法人实体		
申报的省工程研究中心		依托单位	
法定代表人或主要负责人	罗锡文	依托单位名称	华南农业大学
技术带头人	罗锡文	法定代表人	薛红卫
联系人	王在满	联系人	李根
联系电话	13642730710	联系电话	18819266170
地址	广州市天河区五山路483号	单位地址	广州市天河区五山路483号

省工程研究中心基本数据

序号	类别	数据名称	单位	数据	备注（数据来源）
一	依托单位情况	年度科研经费	万元	1810	附表：省工程研究中心科研经费收入统计表
		其中：横向科研经费	万元	365	
二	省工程研究中心基础条件	研发人员数	人	76	附表：省工程研究中心研发人员汇总表
		其中，高级专家	人	17	
		其中，博士	人	21	
		研发设备原值	万元	5000	附表：省工程研究中心研发设备原值汇总表
		研发场地面积	平方米	10000	附表：省工程研究中心研发场地统计表
		主持（承担）过省级以上科研项目数量	人	15	附表：省工程研究中心科研项目汇总表
		主持（参与）国际、国家与行业标准数量	项	3	附表：省工程研究中心主持或参与制定标准汇总表
三	成果与行业贡献	拥有有效发明专利数（含软件和集成电路布图设计）	项	105	附表：省工程研究中心发明专利汇总表
		近三年授权发明专利	项	75	
		有效PCT发明专利数	项	1	
		年度被受理的发明专利申请数	项	45	
		近三年专利所有权转让及许可收入	万元	241.3	附表：省工程研究中心专利所有权转让及许可收入汇总表
四	加分项	近三年国家、省部级奖项	项	11	附表：省工程研究中心获国家和省部级奖励汇总表

备注：

1．年度指标为2022年度全年数据。

2．所属战略性新兴产业：新一代信息技术产业、高端装备制造产业、新材料产业、生物产业、新能源汽车产业、节能环保产业、数字创意产业、相关服务业。

3．省工程研究中心负责人须全职在省工程中心工作。

4．省工程研究中心依托单位只能有1家。

目录

一、项目摘要……1
二、项目建设的依据、背景与意义……3
1 项目建设的依据……3
2 项目建设的背景……4
3 项目建设的意义……4
三、技术发展与应用前景分析……5
1 国内外技术发展现状与趋势预测分析……5
2 技术发展的比较……7
四、主要方向、任务与目标……10
1 广东省工程研究中心拟突破的技术方向……10
  1.1 大田作物智能化种植装备共性技术……10
  1.2 水稻智能化种植关键技术与装备……10
  1.3 蔬菜智能化种植关键技术与装备……10
2 广东省工程研究中心的主要功能与任务……10
  2.1 主要功能……10
  2.2 主要任务……11
3 广东省工程研究中心的近期和中期目标……13
  3.1 近期目标（2023年-2026年）：……13
  3.2 中期目标（2026年-2030年）：……14
五、组织机构、管理与运行机制……14
1 项目单位概况……14
2 广东省工程研究中心的机构设置与职责……17
  2.1 工程研究中心机构设置……17
  2.2 工程中心主要职责……18
3 主要技术带头人、管理人员概况及技术团队情况……20
  3.1 带头人情况及管理人员概况……20
  3.2 技术团队概况……26
4 运行和管理机制……30
  4.1 中心负责人制度……30
  4.2 人员聘任和考核制度……30
  4.3 考核内容……30

4.4 人员聘任程序......30
4.5 其他管理机制......30
六、筹建期建设方案......31
1 建设内容、建设规模与建设地点......31
2 项目招标方案......36
七、节能与环境影响......37
1 节能分析......37
2 环境影响评价......37
八、项目实施进度与管理......38
1 建设周期......38
2 项目实施进度与管理......38
3 建设期的项目管理......38
九、投资估算及资金筹措方案......39
1 项目总投资估算表......39
2 建设投资估算......39
3 分年度投资计划表......39
4 项目资金筹措方案及其落实情况......40
十、项目经济和社会效益分析......40
1 经济效益分析......40
2 社会效益分析......41
十一、项目风险分析......41
1 技术风险......41
2 技术应用及市场风险......41
3 其它风险......42
十二、其他需说明的问题......42
十三、相关附件、附图和附表......42
附录一：近三年开展研究主要项目情况......43
附录二：近三年开展产学研合作情况......46
附录三：近5年授权发明专利情况......48
附录四：获得科学技术奖励情况......53
附录五：近五年技术成果转化情况......54
附录六：近五年发表学术论文......55
附录七：标准编制情况......62

3.2 技术团队概况

团队由华南农业大学和华南农业大学黄埔创新研究院的专家和技术人员组成，共有研发人员76人，其中专职人员32人，博/硕士研究生44人，高级职称17人，中级职称7人，有博士学位人员21人；。团队拥有中国工程院院士1人、国家产业技术体系岗位科学家4人（副首席1人）、青年长江学者1人、农业部神农英才3人、广东省杰青2人、广东省蔬菜产业技术体系首席专家1人。

研究团队王在满、臧英、杨文武、张明华、何杰等作为华南农业大学派驻华南农业大学黄埔创新研究院的技术高管在研究院兼职工作多年，目前均是研究院主要负责人，在水稻蔬菜智能化种植技术与装备研究与生产制造等方面具有丰富实践经验。工程研究中心组建的研究队伍是一支集成科学研究、技术开发、生产制造的优秀团队，完全具备完成中心建设目标和各项任务的能力。

工程中心主要研究人员表

序号	姓名	性别	年龄	职称	职务	学历	专业
1	罗锡文	男	78	教授	主任	硕士	农业机械化工程
2	王在满	男	44	研究员	副主任	博士	农业机械化工程
3	杨文武	男	40	副教授	副主任	博士	农业机械化工程
4	张明华	男	36	副研究员	副主任	博士	农业机械化工程
5	臧英	女	50	教授	骨干	博士	农业机械化工程
6	辜松	男	60	教授	骨干	博士	农业机械化工程
7	曾山	男	50	研究员	骨干	博士	农业机械化工程
8	周志艳	男	51	教授	骨干	博士	农业机械化工程

9	胡炼	男	38	教授	骨干	博士	农业电气化工程
10	齐龙	男	44	教授	骨干	博士	农业电气化工程
11	张智刚	男	46	副教授	骨干	博士	农业电气化工程
12	夏红梅	女	48	教授	骨干	博士	农业电气化工程
13	何杰	男	39	高级实验师	骨干	博士	农业电气化工程
14	李杰浩	男	34	副教授	骨干	博士	控制科学与工程
15	汪沛	女	40	副教授	骨干	博士	农业电气化工程
16	廖娟	女	36	讲师	骨干	博士	农业电气化工程
17	张闻宇	男	38	讲师	骨干	博士	农业工程
18	黄培奎	男	34	副教授	骨干	博士	农业电气化工程
19	姜锐	男	30	副教授	骨干	博士	农业电气化工程
20	秦伟	男	29	博士后	骨干	博士	农业电气化工程
21	何剑飞	男	44	实验师	骨干	博士	农业机械化工程
22	汪隽	男	32	中级	骨干	硕士	工业设计
23	贾维卿	男	43	中级	骨干	博士	微电子学
24	覃兴谋	男	41	无	骨干	本科	农学
25	林嘉辉	男	28	无	骨干	本科	农业机械化
26	黎观炯	男	25	无	骨干	本科	农业机械化
27	吴淦泓	男	25	无	骨干	本科	工业设计
28	万岩伏	男	22	无	技术员	中专	农机制造
29	杨超	男	22	无	技术员	中专	农机制造
30	刘琳	男	28	无	技术员	大专	农村机电
31	吴林嵘	男	23	无	技术员	大专	计算机科学

广东省农业技术推广奖

获奖证书

为表彰在农业技术推广工作中做出贡献的单位和个人，特颁发此证书，以资鼓励。

获奖项目：农用无人飞机作业关键技术研发及推广应用

奖励等级：一等奖

奖励个人：姜 锐

奖励日期：2022年12月15日

证 书 号：2021-1-N02-R05

广东省农业技术推广奖
评审委员会

荣誉证书

CERTIFICATE OF HONOR

姜锐：

在广州农村科技特派员大赛中荣获

优秀农村科技特派员

广州产业投资控股集团
有限公司

广州市科技进步
基金会

广州生产力促进中心
有限公司

2024年1月25日

证书编号：20241217003

科学技术成果评价证书

中农工（评价）字[2024]第3号

成果名称： 基于农用无人飞机的水稻智能化作业关键技术及应用

完成单位： 华南农业大学、深圳市大疆创新科技有限公司、中国农业大学、袁隆平农业高科技股份有限公司、北京市农林科学院信息技术研究中心、广东省农业技术推广中心、农业农村部南京农业机械化研究所、广东天禾农资股份有限公司、广东万绿智慧农业科技有限公司、广州五山农业服务有限责任公司

主要完成人： 周志艳、罗锡文、何雄奎、姜锐、臧英、姚俊豪、徐波、刘爱民、刘燕、罗国武、宋坚利、汪沛、廖娟、张青、王飞钊、王键宽、林键沁、欧媛珍

成果水平： 整体达到国际先进水平，其中在水稻长势低空遥感监测解析技术、无人飞机变量精准施肥技术方面达到国际领先水平

发证日期： 2024年12月17日

评价机构： 中国农业工程学会

今欲振中國
在廣人才
欲廣人才
在興學會
欲興農學
則農學會之才
不可勝用也

梁啓超

聘书

姜 锐 同志：

兹聘任您为**中国农学会农业信息分会**委员，聘期自 2024 年 1 月至 2029 年 1 月。

中国农学会
2024 年 1 月

证 书

姜锐 同志：

经中国农业机械学会农业航空分会换届会议选举，您当选为中国农业机械学会农业航空分会第二届委员会副秘书长（2021~2025年）。

特颁此证。

证书编号：CSAM/BR17-014

中国农业机械学会
2022年12月1日

授　予

华南农业大学南方农业机械与装备
关键技术教育部重点实验室团队：

第二十五届“广东青年五四奖章集体”。

共青团广东省委员会　广东省青年联合会
二〇二三年五月

我院教师团队获评2022广东农技服务“轻骑兵”十大先锋队伍及十大典型服务案例

发布者：园艺学院 发布时间：2022-12-16 浏览次数： 90

12月12日，第二十一届广东种业大会暨2022世界数字农业大会在广州隆重举行。会上，备受瞩目的2022广东农技服务“轻骑兵”年度评选结果揭晓，我院胡桂兵教授荔枝团队荣获2022“轻骑兵”十大先锋队伍，陈厚彬研究员服务茂名荔枝产业的案例荣获2022“轻骑兵”十大典型服务案例。

由广东省农业技术推广中心组织的2022广东农技服务评选活动包括“轻骑兵”“十大先锋人物、十大先锋队伍、十大典型服务案例、十大典型服务模式”四大奖项，40个席位。经过全省推选，我校在评选中成绩喜人，40个席位中占据7个，除了我院获评先锋队伍和典型服务案例外2个外，电子工程学院（人工智能学院）岳学军教授荣获2022“轻骑兵”十大先锋人物；工程学院罗锡文院士智慧农业团队荣获2022“轻骑兵”十大先锋队伍；由我校创建的“1+1+N”共同体模式、产学研三位一体温氏服务模式、“轻骑兵+电商+金融”新农院茂名分院服务模式荣获2022“轻骑兵”十大服务模式。

我院一直以来高度重视农业技术推广工作,今后将持续发力加强农业技术推广,更好地服务于“三农”，促进农村稳定，农业增效，农民增收，助力乡村振兴。

2022 广东农技服务“轻骑兵”十大先锋人物、十大先锋队伍

团队负责人：罗锡文院士

团队主要成员：臧英、周志艳、王在满、胡炼、曾山、张智刚、杨文武、汪沛、何杰、张明华、廖娟、张闻宇、姜锐等。

工作照片：


田间科技小院


华南农业大学高端创新研究院庆祝中国农民丰收节（广州大吉沙岛）

中央宣传部公布2021年全国文化科技卫生“三下乡”活动示范项目、优秀团队、服务标兵名单

2022-02-25 07:49　来源：　新华社

新华社北京2月24日电　近日，中央宣传部公布2021年全国文化科技卫生“三下乡”活动示范项目、优秀团队、服务标兵名单，推选四川省民法典走进乡村（社区）“三个一百”主题宣讲活动等102个项目为示范项目，“天津市人民满意的好医生走基层送健康”志愿服务团队等102个集体为优秀团队，哈亦琦等102名个人为服务标兵。

党的十八大以来，各地各有关部门坚持以习近平新时代中国特色社会主义思想为指导，从农村实际和农民需要出发，引导动员社会力量广泛参与“三下乡”活动，形成了一大批工作基础好、带动效应强的优质项目，涌现出一大批深入农村基层、热情服务群众的先进典型，为促进农业高质高效、乡村宜居宜业、农民富裕富足贡献重要力量。“三下乡”活动日益成为助力全面推进乡村振兴的民心工程，成为深化农村思想道德建设和精神文明建设的响亮品牌。

为总结经验、激励先进，2021年，中央宣传部、中央文明办、国家发展改革委、教育部、科技部、司法部、农业农村部、文化和旅游部、国家卫生健康委、广电总局、国家乡村振兴局、共青团中央、全国妇联、中国文联、中国科协组织开展了全国文化科技卫生“三下乡”示范项目、优秀团队、服务标兵推介展示活动。此次公布的示范项目、优秀团队、服务标兵，涵盖理论宣讲、文化惠民、科技兴农、健康义诊、法治宣传等领域，工作基础好、群众评价高、带动效应强，充分展现了“三下乡”活动取得的丰硕成果和显著成效。

中央宣传部要求，各地各有关部门要抓住用好此次推介展示活动的有利契机，进一步加强组织领导，加大投入力度，出台扶持政策，完善工作机制，推动“三下乡”活动提质扩面、提档升级，汇聚起农民群众创造美好生活、实现共同富裕的强大精神力量，以实际行动迎接党的二十大胜利召开。

2021年全国文化科技卫生“三下乡”活动示范项目名单

（共102个）

北京市

北京农民艺术节

“到人民中去”文艺志愿服务

科普驿站助力乡村振兴

天津市

水稻基质育秧技术示范推广项目

天津市眼科医院社区志愿服务直通车

实施“法律明白人”培养工程

河北省

基层科普行动计划

河北医科大学乡村医师学院医疗惠民服务项目

国网河北电力石家庄市平山县乡村电气化示范项目

山西省

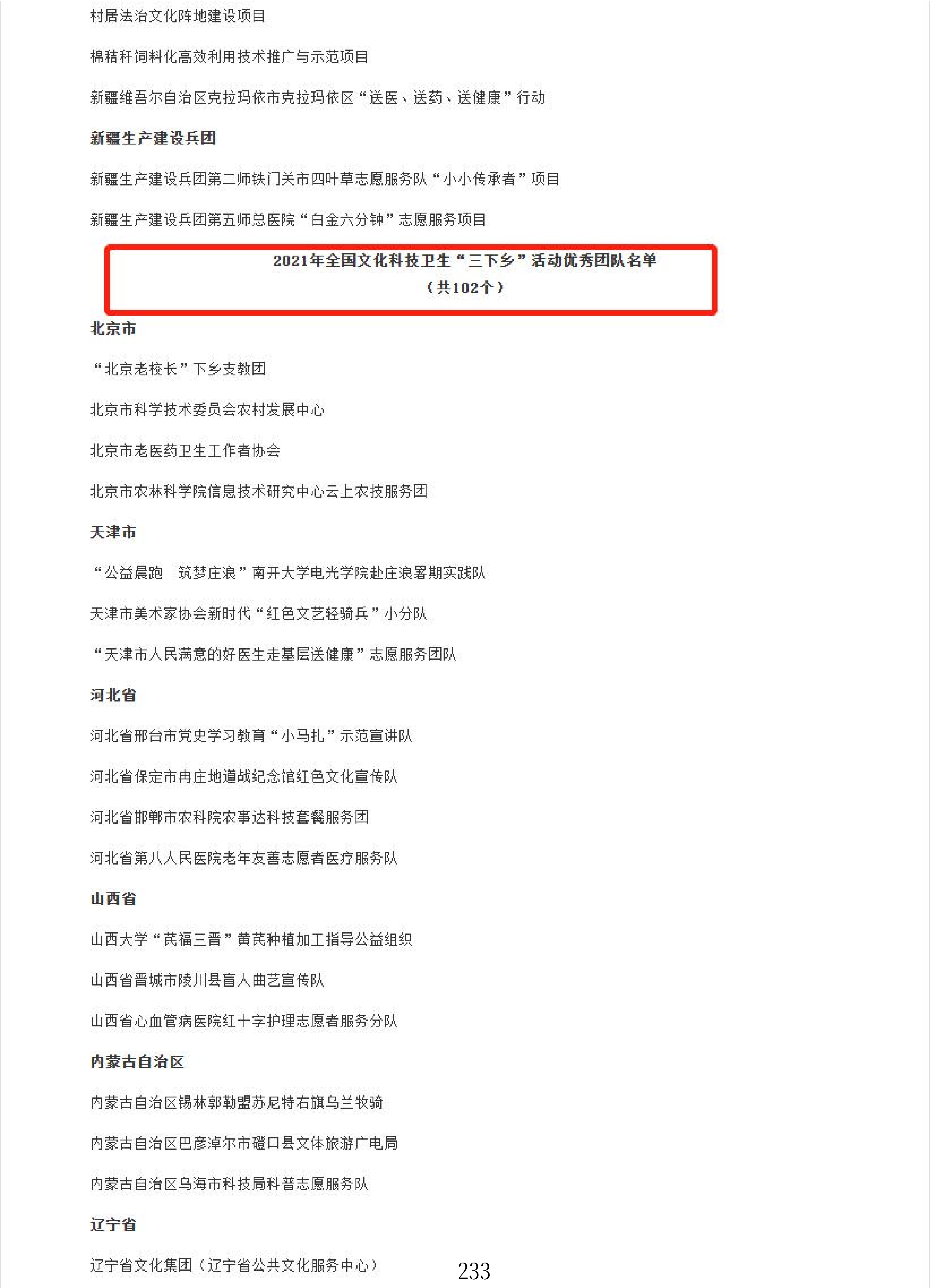

村居法治文化阵地建设项目

棉秸秆饲料化高效利用技术推广与示范项目

新疆维吾尔自治区克拉玛依市克拉玛依区“送医、送药、送健康”行动

新疆生产建设兵团

新疆生产建设兵团第二师铁门关市四叶草志愿服务队“小小传承者”项目

新疆生产建设兵团第五师总医院“白金六分钟”志愿服务项目

2021年全国文化科技卫生“三下乡”活动优秀团队名单

（共102个）

北京市

“北京老校长”下乡支教团

北京市科学技术委员会农村发展中心

北京市老医药卫生工作者协会

北京市农林科学院信息技术研究中心云上农技服务团

天津市

“公益晨跑　筑梦庄浪”南开大学电光学院赴庄浪暑期实践队

天津市美术家协会新时代“红色文艺轻骑兵”小分队

“天津市人民满意的好医生走基层送健康”志愿服务团队

河北省

河北省邢台市党史学习教育“小马扎”示范宣讲队

河北省保定市冉庄地道战纪念馆红色文化宣传队

河北省邯郸市农科院农事达科技套餐服务团

河北省第八人民医院老年友善志愿者医疗服务队

山西省

山西大学“芪福三晋”黄芪种植加工指导公益组织

山西省晋城市陵川县盲人曲艺宣传队

山西省心血管病医院红十字护理志愿者服务分队

内蒙古自治区

内蒙古自治区锡林郭勒盟苏尼特右旗乌兰牧骑

内蒙古自治区巴彦淖尔市磴口县文体旅游广电局

内蒙古自治区乌海市科技局科普志愿服务队

辽宁省

辽宁省文化集团（辽宁省公共文化服务中心）

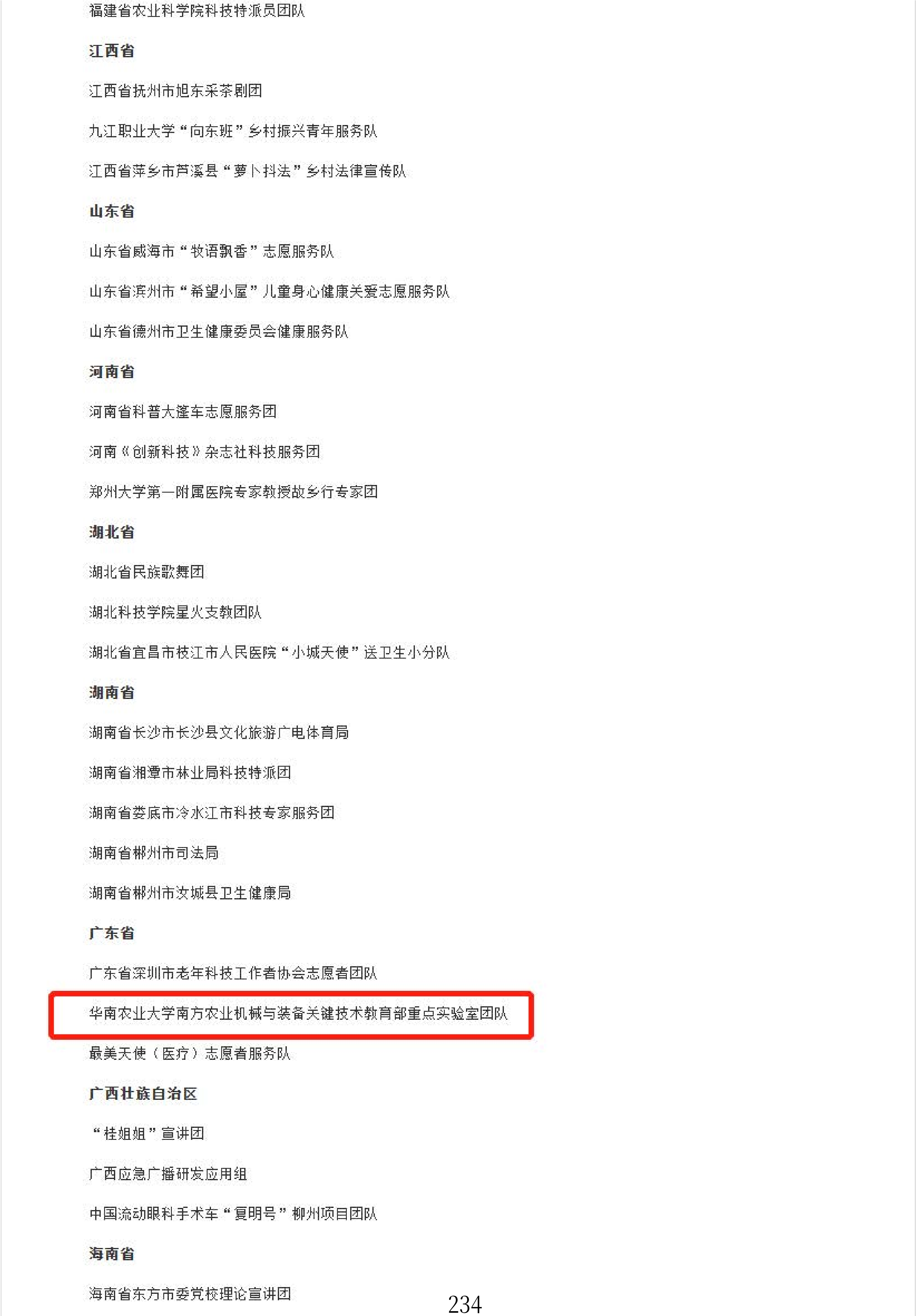

福建省农业科学院科技特派员团队

江西省

江西省抚州市旭东采茶剧团

九江职业大学“向东班”乡村振兴青年服务队

江西省萍乡市芦溪县“萝卜抖法”乡村法律宣传队

山东省

山东省威海市“牧语飘香”志愿服务队

山东省滨州市“希望小屋”儿童身心健康关爱志愿服务队

山东省德州市卫生健康委员会健康服务队

河南省

河南省科普大篷车志愿服务团

河南《创新科技》杂志社科技服务团

郑州大学第一附属医院专家教授故乡行专家团

湖北省

湖北省民族歌舞团

湖北科技学院星火支教团队

湖北省宜昌市枝江市人民医院“小城天使”送卫生小分队

湖南省

湖南省长沙市长沙县文化旅游广电体育局

湖南省湘潭市林业局科技特派团

湖南省娄底市冷水江市科技专家服务团

湖南省郴州市司法局

湖南省郴州市汝城县卫生健康局

广东省

广东省深圳市老年科技工作者协会志愿者团队

华南农业大学南方农业机械与装备关键技术教育部重点实验室团队

最美天使（医疗）志愿者服务队

广西壮族自治区

“桂姐姐”宣讲团

广西应急广播研发应用组

中国流动眼科手术车“复明号”柳州项目团队

海南省

海南省东方市委党校理论宣讲团

蓝桥杯大赛

获奖证书

华南农业大学尹旺奎：

荣获第十五届蓝桥杯全国软件和信息技术专业人才大赛广东赛区C/C++程序设计大学B组一等奖。

特发此证，以资鼓励。

证书编号：021505090

证件号码：361130200409228012

工业和信息化部
人才交流中心

1101081336207

蓝桥杯大赛组委会

2024年4月29日

获奖证书

CERTIFICATE OF AWARD

在 2024 年“丁颖杯”广东大学生课外学术科技作品竞赛工程学院院内选拔赛中，

荣获

一 等 奖

特发此证，以资鼓励。

项目名称：原位半地埋式田间农情信息采集装置

获奖学生：尹旺奎 李里鹏 黄健斌 梁浩伟 林涵 尹伯文 蒋生迪

指导教师：姜锐

华南农业大学工程学院

二〇二四年十月

获奖证书

CERTIFICATE OF AWARD

在 2024 年海格电气杯华南农业大学第十届国际大学生智能农业装备创新大赛中，荣获

一 等 奖

特发此证，以资鼓励。

项目名称： 低空机载式单目高分多光谱遥感传感器

获奖学生： 欧媛珍、林键沁、邓孔洪、王焕宇、雷景行

指导教师： 姜锐

华南农业大学工程学院

二零二四年十月

華南農業大學
South China Agricultural University

大学生创新创业训练计划
项目申报书模板

项目名称 基于自主感知决策执行的电动自行车座垫防护系统研究

项目类型 ☑创新训练项目□创业训练项目□创业实践项目

所在学院 工程学院

项目负责人 严创稀

项目负责人学号 202321110124

指导教师 姜 锐

起止年月 2024年5月—2025年11月

华南农业大学创新创业学院 制

二〇二四年五月

一、 基本情况

项目名称	基于自主感知决策执行的电动自行车座垫防护系统研究						
所属学科	自动化类						
项目来源	☑ A、学生自主选题，来源于自己对课题的长期积累与兴趣 □ B、学生来源于教师科研项目选题 □ C、学生承担社会、企业委托项目选题 □ D、拔尖专项 □ E、竞赛专项 □ F、研修专项						
申请金额	0.5万元	项目期限	1.5年	拟申报项目级别		省级	
负责人	严创稀	性别	男	民族	汉	出生年月	2005年8月
学号	202321110124	联系电话	19902421252				
指导教师	姜 锐	联系电话	13424049263				
项目简介	电动自行车的核心关键技术近年来得到迅猛发展，作为一种短途便捷式低碳交通工具，极大地方便了人们的出行。目前，全国电动自行车保有量达到了 4.2 亿辆，其中共享电动自行车超过 200 万辆，相关企业也达到约 2000 家。然而，在如此大的市场规模下，电动自行车的座垫保护和保养装置和产品少有报道，不计其数的座垫遭受了阳光暴晒和雨水侵蚀的影响，座垫表面皮革包裹层出现老化皲裂的情况屡见不鲜，骑行舒适度也大打折扣。因此，针对这个问题，项目组拟研究一款电动自行车座垫自动保护装置，设计基于天气情况自主感应的车座保护机制，实现对车座防雨、防晒等主动保护，从而解决现在市场上电动自行车，特别是共享电动自动车的座垫易损问题，提高座垫的使用寿命，降低电动自行车的维护成本。						

<table>
<tr><td>负责人曾经参与科研的情况</td><td colspan="6">项目负责人严创稀目前已经加入华南农业大学工程学院农业航空实验室，正在参与相关科研项目的研发过程。</td></tr>
<tr><td>指导教师承担科研课题情况</td><td colspan="6">[1] 国家自然科学基金青年基金项目，32301707，国家自然科学基金委员会，项目主持，在研
[2] 国家重点研发计划子课题，2022YFD200150102，中华人民共和国科技部，项目主持，在研
[3] 广东省自然科学基金-面上项目，广东省科学技术厅，项目主持，在研
[4] 广州市重点研发计划课题，2024B03J1356，广州市科学技术局，项目主持，在研
[5] 吉安市重点研发计划课题，20211-055312，吉安市科学技术局，项目主持，在研</td></tr>
<tr><td>指导教师对本项目的支持情况</td><td colspan="6">指导教师认可学生团队的自主选题，承诺在项目实施期间，为项目团队成员提供该项目开展所需的试验研究场地、测试仪器设备和技术指导，并积极推动目标成果的推广应用。</td></tr>
<tr><td rowspan="7">项目组主要成员</td><td>姓名</td><td>学号</td><td>学院</td><td>专业班级</td><td>联系电话</td><td>项目分工</td></tr>
<tr><td>严创稀</td><td>202321110124</td><td>工程学院</td><td>农业机械化及其自动化1班</td><td>19902421252</td><td>统筹项目</td></tr>
<tr><td>黄健斌</td><td>202321120107</td><td>工程学院</td><td>农业机械化及其自动化丁颖创新班</td><td>15218551581</td><td>结构设计或者测试</td></tr>
<tr><td>梁浩伟</td><td>202321120110</td><td>工程学院</td><td>农业机械化及其自动化丁颖创新班</td><td>13059321684</td><td>电控系统设计</td></tr>
<tr><td>林焯枫</td><td>202321120113</td><td>工程学院</td><td>农业机械化及其自动化丁颖创新班</td><td>18923061218</td><td>机械结构优化</td></tr>
<tr><td>林衍承</td><td>202321120112</td><td>工程学院</td><td>农业机械化及其自动化丁颖创新班</td><td>13420365547</td><td>软件与小程序开发</td></tr>
<tr><td>尹旺奎</td><td>202321110224</td><td>工程学院</td><td>农业机械化及其自动化2班</td><td>15707071439</td><td>试验器件准备与测试</td></tr>
<tr><td>指导教师</td><td>姜 锐</td><td>30005232</td><td>工程学院</td><td>/</td><td>13424049263</td><td>项目实施指导</td></tr>
</table>

（4）预期成果：

表 1 预期成果及完成时间

完成时间	**成果名称**	**成果形式**
2024年10月	一种自动保护电动自行车座垫的装置与方法	专利
2024年12月	一种自动保护电动自行车座垫的装置	样机
2025年2月	远程控制保护装置小程序	小程序
2025年4月	《关于电动自行车座垫自动保护装置使用的调研报告》	调研报告
2025年11月	《基于电动自行车座垫自动保护装置的研究》	论文（核心）

6. 项目研究进度安排

表 2 项目研究计划表

2024年5月-6月	购买组装电动自行车座垫自动保护装置的材料，并熟悉试验器材，组装设备
2024年7月-9月	软件设计和电机调试
2024年10月-12月	将设备在试验室进行调试
2025年1月-3月	将设备投放至室外，进行实地测试，收集试验数据
2025年4月-5月	试验数据分析，检查装置有无问题，进行完善
2025年6月-8月	试验资料整理，撰写并发表论文，申请专利
2025年9月-11月	准备结题和答辩

7. 已有基础

（1）与本项目有关的研究积累和已取得的成绩

关于电动自行车座垫保护装置的研究，项目组成员已经具备较扎实的技术基础。以下是项目组成员具备的技能、学过的课程、参加的竞赛以及获奖项目等。

序号	姓名	已有基础
1	尹旺奎	获得2024年第十五届蓝桥杯软件赛C/C++程序设计大赛大学B组省一等奖，学过html，css，javascript等课程并对此具备较高的掌握程度。
2	严创稀	熟练使用AUTO CAD 2023 ，精通多种机械结构的维修与构建搭配，拥有一定的焊接技术能熟练焊接ESC与飞塔。
3	林焯枫	熟悉Soildworks、CATIA，具备一定的建模能力，可以设计完成建模。
4	梁浩伟	熟悉STM32单片机的使用，可以完成电控方面的工作，已参与《一种基于混合光谱控制波段约束分解的单目高分作物多光谱表型参数感知系统和方法》的专利。
5	黄健斌	有一定市场调研经验，获得第24届“广发杯”优秀奖，团队协作能力强，实践能力强，在寒假“返家乡”活动中被评为优秀团队，熟练掌握Solidworks，CAD等制图软件，已参与《一种基于主动光源的植物叶片透射与反射纹理影像同步采集装置与方法》的专利。
6	林衍承	熟练掌握python的开发与界面设计，熟练编写代码，运行程序。具备绘制坐标轴并完成函数图像表达的能力。已参与《一种原位半地埋式田间农情信息采集装置与方法》的专利。

此外，电动自行车座垫保护装置的3D图纸设计已经接近完善，可以进入购买材料、组建初代模型阶段。此外，电动自行车座垫自动保护装置的专利已起草，正在专利代理人修改中，等待审核。

（2）已具备的条件，尚缺少的条件及解决方法

1）已具备条件

所在实验室已具备该项目开展所需的基本仪器设备，电动自行车座垫自动保护装置的图纸已经基本完成，相关软、硬件材料和工作也已有序开展。

2）尚缺少的条件

动态仿真、动力学分析以及系统能耗等计算还未开展。

3）解决方法

以项目推进驱动学习，主动了解项目开展需要的基础理论知识，通过不停开展测试试验推动项目进度。

三、 经费预算

开支科目	**预算经费（元）**	**主要用途**	**阶段下达经费计划（元）**	
			前半阶段	**后半阶段**
预算经费总额	5000	用于试验样机研制与试验开展	3500	1500
1. 业务费	2000	/	500	1500
（1）计算、分析、测试费	0	/	0	0
（2）能源动力费	0	/	0	0
（3）会议、差旅费	1000	前往实地投放装置，开展调研	500	500
（4）文献检索费	0	/	0	
（5）论文出版费	1000	发表相关成果	0	1000
2. 仪器设备购置费	0	/	/	
3. 试验装置试制费	1000	部分需要3D打印与金属加工	1000	0
4. 材料费	2000	购买相关易损耗材	2000	0
学校拨款	5000			
财政拨款	/			

四、 项目组成员签名

吴剑锋 林烨枫 梁浩伟 尹旺奎 林衍承 黄健斌

五、 指导教师意见

同意推荐。

导师（签章）： 姜锐

2024 年 5 月 4 日

六、 院系推荐意见

盖 章:

年 月 日

七、 学校推荐意见

盖 章:

年 月 日

-

生产实践锻炼证明

华南农业大学：

广东省农业航空应用工程技术研究中心重点围绕智能感知、智慧决策、精准作业三个方面开展水稻无人农场关键技术研究，培养智慧农业人才，服务国家农业发展。

为了建设丝苗米省级现代农业产业园，也为东源现代农业发展提供技术支撑，辐射带动东源农业科技快速发展，研究中心结合东源农业发展需要在柳城镇下坝村科技小院开展了一系列科技兴农生产实践活动。期间，工程学院姜锐老师于 2022 年 9 月 1 日-至今在科技小院开展了以遥感监测、智能感知、智慧决策、精准作业等多个方面的水稻无人农场关键技术研究，累计超过 200 天，为我国农业向现代化、信息化、智慧化方向发展提供了有力的技术力量。

特此证明！

广东省农业航空应用工程技术研究中心

证明人：

2024 月 2 日 1 日

关于赴河源市东源县柳城镇开展培训学习交流的函

河源市东源县柳城镇人民政府：

为响应国家乡村振兴战略强化农业科技和装备支撑、加快先进农机研发推广的号召，培养新时代新农人，我单位联合中国农业机械学会农业航空分会、国家农业航空产业技术创新战略联盟，拟组织华南农业大学师生 24 人，于 2023 年 7 月 10 日至 7 月 12 日在河源市东源县柳城镇水稻智慧农场开展农用无人机的操作培训与相关试验、推广活动，望贵单位予以支持为盼。

特此函达。

华南农业大学

广东省农业航空应用工程技术研究中心

2023 年 7 月 9 日

附赴河源市东源县柳城镇人员名单：

周志艳 华南农业大学工程学院教授、广东省农业航空应用工程技术研究中心主任、国家农业航空产业技术创新战略联盟秘书长

姜 锐 华南农业大学工程学院助理研究员、中国农业机械学会农业航空分会副秘书长

郭晓燕 华南农业大学工程学院讲师

黄俊浩等 20 人 华南农业大学在读学生

司机 1 名


农用无人飞机操作培训班
耕地保护


田间科技小院
农用无人飞机操作培训班
华南农业大学
东源县水稻智慧农场
技术创新研究中心
华南农业大学
产学研合作基地

部分推广应用活动图集

一、全省代表性推广应用活动

（1）2021 年全省春季农业生产暨支农服务下乡现场会

2021 年 3 月 5 日，全省春季农业生产暨支农服务下乡现场会在茂名举行，农用无人飞机参与演示示范。

图 1　2021 年全省春季农业生产暨支农服务下乡现场会

（2）2020 年第十九届广东种业博览会

2020 年 12 月 11 日，2020 年世界数字农业大会第十九届广东种业博览会中直播介绍华南农业大学变量施肥无人机，观看人数：25.95 万，直播地址：https://wx.vzan.com/live/tvchat-497277404? Shareuid =38043392 &vprid=0 & sharetstamp =1607672739872#/

图 2　2020 年世界数字农业大会第十九届广东种业博览会中直播

（3）中央电视台报道

2020 年以来，中央电视台十套、二套，人民网广东频道，分别报道了“无人机遥感信息获取与水稻养分精准管理技术”成果在稻米生产中的应用情况。

图 3　2020 年 3 月份中央电视台 10 套、2 套报道无人机精准施肥技术

图 4　2020 年 6 月份中央电视台 13 套、10 套、2 套报道无人机精准撒播技术

图 5　2021 年 4 月 15 日央视 2 套报道 4 月 15 日东源县春耕现场会的变量施肥演示

二、广州市推广应用活动

变量施肥无人飞机推广应用

项目组于 2015 年起，每年早稻、晚稻种植季先后多次在广东省增城水稻试验基地开展水稻氮素营养的遥感信息获取试验，获得了大量的低空遥感试验数据，用于后续的遥感数据处理算法及水稻养分精准管理决策研究。

图 6 水稻试验示范遥感影像

图 7　2020 年 12 月 8 日广州市增城区农用无人飞机现场演示会

图 8　　2021 年 9 月 6 日广州市增城区点射播种无人飞机现场测产验收

图 9 广州市增城区作业航迹图

三、云浮市推广应用活动

采用前述的飞翼及多旋翼无人飞机遥感信息获取平台，项目组于 2017 年早稻种植季开始进行试验示范，先后多次在云浮市罗定稻香园公司水稻试验基地开展水稻氮素营养的遥感信息获取试验，并开辟了核心示范区，进行农民传统施肥方式与遥感模型决策施肥方式的对比。

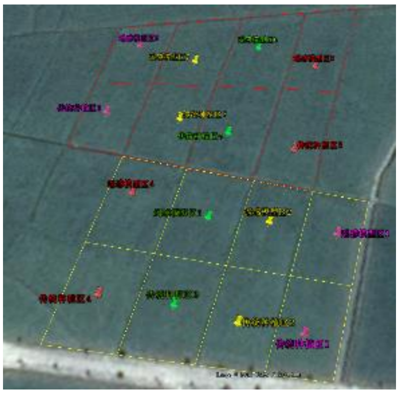

图 10 广东省罗定水稻核心试验示范基地

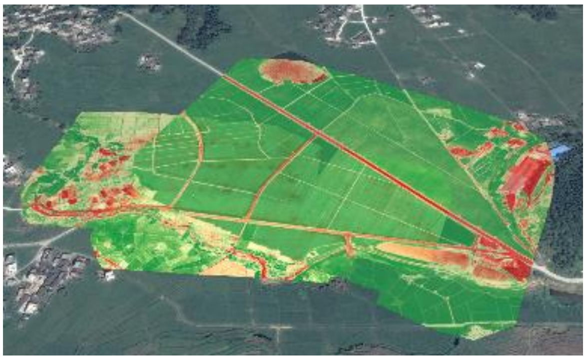

图 11 广东省罗定水稻试验示范遥感影像

图 12 采用飞翼无人机遥感平台在罗定开展水稻遥感监测应用示范

图 13 2017 年核心示范区对比试验验收现场会

图 14 罗定核心示范区对比试验水稻长势情况

图 15 2017 年无人机遥感信息获取与水稻养分管理技术研讨会

图 16　2020 年 6 月 20 日早稻罗定市太平镇无人机精准施肥作业现场会

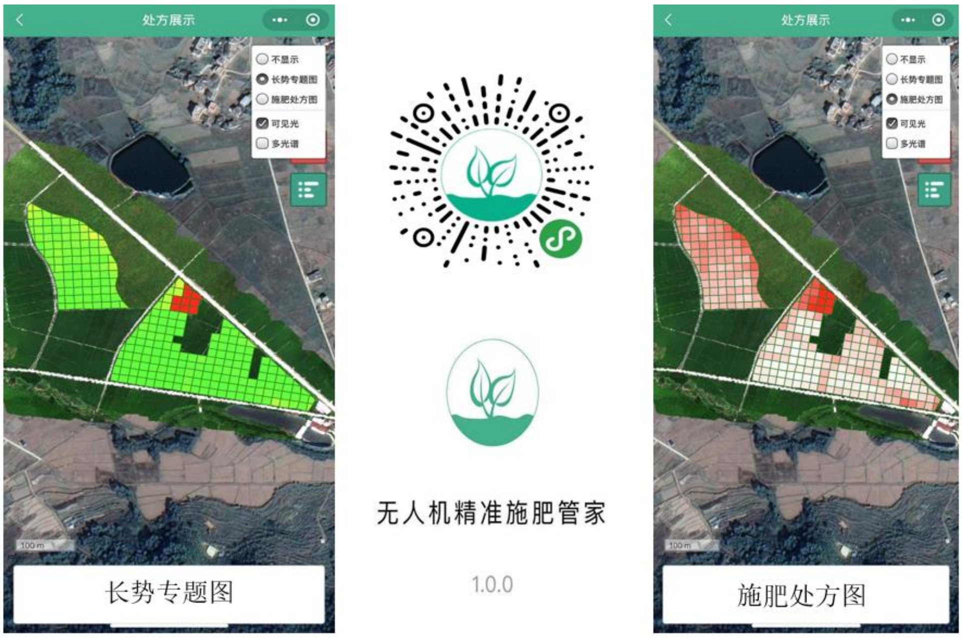

图 17　罗定市太平镇 2020 年晚稻水稻种植应用示范区及精准施肥作业处方图

图 18　2020 年晚稻罗定市太平镇无人机精准施肥作业现场会

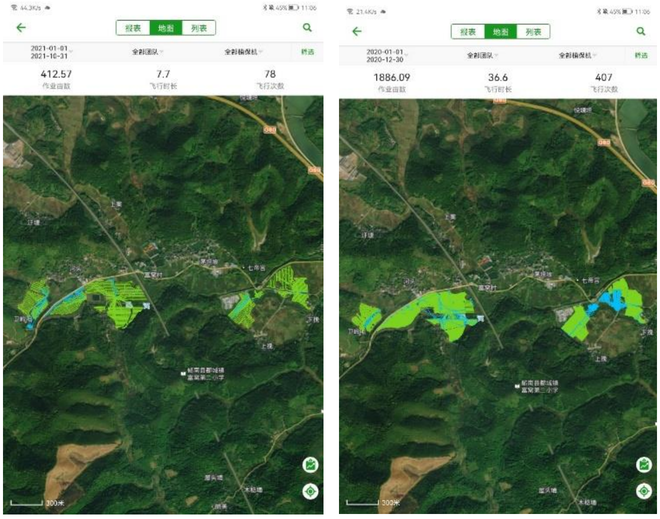

2021-01-01 2021-10-31

412.57 作业亩数

7.7 飞行时长

78 飞行次数

2020-01-01 2020-12-30

1886.09 作业亩数

36.6 飞行时长

407 飞行次数

图 19 云浮市作业航迹图

四、韶关市推广应用活动

韶关市南雄试验基地采用烟稻轮作的模式，项目组结合当地的种植习惯，并按照美香占 2 号种植规程设定的农事安排表，在每个施肥节点前，先后采用固定翼无人机遥感平台进行了多年低空遥感数据采集（穗肥、粒肥、营养生长到生殖生长过渡阶段、熟色阶段），并制定了施肥方案供农户参考，并在收获时进行了测产验证。

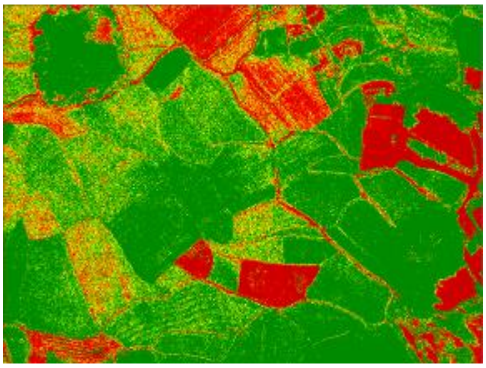

图20 广东省南雄市油山镇、黄坑镇美香占标准种植基地航拍图

图 21 2017 年南雄开展水稻遥感监测应用示范

图 22 2017 年演示会现场

图 23 2017 年现场会合影

图 24 2017 年培训会现场

图 25 与会代表合影

图 26 2017 年南雄核心示范区测产现场会

图 27 南雄核心示范区水稻长势情况

五、清远市推广应用活动

图28　2020 年 8 月 5 日清远市阳山县现场会

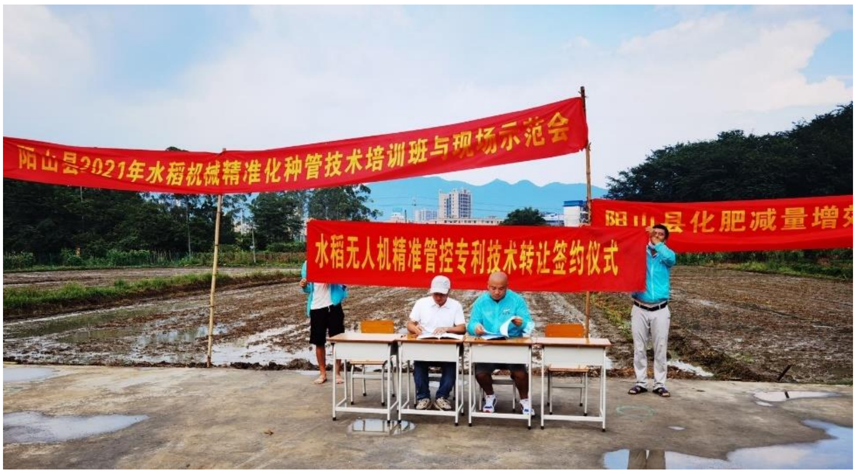

图29 水稻无人机精准管控专利技术许可转让签约

图 30 万亩水稻精准统防统治示范

2021 年 8 月 15 日，在清远市的应用示范中，共完成了四次较大规模的培训，

共计 129 人次参加农用无人飞机操作培训。

图 31 2021 年 3 月 6 日清远市阳山县精准管控关键技术的无人机操作员培训

图 32 精准管控关键技术的收割测产及技术演示现场培训

图 33 无人飞机精准变量施肥示范培训

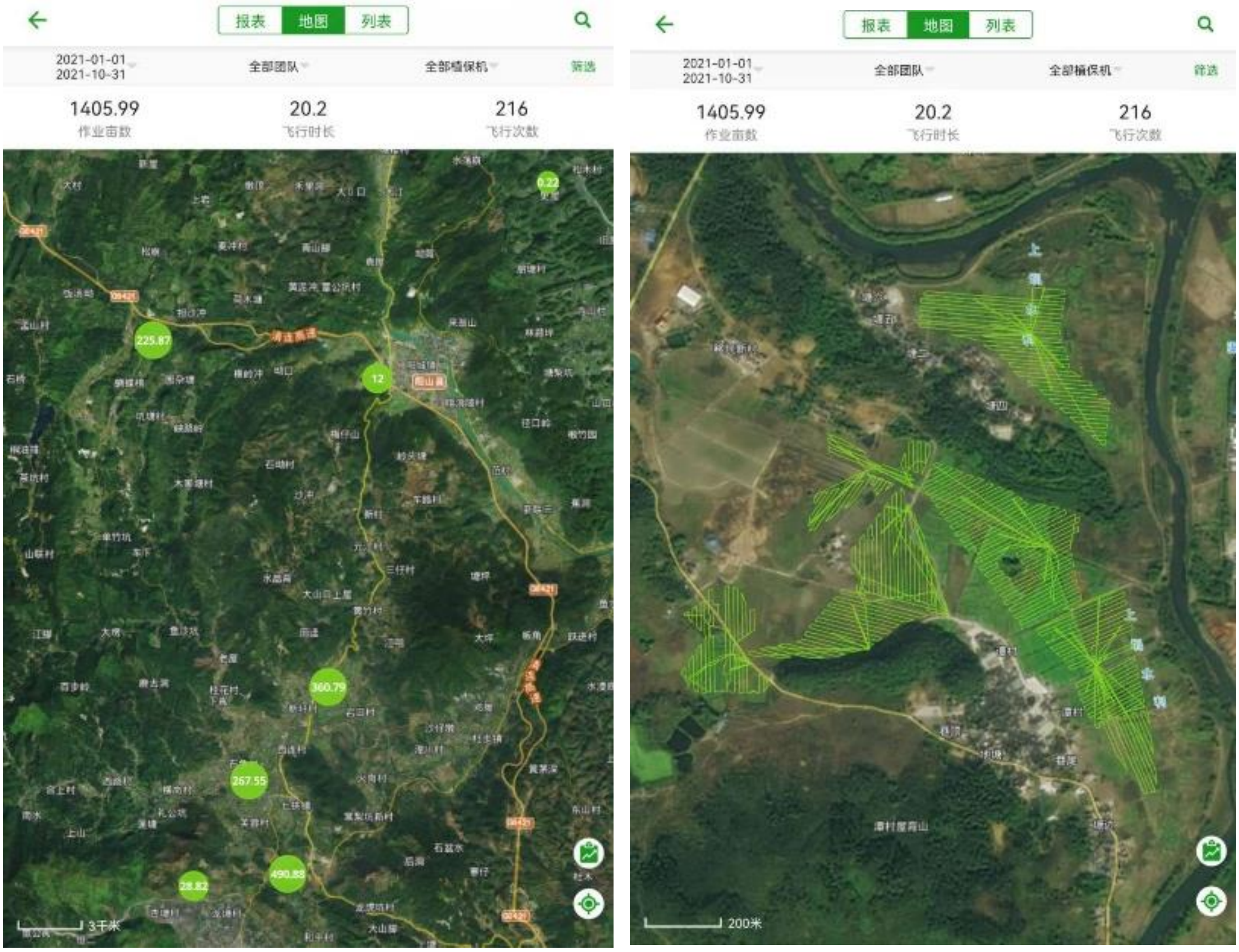

图 34 清远市阳山县作业航迹图

八、河源市推广应用活动

图 35 2021 年 4 月 15 日河源市东源县春耕现场会

图 36 2023年 3月 1日 河源市东源县广东省春耕现场会

图 37 2021 年 6 月 6 日河源市东源县无人农场现场会

图 38 2021 年 9 月 23 日河源市东源县柳城镇农民丰收节现场会

2021-01-01
2021-10-31
全部团队
全部植保机
筛选

9200.72	177.3	4290
作业亩数	飞行时长	飞行次数

2021-01-01
2021-10-31
全部团队
全部植保机
筛选

9200.72	177.3	4290
作业亩数	飞行时长	飞行次数

图 39 河源市东源县作业航迹图

2022 年化肥减量增效工作总结及“三新”技术模式典型案例

农业农村部种植业管理司

全国农业技术推广服务中心

2022 年 11 月

目 录

前 言……1

2022 年化肥减量增效工作总结……3

夏玉米种肥同播及果树水肥一体化技术模式……14
——河北省三河市化肥减量增效典型案例……14
水稻果树无人机喷肥技术模式……21
——辽宁省营口市化肥减量增效典型案例……21
春玉米“测土配方+叶面喷施”技术模式……27
——吉林省双辽市化肥减量增效典型案例……27
水稻油菜 “测土配方施肥+机械施肥”技术模式……32
——江西省瑞昌市化肥减量增效典型案例……32
小麦 “种肥同播+”技术模式……37
——山东省陵城区化肥减量增效典型案例……37
小麦玉米“测土配方施肥+水肥一体化”技术模式……44
——河南省获嘉县化肥减量增效典型案例……44
玉米 “种肥同播+叶面喷施” 技术模式……52
——河南省叶县化肥减量增效典型案例……52
水稻无人机低空遥感精准施肥技术模式……58
——广东省东源县化肥减量增效典型案例……58
水稻侧深施肥及无人机喷施技术模式……64
——广西自治区港南区化肥减量增效典型案例……64
施肥一大片 不如机械一条线……70
——江苏省东台市水稻侧深施肥典型案例……70
水稻“麦秸秆还田+增施有机肥+侧深施肥应用缓释肥”技术模式……74
——江苏省六合区化肥减量增效典型案例……74
稻麦油“机械施肥+”技术模式……80
——安徽省广德市化肥减量增效典型案例……80

粮经作物“三新”技术模式 87

——福建省上杭县化肥减量增效典型案例 87

“浙样施”+“浙农优品”互连互通数字赋能技术模式 94

——浙江省永康市化肥减量增效典型案例 94

水稻“精准施肥+” 技术模式 101

——贵州省播州区化肥减量增效典型案例 101

辣椒“水溶性肥料+水肥一体化”技术模式 106

——海南省澄迈县化肥减量增效典型案例 106

水稻高粱轻简化栽培技术模式 111

——重庆市合川区化肥减量增效典型案例 111

小麦水稻柑橘 “三新” 技术模式 118

——四川省西充县化肥减量增效典型案例 118

大豆—玉米带状复合种植“精准施肥+无人机喷施”技术模式 125

——云南省楚雄州化肥减量增效典型案例 125

小麦玉米葡萄 “配方肥+” 技术模式 129

——陕西省合阳县化肥减量增效典型案例 129

小麦浅埋滴灌及蔬菜叶面喷施、水肥一体化技术模式 135

——甘肃省金川区化肥减量增效典型案例 135

粮油作物无人机喷施有机叶面肥技术模式 141

——青海省大通县化肥减量增效典型案例 141

大豆—玉米带状复合种植无人机叶面喷施技术模式 146

——宁夏自治区惠农区化肥减量增效典型案例 146

“卫星遥感诊断监测+水肥一体化智能配肥”云服务技术模式 150

——新疆拜城县化肥减量增效典型案例 150

水稻无人机低空遥感精准施肥技术模式

——广东省东源县化肥减量增效典型案例

一、基本情况

东源县是广东省水稻种植大县，2021 年全县粮食播种面积达 38.08 万亩、产量达 15.38 万吨，其中水稻种植面积约 35.09 万亩、产量 14.69 万吨，化肥年施用总量（折纯）14431 吨。为加快推进东源县农业生产现代化建设，促进农业绿色可持续发展，开展了化肥减量增效新技术、新产品、新机具的“三新”技术应用示范，并在柳城镇下坝村建立了无人机低空遥感精准施肥应用示范基地。

二、技术模式

水稻无人机低空遥感精准施肥技术模式是采用无人机低空遥感高时效获取水稻长势信息，构建水稻施肥精准管理体系。

在水稻生产管理中，需要根据生长期需要，进行及时的长势监测，以适时调控决策肥料投入，按需进行变量施肥，充分提高肥料的利用率。为此，东源县与华南农业大学合作，研发了适用于无人机低空遥感的感算一体遥感传感器系统及其遥感数据同步高效获取和解析方法，基于快速生成的水稻群体长势专题图对水稻氮素进行了变量精准调控，开发了配套的无人机精准施肥管家系统和变量施肥无人机，全流程地实现了对水稻长势数字化感知、智能化决策、精准化作业。

（一）数字化感知

低空遥感无人机搭载 5 通道多光谱遥感相机，使用 60 °无畸变成像镜头，5 通道并行获取和处理技术，配合独立自适应曝光实现作物冠层反射率的精准获取。数据感知计算一体进行，可实现 300 亩/分钟的数据解析效率，无人机落地数分钟内即可生成作物长势专题图。

低空遥感无人机

（二）智能化决策

通过对作物“察颜观色”生成的长势专题图进行作物群体生长情况评估，结合特定作物品种的生长模型和专家知识库，利用“3S”技术生成变量施肥处方图，实现作物养分精准评估和决策。

（三）精准化作业

变量施肥无人机载重 30 公斤，撒播幅宽 8m，最大排量 40 公斤/min，可全程自主作业，余量自动监测，断点记录与续航，搭载变量施肥系统可实现变量施肥。通过加载处方图获取田块中

各位置点的施肥量，变量施肥系统实时解析无人机当前位置的目标施肥量，依据飞行速度、作业幅宽、GPS 坐标位置信息计算出槽轮转速，由步进电机实时精确控制槽轮转速，从而调节施肥量实现变量施肥，并具有撒肥落点预判，撒肥位置精准。

变量施肥无人机

水稻精准施肥管控技术操作流程：

1、无人机遥感监测；

2、作物群体长势解析；

3、智能养分决策系统生成施肥处方图；

4、变量施肥无人机加载处方图进行作业。

无人机精准施肥技术体系

农事作业情况如表 1 所示。

表 1 各农事节点的数据记录（2022 年）

时间节点	农事安排	作业方式	用量 （亩）	用药/肥处方
3 月 7 日	整地	旋耕机	/	/
3 月 12 日	基肥	无人机撒施	20 公斤	芭田复合肥 18—8—15
3 月 13 日	播种	无人驾驶水直播	2.5 公斤	/
3 月 16 日	封闭除草	植保无人机	/	/
4 月 13 日	分蘖肥	无人机撒施	5 公斤	尿素 总氮≥46%
4 月 13 日	分蘖肥	无人机撒肥	2.5 公斤	芭田复合肥 18—8—15
5 月 25 日	第一次常规防治	植保无人机	/	每亩使用：30%苯甲丙环唑悬浮剂 30g、18 杀虫双乳剂 400ml、5%阿维菌素乳油 100ml、10%三氟苯嘧啶悬浮剂 25ml、航侣飞防助剂 10ml、兑水 3L
6 月 3 日	穗肥	无人机变量施肥	根据处方图变量	芭田复合肥 18—8—15
6 月 12 日	第二次常规防治	植保无人机	/	每亩使用：40%三环唑 50ml、50%氯溴异氰尿酸 60g、10%三氟苯嘧啶 25ml、航侣飞防助剂 10ml

三、主要成效

今年早稻试验表明，处方图变量施肥作业总施肥量 158.71 公斤（复合肥 18—8—15），折算复合肥用量为 6.35 公斤/亩（其中纯氮为 1.14 公斤/亩），相比常规施肥的 7.5 公斤/亩，节省肥料用量 15.35%。示范区内水稻营养生长整齐一致，穗大粒多，结实率高，青枝腊秆，籽粒饱满，平均产量达 537.5 公斤/亩，比传统施肥处理增产 6%—10%，亩均增收节支 100 元。该技术通过精准用肥，从而达到了稳产、节本的效果。

表 2 测产结果

区域编号	实收面积(m^2)	鲜谷重(公斤)	实测含水率(%)	折合产量(公斤/亩)
1	1	0.8323	23.7667	484.3692
2	1	0.8554	22.5667	505.6180
3	1	0.9627	22.9	566.6179
4	1	0.9357	21.2667	562.3931
5	1	0.9294	19.8667	568.5395
平均值	/	/	22.0734	537.5075

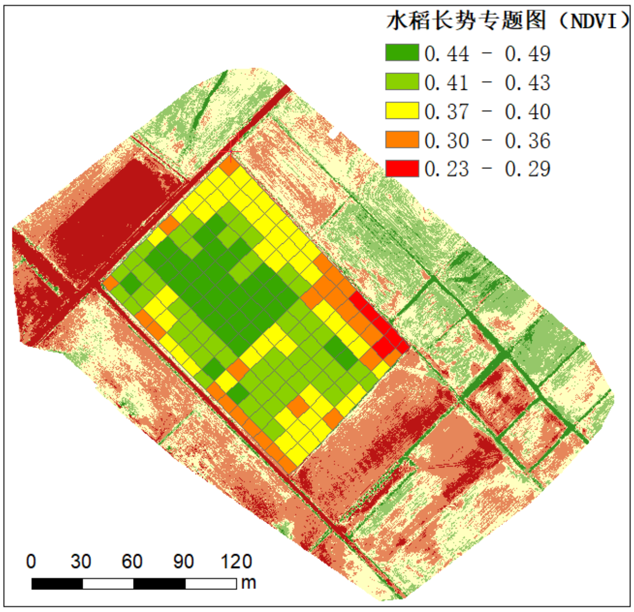

水稻长势专题图

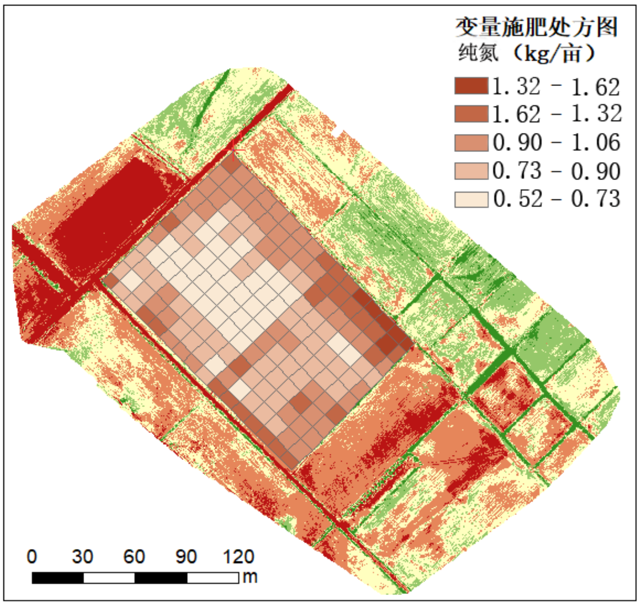

变量施肥处方图

四、主要做法及经验

水稻无人机低空遥感精准施肥技术模式依靠无人机遥感高时效、多波谱和宽视野的特点，在关键施肥节点对水稻长势情况进行监测，依据水稻实际养分的丰缺情况对地块进行栅格化长势分析，并精准计算施肥量，生成变量施肥处方图。变量施肥无人机根据施肥处方图进行精准按需补肥。变量施肥可以提高整体肥料利用率，减少化肥施用，提高粮食产量。